



UNIVERSIDADE FEDERAL DO PARÁ  
INSTITUTO DE CIÊNCIAS EXATAS E NATURAIS  
PROGRAMA DE PÓS-GRADUAÇÃO EM FÍSICA

**COMPACT OBJECTS IN GENERAL RELATIVITY  
AND BEYOND**

Caio Filipe Bezerra Macedo

Belém-Pará  
August 6, 2015

# Compact Objects in General Relativity and Beyond

Caio Filipe Bezerra Macedo

Thesis submitted to the Programa de Pós-Graduação em Física da Universidade Federal do Pará (PPGF-UFPa) in partial fulfillment of the requirements for the degree of Doctor in Physics.

Advisor: Prof. Dr. Luís Carlos Bassalo Crispino

## Examiners

---

Prof. Dr. Luís Carlos Bassalo Crispino (Advisor – UFPa)

---

Prof. Dr. Elcio Abdalla (External member – FISMAT/USP)

---

Prof. Dr. Beatriz Leonor Silveira Barbuy (External member – IAG/USP)

---

Prof. Dr. Manuel Eleutério Rodrigues (Internal member – UFPa)

---

Prof. Dr. Fabrício Queiroz Potiguar (Internal member – UFPa)

---

Prof. Dr. José Ademir Sales de Lima (Supplant member – IAG/USP)

---

Prof. Dr. Marc Casals Casanellas (Supplant member – CBPF)

Belém-Pará  
August 6, 2015

---

## Abstract

General relativity passed all experimental tests in the weak-field regime, what made it the standard theory of gravity. However, the characterization of strong field regime of general relativity is still a challenge, due to the lack of definitive observational data from high curvature regions. It is in the strong regime that general relativity shows its subtleties and where it is possible to test whether or not general relativity should be replaced by an improved theory of gravity. High curvature regions – and therefore regions of strong field – are possible in the vicinity of compact gravitating objects, such as neutron stars, exotic stars, and black holes. Therefore, these compact objects are excellent laboratories to put constraints and to test theories of gravity in the strong regime. The outcome of the investigation of phenomena around these objects may confront crucial characteristics of general relativity as well as rule out possible alternative theories of gravity. With the advent of potential gravitational wave detectors and new or improved telescopes, it is of utmost importance to study the phenomenology around compact astrophysical objects – to understand the nature of the gravitational objects, to improve the description of the current theoretical models, and to understand the theory of gravity itself. In this thesis, we present a collection of studies on compact objects in general relativity and alternative theories of gravity. The thesis is divided in three main parts.

In the first part, we discuss some solutions associated with compact objects. In Chapter 1 we obtain, in closed analytic form, slowly rotating black hole solutions of a general class of theories of gravity, for which the Einstein-Hilbert action is supplemented by all possible quadratic, algebraic curvature invariants coupled to a scalar field. We also discuss possible implications of this solution to the description of accretion disk (thermal) emissions. In Chapter 2 we investigate slowly rotating anisotropic neutron stars in general relativity and in scalar-tensor theories of gravity. We discuss the effect of the fluid anisotropy in the so-called spontaneous scalarization of stars. We also discuss possible ways to constraint the anisotropy of neutron stars.

In the second part, we discuss wave-emission processes around compact objects and quasinormal modes. In Chapter 3 we calculate the emission of scalar waves by a particle orbiting a Kerr black hole, within the context of quantum field theory in curved spacetimes at tree level. In Chapter 5 we discuss astrophysical signatures of a plausible supplant to black holes: boson stars. We obtain quasinormal modes – polar and axial – of boson stars within a fully relativistic approach. We also compute the emission of gravito-scalar waves by a particle in circular orbits around boson stars, showing that the star modes “resonate” for some orbits. In Chapter 4 we discuss two different methods to compute the quasinormal modes of spherically symmetric astrophysical environments, namely: the direct integration method and the continued fraction method. In Chapter 6 we discuss the effect of accretion and dynamical friction in the motion and gravitational wave emission of a particle orbiting around – and through – a dark matter star. We model the dark matter star using uniform density stars and using boson stars. We discuss the cases for which the motion of the particle is subsonic and supersonic.

In the last part, we discuss planar massless scalar waves impinging upon compact objects, considering their absorption and scattering cross sections. In Chapter 8 we compute the absorption cross section of planar massless scalar waves on Kerr black holes. We consider different angles of incidence, such that we explore the role of the rotation of the black hole into the absorption cross section. We also use the “sinc” approximation to compute the absorption cross of Kerr black holes and compare it with our numerical results. In Chapter 9 we analyze a wave

incident on a Schwarzschild black hole surrounded by a thin spherical shell. We show that in the low-frequency limit the absorption cross section approaches the area of the black hole, regardless of the shell characteristics (position and mass). However, in the mid-to-high-frequency limit we show, numerically and analytically, that the absorption cross section can considerably differ from the case of an isolated Schwarzschild black hole with the same ADM mass. In Chapters 10 and 11 we study the absorption and scattering of waves, respectively, incident upon a Bardeen regular black hole. We show that Bardeen black holes can mimic some properties of Reissner-Nordström black holes, considering absorption and scattering of fields.

**Keywords:** compact objects; general relativity; alternative theories of gravity; black holes; neutron stars.

**Fields of Knowledge (CNPq):** 1.05.01.03-7, 1.05.03.01-3, 1.04.02.00-4.

---

## Resumo

A relatividade geral passou por todos os testes experimentais no regime de campo fraco, o que a fez se tornar a teoria padrão para a descrição da gravidade. Entretanto, a caracterização da relatividade no regime de campo forte é ainda um desafio devido à falta de dados observacionais concretos de regiões de curvatura intensa. É no regime de campo forte que a relatividade geral mostra todas as suas sutilezas e onde é possível obter evidências da necessidade de a relatividade geral ser substituída por uma teoria modificada da gravitação. Regiões de curvatura intensa – e portanto de campo forte – são possíveis na vizinhança de objetos compactos, tais como estrelas de nêutrons, estrelas exóticas e buracos negros. Portanto, objetos compactos são laboratórios excelentes para colocar restrições e testar teorias da gravitação em campos fortes. O resultado da investigação de fenômenos em torno de objetos compactos pode por a prova características cruciais da relatividade geral e também descartar possíveis teorias alternativas à gravitação. Com o advento de potenciais detectores de ondas gravitacionais e telescópios melhores e melhorados, é de suma importância estudar a fenomenologia dos objetos compactos, para entender sua natureza, melhorar a descrição dos modelos teóricos atuais e entender a própria teoria da gravitação. Nesta tese, apresentamos um conjunto de estudos envolvendo objetos compactos na teoria da relatividade geral e em teorias alternativas à gravitação. A tese é dividida em três partes principais.

Na primeira parte, discutimos soluções para descrever objetos compactos. No Capítulo 1 obtemos, em uma forma analítica, soluções que descrevem buracos negros com baixa rotação para uma ampla classe de teorias alternativas à gravitação, onde a ação de Einstein-Hilbert é suplementada por todos os termos quadráticos, possíveis invariantes de curvatura algébricos, acoplados com um campo escalar. Discutimos possíveis implicações desta solução para a descrição da emissão térmica por discos de acreção. No Capítulo 2 investigamos soluções de estrelas de nêutrons anisotrópicas com baixa rotação na relatividade geral e em teorias escalares-tensoriais da gravitação. Discutimos os efeitos da anisotropia do fluido na chamada escalarização espontânea de estrelas.

Na segunda parte, discutimos processos de emissão de ondas em torno de objetos compactos e modos quase-normais. No Capítulo 3 calculamos a emissão de ondas escalares por uma partícula orbitando um buraco negro de Kerr, no contexto da teoria quântica de campos em espaços-tempos curvos em nível de árvore. No Capítulo 5 discutimos as assinaturas astrofísicas de um substituto plausível dos buracos negros: as estrelas de bósons. Obtemos os modos quase-normais – polares e axiais – das estrelas de bósons, por um método completamente relativístico. Calculamos a emissão de ondas escalares e gravitacionais por uma partícula em órbita circular em torno das estrelas de bósons, mostrando que os modos da estrela ressoam para algumas órbitas. No Capítulo 4 discutimos dois métodos para calcular os modos quase-normais de cenários astrofísicos com simetria esférica: O método de integração direta e o método da fração continuada. No Capítulo 6 discutimos o efeito da acreção e fricção dinâmica no movimento e na emissão de ondas gravitacionais de uma partícula orbitando através de uma estrela de matéria escura. Modelamos a estrela de matéria escura usando estrelas de densidade uniforme e usando estrelas de bósons. Discutimos os casos em que o movimento da partícula é subsônico e supersônico.

Na última parte, discutimos ondas escalares planas não-massivas incidindo em objetos com-

pactos, investigando seções de choque de absorção e de espalhamento. No Capítulo 8 calculamos a seção de choque de absorção para ondas escalares planas não-massivas incidentes em buracos negros de Kerr. Consideramos vários ângulos de incidência, explorando o papel da rotação na absorção. Também usamos a aproximação sinc para o cálculo da seção de choque de absorção de buracos negros de Kerr, comparando com o método numérico. No Capítulo 9 analisamos uma onda incidente no espaço-tempo de Schwarzschild envolvido por uma casca esférica fina. Mostramos que no limite de baixas frequências a seção de choque de absorção é aproximadamente a área do buraco negro, independente das características da casca esférica (posição e massa). Entretanto, no regime de media para altas frequências mostramos, numericamente que a seção de choque de absorção pode diferir consideravelmente do caso de um buracos negro de Schwarzschild isolado com a mesma massa ADM. Nos capítulos 10 e 11 estudamos a absorção e espalhamento de ondas incidentes num buraco negro regular de Bardeen, respectivamente. Mostramos que os buracos negros de Bardeen podem ser similares aos buracos negros de Reissner-Nordström, no que diz respeito a absorção e espalhamento de campos.

**Palavras-chaves:** Objetos compactos; relatividade geral; teorias alternativas à gravitação; buracos negros; estrelas de nêutrons.

**Áreas de Conhecimento (CNPq):** 1.05.01.03-7, 1.05.03.01-3, 1.04.02.00-4.

*To my family.  
À minha família.*

*A man who can't bear to share his habits is a man who needs to quit them.*  
Stephen King, *The Dark Tower*

## Acknowledgments

Acknowledgments are always complicated: You very likely forget someone that have done something very important. Therefore, I apologize in advance if I forget to mention someone. Motivated on that, I usually will prefer to mention groups of people; people will identify themselves in these groups (that's right... I'm talking to you).

- To my parents, Vilmar and Rita Macedo, for the affection, dedication and love they have given me throughout my entire life.
- To my brothers, Kizz Menezes, Daniela Macedo, and Vilmar Macedo Junior for the companionship and friendship.
- To my niece Thalita Macedo, for all the joy she brings to my life.
- To Carolina Benone, for the patience, love and affection, that made my life easier (and a bit complicated) during these years. I can't imagine how my life would be without you Carol.
- To all my closest relatives (which are many), for the amazing childhood. I wish I could spend more time with you.
- To my friends from inside the Physics sphere, who have contributed with discussions, ideas and suggestions through my entire course.
- To my friends from outside the Physics sphere, who for many times have shown me that there is still life out there.
- To the professors of Physics Faculty of UFPA, which, in the majority, were always available, answering questions of an aspiring physicist.
- To the gravity group of UFPA in Belém-Brazil (Grav@Zon – Gravity @ Amazonia), for all the meetings and discussions.
- To the CENTRA-IST in Lisbon-Portugal, for the hospitality and for all the things I have learned. Also, to the Gravity Group in Lisbon (GRIT).
- To my advisor Luís Crispino, for the excellent guidance and opportunities he provided during the development of my entire career. Thanks for all your work and dedication.
- To my co-advisor Vítor Cardoso in Portugal, who received me in a unknown land, making me feel as I was in my own home. Thanks a lot for all the advices and for the opportunity to work with you.
- To Paolo Pani (who was also a wonderful co-advisor in Lisbon). Thank you Paolo for being my guide throughout the perturbation theory in stars and black holes, and for all illuminating discussions.

- To Emanuele Berti, Sam Dolan, Ednilton Santos de Oliveira, Hirotada Okawa, Hector Okada da Silva and Luiz Carlos dos Santos Leite. Thanks for the opportunity to work with you and all the interesting discussions. This thesis is surely your baby as well! I hope our collaboration will last a lifetime!
- To the sponsoring agencies, in special to the Conselho Nacional de Desenvolvimento Científico e Tecnológico (CNPq), to the Coordenação e Aperfeiçoamento de Pessoal de Nível Superior (CAPES), to the Fundação Amazônia de Amparo a Estudos e Pesquisas do Pará (FAPESPA), to the Fundação para a Ciência e a Tecnologia (FCT), and to the Marie Curie Funding People Action.

# Contents

<b>Preface</b>	<b>xiii</b>
<b>General introduction</b>	<b>1</b>
<b>I Spacetime solutions</b>	<b>7</b>
<b>1 Slowly rotating black holes in alternative theories of gravity</b>	<b>8</b>
1.1 Gravity with quadratic curvature corrections . . . . .	9
1.2 Slowly rotating black holes . . . . .	10
1.3 Geodesic structure . . . . .	12
1.4 Discussion and Conclusion . . . . .	14
<b>2 Slowly rotating anisotropic stars in general relativity and scalar-tensor theory</b>	<b>15</b>
2.1 Anisotropic fluids in scalar-tensor theory of gravity . . . . .	17
2.1.1 Overview of the theory . . . . .	17
2.1.2 Anisotropic fluids . . . . .	18
2.2 Stellar structure in the slow-rotation approximation . . . . .	20
2.3 Numerical results . . . . .	23
2.3.1 The effect of anisotropy in general relativity . . . . .	23
2.3.2 The effect of anisotropy on spontaneous scalarization . . . . .	25
2.3.3 Critical scalarization point in the linearized approximation . . . . .	29
2.4 Conclusions . . . . .	31
<b>II Wave-emission processes and quasinormal modes</b>	<b>34</b>
<b>3 Semi-Classical Analysis of the Scalar Geodesic Synchrotron Radiation in Kerr</b>	
<b>Spacetime</b>	<b>35</b>
3.1 Introduction . . . . .	35
3.2 Scalar field in Kerr spacetime . . . . .	36
3.3 Scalar radiation . . . . .	38

3.4	Numerical procedure and results . . . . .	40
3.4.1	Normalization factor of the spheroidal wave functions . . . . .	40
3.4.2	Radial functions . . . . .	41
3.4.3	Emitted power . . . . .	41
3.4.4	Power observed asymptotically . . . . .	49
3.5	Final remarks . . . . .	50
<b>4</b>	<b>On the quasinormal modes of relativistic stars and interacting fields</b>	<b>51</b>
4.1	Methods . . . . .	52
4.1.1	Direct integration method . . . . .	52
4.1.2	Continued fraction method . . . . .	54
4.2	Application: Quasinormal modes of boson stars . . . . .	56
4.3	Discussion and final remarks . . . . .	60
<b>5</b>	<b>Astrophysical signatures of boson stars: Quasinormal modes and inspiral resonances</b>	<b>61</b>
5.1	Einstein's equation for a particle orbiting a boson star . . . . .	63
5.1.1	Background solutions . . . . .	63
5.1.2	Perturbations . . . . .	64
5.2	Solving the background equations . . . . .	69
5.2.1	Mini boson stars . . . . .	70
5.2.2	Massive boson stars . . . . .	71
5.2.3	Solitonic boson stars . . . . .	72
5.3	Geodesics around boson stars . . . . .	73
5.4	Quasinormal modes of boson stars . . . . .	75
5.4.1	Axial quasinormal modes . . . . .	75
5.4.2	Polar quasinormal modes . . . . .	78
5.4.3	Results for boson star quasinormal modes . . . . .	81
5.5	Point-particle orbiting a boson star . . . . .	83
5.5.1	Axial sector . . . . .	83
5.5.2	Polar sector . . . . .	85
5.5.3	Emitted polar flux and inspiral resonances . . . . .	86
5.6	Conclusions and outlook . . . . .	90
<b>6</b>	<b>Into the lair: Gravitational wave signatures of dark matter</b>	<b>92</b>
6.1	GW-signatures of EMRIs inside compact DM configurations . . . . .	94
6.1.1	Accretion- and gravitational drag-driven inspiral . . . . .	95
6.1.2	Numerical evolution of the inspiral in the interior . . . . .	100
6.1.3	Gravitational waveforms . . . . .	103
6.1.4	Analytical Fourier waveforms in the stationary-phase approximation . . . . .	105
6.2	Relativistic analysis for the external inspiral . . . . .	108
6.2.1	Relativistic models of supermassive DM objects . . . . .	109
6.2.2	Geodesics around boson stars . . . . .	110

6.2.3	Point-particle orbiting a boson star, resonant fluxes and quasinormal modes . . . . .	112
6.3	Conclusions and outlook . . . . .	117
<b>7</b>	<b>Light rings as observational evidence for event horizons: Long-lived modes, ergoregions and nonlinear instabilities of ultracompact objects</b>	<b>119</b>
7.1	Ultracompact objects . . . . .	120
7.1.1	Constant-density stars . . . . .	121
7.1.2	Thin-shell gravastars . . . . .	122
7.2	Perturbations of ultracompact objects . . . . .	122
7.3	Long-lived modes of ultracompact objects . . . . .	124
7.3.1	A WKB analysis . . . . .	124
7.3.2	Numerical results: the spectrum of linear perturbations . . . . .	126
7.3.3	Numerical results: time evolution of wavepackets . . . . .	127
7.4	Spinning ultracompact objects and the ergoregion instability . . . . .	129
7.5	The nonlinear regime . . . . .	131
7.6	Conclusions . . . . .	133
<b>III</b>	<b>Absorption and scattering of planar scalar waves</b>	<b>135</b>
<b>8</b>	<b>Absorption of planar massless scalar waves by Kerr black holes</b>	<b>136</b>
8.1	Scalar field in the Kerr spacetime . . . . .	137
8.2	Absorption cross section . . . . .	139
8.2.1	Low-frequency regime . . . . .	140
8.2.2	High-frequency regime . . . . .	140
8.3	Numerical results . . . . .	145
8.4	Conclusion . . . . .	149
<b>9</b>	<b>Scalar waves impinging in a dirty black hole: Schwarzschild black holes surrounded by thin spherical shells</b>	<b>150</b>
9.1	Black holes with surrounding spherical shells . . . . .	152
9.2	Scalar field . . . . .	154
9.3	Absorption cross section . . . . .	156
9.3.1	Partial-waves approach . . . . .	156
9.3.2	Low-frequency regime . . . . .	157
9.3.3	Null geodesics: high-frequency . . . . .	157
9.4	Results . . . . .	162
9.5	Final remarks . . . . .	163
<b>10</b>	<b>Absorption of planar massless scalar waves by Bardeen black holes</b>	<b>165</b>
10.1	Bardeen regular black holes . . . . .	166
10.2	Absorption cross section . . . . .	167

10.2.1	Partial-waves approach . . . . .	167
10.2.2	Low- and high-frequency limits . . . . .	170
10.3	Results . . . . .	171
10.4	Final remarks . . . . .	175
<b>11</b>	<b>Scattering by regular black holes: Planar massless scalar waves impinging upon a</b>	
	<b>Bardeen black hole</b>	<b>177</b>
11.1	Classical scattering and semiclassical glory . . . . .	179
11.1.1	Geodesic scattering . . . . .	179
11.1.2	Glory scattering . . . . .	181
11.2	Planar wave scattering . . . . .	182
11.3	Results . . . . .	183
11.4	Final remarks . . . . .	186
	<b>Appendices</b>	<b>188</b>
<b>A</b>	<b>Slowly rotating approximation</b>	<b>189</b>
<b>B</b>	<b>Derivation of equation (2.32)</b>	<b>191</b>
<b>C</b>	<b>Massive scalar modes of a constant density star</b>	<b>192</b>
<b>D</b>	<b>Radiation-driven inspiral in the exterior</b>	<b>195</b>
<b>E</b>	<b>Motion of particles in a spring-like potential</b>	<b>197</b>
<b>F</b>	<b>Energy conditions</b>	<b>199</b>

# Preface

This thesis is basically the result of the research developed during the graduate studies of the author. It is a collection of all scientific papers (published, accepted, submitted, and in final stages of preparation) by the author and collaborators, organized in a logical – bias dependent – manner.

The content of this thesis is based on the following scientific articles:

- P. Pani, C. F. B. Macedo, V. Cardoso, and L. C. B. Crispino, Slowly rotating black holes in alternative theories of gravity, *Phys. Rev. D*, vol. 84, p. 087501 (2011) – (Chapter 1);
- C. F. B. Macedo, L. C. B. Crispino, and V. Cardoso, Semiclassical analysis of the scalar geodesic synchrotron radiation in Kerr spacetime, *Phys. Rev. D*, vol. 86, p. 024002 (2012) – (Chapter 3);
- C. F. B. Macedo, P. Pani, V. Cardoso, and L. C. B. Crispino, Into the lair: gravitational-wave signatures of dark matter, *Astrophys. J.*, vol. 774, p. 48 (2013) – (Chapter 6);
- C. F. B. Macedo, P. Pani, V. Cardoso, and L. C. B. Crispino, Astrophysical signatures of boson stars: quasinormal modes and inspiral resonances, *Phys. Rev. D*, vol. 88, p. 064046 (2013) – (Chapter 5);
- C. F. B. Macedo, L. C. S. Leite, E. S. Oliveira, S. Dolan, and L. C. B. Crispino, Absorption of planar massless scalar waves by Kerr black holes, *Phys. Rev. D*, vol. 88, p. 064033 (2013) – (Chapter 8);
- V. Cardoso, L. C. B. Crispino, C. F. B. Macedo, H. Okawa, and P. Pani, Light rings as observational evidence for event horizons: long-lived modes, ergoregions and nonlinear instabilities of ultracompact objects, *Phys. Rev. D*, vol. 90, p. 044069 (2014) – (Chapter 7);
- C. F. B. Macedo, and L. C. B. Crispino, Absorption of planar massless scalar waves by Bardeen regular black holes, *Phys. Rev. D*, vol. 90, p. 064001 (2014) – (Chapter 10);
- H. O. Silva, C. F. B. Macedo, E. Berti, and L. C. B. Crispino, Slowly Rotating Anisotropic Neutron Stars in General Relativity and Scalar-Tensor Theory, to appear in *Classical Quantum Gravity* (2015); This article was selected to appear in *Classical Quantum Gravity Plus as Authors' Insight* – (Chapter 2);

- C. F. B. Macedo, E. S. de Oliveira, and L. C. B. Crispino, Scattering by regular black holes: Planar massless scalar waves impinging upon a Bardeen black hole, to appear in Phys. Rev. D (2015) – (Chapter 11);
- L. C. S. Leite, C. F. B. Macedo, and L. C. B. Crispino, Scalar waves impinging in a dirty black hole: Schwarzschild black holes surrounded by thin spherical shells, in preparation (2015) – (Chapter 9);
- C. F. B. Macedo, V. Cardoso, L. C. B. Crispino, and P. Pani, On the quasinormal modes of relativistic stars and interacting fields, in preparation (2015) – (Chapter 4).

Additionally, the author also produced the following conference proceedings:

- C. F. B. Macedo, L. C. B. Crispino, P. Pani, and V. Cardoso, Imprints of Quadratic Theories of Gravity on Accreting Matter, The Thirteenth Marcel Grossmann Meeting, chap. 132, p. 1231-1233 (2015);
- C. F. B. Macedo, L. C. B. Crispino, V. Cardoso, H. Okawa, and P. Pani, Evidence for event horizons: long-lived modes in ultracompact objects, to appear in IJMPD (2015);

and the following monographs:

- C. F. B. Macedo, Radiação Síncrotron Geodésica no Espaço-Tempo de Kerr, Master Thesis, Universidade Federal do Pará, Belém (2011);
- C. F. B. Macedo, Gravitational Imprints of Compact Dark Matter Configurations, Qualifying Monograph, Universidade Federal do Pará, Belém (2014).

# General introduction

Gravity is the weakest of all fundamental forces in nature. The fact that gravity is weak is experienced in our everyday life – we don't need effort to pull two apples apart against their mutual gravity, in contrast with the case of two magnets, in which we feel notably the electromagnetic force. In fact, this discrepancy between the electromagnetic and gravitational forces is the reason why we don't fall through the ground! The earliest object for which all of us perceive gravity – painfully, some of the times – is the Earth: The most immediate (very) massive body close to us. As we mentioned, we do not feel the gravitational attraction between two apples, but if we lose the apples from a height we immediately see them fall to the ground. This is because the mass of the Earth is big enough, such that in the free fall of apples gravity is important. It is not only how massive, however, the body is that tells us that gravity plays an important role. For gravity purposes, the size of the gravitational object also matters.

At first sight, the size of an object does not seem to be relevant. For instance, take the Newtonian theory, for which the gravitational field is given by<sup>1</sup>

$$\mathbf{g} = -G \frac{m(r)}{r^2} \hat{\mathbf{r}}, \quad (1)$$

where  $G$  is the Newton's gravitational constant,  $m(r)$  a mass function,  $r$  is the radial distance to the center of the object, and  $\hat{\mathbf{r}}$  is the unit vector pointing outwards from the center of the object. The size does not appear explicitly in the standard form of Newton's law (1). In fact, the size is masqueraded in the mass function  $m(r)$ . If we consider a star with a uniform density  $\rho$  (with radius  $R$  and total mass  $M$ ), for which  $m$  takes the simple form

$$m(r) = \frac{4}{3}\pi r^3 \rho = \frac{Mr^3}{R^3}, \quad (2)$$

we have that the gravitational field (1) inside the star can be written as

$$\mathbf{g} = -G \frac{M}{R^3} r \hat{\mathbf{r}}, \quad (3)$$

---

<sup>1</sup>For simplicity, we are considering spherically symmetric distributions. In this case, the Gauss theorem allows us to write the Newton's law in terms of an effective mass  $m(r)$ .

Table 1: Approximate values of the compactness parameter, as defined by Eq. (4), for some objects. The higher the compactness is the more relevant is gravity.

Object	Compactness parameter ( $\epsilon$ )
Apple	$10^{-27}$
Earth	$10^{-11}$
Sun	$10^{-6}$
Neutron star	0.3
Schwarzschild black hole	0.5
Highly spinning Kerr black hole	1

such that *inside* the gravitational object (and at its surface) the gravitational field is proportional to the radial distance to the center of the star. Note from Eq. (3) that the gravitational field is proportional to the total mass, but inversely proportional to  $R^3$ . For the case of uniform density stars, Eq. (3) describes the gravitational field experienced inside the star and Eq. (1) describes the field outside the star [where  $\rho(r) = 0$ ], with  $m(r > R) \equiv M$  being the star's total mass. Moreover, our analysis shows that the gravitational field is maximum at the star's surface.

The above analysis, although being very simplified, gives us a way to infer how strong gravity is for celestial objects. In fact, if we combine the constants of the theory – the speed of light  $c$ , and Newton's constant  $G$  – with the mass and radius of the objects, we can define the dimensionless compactness parameter given by<sup>2</sup> [1]

$$\epsilon \equiv \frac{GM}{c^2 R}, \quad (4)$$

to measure how compact the object is and how important gravity is in the description of the physics around it. Note that in the definition (4) of the compactness parameter we used the two characteristics previously stated to have an influence in the perception of the gravitational field: The mass of the object  $M$  and its radius  $R$ . In Table 1 we provide some examples of the value of this parameter. The compactness parameter allows us to see more directly why for some objects, although commonly said to be compact in the everyday terminology, we do not feel gravity. We take the opportunity to state what we shall define as compact in *our terminology*: Gravitational objects are said to be compact if the compactness parameter is high enough, usually  $\epsilon \gtrsim 0.1$ . Therefore, the higher the value of  $\epsilon$ , the more we can feel gravity<sup>3</sup>. If you think gravity is important on Earth – for which  $\epsilon \sim 10^{-11}$  – imagine in a highly spinning Kerr black hole – for which  $\epsilon \sim 1$ !

The Newtonian theory of gravity describes very well the gravitational field around objects with low compactness. It gives very precise results on many phenomena on Solar System scales (see Ref. [2] for a very interesting counter-example), and many stages of the star formation can be described by it. However, as the compactness of the configurations increases, we need to

<sup>2</sup>Throughout the thesis, this parameter may appear defined with a multiplicative factor of 2. This does not have a major role in the discussion presented in here.

<sup>3</sup>Note, however, that at the center of the star, as may be evident from Eq. (3), the gravitational field is zero, regardless of the compactness parameter. Hence, with 'feel gravity' we assume that we are at the surface of the object.

replace Newtonian gravity by an improved theory of gravity. This is when Einstein's theory of gravity enters the scenario.

In 1915 Albert Einstein proposed a theory for the gravitational field that revolutionized physics<sup>4</sup>. In Einstein's general relativity, gravity is described by deformations of space-time, and particles subjected to these deformations (and therefore to gravity) follow natural paths called geodesics. General relativity passed all the Solar System tests extremely well [1, 2], and in the regions that gravity is weak it reduces to the Newtonian theory, as expected. Compact objects are inserted in a context for which gravity is intense. Therefore, general relativity is very important to describe them.

Although being a very successful theory – considered to be the standard theory to describe gravitational phenomena – general relativity presents some problems which seem to arise from its own structure. For instance, the formation of singularities – points in which the physical description breaks down – is very common in some general relativity physical (reasonable) scenarios [4, 5]. Singularities appeared even in the very first solution of general relativity – the Schwarzschild solution, in 1916 [6] – and it is very difficult to know whether or not this issue will be completely clarified in the current understanding of gravity. Moreover, general relativity is non-renormalizable within the standard quantum field theory procedures [7], such that many people believe that it should be modified to include quantum descriptions [8].

The above problems appear mostly at the strong field regime of general relativity. The strong field regime is still an unresolved domain regarding observational data [9]. Although general relativity predicts the existence of very compact objects (such as neutron stars and black holes), it is difficult to tell if the compact objects presented by general relativity are exactly the ones observed in the Universe [10, 11]. For instance, observational data that comes from orbiting particles may carry only kinematical characteristics of the spacetime, such that general relativity results get degenerated with many other theories of gravity [1, 12, 13]. Therefore, the more we know about the variety of compact objects, the better we can understand and compare them, helping to analyze the observational data coming from future measurements.

## Outline

In this thesis we study compact objects within general relativity and other theories of gravity. It is a collection of scientific works elaborated with the participation of the author of the thesis (see the Preface). Each chapter corresponds to a published, accepted, submitted, or in final stages of preparation scientific work/paper – hence, each chapter is self-consistent. The scientific works/papers are not presented in a chronological order, but rather in a way that seems to be logical from the author's – bias dependent – point of view. All the works/papers are about compact objects in general relativity and alternative theories of gravity. We found relevant to separate the thesis presentation in three different parts, grouping them into categories.

- **Part I – Spacetime solutions**

In part I we present the metric solutions within general relativity and beyond.

---

<sup>4</sup>The seminal works by Einstein can be freely downloaded in [3].

In Chapter 1 we present, in a closed analytic form, a general stationary, slowly rotating black hole, which is solution to a large class of alternative theories of gravity in four dimensions. In these theories, the Einstein-Hilbert action is supplemented by all possible quadratic, algebraic curvature invariants coupled to a scalar field. The solution is found as a deformation of the Schwarzschild metric in general relativity. We explicitly derive the changes to the orbital frequency at the innermost stable circular orbit and at the light ring in closed form.

In Chapter 2 we study the effects of anisotropy on slowly rotating stars in general relativity. We also consider one of the most popular extensions of Einstein's theory, called scalar-tensor theories, allowing for spontaneous scalarization (a phase transition similar to spontaneous magnetization in ferromagnetic materials). Anisotropy affects the moment of inertia of neutron stars – a quantity that could potentially be measured in binary pulsar systems. We find that the effects of scalarization increase (decrease) when the tangential pressure is bigger (smaller) than the radial pressure, and we present a simple criterion to determine the onset of scalarization by linearizing the scalar-field equation.

- **Part II – Wave-emission processes and quasinormal modes**

In part II we present the investigations related to wave-emission by inspirals and quasinormal modes of compact objects.

In Chapter 3 we analyze the scalar synchrotron radiation emitted by a source in circular orbits, stable and unstable, direct and retrograde, around a Kerr black hole within the framework of quantum field theory in curved spacetimes at tree level. We also analyze the radiation which escapes to infinity, showing that, in accordance with superradiance, it can be amplified for the case of direct orbits.

In Chapter 5 we perform a detailed study of boson stars and their gravitational-wave signatures in a fully relativistic setting. We construct several fully relativistic boson star configurations, and we analyze their geodesic structure and free oscillation spectra, or quasinormal modes. We explore the gravitational and scalar response of boson star spacetimes to an inspiraling stellar-mass object and compare it to its black hole counterpart. We find that a generic signature of compact boson stars is the resonant-mode excitation by a small compact object on stable quasicircular geodesic motion.

In Chapter 4 we discuss two different methods to compute the quasinormal modes of spherical astrophysical environments, namely: the direct integration method and the continued fraction method. The methods assume that there is a set of equations for which the proper boundary conditions can be imposed, and the interaction between the perturbation components is localized within a finite region. As an application we compute the polar quasinormal modes of boson stars using the continued fraction method. The methods can be applied to astrophysical situations in which the perturbations components (matter and fields) couple only in a finite region of space.

In Chapter 6 we discuss the most promising dissection tool of compact dark matter configurations: the inspiral of a compact stellar-size object and consequent gravitational-wave emission. The inward motion of this “test probe” encodes unique information about the nature of the central, supermassive dark matter configuration. When the probe travels

through some compact dark matter profile we show that, within a Newtonian approximation, the quasi-adiabatic evolution of the inspiral is mainly driven by dark matter accretion into the small compact object and by dynamical friction, rather than by gravitational-wave radiation-reaction. In the exterior region we study a relativistic model in which the inspiral is driven by the emission of gravitational and scalar waves. Resonances in the energy flux appear whenever the orbital frequency matches the mass of the dark matter particle and they correspond to the excitation of the central object's quasinormal frequencies. We discuss some observational consequences of these effects for gravitational-wave detection.

In Chapter 7 we explore in some depth the mode structure of ultracompact stars, in particular constant-density stars and gravastars. We show that the existence of very long-lived modes – localized near a second, stable null geodesic – is a generic feature of gravitational perturbations of such configurations. Already at the linear level, such modes become unstable if the object rotates sufficiently fast to develop an ergoregion. Finally, we conjecture that the long-lived modes become unstable under fragmentation via a Dyson-Chandrasekhar-Fermi mechanism at the nonlinear level. Depending on the structure of the star, it is also possible that nonlinearities lead to the formation of small black holes close to the stable light ring.

- **Part III – Absorption and scattering of plane waves**

In part III we present the results related to scattering wave processes.

In Chapter 8 we consider planar massless scalar waves impinging upon a Kerr black hole, for general angles of incidence. We compute the absorption cross section via the partial wave approach, and present a gallery of results. In the low-frequency regime, we show that the cross section approaches the horizon area; in the high-frequency regime, we show that the cross section approaches the geodesic capture cross section. In the aligned case, we extend the complex angular momentum method to obtain a “sinc” approximation, which relates the regular high-frequency oscillations in the cross section to the properties of the polar null orbit. In the nonaligned case, we show, via a semianalytic approximation, that the reduction in symmetry generates a richer, less regular absorption cross section. We separate the absorption cross section into corotating and counterrotating contributions, showing that the absorption is larger for counterrotating waves, as expected.

In Chapter 9 we study the absorption of planar massless scalar wave by Schwarzschild black holes surrounded by a thin spherical shell. We compute the absorption cross section in the high-frequency limit through a geodesic approximation and through the sinc approximation. We also analyze the low-frequency limit, showing numerically that the absorption cross section goes to the area of the black hole event horizon, regardless of the shell position and mass. We analyze the effect of the shell in the absorption cross section for arbitrary values of the frequency of the field.

In Chapter 10 we study the absorption of planar massless scalar waves by Bardeen regular black holes. We compare the absorption cross section of Bardeen and Reissner-Nordström black holes, showing that the former always have a bigger absorption cross section for fixed values of the field frequency and of the normalized black hole charge.

We also show that it is possible for a Bardeen black hole to have the same high-frequency absorption cross section of a Reissner-Nordström black hole.

In Chapter 11 we consider the scattering of planar massless scalar wave by a Bardeen black hole. We compare the scattering cross section computed using a partial-wave description with the classical geodesic scattering of a stream of null geodesics, as well as with the semi-classical glory approximation. We obtain that, for some values of the corresponding black hole charge, the scattering cross section of a Bardeen black hole has a similar interference pattern as that of a Reissner-Nordström black hole.

As stated before, each chapter is self-consistent. Therefore, in the end of each chapter we present our conclusion remarks, discussions and perspectives.

# **Part I**

## **Spacetime solutions**

# Chapter 1

## Slowly rotating black holes in alternative theories of gravity

General relativity (GR) is an elegant theory which agrees with all observations at Solar System scale and beyond [1, 2]; however its nonlinear, strong-field structure still remains elusive and difficult to test [14]. This, together with some long-standing problems in Einstein theory (like the presence of singularities, difficulties in explaining the accelerated universe and galaxy rotation curves, etc), has motivated the study of viable alternative theories of gravity. These theories, also known as modified theories of gravity, aim to reproduce GR in the weak-field regime, but they can differ substantially from it in the strong curvature regime, where nonlinear effects become dominant. In order to pass current experiments, alternative theories should have the same post-Newtonian expansion as GR, at least to lowest order. However, large deviations are possible in relativistic systems: black holes (BHs), neutron stars, and cosmological models.

BHs are natural candidates to investigate strong curvature corrections to GR. In the next decade, gravitational-wave detectors [15] and high-frequency very long baseline interferometry (VLBI) [16] may provide direct observations of these objects and of their nonlinear structure, completing the wealth of information from current electromagnetic observations [14]. The geometric structure of BHs encodes information about the underlying theory of gravity. Within GR, no-hair theorems (see Ref. [17] and references therein) guarantee that stationary BHs are described by the Kerr solution and this assumption enters most of the calculations, including gravitational-wave emission, gravitational lensing and properties of the accretion disks. However, when corrections to GR are considered, BHs can support non-trivial hairs [18] and new classes of solutions may exist. Hence, it is important to derive deformations to the Kerr metric [19–21] arising from alternative theories of gravity and to predict astrophysical observables within a more general, bias-independent framework.

Previous studies on BH solutions in alternative theories of gravity suffer from two major limitations. First, given the plethora of alternative theories that have been recently proposed, most of the approaches have focused on a case-by-case analysis (with the notable exceptions of Refs. [20, 21]). Secondly, motivated and well-behaved corrections to GR are usually involved, so that BHs must be constructed numerically. In particular, rotating solutions are extremely

challenging to find in closed form and the Kerr metric is usually regarded as unique in this context. Thus, analytical solutions describing rotating BHs in a broad class of alternative theories, as the one we present here, are of utmost importance.

In this chapter, we derive the metric of slowly rotating BHs arising as solutions of a large class of alternative theories of gravity, in which the Einstein-Hilbert action is supplemented by all quadratic, algebraic curvature terms coupled to a scalar field. Rotating BH solutions are relevant for several reasons. Astrophysical BHs are likely to be (rapidly) spinning, due to accretion effects. Thus, any realistic computation (for example the properties of accretion disks) must take rotation into account. Furthermore, the imprints of possible strong curvature corrections are expected to be stronger for those processes taking place close to near-extremal rotating BHs, for which the curvature is larger. For example, the Kretschmann invariant,  $\mathcal{K} = R_{abcd}R^{abcd}$ , on the equatorial event horizon of a Kerr BH of mass  $M$  and angular momentum  $J = aM$  in Boyer-Lindquist coordinates reads  $\mathcal{K} = 48M^2 [M + \sqrt{M^2 - a^2}]^{-6}$ , where here and in the rest of the chapter we use  $G = c = 1$  units. For a Schwarzschild BH ( $a = 0$ ),  $\mathcal{K}M^4 = 3/4$ . However, for extremal Kerr BHs ( $a = M$ ) this scalar invariant is  $\sim 60$  times larger,  $\mathcal{K}M^4 = 48$ .

## 1.1 Gravity with quadratic curvature corrections

We consider a class of alternative theories of gravity in four dimensions obtained by including all quadratic, algebraic curvature invariants, generically coupled to a single scalar field [13]. The action of this theory reads

$$\begin{aligned}
S &= \frac{1}{16\pi} \int \sqrt{-g} d^4x \left[ R - 2\nabla_a \phi \nabla^a \phi - V(\phi) + f_1(\phi) R^2 \right. \\
&\quad \left. + f_2(\phi) R_{ab} R^{ab} + f_3(\phi) R_{abcd} R^{abcd} + f_4(\phi) R_{abcd} {}^* R^{abcd} \right] \\
&\quad + S_{\text{mat}} [\gamma(\phi) g_{\mu\nu}, \Psi_{\text{mat}}] ,
\end{aligned} \tag{1.1}$$

where, in the matter action  $S_{\text{mat}}$ , we have generically included a non-minimal coupling, which naturally arises in some string theories defined in the Einstein frame. In the following, we neglect the scalar self-potential  $V(\phi)$ . Its inclusion, along with theories in asymptotically non-flat spacetimes, is a natural extension of the present chapter.

When  $f_1 = \alpha e^{-2\phi}$ ,  $f_2 = -4f_1$ ,  $f_3 = f_1$  and  $f_4 = 0$ , the theory reduces to the bosonic sector of heterotic string theory and the quadratic corrections reduce to the Gauss-Bonnet invariant. In that case matter is non-minimally coupled to gravity,  $\gamma(\phi) = e^\phi$ . Static BH solutions in Gauss-Bonnet gravity were found analytically in the small coupling limit [22, 23] and numerically for general coupling [18] (see also Ref. [24]). Stationary BHs with Gauss-Bonnet corrections were considered numerically in Ref. [25] for slow rotations, whereas their highly spinning counterpart was recently constructed in Ref. [26]. Furthermore, when  $f_1 = f_2 = f_3 = 0$  and  $f_4 = \alpha_4 \phi$ , the above theory reduces to Chern-Simons gravity [27] and slowly rotating BHs in this theory were obtained in Ref. [28]. The field equations arising from Eq. (1.1) are explicitly given in Ref. [13], where analytical, static BH solutions were also obtained in the small coupling limit. Here we generalize previous studies by constructing slowly rotating BHs in the general

theory (1.1).

The theory (1.1) has to be considered as an effective action, obtained as a truncation from a more general theory. For example in the low-energy expansion of some string theories, the Gauss-Bonnet and Chern-Simons terms arise as second order corrections in curvature. The Einstein-Hilbert term is considered as the first order term in a (possibly infinite) series expansion containing all possible curvature corrections. In this sense, GR may be only accurate up to  $\mathcal{O}(\alpha R^2)$  and second order corrections may be important when dealing with nonlinear, relativistic solutions. For the same reason, we work in a perturbative regime in which possible higher order terms in (1.1) can be safely neglected. We consider the weak-field expansion of the coupling functions

$$f_i(\phi) = \eta_i + \alpha_i \phi + \mathcal{O}(\phi^2), \quad i = 1, 2, 3, 4$$

where  $\eta_i$  and  $\alpha_i$  are dimensional coupling constants. When the coupling functions are constant, i.e.  $\alpha_i = 0$ , the theories above are usually labeled “non-dynamical” and they admit all vacuum GR solutions [13]. As a result, for small scalar fields the background solutions do not depend on  $\eta_i$ . Although non-dynamical theories would have a different linear response, for example a different gravitational-wave emission [29, 30], here we are interested in modified *background* solutions and we then focus on dynamical couplings. Remarkably, in the small coupling limit, the dynamical theory only depends on four couplings,  $\alpha_i$ , regardless of the coupling functions  $f_i(\phi)$ .

## 1.2 Slowly rotating black holes

We consider the following metric ansatz for the stationary, slowly rotating limit,

$$ds^2 = -f(r, \theta)dt^2 + g(r, \theta)^{-1}dr^2 - 2\omega(r) \sin^2 \theta dt d\varphi + r^2 \Theta(r, \theta) d\theta^2 + r^2 \sin^2 \theta \Phi(r, \theta) d\varphi^2 \quad (1.2)$$

together with the scalar field  $\phi = \phi(r, \theta)$ . In Appendix A we solve the field equations [13] order by order in a perturbative scheme for slow rotations and small couplings. Here, we simply report

the final result. We obtain that the slowly rotating BH metric functions read

$$f(r, \theta) = 1 - \frac{2M}{r} + \frac{\alpha_3^2}{4} \left[ -\frac{49}{40M^3r} + \frac{1}{3Mr^3} + \frac{26}{3r^4} + \frac{22M}{5r^5} + \frac{32M^2}{5r^6} - \frac{80M^3}{3r^7} \right] + a^2 \frac{2M \cos^2 \theta}{r^3}, \quad (1.3)$$

$$g(r, \theta) = 1 - \frac{2M}{r} + \frac{\alpha_3^2}{4} \left[ -\frac{49}{40M^3r} + \frac{1}{M^2r^2} + \frac{1}{Mr^3} + \frac{52}{3r^4} + \frac{2M}{r^5} + \frac{16M^2}{5r^6} - \frac{368M^3}{3r^7} \right] + a^2 \frac{r - (r - 2M) \cos^2 \theta}{r^3}, \quad (1.4)$$

$$\omega(r) = \frac{2aM}{r} - \frac{a\alpha_3^2}{4} \left[ \frac{3}{5Mr^3} + \frac{28}{3r^4} + \frac{6M}{r^5} + \frac{48M^2}{5r^6} - \frac{80M^3}{3r^7} \right] - a\alpha_4^2 \frac{5}{2} \left[ \frac{1}{r^4} + \frac{12M}{7r^5} + \frac{27M^2}{10r^6} \right], \quad (1.5)$$

$$\Theta(r, \theta) = 1 + \frac{\cos^2 \theta}{r^2} a^2, \quad \Phi(r, \theta) = 1 + \frac{r + 2M \sin^2 \theta}{r^3} a^2, \quad (1.6)$$

whereas the scalar field reads

$$\phi(r, \theta) = \alpha_3 \left[ \frac{1}{2Mr} + \frac{1}{2r^2} + \frac{2M}{3r^3} \right] + a\alpha_4 \frac{5 \cos \theta}{8M} \left[ \frac{1}{r^2} + \frac{2M}{r^3} + \frac{18M^2}{5r^4} \right] - \frac{\alpha_3 a^2}{2} \left[ \frac{1}{10r^4} + \frac{1}{5Mr^3} + \frac{1}{4M^2r^2} + \frac{1}{4M^3r} + \cos^2 \theta \left( \frac{48M}{5r^5} + \frac{21}{5r^4} + \frac{7}{5Mr^3} \right) \right], \quad (1.7)$$

where the novel terms are those proportional to  $a\alpha_3^2$  and to  $a^2\alpha_3$  in Eq. (1.5) and Eq. (1.7), respectively. Interestingly, these terms are the dominant corrections at large distances, because they scale with a lower power of  $r$  than those proportional to  $\alpha_4$ . As explained in the appendix, the metric is found by requiring asymptotic flatness and regularity for  $r > 0$ . The curvature invariants are regular in the exterior spacetime. The angular momentum of the BH reads  $J = aM$ , whereas the physical (ADM) mass of the BH is  $\mathcal{M} = M(1 + 49\alpha_3^2/(320M^4))$  and the metric coefficient can be also written in terms of  $\mathcal{M}$  as explained in Ref. [13]. The above solution is accurate up to order  $\mathcal{O}(a^2/M^2, \alpha_i^2/M^4, a\alpha_i^2/M^5)$  in the metric and up to order  $\mathcal{O}(a^2/M^2, \alpha_i^2/M^4, a\alpha_i^2/M^5, a^2\alpha_i/M^3)$  in the scalar field. At this order, the angular metric functions  $\Theta$  and  $\Phi$  are simply given by the slowly rotating Kerr solution. For  $a = 0$ , the slowly rotating BH correctly reduces to the static one setting, in the notation of Ref. [13],  $\alpha_i = \alpha_i/(16\pi)$ ,  $\beta = 1/(4\pi)$ ,  $\kappa = 1/(16\pi)$ . Furthermore, for  $\alpha_3 = 0$ , it reduces to the slowly rotating Chern-Simons BH [28]. Interestingly, this solution only depends on the couplings  $\alpha_3$  and  $\alpha_4$ , since the terms proportional to  $\alpha_1$  and  $\alpha_2$  do not contribute to this order. Moreover, the corrections to the scalar field arising from  $\alpha_3$  and  $\alpha_4$  enter at different order in  $a$ : the Kretschmann correction only introduces even powers of  $a$ , while the Chern-Simons term only

introduces odd powers [13]. Nevertheless, both corrections affect the gravitomagnetic part of the metric, for example giving a modified frame-dragging effect. Finally, the corrections proportional to  $\alpha_3$  scale with a lower power of  $r$  than those proportional to  $\alpha_4$ . Hence, they are expected to be dominant at large distances.

### 1.3 Geodesic structure

Many interesting and potentially observable effects around astrophysical BHs ultimately depend on how particles move in the region few Schwarzschild radii away from the event horizon. For example, the inner properties of the accretion disk are strongly affected by the location of the innermost stable circular orbit (ISCO) and, in turn, by the geodesic structure of the underlying spacetime. Most of the computations assume that the spacetime is described by a Kerr BH. However, deformed solutions arising in alternative theories would also affect particle motion, with potentially observable consequences. In the modified theories considered here, test-particles follow spacetime geodesics. This follows from the conservation of the stress-energy tensor,  $\nabla^\mu T_{\mu\nu} = 0$ , which is guaranteed by the diffeomorphism invariant action (1.1). In many situations the geodesic motion of massive and massless particles is enough to fully describe many effects of astrophysical interest.

We consider the following matter action for a point-like particle

$$S_{\text{mat}} = -m \int dt \sqrt{-\gamma(\phi) g_{\mu\nu} \dot{x}^\mu \dot{x}^\nu}, \quad (1.8)$$

where  $m$  is the mass of the particle and  $\gamma(\phi)$  is a possible coupling function between the matter and the scalar field. For low-energy modifications from heterotic string theory,  $\gamma = e^\phi$ . In the small field limit, we may write

$$\gamma(\phi) = 1 + 4b\phi + \mathcal{O}(\phi^2), \quad (1.9)$$

where  $b = 0$  for minimal coupling and  $b = 1/4$  in heterotic string theory. We focus on equatorial motion ( $\theta = \pi/2$ ,  $\dot{\theta} \equiv 0$ ). The radial geodesic motion on the equatorial plane can be derived from the equation

$$\dot{r}^2 = V(r) = \frac{g}{\gamma^2} \left( \frac{hE^2 - fL^2 + 2jEL}{j^2 + fh} - \delta\gamma \right), \quad (1.10)$$

where  $j = -\omega(r)$ ,  $h = \Phi(r)r^2$ , and  $\delta = 0, 1$  for massless and massive particles, respectively. Here  $E$  and  $L$  are the energy per unit of mass and the angular momentum per unit of mass of the orbiting particle, respectively. For circular orbits at  $r = r_c$ , the corresponding values of  $E$  and  $L$  can be found by imposing  $V(r_c, E_c, L_c) = 0 = V'(r_c, E_c, L_c)$  and, for  $\delta = 1$ , the ISCO location is defined through  $V''(r_{\text{ISCO}}, E_c, L_c) = 0$ . Finally, the angular frequency at the ISCO reads

$$\Omega_{\text{ISCO}} = \left. \frac{\dot{\phi}}{\dot{t}} \right|_{r_{\text{ISCO}}} = \frac{f - jE_c/L_c}{hE_c/L_c + j}. \quad (1.11)$$

In line with our approximation scheme, we expand the geodesic quantities around their Schwarzschild value, i.e.

$$\begin{aligned} X &= X^{(0)} + X^{(1)}a + X^{(2)}a^2 + X^{(3)}\alpha_3 + X^{(4)}\alpha_3^2 \\ &+ X^{(5)}a\alpha_3 + X^{(6)}a\alpha_3^2 + X^{(7)}a^2\alpha_3 + X^{(8)}a\alpha_4^2, \end{aligned} \quad (1.12)$$

where  $X$  schematically denotes  $r_c$ ,  $E_c$  and  $L_c$ . In general, the coupling  $b$  introduces lower order contributions, like those proportional to  $\alpha_3$ . This is due to the lower order dependence of the scalar field in Eq. (1.7). For the same reason, such corrections do not arise for terms proportional to  $\alpha_4$ , since the odd-parity correction to the scalar field vanishes on the equatorial plane. Substituting the expansion (1.12) and solving order by order, we obtain the following ISCO location and the frequency at the ISCO, normalized by the physical mass  $\mathcal{M}$ ,

$$\begin{aligned} \frac{r_{\text{ISCO}}}{\mathcal{M}} &= 6 - 4\sqrt{\frac{2}{3}}\frac{a}{M} - \frac{7a^2}{18M^2} + \frac{16b\alpha_3}{9M^2} - \frac{17}{27}\sqrt{\frac{2}{3}}\frac{ba\alpha_3}{M^3} \\ &- \left(\frac{16297}{38880} - \frac{22267a}{17496\sqrt{6}M}\right)\frac{\alpha_3^2}{M^4} + \frac{77a}{216\sqrt{6}M^5}\alpha_4^2, \\ \mathcal{M}\Omega_{\text{ISCO}} &= \frac{1}{6\sqrt{6}} + \frac{11a}{216M} + \frac{59a^2}{648\sqrt{6}M^2} - \frac{12113a}{5225472M^5}\alpha_4^2 \\ &- \frac{29}{216\sqrt{6}}\frac{b\alpha_3}{M^2} - \frac{169}{3888}\frac{ba\alpha_3}{M^3} \\ &+ \left(\frac{32159}{2099520\sqrt{6}} - \frac{49981a}{75582720M}\right)\frac{\alpha_3^2}{M^4}, \end{aligned} \quad (1.13)$$

where we have kept only dominant terms in  $b$  and we are considering corotating orbits only. Counter-rotating orbits can be simply obtained by inverting the sign of  $a$ . The behavior of the ISCO frequency depends on several couplings. For  $b = 0$ , the dominant correction is  $\mathcal{O}(\alpha_3^2)$  and contribute to increase the frequency. The first corrections proportional to the BH spin are  $\mathcal{O}(a\alpha_3^2)$  and  $\mathcal{O}(a\alpha_4^2)$  and they contribute to lower the frequency. However, when a non-minimal coupling is turned on, its effect is dominant [25]. The ISCO frequency gets *negative*  $\mathcal{O}(b\alpha_3)$  corrections. Since this is the dominant effect, a decrease in the ISCO frequency could be seen as a general signature of non-minimal couplings, regardless of the relative strength of  $a$ ,  $\alpha_3$  and  $\alpha_4$ .

The same procedure can be applied to null geodesics, which are the trajectories of massless particles. In this case, it is easy to show that the result does not depend on the coupling  $\gamma$ . We

get

$$\begin{aligned} \frac{r_{\text{null}}}{\mathcal{M}} &= 3 - \frac{2a}{\sqrt{3}M} - \frac{2a^2}{9M^2} + \frac{31}{81\sqrt{3}} \frac{a\alpha_4^2}{M^5} \\ &\quad - \left( \frac{961}{3240} - \frac{33667a}{174960\sqrt{3}M} \right) \frac{\alpha_3^2}{M^4}, \end{aligned} \quad (1.14)$$

$$\begin{aligned} \mathcal{M}\Omega_{\text{null}} &= \frac{1}{3\sqrt{3}} + \frac{2a}{27M} + \frac{11a^2}{162\sqrt{3}M^2} - \frac{131}{20412} \frac{a\alpha_4^2}{M^5} \\ &\quad + \left( \frac{4397}{262440\sqrt{3}} + \frac{24779a}{4723920M} \right) \frac{\alpha_3^2}{M^4}, \end{aligned} \quad (1.15)$$

where  $\Omega_{\text{null}} = L_{\text{null}}/E_{\text{null}}$ . The dominant correction is  $\mathcal{O}(\alpha_3^2)$  and it is positive, whereas the  $\mathcal{O}(a\alpha_3^2)$  and  $\mathcal{O}(a\alpha_4^2)$  corrections have an opposite relative sign.

## 1.4 Discussion and Conclusion

We have found slowly rotating BHs, solutions of a class of alternative theories as general as the action (1.1). This theory supplements GR by all quadratic, algebraic curvature terms coupled to a scalar field. Our solution is presented in closed form up to some order in the angular momentum and in the coupling parameters. To the same order, we discussed the most relevant properties of the equatorial geodesic motion, giving the ISCO and light-ring frequencies.

With the analytical solution at hand, several extensions of the present chapter are possible. The properties of the (modified) accretion disk can be used to constrain the parameters of the theory [14]. Furthermore, the study of the geodesic structure can be generalized to include non-equatorial orbits and an analysis similar to Ref. [31] can be performed. Another interesting issue is the linear response of the slowly rotating BH. Strong curvature corrections to GR affect the linear stability analysis [25] and the gravitational-wave emission [32].

In addition, several extensions of the present solution are conceivable. First of all, going further in the approximation scheme, up to order  $a^2\alpha_i^2$ , corrections to the event horizon location and to the ergoregion would appear. This can have a profound impact on the stability of these solutions. Furthermore, highly spinning BHs are phenomenologically more relevant and larger deviations from the Kerr metric may be expected. However, they have to be constructed numerically [26] on the basis of a case-by-case analysis. In this case, our analytical solution can be useful; for example it can be used as an initial profile to start numerical relaxation methods, or to check numerical solutions.

We report here that the slowly rotating metric we found can be mapped onto the bumpy BH formalism along the same lines as discussed in Ref. [20], although the mapping is non-trivial. On the other hand, this solution does not belong to the class of deformed Kerr BHs proposed in Ref. [21].

## Chapter 2

# Slowly rotating anisotropic stars in general relativity and scalar-tensor theory

Most investigations of the structure of neutron stars (NSs) assume isotropic matter with a perfect-fluid equation of state (EoS) relating the pressure and density in the stellar interior. However, various physical effects can lead to local anisotropies (see [33] for a review). Anisotropy can occur for stars with a solid core [34] or strong magnetic fields [35–37]. Spaghetti- and lasagna-like structures would induce anisotropic elastic properties that could be important for NS quakes [38]. Nuclear matter may be anisotropic at very high densities [39, 40], where the nuclear interactions must be treated relativistically and phase transitions (e.g. to pion condensates [41] or to a superfluid state [42]) may occur. For example, Nelmes and Piette [43] recently considered NS structure within the Skyrme model, a low energy, effective field theory for Quantum Chromodynamics (QCD), finding significant anisotropic strains for stars with mass  $M \gtrsim 1.5M_{\odot}$  (see also [44, 45]). From a mathematical point of view, two-fluid systems can be shown to be equivalent to a single anisotropic fluid [46]. Anisotropy affects the bulk observable properties of NSs, such as the mass-radius relation and the surface redshift [47]: it can increase the maximum NS mass for a given EoS [47, 48] and stabilize otherwise unstable stellar configurations [49]. Incidentally, exotic objects such as gravastars [50] and boson stars [51] (see also Chapters 5 and 6) are also equivalent to anisotropic fluids (i.e., they have anisotropic pressure).

It is known that rotation can induce anisotropy in the pressure due to anisotropic velocity distributions in low-density systems [33], but to the best of our knowledge – with the exception of some work by Bayin [52] – slowly rotating anisotropic stars have never been investigated in general relativity (GR). The goal of this chapter is to fill this gap using two different phenomenological models for anisotropy [47, 48], and to extend the analysis of slowly rotating anisotropic stars to scalar-tensor theories of gravity.

Scalar-tensor theories are among the simplest and best studied extensions of GR [53]. In addition to the metric, in these theories gravity is also mediated by a scalar field. Scalar-tensor theories arise naturally from the dimensional reduction of higher-dimensional proposals to unify gravity with the Standard Model, and they encompass  $f(R)$  theories of gravity as spe-

cial cases [54, 55]. The simplest variant of scalar-tensor theory, Brans-Dicke theory, is tightly constrained experimentally [56], but certain versions of the theory could in principle differ from GR by experimentally measurable amounts in the strong-field regime, as shown by Damour and Esposito-Farèse [57, 58].

From an astrophysical standpoint, compact objects such as black holes and NSs are the most plausible candidates to test strong-field gravity [59]. Compared to black holes, NSs are a more promising strong-field laboratory to distinguish scalar-tensor gravity from GR, because a large class of scalar-tensor theories admits the *same* black-hole solutions as GR (see [60] and references therein), and the dynamics of black holes can differ from GR only if the black holes are surrounded by exotic forms of matter [61–64] or if the asymptotic behavior of the scalar field is nontrivial [65, 66].

The study of NS structure in GR is textbook material [67–70], and there is an extensive literature on stellar configurations in scalar-tensor theories as well (see e.g. [11, 71] and references therein). One of the most intriguing phenomena in this context is “spontaneous scalarization” [58], a phase transition analogous to the familiar spontaneous magnetization in solid state physics [72]: in a certain range of central densities, asymptotically flat solutions with a nonzero scalar field are possible and energetically favored with respect to the corresponding GR solutions.

In the absence of anisotropy, the degree of scalarization depends on a certain (real) theory parameter  $\beta$ , defined in Eq. (2.2) below. Theory predicts that scalarization cannot occur (in the absence of anisotropy) when  $\beta \gtrsim -4.35$  [73]. Present binary pulsar observations yield a rather tight experimental constraint:  $\beta \gtrsim -4.5$  [74, 75]. One of our main findings is that the effects of scalarization, as well as the critical  $|\beta|$  for spontaneous scalarization to occur, increase (decrease) for configurations in which the tangential pressure is bigger (smaller) than the radial pressure. Therefore binary pulsars can be used to constrain the degree of anisotropy at fixed  $\beta$ , or to constrain  $\beta$  for a given degree of anisotropy. This may open the door to experimental constraints on the Skyrme model via binary pulsar observations. Other notable findings of this study are (i) an investigation of the dependence of the stellar moment of inertia on the degree of anisotropy  $\lambda$  (more precisely,  $\lambda_H$  and  $\lambda_{BL}$ , because we consider two different anisotropy models [47, 48]); and (ii) an investigation of the threshold for scalarization for different values of  $\beta$  and  $\lambda$  in terms of a simple linear stability criterion, along the lines of recent work for black holes surrounded by matter [63, 64].

The plan of this chapter is as follows. In Section 2.1 we introduce the equations of motion in scalar-tensor theory and the stress-energy tensor describing anisotropic fluids that will be used in the rest of the chapter. In Section 2.2 we present the equations of structure for relativistic stars at first order in the slow-rotation expansion. The macroscopic properties of NSs obtained by integrating these equations for two different models of anisotropic stars are presented in Section 2.3. Section 2.3.3 shows that a linear approximation is sufficient to identify the threshold for spontaneous scalarization for different values of  $\beta$  and  $\lambda$ . Section 2.4 summarizes our main conclusions and points out possible avenues for future work. Finally, in Appendix B we give a detailed derivation of an integral formula to compute the moment of inertia. Throughout this chapter, quantities associated with the Einstein (Jordan) frame will be labeled with an asterisk (tilde). We use geometrical units ( $c = G_* = 1$ ) unless stated otherwise and signature  $(-, +, +, +)$ .

## 2.1 Anisotropic fluids in scalar-tensor theory of gravity

### 2.1.1 Overview of the theory

We consider a massless scalar-tensor theory described by an Einstein-frame action [58, 72]

$$S = \frac{c^4}{16\pi G_*} \int d^4x \frac{\sqrt{-g_*}}{c} (R_* - 2g_*^{\mu\nu} \partial_\mu \varphi \partial_\nu \varphi) + S_M[\psi_M; A^2(\varphi)g_{*\mu\nu}], \quad (2.1)$$

where  $G_*$  is the bare gravitational constant,  $g_* \equiv \det[g_{*\mu\nu}]$  is the determinant of the Einstein-frame metric  $g_{*\mu\nu}$ ,  $R_*$  is the Ricci curvature scalar of the metric  $g_{*\mu\nu}$ , and  $\varphi$  is a massless scalar field.  $S_M$  is the action of the matter fields, collectively represented by  $\psi_M$ . Free particles follow geodesics of the Jordan-frame metric  $\tilde{g}_{\mu\nu} \equiv A^2(\varphi)g_{*\mu\nu}$ , where  $A(\varphi)$  is a conformal factor. Here we assume that  $A(\varphi)$  has the form

$$A(\varphi) \equiv e^{\frac{1}{2}\beta\varphi^2}, \quad (2.2)$$

where  $\beta$  is the theory's free parameter and, as we recalled in the introduction, current binary pulsar observations constrain it to the range  $\beta \gtrsim -4.5$  [74, 75].

The field equations of this theory, obtained by varying the action  $S$  with respect to  $g_*^{\mu\nu}$  and  $\varphi$ , are given by

$$R_{*\mu\nu} = 2\partial_\mu \varphi \partial_\nu \varphi + 8\pi (T_{*\mu\nu} - \frac{1}{2}T_* g_{*\mu\nu}), \quad (2.3)$$

$$\square_* \varphi = -4\pi\alpha(\varphi)T_*, \quad (2.4)$$

where  $R_{*\mu\nu}$  is the Ricci tensor,  $\alpha(\varphi) \equiv d \log A(\varphi) / d\varphi$  (in the language of [58, 72]) is the ‘‘scalar-matter coupling function’’ and  $\square_*$  is the d'Alembertian operator associated to the metric  $g_{*\mu\nu}$ . GR is obtained in the limit where the scalar field decouples from matter, i.e.  $\alpha(\varphi) \rightarrow 0$ . Under the particular choice of the conformal factor (2.2), this is equivalent to letting  $\beta = 0$ . In this chapter, all equations will be derived within the context of scalar-tensor gravity.

Finally,  $T_*^{\mu\nu}$  is the energy-momentum tensor of the matter fields, defined as

$$T_*^{\mu\nu} \equiv \frac{2}{\sqrt{-g_*}} \frac{\delta S_M[\psi_M, A^2(\varphi)g_{*\mu\nu}]}{\delta g_{*\mu\nu}}, \quad (2.5)$$

and  $T_* \equiv T_*^{\mu\nu} g_{*\mu\nu}$  is its trace. The energy-momentum tensor in the Jordan frame  $\tilde{T}^{\mu\nu}$ , with trace  $\tilde{T} \equiv \tilde{T}^{\mu\nu} \tilde{g}_{\mu\nu}$ , is defined in an analogous fashion:

$$\tilde{T}^{\mu\nu} \equiv \frac{2}{\sqrt{-\tilde{g}}} \frac{\delta S_M[\psi_M, \tilde{g}_{\mu\nu}]}{\delta \tilde{g}_{\mu\nu}}. \quad (2.6)$$

The two energy-momentum tensors (and their traces) are related as follows:

$$T_*^{\mu\nu} = A^6(\varphi)\tilde{T}^{\mu\nu}, \quad T_{*\mu\nu} = A^2(\varphi)\tilde{T}_{\mu\nu}, \quad T_* = A^4(\varphi)\tilde{T}. \quad (2.7)$$

The covariant divergence of the energy-momentum tensor satisfies

$$\nabla_{*\mu} T_*^{\mu\nu} = \alpha(\varphi) T_* \nabla_{*\mu} \varphi, \quad (2.8)$$

$$\tilde{\nabla}_{\mu} \tilde{T}^{\mu\nu} = 0, \quad (2.9)$$

in the Einstein and Jordan frames, respectively.

### 2.1.2 Anisotropic fluids

An anisotropic fluid with radial pressure  $\tilde{p}$ , tangential pressure  $\tilde{q}$  and total energy density  $\tilde{\epsilon}$  can be modeled by the Jordan-frame energy-momentum tensor [47, 76]

$$\tilde{T}_{\mu\nu} = \tilde{\epsilon} \tilde{u}_{\mu} \tilde{u}_{\nu} + \tilde{p} \tilde{k}_{\mu} \tilde{k}_{\nu} + \tilde{q} \tilde{\Pi}_{\mu\nu}, \quad (2.10)$$

where  $\tilde{u}_{\mu}$  is the fluid four-velocity,  $\tilde{k}_{\mu}$  is a unit radial vector ( $\tilde{k}_{\mu} \tilde{k}^{\mu} = 1$ ) satisfying  $\tilde{u}^{\mu} \tilde{k}_{\mu} = 0$ , and  $\tilde{\Pi}_{\mu\nu} \equiv \tilde{g}_{\mu\nu} + \tilde{u}_{\mu} \tilde{u}_{\nu} - \tilde{k}_{\mu} \tilde{k}_{\nu}$ .  $\tilde{\Pi}_{\mu\nu}$  is a projection operator onto a two-surface orthogonal to both  $\tilde{u}_{\mu}$  and  $\tilde{k}_{\mu}$ : indeed, defining a projected vector  $\tilde{A}^{\mu} \equiv \tilde{\Pi}^{\mu\nu} \tilde{V}_{\nu}$ , one can easily verify that  $\tilde{u}_{\mu} \tilde{A}^{\mu} = \tilde{k}_{\mu} \tilde{A}^{\mu} = 0$ . At the center of symmetry of the fluid distribution the tangential pressure  $\tilde{q}$  must vanish, since  $\tilde{k}^{\mu}$  is not defined there [76]. The trace of the Einstein-frame stress-energy tensor for an anisotropic fluid is

$$T_* = A^4(\varphi) [-(\tilde{\epsilon} - 3\tilde{p}) - 2(\tilde{p} - \tilde{q})]. \quad (2.11)$$

As emphasized by Bowers and Liang [47],  $\tilde{p}$  and  $\tilde{q}$  contain contributions from fluid pressures and other possible stresses inside the star, therefore they should not be confused with purely hydrostatic pressure. Additional stresses could be caused, for instance, by the presence of a solid core [34], strong magnetic fields [35] or a multi-fluid mixture [46]. The derivation of a microphysical model for anisotropy is a delicate issue, so we will adopt a phenomenological approach. We will assume that  $\tilde{p}$  is described by a barotropic EoS, i.e.  $\tilde{p} = \tilde{p}(\tilde{\epsilon})$ . For brevity in this chapter we focus on the APR EoS [77], but we have verified that our qualitative results do not depend on this choice. The APR EoS supports NS models with a maximum mass  $M$  larger than  $2.0 M_{\odot}$ , and therefore it is compatible with the recent observations of the  $M = 1.97 \pm 0.04 M_{\odot}$  pulsar PSR J1614-2230 [78] and of the  $M = 2.01 \pm 0.04 M_{\odot}$  pulsar PSR J0348+0432 [79].

The functional form of the anisotropy  $\tilde{\sigma} \equiv \tilde{p} - \tilde{q}$  [47, 76, 80] depends on microscopic relationships between  $\tilde{p}$ ,  $\tilde{q}$  and  $\tilde{\epsilon}$ , that unfortunately are not known. However we can introduce physically motivated functional relations for  $\tilde{\sigma}$  that allow for a smooth transition between the isotropic and anisotropic regimes. Many such functional forms have been studied in the litera-

ture. As an application of our general formalism we will consider two of these phenomenological relations, described below.

### Quasi-local equation of state

Horvat et al. [48] proposed the following quasi-local equation for  $\tilde{\sigma}$ :

$$\tilde{\sigma} \equiv \lambda_H \tilde{p} \tilde{\gamma}, \quad (2.12)$$

where  $\tilde{\gamma} \equiv 2\mu(r)/r$ . The “mass function”  $\mu(r)$ , defined in Eq. (2.15) below, is essentially the mass contained within the radius  $r$ , so the quantity  $\tilde{\gamma}$  is a local measure of compactness, whereas  $\lambda_H$  is a free (constant) parameter that controls the degree of anisotropy.

The calculations of [41] show that, if anisotropy occurs due to pion condensation,  $0 \leq \tilde{\sigma}/\tilde{p} \leq 1$ , therefore  $\lambda_H$  could be of order unity [76]. More recently, Nelmes and Piette [43] considered NS structure within a model consisting of a Skyrme crystal, which allows for the presence of anisotropic strains. They found that  $\lambda_H$ , as defined in Eq. (2.12), has a nearly constant value  $\lambda_H \approx -2$  throughout the NS interior. The nonradial oscillations of anisotropic stars were studied in [76] using the model of Eq. (2.12). Following Doneva and Yazadjiev [76], we will consider values of  $\lambda_H$  in the range  $-2 \leq \lambda_H \leq 2$ .

### Bowers-Liang model

As a second possibility we will consider the functional form for  $\tilde{\sigma}$  proposed by Bowers and Liang [47], who suggested the relation<sup>1</sup>

$$\tilde{\sigma} \equiv \frac{1}{3} \lambda_{BL} (\tilde{\epsilon} + 3\tilde{p}) (\tilde{\epsilon} + \tilde{p}) \left(1 - \frac{2\mu}{r}\right)^{-1} r^2. \quad (2.13)$$

The model is based on the following assumptions: (i) the anisotropy should vanish quadratically at the origin (the necessity for this requirement will become clear in Sec. 2.2), (ii) the anisotropy should depend nonlinearly on  $\tilde{p}$ , and (iii) the anisotropy is (in part) gravitationally induced. The parameter  $\lambda_{BL}$  controls the amount of anisotropy in the fluid.

This ansatz was used in [47] to obtain an exact solution for incompressible stars with  $\tilde{\epsilon} = \tilde{\epsilon}_0 = \text{constant}$ . In their simple model, the requirement that equilibrium configurations should have finite central pressure  $\tilde{p}_c$  implies that  $\lambda_{BL} \geq -2$ . The Newtonian limit of the Bowers-Liang ansatz was also considered in a recent study of the correspondence between superradiance and tidal friction [80]. In our calculations we will assume that  $-2 \leq \lambda_{BL} \leq 2$ .

<sup>1</sup>The factor of 1/3 in Eq. (2.13) is chosen for convenience. Also, there is a sign difference between our definition of  $\tilde{\sigma}$  and the one in [47]. Our parameter  $\lambda_{BL}$  is related with the Bowers-Liang (physically equivalent) parameter  $C$  by  $\lambda_{BL} = -3C$ .

## 2.2 Stellar structure in the slow-rotation approximation

In this Section we approximate the metric of a slowly, rigidly rotating, anisotropic star following the seminal work by Hartle and Thorne [81,82]. The idea is to consider the effects of rotation as perturbations of the spherically symmetric background spacetime of a static star. We generalize the results of [81,82] (in GR) and [72] (in scalar-tensor theory) to account for anisotropic fluids up to first order in rotation, so we can study how anisotropy and scalarization affect the moment of inertia of the star and the dragging of inertial frames.

We remark that the moment of inertia  $I$ , the star's uniform angular velocity  $\Omega$  and the angular momentum  $J \equiv I\Omega$  are the same in the Jordan and Einstein frames (cf. [72,83]). Therefore, to simplify the notation, we will drop asterisks and tildes on these quantities. Working up to order  $\mathcal{O}(\Omega)$ , the line element of a stationary axisymmetric spacetime in the Jordan frame reads

$$d\tilde{s}^2 = A^2(\varphi) \left[ -e^{2\Phi(r)} dt^2 + e^{2\Lambda(r)} dr^2 + r^2 d\theta^2 + r^2 \sin^2 \theta d\phi^2 - 2\omega(r, \theta) r^2 \sin^2 \theta dt d\phi \right], \quad (2.14)$$

where

$$e^{-2\Lambda(r)} \equiv 1 - \frac{2\mu(r)}{r}, \quad (2.15)$$

$\mu(r)$  is the mass function and  $\omega(r, \theta) \sim \mathcal{O}(\Omega)$  is the angular velocity acquired by a particle falling from infinity as measured by a static asymptotic observer [81].

The four-velocity of the rotating fluid is such that  $\tilde{u}_\mu \tilde{u}^\mu = -1$ , and it has components [81]

$$\tilde{u}^0 = \left[ -(\tilde{g}_{00} + 2\Omega\tilde{g}_{03} + \Omega^2\tilde{g}_{33}) \right]^{-1/2}, \quad (2.16)$$

$$\tilde{u}^1 = \tilde{u}^2 = 0, \quad (2.17)$$

$$\tilde{u}^3 = \Omega\tilde{u}^0. \quad (2.18)$$

Using (2.14), at first order in the slow-rotation parameter we obtain:

$$\tilde{u}^\mu = A^{-1}(\varphi) (e^{-\Phi}, 0, 0, \Omega e^{-\Phi}). \quad (2.19)$$

Following the standard procedure [68,81,84], the field equations (2.3), (2.4) and (2.8) with

the metric given by (2.14) yield the following set of ordinary differential equations:

$$\frac{d\mu}{dr} = 4\pi A^4(\varphi) r^2 \tilde{\epsilon} + \frac{1}{2} r (r - 2\mu) \psi^2, \quad (2.20)$$

$$\frac{d\Phi}{dr} = 4\pi A^4(\varphi) \frac{r^2 \tilde{p}}{r - 2\mu} + \frac{1}{2} r \psi^2 + \frac{\mu}{r(r - 2\mu)}, \quad (2.21)$$

$$\begin{aligned} \frac{d\psi}{dr} = & 4\pi A^4(\varphi) \frac{r}{r - 2\mu} [\alpha(\varphi)(\tilde{\epsilon} - 3\tilde{p}) + r(\tilde{\epsilon} - \tilde{p})\psi] \\ & - \frac{2(r - \mu)}{r(r - 2\mu)} \psi + 8\pi A^4(\varphi) \alpha(\varphi) \frac{r\tilde{\sigma}}{r - 2\mu}, \end{aligned} \quad (2.22)$$

$$\frac{d\tilde{p}}{dr} = -(\tilde{\epsilon} + \tilde{p}) \left[ \frac{d\Phi}{dr} + \alpha(\varphi)\psi \right] - 2\tilde{\sigma} \left[ \frac{1}{r} + \alpha(\varphi)\psi \right], \quad (2.23)$$

$$\begin{aligned} \frac{d\varpi}{dr} = & 4\pi A^4(\varphi) \frac{r^2}{r - 2\mu} (\tilde{\epsilon} + \tilde{p}) \left( \varpi + \frac{4\bar{\omega}}{r} \right) + \left( r\psi^2 - \frac{4}{r} \right) \varpi \\ & + 16\pi A^4(\varphi) \frac{r\tilde{\sigma}}{r - 2\mu} \bar{\omega}, \end{aligned} \quad (2.24)$$

where we defined  $\psi \equiv d\varphi/dr$ ,  $\varpi \equiv d\bar{\omega}/dr$ , and  $\bar{\omega} \equiv \Omega - \omega$ . The equations above reduce to the Tolman-Oppenheimer-Volkoff (TOV) equations for anisotropic stars in GR [47] when  $\alpha \rightarrow 0$ , to the results of [58] in the isotropic limit  $\tilde{\sigma} \rightarrow 0$ , and to the usual TOV equations when both quantities are equal to zero [68]. In the GR limit, our frame-dragging equation (2.24) agrees with Bayin's [52] result<sup>2</sup>.

To obtain the interior solution we integrate the generalized TOV equations (2.20)-(2.24) from a point  $r_c$  close to the stellar center  $r = 0$  outwards up to a point  $r = r_s$  where the pressure vanishes, i.e.  $\tilde{p}(r_s) = 0$ . This point specifies the Einstein-frame radius  $R_* \equiv r_s$  of the star. If  $\varphi_s = \varphi(r_s)$ , the Jordan-frame radius  $\tilde{R}$  is

$$\tilde{R} = A(\varphi_s) R_*. \quad (2.25)$$

In practice, to improve numerical stability, given  $\tilde{\epsilon}_c$ ,  $\Phi_c$ ,  $\varphi_c$  and  $\mu_c$  (where the subscript  $c$

<sup>2</sup>In principle, as mentioned in the introduction, rotation may induce anisotropy. Therefore the Horvat et al. and Bowers-Liang models for  $\tilde{\sigma}$  should contain terms proportional to  $\Omega$ . However, Eq. (2.24) implies that such terms in  $\tilde{\sigma}$  would lead to corrections of second order in the angular velocity  $\Omega$ . These corrections are beyond the scope of the  $\mathcal{O}(\Omega)$  approximation considered in our work.

means that all quantities are evaluated at  $r = 0$ ) we use the following series expansions:

$$\begin{aligned}
\mu &= \frac{4}{3}\pi A_c^4 \tilde{\epsilon}_c r^3 + \mathcal{O}(r^4), \\
\Phi &= \Phi_c + \frac{2}{3}\pi A_c^4 (\tilde{\epsilon}_c + 3\tilde{p}_c) r^2 + \mathcal{O}(r^4), \\
\tilde{p} &= \tilde{p}_c + \frac{2}{3}\pi r^2 A_c^4 (\tilde{\epsilon}_c + \tilde{p}_c) [3\tilde{p}_c (\alpha_c^2 - 1) - \tilde{\epsilon}_c (\alpha_c^2 + 1)] + \\
&\quad - \frac{1}{3}r^2 (2r\sigma_3 + 3\sigma_2) + \mathcal{O}(r^4), \\
\varphi &= \varphi_c + \frac{2\pi}{3} A_c^4 \alpha_c (\tilde{\epsilon}_c - 3\tilde{p}_c) r^2 + \mathcal{O}(r^4), \\
\bar{\omega} &= \bar{\omega}_c + \frac{8\pi}{5} A_c^4 \bar{\omega}_c (\tilde{\epsilon}_c + \tilde{p}_c) r^2 + \mathcal{O}(r^4), \\
\tilde{\sigma} &= \sigma_2 r^2 + \sigma_3 r^3 + \mathcal{O}(r^4),
\end{aligned} \tag{2.26}$$

where  $\sigma_2$  and  $\sigma_3$  depend on the particular anisotropic model.

In the vacuum exterior we have  $\tilde{p} = \tilde{\epsilon} = \tilde{\sigma} = 0$ . Eqs. (2.20)–(2.22) must be integrated outwards starting from the stellar radius to obtain the stellar mass, angular momentum and scalar charge. For large  $r$  we can expand the relevant functions as follows:

$$\mu(r) = M - \frac{Q^2}{2r} - \frac{MQ^2}{2r^2} + \mathcal{O}(r^{-3}) \tag{2.27}$$

$$e^{2\Phi} = 1 - \frac{2M}{r} + \mathcal{O}(r^{-3}), \tag{2.28}$$

$$\varphi(r) = \varphi_\infty + \frac{Q}{r} + \frac{MQ}{r^2} + \mathcal{O}(r^{-3}), \tag{2.29}$$

$$\bar{\omega}(r) = \Omega - \frac{2J}{r^3} + \mathcal{O}(r^{-4}), \tag{2.30}$$

where  $M$  is the Arnowitt-Deser-Misner (ADM) mass of the NS,  $Q$  is the scalar charge,  $J$  is the star's angular momentum and  $\varphi_\infty$  is the (constant) cosmological value of the scalar field, here assumed to be zero. Under this assumption the mass  $M$  is the same in the Jordan and Einstein frames [83]. By matching the numerical solution integrated from the surface of the star with the asymptotic expansions (2.27)–(2.30) we can compute  $M$ ,  $Q$  and  $J$ .

We compute the moment of inertia of the star  $I$  in two equivalent ways. The first method consists of extracting the angular momentum as described above and using

$$I = \frac{J}{\Omega}. \tag{2.31}$$

Alternatively, we can compute  $I$  through an integral within the star. Combining Eqs. (2.15),

(2.20)-(2.21) and (2.24) we obtain the following integral expression:

$$I = \frac{8\pi}{3} \int_0^{R_*} A^4(\varphi) e^{\Lambda - \Phi} r^4 (\tilde{\epsilon} + \tilde{p}) \left(1 - \frac{\tilde{\sigma}}{\tilde{\epsilon} + \tilde{p}}\right) \left(\frac{\bar{\omega}}{\Omega}\right) dr \quad (2.32)$$

(see Appendix B for details). As  $A(\varphi) \rightarrow 1$  and  $\tilde{\sigma} \rightarrow 0$  we recover Hartle's result [81], and in the isotropic limit  $\tilde{\sigma} \rightarrow 0$  we match the result of [84]. The numerical values of  $I$  obtained with (2.31) and (2.32) are in excellent agreement.

For each stellar model we also calculate the *baryonic mass*  $M_b$ , defined as [58]

$$M_b \equiv 4\pi \tilde{m}_b \int_0^{R_*} \tilde{n} A^3(\varphi) \frac{r^2}{\sqrt{1 - 2\mu/r}} dr, \quad (2.33)$$

where  $\tilde{m}_b = 1.66 \times 10^{-24}$  g is the atomic mass unit and  $\tilde{n}$  is the baryonic number density.

## 2.3 Numerical results

The tools developed so far allow us to investigate the effect of anisotropy on the bulk properties of rotating stars. In Section 2.3.1 we will focus on slowly rotating stars in GR. To the best of our knowledge – and to our surprise – rotating anisotropic stars have not been studied in the GR literature, with the only exception of a rather mathematical paper by Bayin [52]<sup>3</sup>. In Section 2.3.2 we extend our study to scalar-tensor theories. Our main motivation here is to understand whether anisotropy may increase the critical value  $\beta = \beta_{\text{crit}}$  above which spontaneous scalarization cannot happen, and therefore allow for observationally interesting modifications to the structure of NSs that would still be compatible with the stringent bounds from binary pulsars [74, 75].

### 2.3.1 The effect of anisotropy in general relativity

In the top panels of Figure 2.1 we show the mass-radius relation for anisotropic NS models in GR. All curves are truncated at the central density corresponding to the maximum NS mass, because models with larger central densities are unstable to radial perturbations [67, 68]. Solid lines correspond to  $\tilde{\sigma} = 0$ , i.e. the isotropic fluid limit. The horizontal shaded band in the upper panels represents the largest measured NS mass  $M = 2.01 \pm 0.04 M_\odot$  (PSR J0348+0432: cf. [79]).

Recall that  $\tilde{\sigma} = \tilde{p} - \tilde{q}$  is proportional to  $\lambda_H$  and  $\lambda_{BL}$  (with a positive proportionality constant) in both models, and that  $\tilde{p}$  and  $\tilde{q}$  represent the “radial” and “tangential” pressures, respectively. Therefore positive values of  $\lambda_H$  and  $\lambda_{BL}$  mean that the radial pressure is larger than the tangential pressure (dashed lines); the opposite is true when the anisotropy parameters are negative (dotted lines).

<sup>3</sup>Note, however, here we are referring to the anisotropy in the fluid, not the one induced by the star rotation.

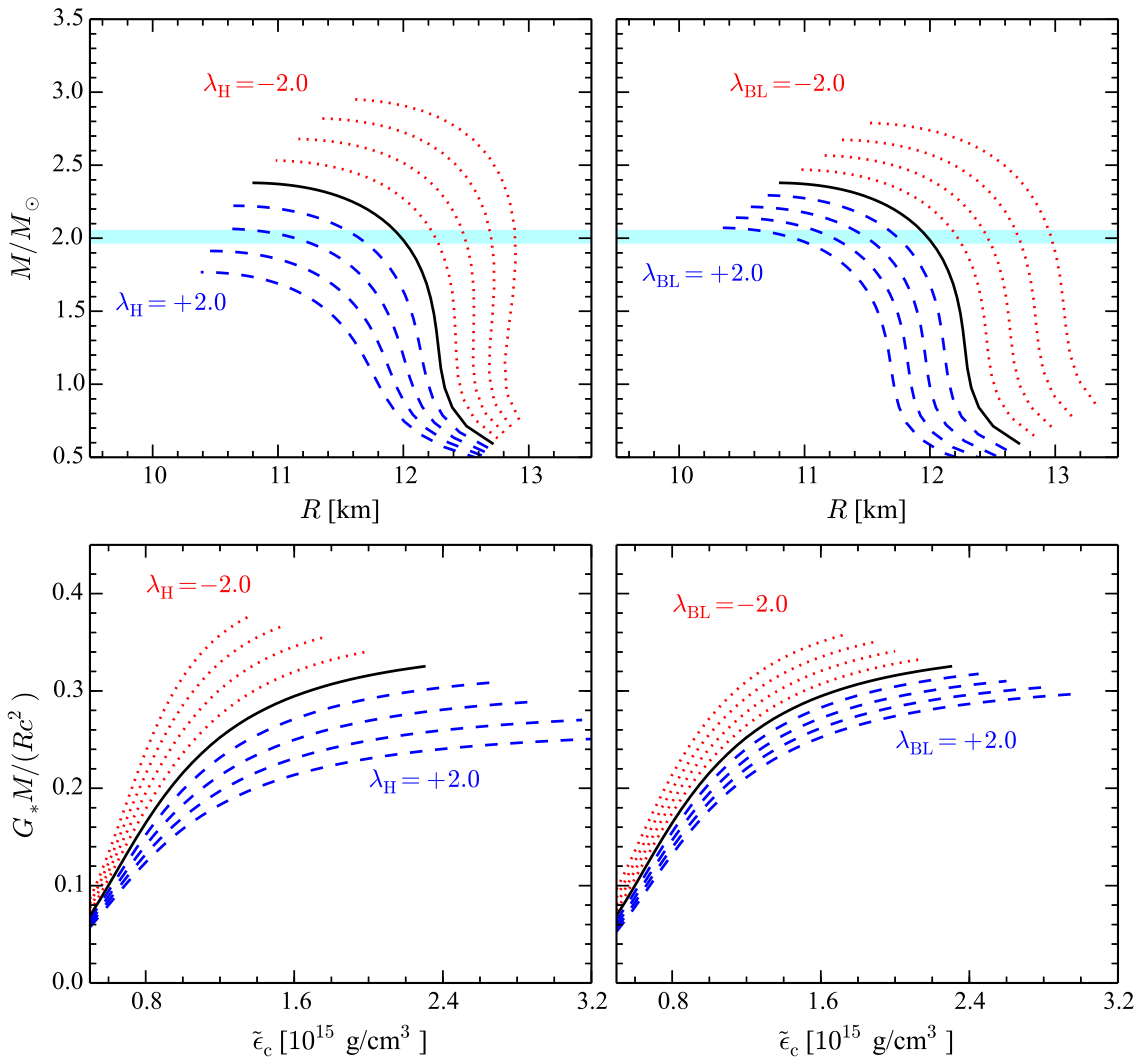


Figure 2.1: Mass-radius relation (top panels) and dimensionless compactness  $G_*M/Rc^2$  as a function of the central density (bottom panels) for anisotropic stars in GR using EoS APR. In the left panels we use the quasi-local model of [48]; in the right panels, the Bowers-Liang model [47]. Different curves correspond to increasing  $\lambda_H$  (or  $\lambda_{BL}$ ) in increments of  $0.5$  between  $-2$  (top) and  $2$  (bottom). The shaded blue bar corresponds to the mass  $M = 2.01 \pm 0.04 M_\odot$  of PSR J0348+0432 [79].

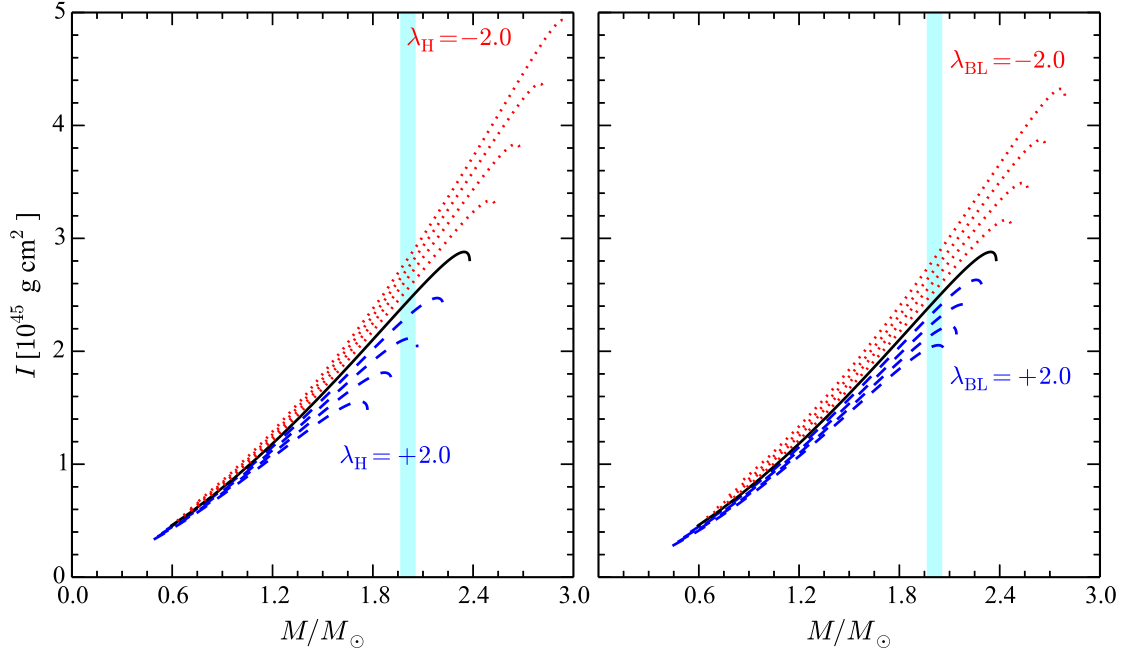


Figure 2.2: The moment of inertia  $I$  as function of the mass  $M$  for anisotropic stars in GR using EoS APR, increasing  $\lambda_H$  (or  $\lambda_{BL}$ ) in increments of 0.5 between  $-2$  (top curves) and  $2$  (bottom curves). As in Figure 2.1, the vertical shaded region marks the largest measured NS mass [79].

The trend in the top panels of Figure 2.1 is clear: for both anisotropy models, positive (negative) anisotropy parameters yield smaller (larger) radii at fixed mass, and smaller masses at fixed radius. The lower panels of Figure 2.1 show that the stellar compactness  $G_*M/(Rc^2)$  decreases (for a given EoS and fixed central density) as the anisotropy degree increases. Nuclear matter EoSs are usually ordered in terms of a “stiffness” parameter, with stiffer EoSs corresponding to larger sound speeds (more incompressible matter) in the stellar interior, and larger values of the compactness  $M/R$ . The qualitative effect of increasing anisotropy (with our sign conventions) is *opposite* (for a given EoS) to the qualitative effect of increasing stiffness.

Figure 2.2 is, to our knowledge, the first calculation of the effect of anisotropy on the moment of inertia  $I$ . As in Figure 2.1, solid lines corresponds to the isotropic limit. In the right panel we use the quasi-local model of [48]; in the left panel, the Bowers-Liang model [47]. Hypothetical future observations of the moment of inertia of star A, from the double pulsar PSR J0737-3039 [85–87], or preferably from large-mass NSs, may be used to constrain the degree of anisotropy under the assumptions that GR is valid and that the nuclear EoS is known.

### 2.3.2 The effect of anisotropy on spontaneous scalarization

In Figures 2.3 and 2.4 we display the properties of nonrotating, spontaneously scalarized stars within the anisotropy models of Horvat et al. [48] and Bowers-Liang [47], respectively. The main panel in each Figure shows the mass-radius relation as the anisotropy parameter increases (in increments of 1, and from top to bottom) in the range  $-2 \leq \lambda_H \leq 2$  (Figure 2.3) or  $-2 \leq \lambda_{BL} \leq 2$  (Figure 2.4). Solid lines correspond to the GR limit; dotted, dashed and dash-dotted lines correspond to  $\beta = -4.3, -4.4$  and  $-4.5$ , as indicated in the legend. The lower

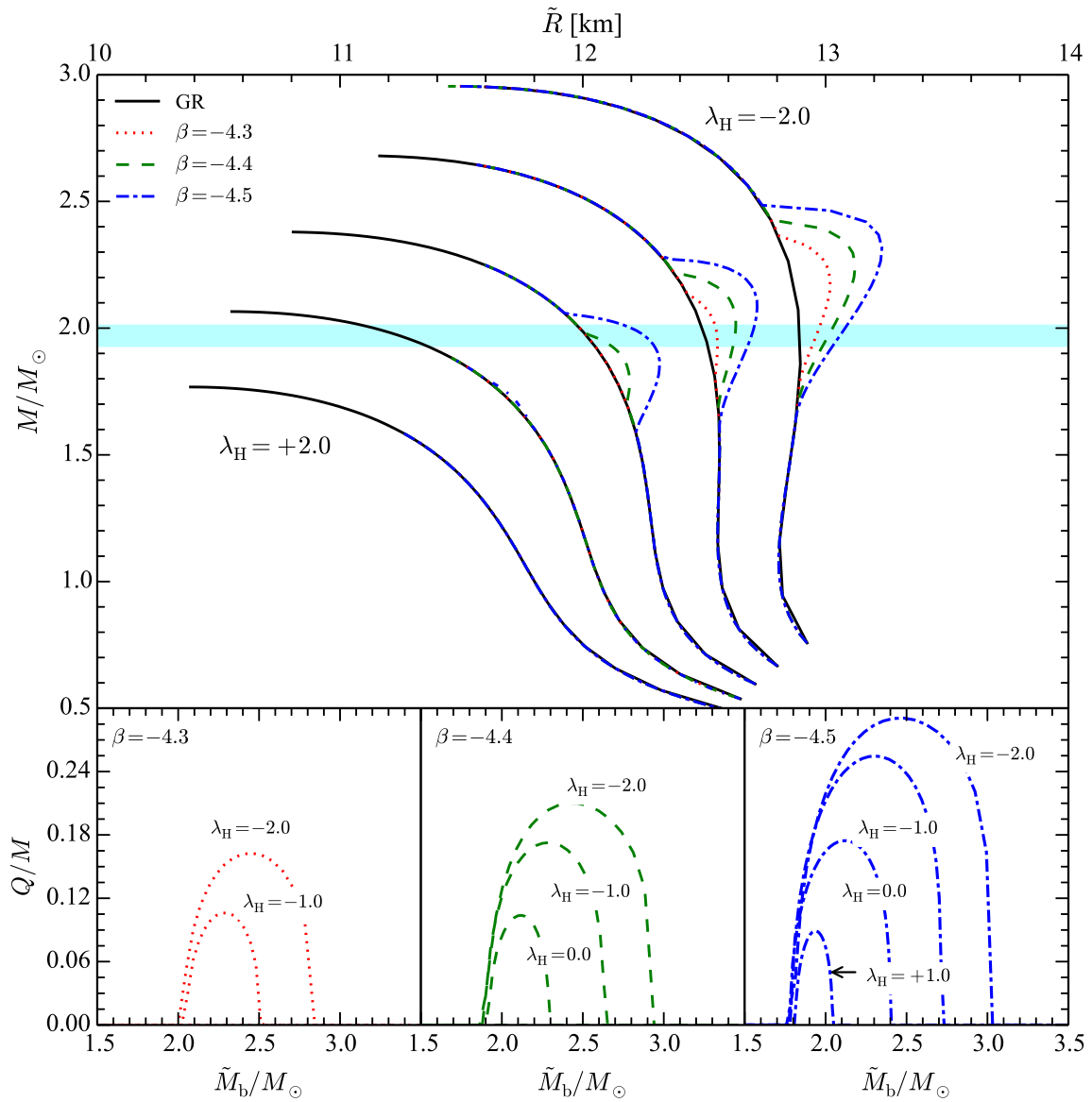


Figure 2.3: Spontaneous scalarization in the quasi-local model of Horvat et al. [48]. See the main text for details.

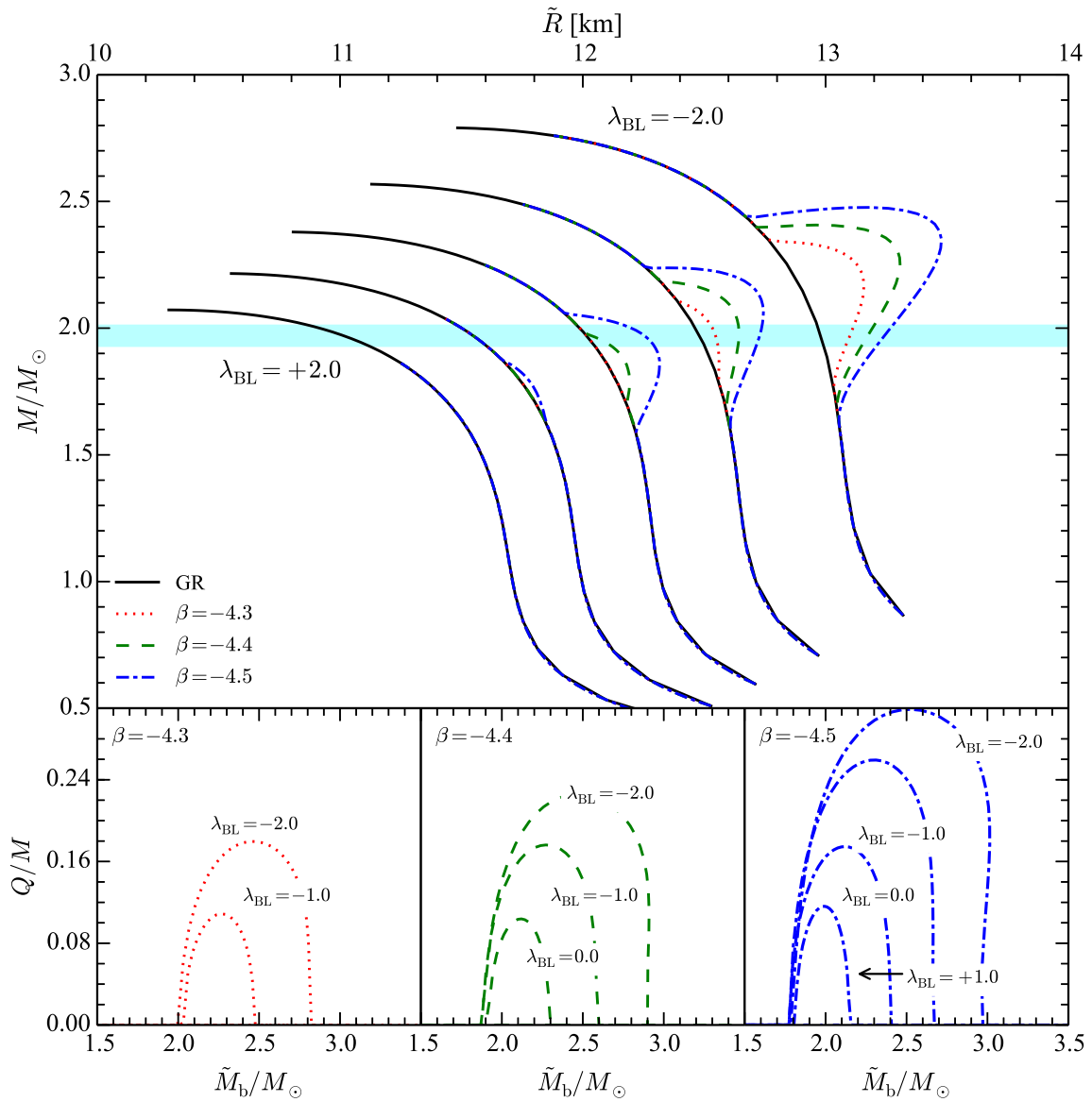


Figure 2.4: Same as Figure 2.3, but for the Bowers-Liang anisotropy model [47].

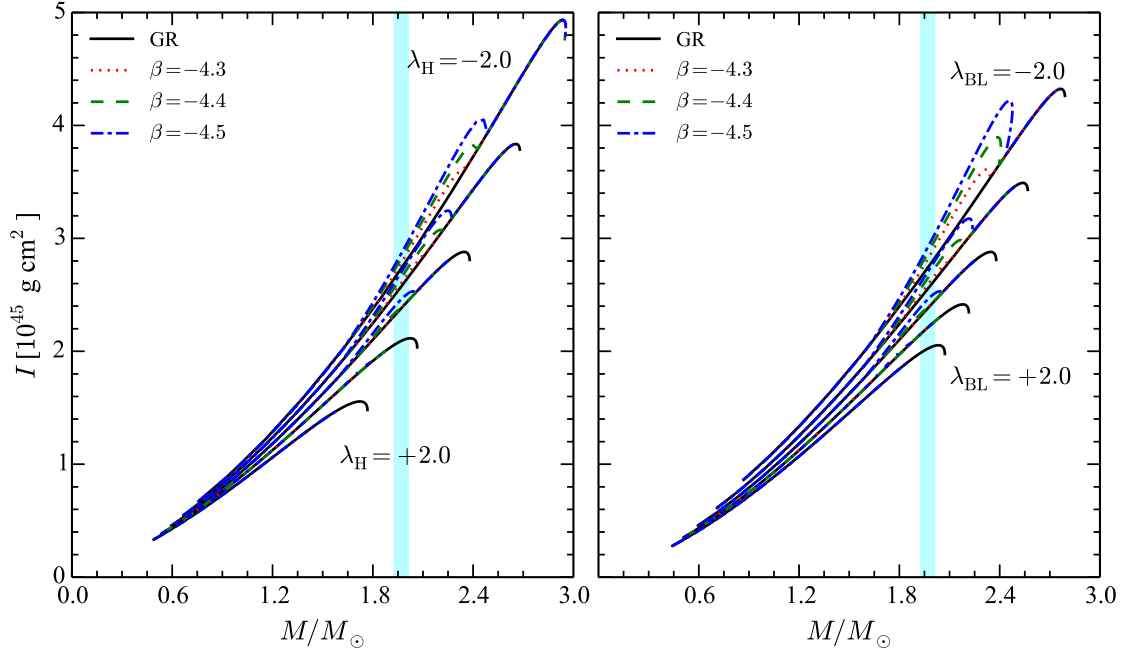


Figure 2.5: Same as Figure 2.2, but in scalar-tensor theories with different values of  $\beta$ .

panels show the scalar charge  $Q/M$  as a function of the baryonic mass. In each of these panels we plot the scalar charge for a fixed value of  $\beta$  and different anisotropy parameters.

For isotropic EoSs in GR, Harada [73] used catastrophe theory to show that scalarization is only possible when  $\beta \lesssim -4.35$ . We find that scalarization can occur for larger values of  $\beta$  in the presence of anisotropy. For example, for a value of  $\lambda_H \sim -2$  (compatible with the Skyrme model predictions of [43]) scalarization is possible when  $\beta \simeq -4.15$ , and for  $\beta \simeq -4.3$  scalarization produces rather large ( $\approx 10\%$ ) deviations in the mass-radius relation. This qualitative conclusion applies to both anisotropy models considered by us. The lower panels show that: (i) for fixed  $\beta$  (i.e., for a fixed theory) and for a fixed central density, the “strength” of scalarization – as measured by the scalar charge of the star – increases for large negative  $\lambda$ 's, i.e. when the tangential pressure is significantly larger than the radial pressure, for both anisotropy models; (ii) scalarization occurs in a much wider range of baryonic masses, all of which are compatible with the range where anisotropy would be expected according to the Skyrme model predictions of [43]. These calculations are of course preliminary and should be refined using microphysical EoS models. However, let us remark once again that the scalarization threshold in the absence of anisotropy is to a very good approximation EoS-independent, and stars only acquire significant scalar charge when  $\beta < -4.35$  (as shown in [73] and in Figure 2.6 below). In the admittedly unlikely event that binary pulsar observations were to hint at scalarization with  $\beta > -4.35$ , this would be strong evidence for the presence of anisotropy<sup>4</sup> and even lead to experimental constraints on the Skyrme model and QCD.

As in Figure 2.2, in the left panel of Figure 2.5 we show the moment of inertia as a function

<sup>4</sup>An important caveat here is that *fast* rotation can also strengthen the effects of scalarization: according to [88], scalarization can occur for  $\beta < -3.9$  for NSs spinning at the mass-shedding limit. However the NSs found in binary pulsar systems are relatively old, as they are expected to be spinning well below the mass-shedding limit, where the slow-rotation approximation works very well [89].

of the stellar mass for the quasi-local model of [48], while the right panel refers to the Bowers-Liang model [47]. Solid lines corresponds to the GR limit for different anisotropy parameters. Unsurprisingly, the largest modifications to the moment of inertia occur for large negative  $\lambda$ 's, and they follow the same trends highlighted in our discussion of the mass-radius relation.

### 2.3.3 Critical scalarization point in the linearized approximation

The condition for spontaneous scalarization to occur can be found in a linearized approximation to the scalar-field equation of motion. The idea is that *at the onset* of scalarization the scalar field must be small, so we can neglect its backreaction on the geometry and look for bound states of the scalar field by dropping terms quadratic in the field [58, 72]. Here we study general conditions for the existence of bound states in the linearized regime, and we show that (as expected based on the previous argument) the linearized theory does indeed give results in excellent agreement with the full, nonlinear calculation.

Redefining the scalar field as  $\varphi(t, r) = r^{-1}\Psi(r)e^{-i\nu t}$  and neglecting terms  $\mathcal{O}(\varphi^2)$ , Eq. (2.4) can be written as a Schrödinger-like equation:

$$\frac{d^2\Psi}{dx^2} + [\nu^2 - V_{\text{eff}}(x)] \Psi = 0, \quad (2.34)$$

where the tortoise radial coordinate  $x$  is defined by  $dx \equiv dr e^{-\Phi}/\sqrt{1 - 2\mu/r}$ . The effective potential is

$$V_{\text{eff}}(r) \equiv e^{2\Phi} \left[ \mu_{\text{eff}}^2(r) + \frac{2\mu}{r^3} + 4\pi(\tilde{p} - \tilde{\epsilon}) \right], \quad (2.35)$$

where we have introduced an effective (position-dependent) mass

$$\mu_{\text{eff}}^2(r) \equiv -4\pi\beta T_*. \quad (2.36)$$

Eq. (2.34) with the potential (2.35) is a wave equation for a scalar field with effective mass  $\mu_{\text{eff}}$ . From Eq. (2.11) we see that anisotropy affects the effective mass (and therefore the scalarization threshold) because  $T_*$  contains a term proportional to  $\tilde{\sigma}$ , that in turn is proportional to either  $\lambda_{\text{H}}$  or  $\lambda_{\text{BL}}$ : cf. Eqs. (2.12) and (2.13). The case of spontaneous scalarization around black holes (studied in [63, 64]) can be recovered by setting  $\tilde{\epsilon} = \tilde{p} = 0$ .

The scalarization threshold can be analyzed by looking for the zero-energy ( $\nu \sim 0$ ) bound state solutions of Eq. (2.34). In this case, the scalar field satisfies the following boundary conditions:

$$\Psi \sim \begin{cases} \varphi_c r & \text{as } r \rightarrow 0, \\ \varphi_\infty & \text{as } r \rightarrow \infty, \end{cases} \quad (2.37)$$

and we impose  $\Psi'(r \rightarrow \infty) = 0$ , where the prime denotes derivative with respect to  $r$ . To obtain the scalarization threshold we integrate Eq. (2.34) outwards, starting from  $r = 0$ , with the above boundary conditions. Since the equation is linear,  $\varphi_c$  is arbitrary. At infinity we impose that the first derivative of  $\Psi$  with respect to  $r$  must be zero. This is a two-point boundary value

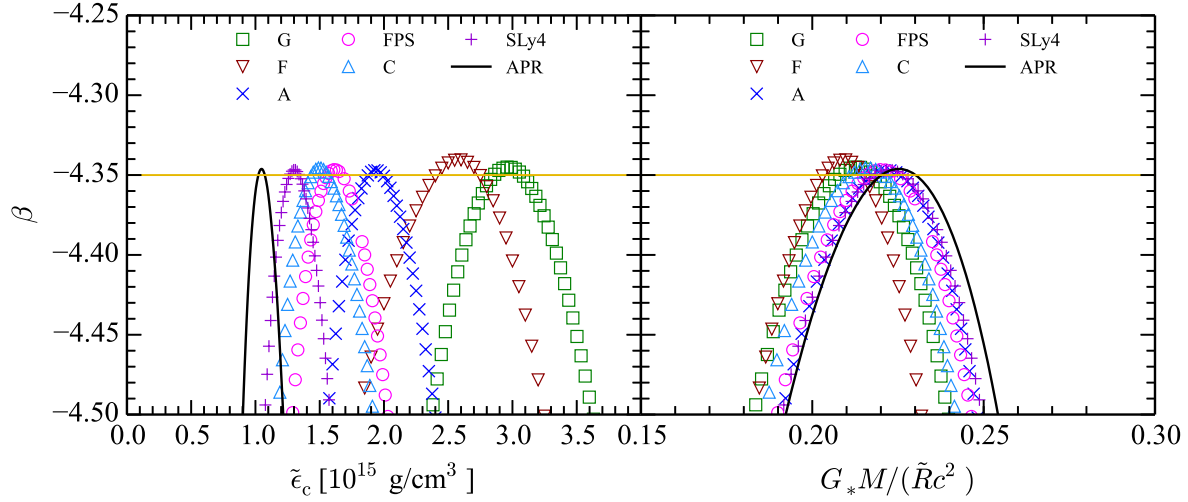


Figure 2.6: Critical  $\beta$  for scalarization as a function of the central density (left panel) and of the stellar compactness (right panel) for nonrotating NS models constructed using different nuclear-physics based EoSs, in the absence of anisotropy.

problem that can be solved with a standard shooting method to find the critical value of the central density  $\tilde{\epsilon}_c$  for which the above conditions are satisfied, given fixed values of  $\beta$  and  $\lambda_H$  (or  $\lambda_{BL}$ ). The solution is some

$$\tilde{\epsilon}_i = \tilde{\epsilon}_i(\beta), \quad (2.38)$$

where  $\tilde{\epsilon}_i$  is the smallest critical density at which scalarization can occur for the given  $\beta$ . The largest critical density producing scalarization can be similarly obtained by looking for zero-energy bound state solutions to find some

$$\tilde{\epsilon}_f = \tilde{\epsilon}_f(\beta). \quad (2.39)$$

It can be shown that in these two regimes (i.e., at the starting and ending points of the scalarization regime) the derivative of  $\Psi'(r \rightarrow \infty)$  with respect to  $\tilde{\epsilon}_c$  has opposite signs:

$$\frac{\partial}{\partial \tilde{\epsilon}_c} \Psi'(r \rightarrow \infty) \begin{cases} < 0 & \text{for } \tilde{\epsilon}_c = \tilde{\epsilon}_i, \\ > 0 & \text{for } \tilde{\epsilon}_c = \tilde{\epsilon}_f. \end{cases} \quad (2.40)$$

As a warm-up, in Figure 2.6 we compute the scalarization threshold for nonrotating isotropic stars with several nuclear-physics based EoSs. The original references for the subset of EoSs used here can be found in [90] (the one exception is SLy4: cf. [91]). The EoSs are sorted by stiffness, with APR EoS being the stiffest and G EoS the softest in our catalog. As a trend, for stiffer EoSs scalarization occurs at lower values of the central densities and at higher values of the compactness. The most remarkable fact is that the value  $\beta = \beta_{\max}$  above which scalarization cannot occur is very narrow: it ranges from  $\beta_{\max} = -4.3462$  for APR EoS to  $\beta_{\max} = -4.3405$  for F EoS [92]. This is consistent with Harada's study based on catastrophe theory, that predicts a threshold value  $\beta_{\max} \simeq -4.35$  (horizontal line in the figure) in the absence of anisotropy [73] (see also [93]).

Table 2.1: Critical density values obtained through the linearized theory and the full nonlinear equations for APR EoS, different values of the Horvat et al. anisotropy parameter  $\lambda_H$  and  $\beta = -4.5$ : for these choices of parameters, the solution is scalarized if  $\tilde{\epsilon}_i < \tilde{\epsilon}_c < \tilde{\epsilon}_f$ . The last column lists the critical value  $\beta = \beta_{\max}$  above which scalarization is not possible.

$\lambda_H$	Linearized		Full nonlinear		
	$\tilde{\epsilon}_i$ (g cm $^{-3}$ )	$\tilde{\epsilon}_f$ (g cm $^{-3}$ )	$\tilde{\epsilon}_i$ (g cm $^{-3}$ )	$\tilde{\epsilon}_f$ (g cm $^{-3}$ )	$\beta_{\max}$
-2	$6.983 \times 10^{14}$	$9.141 \times 10^{14}$	$6.980 \times 10^{14}$	$9.140 \times 10^{14}$	-4.150
-1	$7.819 \times 10^{14}$	$1.053 \times 10^{15}$	$7.817 \times 10^{14}$	$1.053 \times 10^{15}$	-4.239
0	$9.021 \times 10^{14}$	$1.216 \times 10^{15}$	$9.021 \times 10^{14}$	$1.216 \times 10^{15}$	-4.346
1	$1.127 \times 10^{15}$	$1.340 \times 10^{15}$	$1.126 \times 10^{15}$	$1.341 \times 10^{15}$	-4.471

In Table 2.1 we compare the values for  $\tilde{\epsilon}_i$  and  $\tilde{\epsilon}_f$  computed using (i) the linearized method described in this Section, and (ii) the full nonlinear set of equations for anisotropic models constructed using the APR EoS. The results agree remarkably well, showing that the onset of scalarization can be analyzed to an excellent degree of accuracy by neglecting the backreaction effects of the scalar field on the geometry. The last column of Table 2.1 lists  $\beta_{\max}$ , the value of  $\beta$  above which scalarization cannot happen. We do not present results for  $\lambda_H = 2$  because the resulting  $\beta_{\max}$  is already ruled out by binary pulsar observations [74].

In the left panels of Figure 2.7 we analyze the dependence of the critical  $\beta$  on the central density, focusing on EoS APR and selecting different values of the anisotropy parameters  $\lambda_{BL}$  (top) and  $\lambda_H$  (bottom). The shaded region at the top ( $\beta \gtrsim -4.5$ ) is allowed by current binary pulsar observations [74, 75]. The horizontal line is the roughly EoS-independent threshold  $\beta_{\max} \simeq -4.35$  for isotropic stars. For a given theory, the starting and ending points of the scalarization regime are those for which a  $\beta = \text{constant}$  (horizontal) line crosses the curves. Anisotropic models have two distinctive features: (1) when the tangential pressure is larger than the radial pressure (dashed lines in Figure 2.7) scalarization can occur even for  $\beta \geq -4.35$  (for example, for the Horvat et al. model with  $\lambda_H = -2$  we have  $\beta_{\text{crit}} = -4.1513$ , and for the Bowers-Liang model with  $\lambda_{BL} = -2$  we have  $\beta_{\text{crit}} = -4.1354$ ; cf. Table 2.1, Figure 2.4 and Figure 2.3); (2) when the tangential pressure is smaller than the radial pressure (dash-dotted lines in Figure 2.7) scalarized solutions may exist for a much wider range of  $\tilde{\epsilon}_c$ .

In the right panels of Figure 2.7 we plot the critical  $\beta$  as a function of the stellar compactness  $G_*M/\tilde{R}c^2$ . For low compactness ( $M/\tilde{R} \lesssim 0.15$ ) all curves have the same behaviour regardless of  $\lambda_H$  or  $\lambda_{BL}$ . This universality has two reasons: (1) all modern nuclear-physics based EoS have the same Newtonian limit (cf. [94] for an analytic treatment of this regime for constant density stars); (2) for any given EoS, the effects of anisotropy are suppressed in the Newtonian regime, where pressures and densities are low and the local compactness parameter is small: cf. Eqs. (2.12) and (2.13).

## 2.4 Conclusions

Binary pulsar observations require  $\beta \gtrsim -4.5$  [74, 75], and even more stringent constraints are expected in the near future. As shown in Figure 2.6, most “ordinary” nuclear-physics based EoSs for nuclear matter predict that scalarization can only occur for  $\beta < \beta_{\max} = -4.35$ .

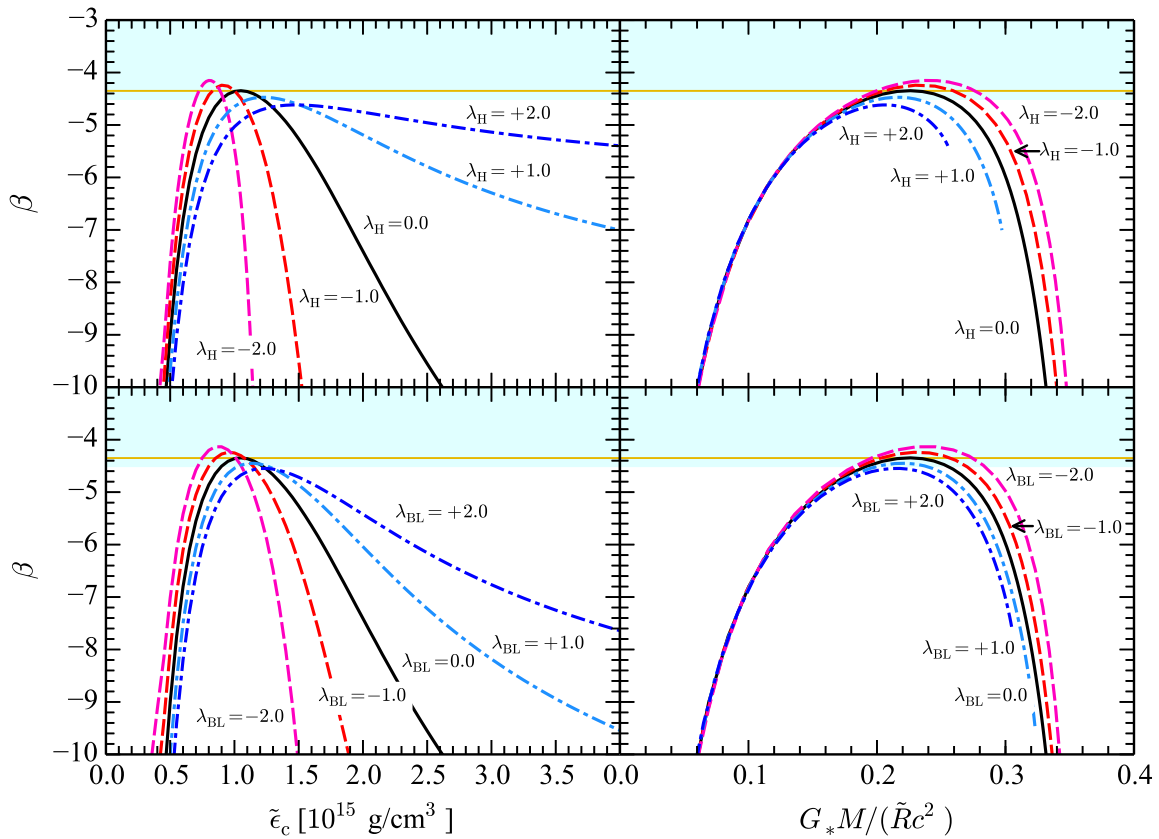


Figure 2.7: Left panels:  $\beta$  versus critical central densities for different values of  $\lambda_{H,BL}$ . Right panels:  $\beta$  versus compactness  $G_* M / \tilde{R}c^2$  of the critical solutions for different values of  $\lambda_{H,BL}$ .

As binary pulsar observations get closer and closer to the limit  $\beta \gtrsim -4.35$ , the spontaneous scalarization mechanism originally proposed by Damour and Esposito-Farèse [58, 72] looks more and more unlikely to be realized in Nature if neutron stars are isotropic.

The admittedly unlikely event of a binary-pulsar observation of scalarization with  $\beta > -4.35$  would be strong evidence for the presence of anisotropy, and it may even lead to experimental constraints on the Skyrme model and QCD. An important caveat here is that *fast* rotation can also strengthen the effects of scalarization: according to [88], scalarization can occur for  $\beta < -3.9$  when NSs spin at the mass-shedding limit. However the NSs found in binary pulsar systems are relatively old, and they are expected to spin well below the mass-shedding limit, where the slow-rotation approximation works very well [89].

Our work can be extended in several directions. An obvious extension is to consider the effects of anisotropy at second or higher order in the Hartle-Thorne expansion. This would allow us to assess whether the recently discovered “I-Love-Q” and “three-hair” universal relations between the multipole moments of the spacetime hold in the presence of anisotropy *and* scalarization [83, 95–98]. A second obvious extension could consider fast rotating, anisotropic stars (cf. [88, 99]) and the orbital and epicyclic frequencies around these objects [100].

Anisotropy can lower the threshold for scalarization to occur, and this could be of interest to test scalar-tensor theories through gravitational-wave asteroseismology [101–103]. We also remark that our study used simplified, phenomenological models for anisotropy, when of course it would be desirable to study realistic microphysical models. Last but not least, our study should be extended to evaluate the stellar sensitivities [104, 105] and to identify exclusion regions in the  $(\beta, \lambda)$  parameter space using binary pulsar observations (cf. e.g. [106]).

## **Part II**

# **Wave-emission processes and quasinormal modes**

# Chapter 3

## Semi-Classical Analysis of the Scalar Geodesic Synchrotron Radiation in Kerr Spacetime

### 3.1 Introduction

The Kerr spacetime [107], which describes chargeless rotating black holes, is one of the most important solutions of Einstein's equation. In the context of standard general relativity, the no-hair theorems guarantee that the Kerr spacetime is the unique stationary, vacuum black hole solution of Einstein's equation [108]. It is estimated, inferred using distinct methods, that most black hole candidates have a considerable value of the rotation parameter (see, e.g., Ref. [109], and references therein). In fact, although the Schwarzschild solution is suitable for a great variety of physical phenomena related to stars and black holes, the Kerr solution becomes very important in the investigation of the electro-dynamical aspects of accretion disks for binary X-ray sources [110, 111]. Moreover, the investigation of how radiation-emission processes are modified by the nontrivial curvature of rotating black holes is particularly important. As an approximation to the phenomena, one can consider a particle in a circular geodesic motion in the equatorial plane of the black hole. The radiation emitted in this configuration is called geodesic synchrotron radiation.

The geodesic synchrotron radiation was investigated in the context of classical field theory in the 70s (see, e.g., Ref. [112]). The results were obtained using the Wentzel-Kramers-Brillouin (WKB) approximation. In the context of quantum field theory in curved spacetimes, using both numerical and analytical procedures, the geodesic synchrotron radiation has been analyzed in the case of the massless scalar field [113, 114], massive scalar field [115] and electromagnetic field [116] in Schwarzschild spacetime as well as for the massless scalar field in Reissner-Nordström spacetime [117].

In the present chapter, we consider a source minimally coupled to a massless scalar field,

orbiting a Kerr black hole, both in stable and unstable circular orbits, considering direct and retrograde orbits. The remainder of this chapter is organized as follows: In Sec. 3.2 we analyze the massless scalar field in Kerr spacetime. In Sec. 3.3 we obtain the expression of the emitted power. In Sec. 3.4 we present the numerical procedure, the results for the power emitted by the source in circular orbits, and compute the amount of radiation which escapes to infinity (asymptotic radiation). Our analysis is made for arbitrary values of the black hole angular momentum. In Sec. 3.5 we present our final remarks. We use the natural units  $c = \hbar = G = 1$  and the signature  $(+ - - -)$  throughout this chapter.

## 3.2 Scalar field in Kerr spacetime

The Kerr line element in the standard Boyer-Lindquist coordinates  $(t, r, \theta, \phi)$ , describing a rotating black hole with mass  $M$  and angular momentum per unit mass  $a$  is given by

$$ds^2 = \left(1 - \frac{2Mr}{\rho^2}\right) dt^2 + \frac{4Mar \sin^2 \theta}{\rho^2} dt d\phi - \frac{\rho^2}{\Delta} dr^2 - \rho^2 d\theta^2 - \left(r^2 + a^2 + \frac{2Mra^2 \sin^2 \theta}{\rho^2}\right) \sin^2 \theta d\phi^2, \quad (3.1)$$

with  $\rho^2 = r^2 + a^2 \cos^2 \theta$ , and  $\Delta = r^2 - 2Mr + a^2$ . The Klein-Gordon equation for the massless scalar field is

$$\nabla_\mu \nabla^\mu \Phi = \frac{1}{\sqrt{-g}} \partial_\mu (\sqrt{-g} g^{\mu\nu} \partial_\nu \Phi) = 0, \quad (3.2)$$

where  $g = -\rho^4 \sin^2 \theta$  is the determinant of Kerr metric  $g_{\mu\nu}$ . Taking advantage of the existence of a Killing-Yano tensor in Kerr spacetime [111, 118], we can write the solutions of Eq. (3.2) as [119, 120]

$$u_{\omega lm} \propto R_{\omega lm}(r) S_{\omega lm}(\theta) e^{im\phi - i\omega t}, \quad \omega > 0, \quad (3.3)$$

with the differential equation for the radial function  $R_{\omega lm}(r)$  given by

$$\Delta \frac{d}{dr} \left( \Delta \frac{dR_{\omega lm}}{dr} \right) + [\omega^2 (r^2 + a^2)^2 - 4Ma\omega mr + m^2 a^2 - (\omega^2 a^2 + \lambda_{lm}) \Delta] R_{\omega lm} = 0, \quad (3.4)$$

where  $\lambda_{lm}$  is a separation constant. The function  $S_{\omega lm}(\theta)$  obeys the following differential equation

$$\frac{1}{\sin \theta} \frac{d}{d\theta} \left( \sin \theta \frac{dS_{\omega lm}}{d\theta} \right) + \left( \lambda_{lm} + \alpha \cos^2 \theta - \frac{m^2}{\sin^2 \theta} \right) S_{\omega lm} = 0, \quad (3.5)$$

where  $\alpha = a^2\omega^2$ . The solutions of Eq. (3.5) are given by the oblate spheroidal wave functions of the first kind [121].

The radial differential equation (3.4) can be rewritten as a Schrödinger-like equation, by performing the transformations

$$R_{\omega lm} = \frac{U_{\omega lm}}{(r^2 + a^2)^{1/2}}, \quad \frac{dx}{dr} = \frac{r^2 + a^2}{\Delta}, \quad (3.6)$$

where  $x$  is the Regge-Wheeler coordinate in Kerr spacetime. The resulting equation is

$$\left( -\frac{d^2}{dx^2} + V_{\omega lm}(x) \right) U_{\omega lm}(x) = \omega^2 U_{\omega lm}(x), \quad (3.7)$$

with the effective potential given by

$$V_{\omega lm}(x) = -\frac{1}{(r^2 + a^2)^2} [m^2 a^2 - 4Mma\omega r - \Delta(\lambda_{lm} + \omega^2 a^2)] + \Delta \frac{\Delta + 2r(r - M)}{(r^2 + a^2)^3} - \frac{3r^2 \Delta^2}{(r^2 + a^2)^4}. \quad (3.8)$$

Let us turn our attention to the asymptotic solutions of the radial equation (3.7). By analyzing the effective potential (3.8) near the exterior horizon ( $x \rightarrow -\infty$ ) and far from it ( $x \rightarrow +\infty$ ), we find the asymptotic solutions

$$U_{\omega lm}^{in}(x) = \begin{cases} e^{-i\omega x} + \mathcal{R}_{\omega lm}^{in} e^{i\omega x} & (x \rightarrow +\infty) \\ \mathcal{T}_{\omega lm}^{in} e^{-i\tilde{\omega} x} & (x \rightarrow -\infty) \end{cases}, \quad (3.9)$$

and

$$U_{\omega lm}^{up}(x) = \begin{cases} \mathcal{T}_{\omega lm}^{up} e^{i\omega x} & (x \rightarrow +\infty) \\ \mathcal{R}_{\omega lm}^{up} e^{-i\tilde{\omega} x} + e^{i\tilde{\omega} x} & (x \rightarrow -\infty) \end{cases}, \quad (3.10)$$

where  $\tilde{\omega} = \omega - m\Omega_+$ , and  $\Omega_+ = a/(2Mr_+)$  is the angular velocity of the outer horizon  $r_+$ . The *in* solution describes a flux coming from past null infinity  $\mathcal{J}^-$  and zero flux coming from past event horizon  $\mathcal{H}^-$ , whereas the *up* solution describes a flux coming from  $\mathcal{H}^-$  and zero flux coming from  $\mathcal{J}^-$  (see Refs. [122, 123] for more details about these solutions).

Using the Klein-Gordon inner product

$$(u_{\omega lm}, u_{\omega' l' m'}) = i \int_S dS^\mu u_{\omega lm}^* \overleftrightarrow{\partial}_\mu u_{\omega' l' m'}, \quad (3.11)$$

with  $S$  being a Cauchy surface [124], we obtain

$$u_{\omega lm}^{in} = \frac{U_{\omega lm}^{in}(r)S_{\omega lm}(\theta)}{\sqrt{8\pi^2\omega(r^2+a^2)}N_{\omega lm}^S} e^{im\phi-i\omega t}, \quad \omega > 0, \quad (3.12)$$

$$u_{\omega lm}^{up} = \frac{U_{\omega lm}^{up}(r)S_{\omega lm}(\theta)}{\sqrt{8\pi^2\tilde{\omega}(r^2+a^2)}N_{\omega lm}^S} e^{im\phi-i\omega t}, \quad \tilde{\omega} > 0, \quad (3.13)$$

where  $N_{\omega lm}^S$  is the normalization factor of the spheroidal wave function (cf. Sec. 3.4). To consider the canonical quantization in Kerr spacetime (see Refs. [7, 122, 125, 126] for more details), we expand the field operator as

$$\hat{\Phi} = \sum_{l=0}^{\infty} \sum_{m=-l}^l \left[ \int d\omega (\hat{a}_{\omega lm}^{in} u_{\omega lm}^{in} + \hat{a}_{\omega lm}^{in\dagger} u_{\omega lm}^{in*}) + \int d\tilde{\omega} (\hat{a}_{\omega lm}^{up} u_{\omega lm}^{up} + \hat{a}_{\omega lm}^{up\dagger} u_{\omega lm}^{up*}) \right], \quad (3.14)$$

where the annihilation ( $\hat{a}_{\omega lm}^{in/up}$ ) and creation ( $\hat{a}_{\omega lm}^{in/up\dagger}$ ) operators obey the following non-vanishing commutation relations

$$\left[ \hat{a}_{\omega lm}^{in}, \hat{a}_{\omega' l' m'}^{in\dagger} \right] = \delta_{ll'} \delta_{mm'} \delta(\omega - \omega'), \quad (3.15)$$

and

$$\left[ \hat{a}_{\omega lm}^{up}, \hat{a}_{\omega' l' m'}^{up\dagger} \right] = \delta_{ll'} \delta_{mm'} \delta(\omega - \omega'). \quad (3.16)$$

### 3.3 Scalar radiation

Let us now compute the radiation emitted by the rotating source using quantum field theory in curved spacetimes at tree level, following Ref. [113]. We assume that the scalar field operator is minimally coupled to the source  $j(x)$ , according to the interaction action

$$\hat{S}_I = \int d^4x \sqrt{-g} j(x) \hat{\Phi}. \quad (3.17)$$

The emission amplitude at tree level of a scalar particle with quantum numbers  $(n, \omega, l, m)$  into the past Boulware vacuum  $|B^-\rangle^1$  is given by

$$\mathcal{A}_{\omega lm}^n \equiv i \langle 1; n\omega lm | S_I | B^-\rangle = i \int d^4x \sqrt{-g} j(x) u_{\omega lm}^{n*}, \quad (3.18)$$

<sup>1</sup>The past Boulware vacuum represents a state with zero particles incident from  $\mathcal{H}^-$  and  $\mathcal{J}^-$ . We could, instead of (3.19), use another vacuum defined by annihilation operators connected with the modes *down* and *out*. This would not modify the results obtained here.

where the index  $n$  stands either for  $in$  or  $up$  modes, and  $|B^-\rangle$  is defined by

$$\hat{a}_{\omega lm}^n |B^-\rangle = 0. \quad (3.19)$$

For a scalar particle in circular motion with radius  $R$  in the equatorial plane  $\theta = \pi/2$  of Kerr spacetime, we have

$$j(x) = \frac{q}{\sqrt{-gu^t}} \delta(r - R) \delta(\theta - \pi/2) \delta(\phi - \Omega t), \quad (3.20)$$

where  $q$  determines the magnitude of the source-field coupling,  $\Omega = d\phi/dt$ , and

$$u^t = \frac{1}{\sqrt{g_{tt} + 2g_{t\phi}\Omega + g_{\phi\phi}\Omega^2}} \quad (3.21)$$

is the  $t$ -component of the source 4-velocity.

We obtain that

$$\mathcal{A}_{\omega lm}^n = \frac{2\pi i q U_{\omega lm}^{n*}(R) S_{\omega lm}^*(\pi/2)}{u^t \sqrt{8\pi^2 f(\omega)(r^2 + a^2)} N_{\omega lm}^{S*}} \delta(\omega - \omega_0), \quad (3.22)$$

where

$$f(\omega) = \begin{cases} \omega, & \text{for } n = in \\ \tilde{\omega}, & \text{for } n = up \end{cases}, \quad (3.23)$$

and  $\omega_0 = m\Omega$ . The power emitted by the rotating source with fixed values of the set  $(n, l, m)$  is

$$W_{lm}^n = \int_0^\infty df(\omega) \omega \frac{|\mathcal{A}_{\omega lm}^n|^2}{T}, \quad (3.24)$$

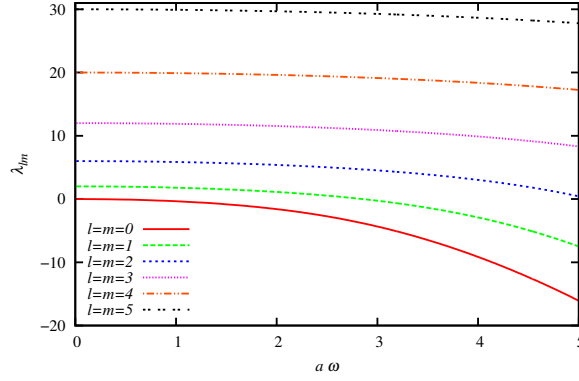
where  $T = 2\pi\delta(0) = \int_{-\infty}^{+\infty} dt$  is the source total time according to asymptotic observers [112]. We obtain the following formulas for the emitted power, for the  $in$  and  $up$  modes

$$W_{lm}^{in} = \frac{q^2}{4\pi(R^2 + a^2)(u^t)^2 |N_{\omega_0 lm}^S|^2} |U_{\omega_0 lm}^{in}(R)|^2 |S_{\omega_0 lm}(\pi/2)|^2, \quad (3.25)$$

$$W_{lm}^{up} = \frac{q^2 \omega_0}{4\pi \tilde{\omega}_0 (R^2 + a^2)(u^t)^2 |N_{\omega_0 lm}^S|^2} |U_{\omega_0 lm}^{up}(R)|^2 |S_{\omega_0 lm}(\pi/2)|^2, \quad (3.26)$$

respectively. The total power irradiated by the rotating source is then given by

$$W^{total} = \sum_{l=1}^{\infty} \sum_{m=1}^l (W_{lm}^{up} + W_{lm}^{in}). \quad (3.27)$$

Figure 3.1:  $\lambda_{lm}$  as a function of  $a\omega$ , for  $l = m = 0, 1, 2, 3, 4, 5$ .

## 3.4 Numerical procedure and results

In this section we shall obtain numerically the radiation emitted by the source rotating around the Kerr black hole.

### 3.4.1 Normalization factor of the spheroidal wave functions

To find the normalization factor  $N_{\omega lm}^S$ , we shall use the boundary conditions

$$S_{\omega lm}(\theta = \pi/2) = P_{lm}(\theta = \pi/2), \quad (3.28)$$

$$\frac{d}{d\theta} S_{\omega lm}(\theta = \pi/2) = \frac{d}{d\theta} P_{lm}(\theta = \pi/2), \quad (3.29)$$

where  $P_{lm}(\theta)$  are the associated Legendre polynomials of the first kind. With these boundary conditions, the spheroidal wave functions of the first kind have the same value as the Legendre polynomials of the first kind when  $a \rightarrow 0$  [121]. We also assume

$$S_{\omega lm}(\theta) = \sum_{\lambda=0,1}^{\infty \prime} d_{\lambda}^{lm}(a\omega) P_{lm}(\theta), \quad (3.30)$$

where the prime in the summation indicates that it only runs over even values of  $\lambda$  when  $l - m$  is even, and over odd values of  $\lambda$  when  $l - m$  is odd. The normalization factor  $N_{\omega lm}^S$  can be found using the standard normalization of Legendre polynomials through

$$\int_0^{\pi} d\theta \sin \theta |S_{\omega lm}(\theta)|^2 = |N_{\omega lm}^S|^2, \quad (3.31)$$

leading to

$$|N_{\omega lm}^S|^2 = 2 \sum_{\lambda=0,1}^{\infty \prime} \frac{(\lambda + 2m)! (d_{\lambda}^{lm})^2}{(2\lambda + 2m + 1)\lambda!}, \quad (3.32)$$

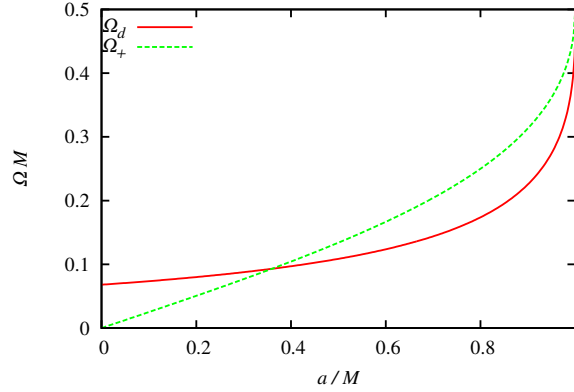


Figure 3.2: Angular velocity  $\Omega_d$  of the source at the DISCO and  $\Omega_+$  as a function of  $a$ . We can see that for the DISCO,  $\tilde{\omega} > 0$  holds for  $a \lesssim 0.35$ .

where the coefficients  $d_\lambda^{lm}(a\omega)$  are determined by the recurrence relation obtained substituting the expansion (3.30) in Eq. (3.5), assuming that the solution is regular (see, e.g., the appendix of Ref. [121]).

As for the numerical precision, we perform the summation of the right hand side of Eq. (3.32) until the next term contributes with less than  $10^{-6}$  of the total value. The number of terms needed to calculate the normalization factor is bigger for bigger values of  $a^2\omega^2$ .

### 3.4.2 Radial functions

To solve the radial equation (3.7) numerically, we must know the eigenvalues  $\lambda_{lm}$ . We obtain these eigenvalues from a transcendental equation, involving  $a^2\omega^2$ ,  $l$  and  $m$ , which follows from the spheroidal wave equation. This equation has the form of an infinite continued fraction, which shall be truncated. We have chosen to truncate the continued fraction when the next term contributes with less than  $10^{-6}$  of the value of  $\lambda_{lm}$ . While solving the resulting equation, one obtains more than one value for  $\lambda_{lm}$ . The value which we are interested in is the one that smoothly connects  $\lambda_{lm}$  with the eigenvalues of the associated Legendre equation in the limit  $a \rightarrow 0$ , i.e.,  $\lambda_{lm} \approx l(l+1)$ , when  $a \approx 0$ . We have compared our values of  $\lambda_{lm}$  with the ones exhibited in Ref. [121], obtaining excellent agreement. In Fig. 3.1 we plot  $\lambda_{lm}$  as a function of  $a\omega$ , for  $l = m = 0, 1, 2, 3, 4, 5$ . We can see that  $l = m = 0$  presents comparatively the major change as  $a\omega$  increases.

### 3.4.3 Emitted power

In this subsection we compute the power emitted by the source in circular orbit around a Kerr black hole. We obtain numerically the emitted power for arbitrary orbits, analyzing its behavior for different values of the black hole rotation parameter  $a$ . We start analyzing the power emitted by the source at the innermost stable circular orbit (ISCO) [112, 127]. For  $a \rightarrow M$  the radius of the direct innermost stable circular orbit (DISCO) approaches the direct light-like circular orbit and both approach the exterior horizon, so that we pass from orbits with non-relativistic velocities to those with relativistic velocities.

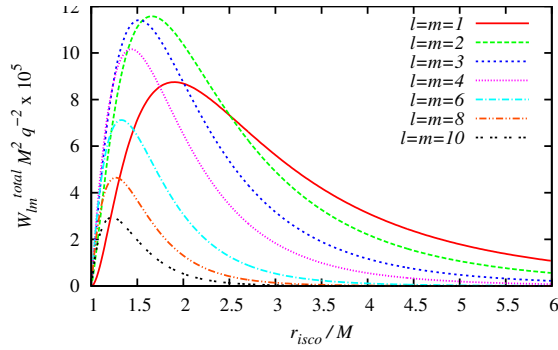


Figure 3.3: Power emitted by the rotating source at DISCO as a function of the radius of the last stable orbit  $r_{isco}$ , for different choices of  $l = m$ . As  $a/M$  varies from 0 to 1,  $r_{isco}/M$  varies from 6 to 1, respectively.

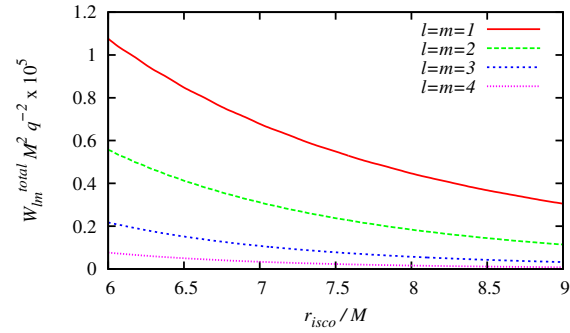


Figure 3.4: Power emitted by the rotating source at the RISCO as a function of the radius of the last stable orbit  $r_{isco}$ , for different choices of  $l = m$ . As  $a/M$  varies from 0 to 1,  $r_{isco}/M$  varies from 6 to 9, respectively.

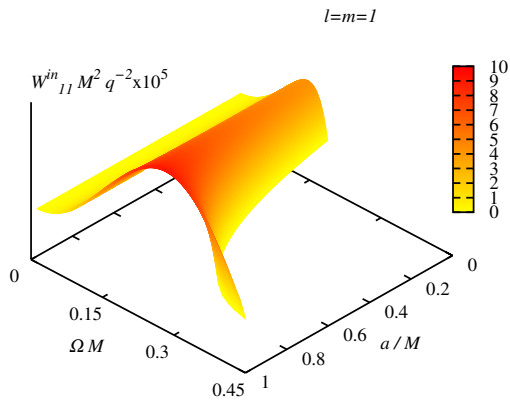


Figure 3.5: Contribution of the  $in$  modes with  $l = m = 1$  to the power emitted by the rotating source in direct orbits, as a function of  $a$  and  $\Omega$ . The right vertical bar gives the intensity of the emitted power of the  $in$  modes ( $W_{11}^{in} M^2 q^{-2} \times 10^5$ ).

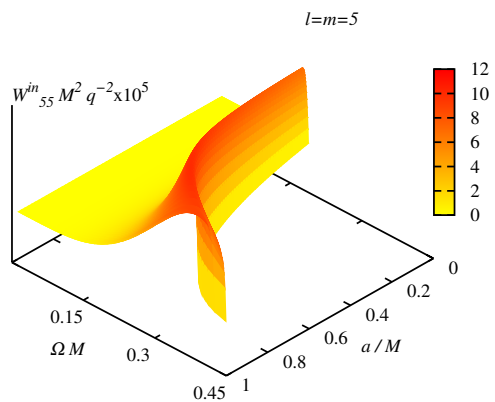


Figure 3.6: Contribution of the  $in$  modes with  $l = m = 5$  to the power emitted by the rotating source in direct orbits, as a function of  $a$  and  $\Omega$ .

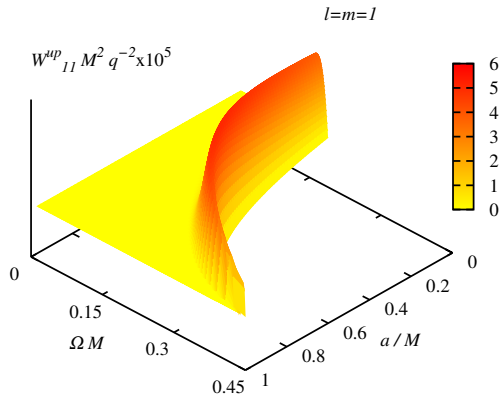


Figure 3.7: Contribution of the  $up$  modes with  $l = m = 1$  to the power emitted by the rotating source in direct orbits, as a function of  $a$  and  $\Omega$ .

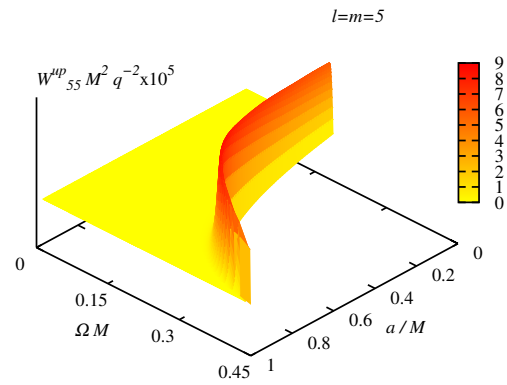


Figure 3.8: Contribution of the  $up$  modes with  $l = m = 5$  to the power emitted by the rotating source in direct orbits, as a function of  $a$  and  $\Omega$ .

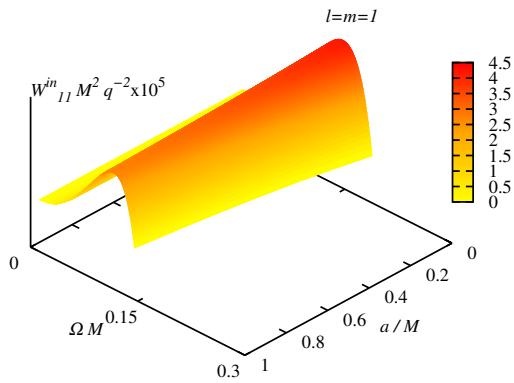


Figure 3.9: Contribution of the  $in$  modes with  $l = m = 1$  to the power emitted by the rotating source in retrograde orbits, as a function of  $a$  and  $\Omega$ .

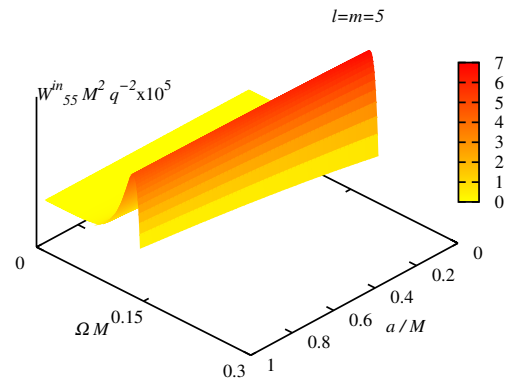


Figure 3.10: Contribution of the  $in$  modes with  $l = m = 5$  to the power emitted by the rotating source in retrograde orbits, as a function of  $a$  and  $\Omega$ .

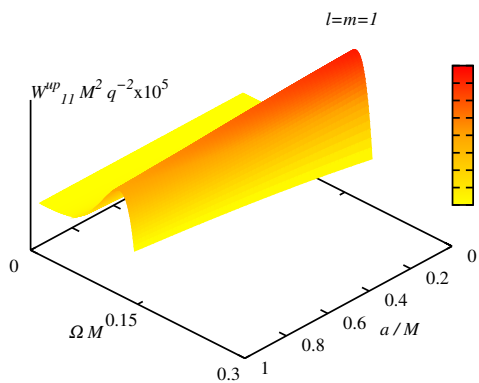


Figure 3.11: Contribution of the  $up$  modes with  $l = m = 1$  to the power emitted by the rotating source in retrograde orbits, as a function of  $a$  and  $\Omega$ .

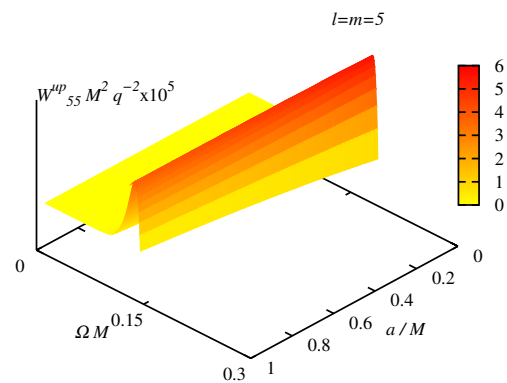


Figure 3.12: Contribution of the  $up$  modes with  $l = m = 5$  to the power emitted by the rotating source in retrograde orbits, as a function of  $a$  and  $\Omega$ .

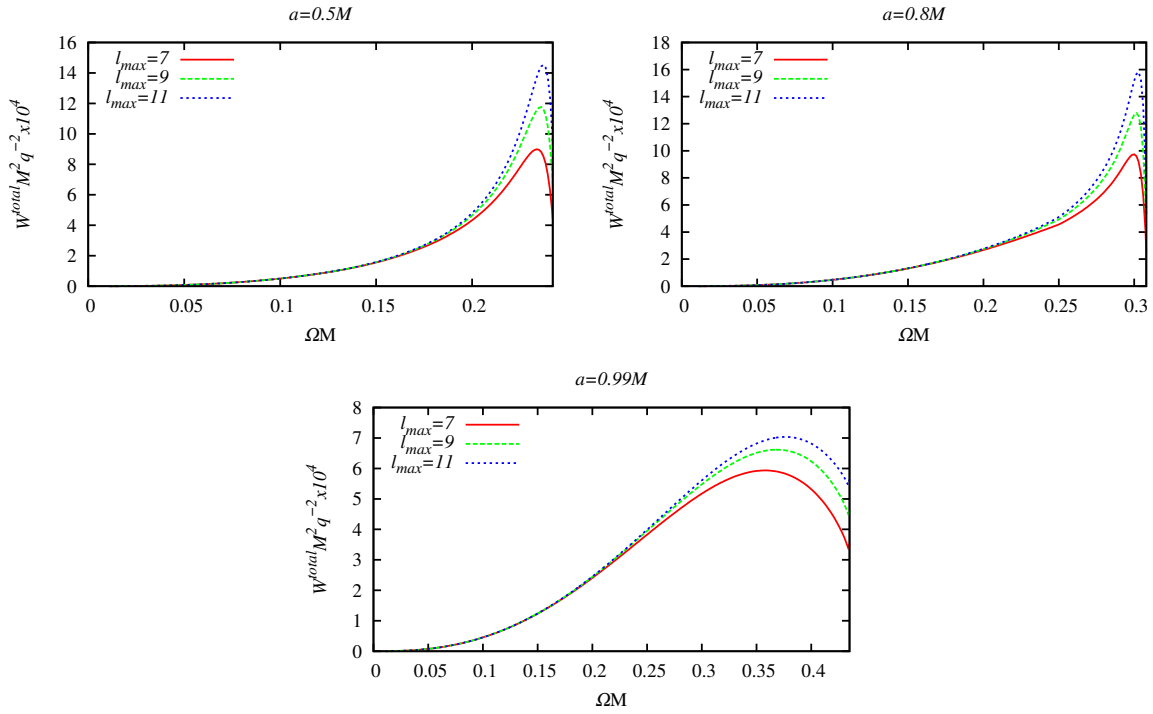


Figure 3.13: Total emitted power in Kerr spacetime for direct orbits, considering different values of  $l_{\text{max}}$  and  $a$ , as a function of  $\Omega$ .

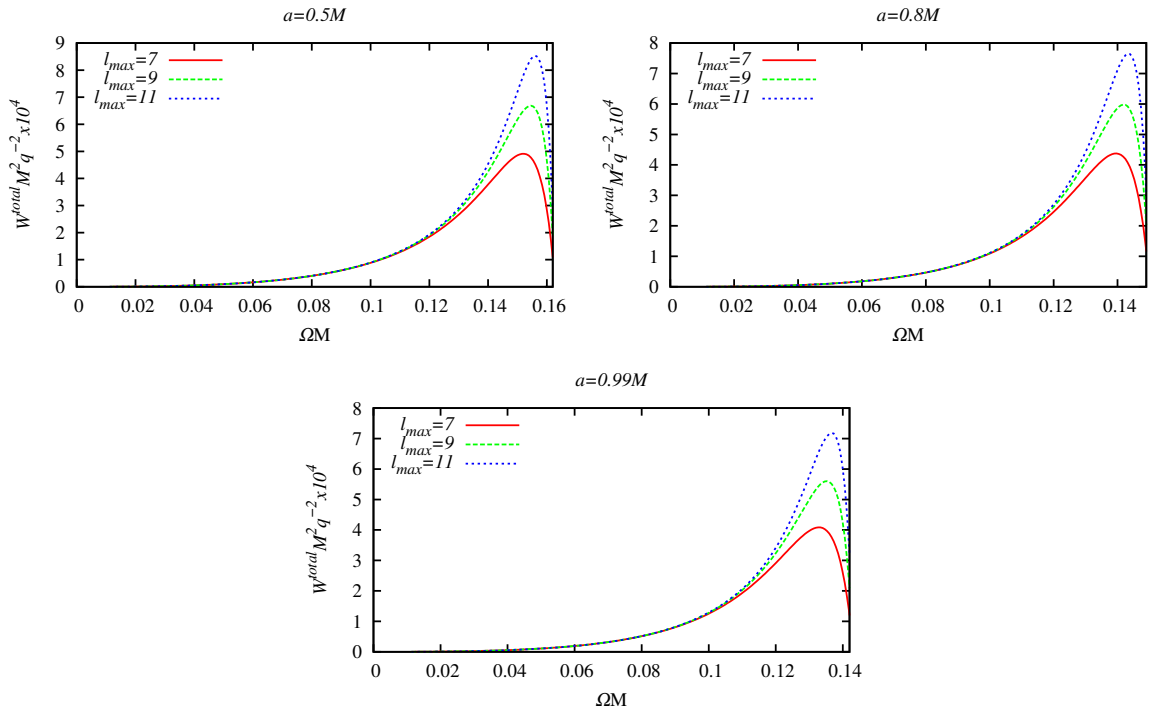


Figure 3.14: Total emitted power in Kerr spacetime for retrograde orbits, considering different values of  $l_{\text{max}}$  and  $a$ , as a function of  $\Omega$ .

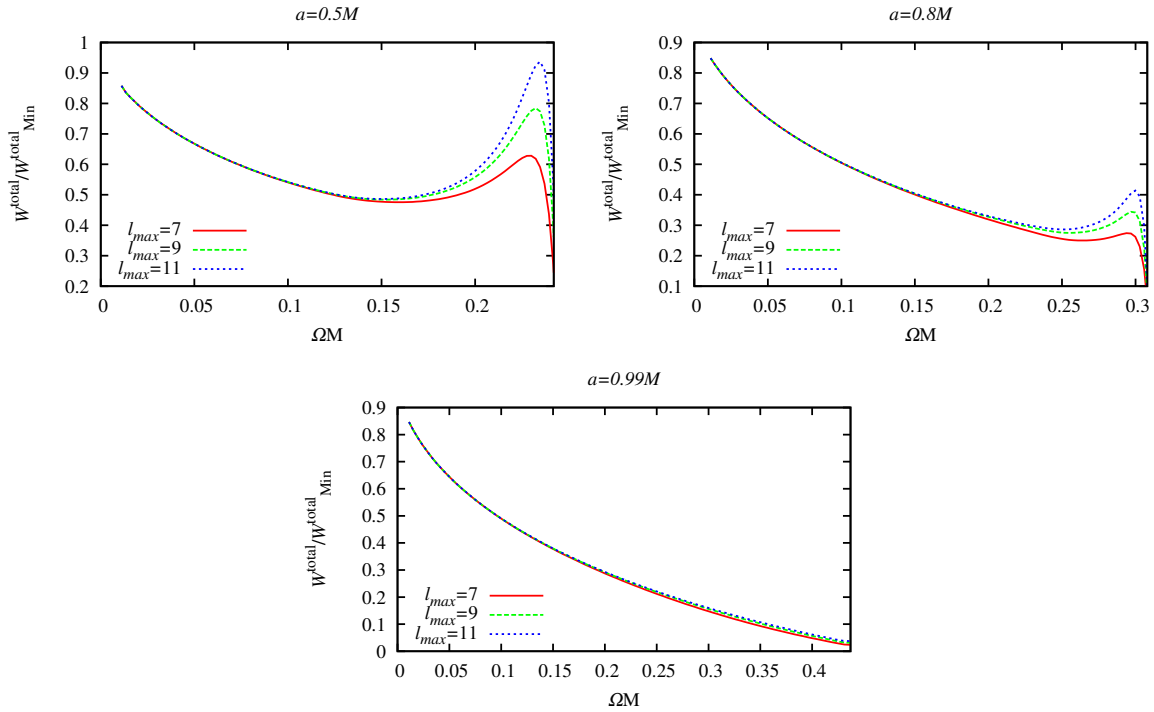


Figure 3.15: Ratio between the emitted power in Kerr spacetime for direct orbits, considering different values of  $l_{\text{max}}$  and  $a$ , and the emitted power in Minkowski spacetime (considering Newtonian gravity).

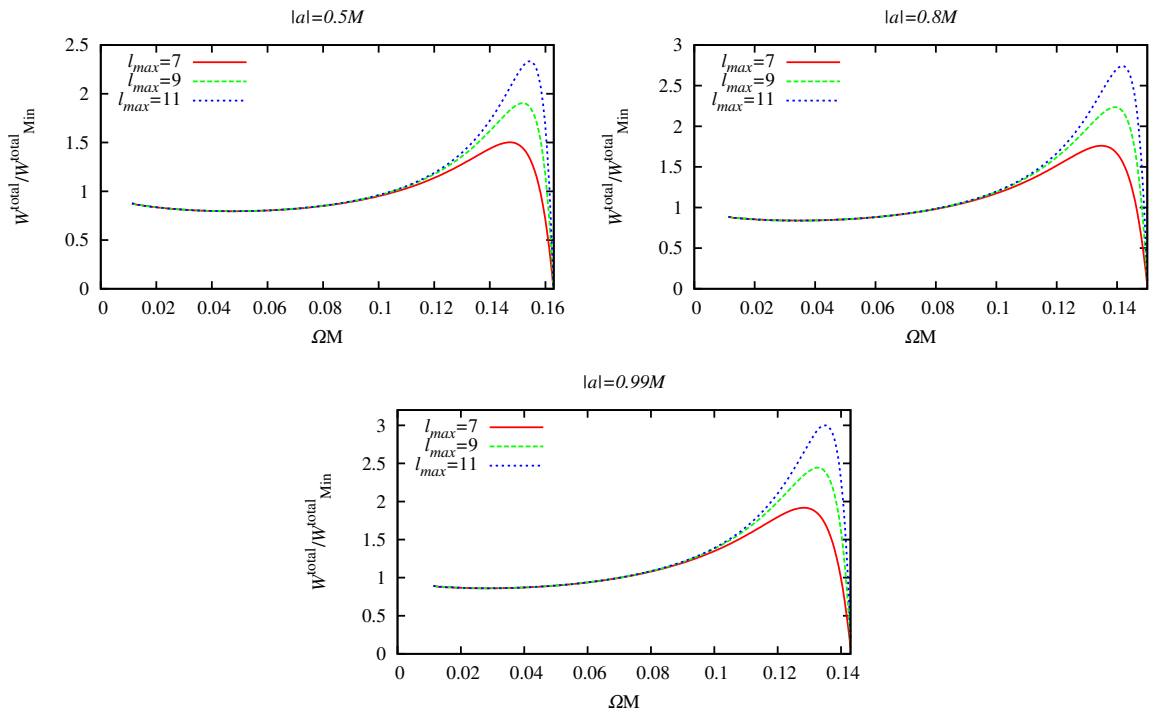


Figure 3.16: Ratio between the emitted power in Kerr spacetime for retrograde orbits, considering different values of  $l_{\text{max}}$  and  $a$ , and the emitted power in Minkowski spacetime.

Prior to the analysis of the power emitted by the source at the ISCO, some points should be emphasized. For a large range of the parameter  $a$ , the modes  $up$  do not contribute to the radiation when the particle is in DISCOs. This is so, because the  $up$  modes are defined only in the  $\tilde{\omega} > 0$  regime, or, equivalently,  $\Omega > \Omega_+$ . For the retrograde innermost stable circular orbits (RISCOs) one can show that the  $up$  modes give a non-vanishing contribution to the emitted power for any value of  $\Omega$ , because  $\tilde{\omega}_0 > 0$ . From Fig. 3.2 we see that the  $up$  modes contribute to the emitted power only for  $a/M \lesssim 0.35$ , for the DISCOs. Another characteristic, as pointed out in Ref. [113,114] for the Schwarzschild case, is that the power associated with the  $up$  modes for stable orbits is negligible when compared to the one associated with the  $in$  modes. The same holds in Kerr case. For instance, the power irradiated by the particle in the DISCO is basically the power associated with the  $in$  modes.

In Fig. 3.3 we plot the power emitted by the rotating source at the DISCO as a function of the radius  $r_{isco}$  of the orbit. We can see that as we increase the value of  $l = m$ , the maximum value of the emitted power grows from  $l = m = 1$  to  $l = m = 2$ , and then decreases for higher values of  $l = m$ . The rotation of the black hole considerably affects the emitted power. For example, for  $l = m = 2$ , we see that at  $r_{isco} \approx 1.65M$  ( $a \approx 0.977M$ ) the emitted power is more than 20 times bigger than the power emitted by a source at the last stable orbit in Schwarzschild spacetime ( $r_{isco} = 6M$ ).

By using the WKB method to find the solution of the radial equation (3.7) in the high-frequency regime (see, e.g., Refs. [117,128]), one can confirm that the emitted power is negligible for high values of  $l$  and  $m$ . Therefore, indeed, there is no considerable amount of emitted power for direct orbits by the source in DISCO as  $a \rightarrow M$  in the high-frequency regime. This was shown in the classical context in Ref. [129]. Here (see Fig. 3.3) we have obtained the same behavior using numerical computations to find non-approximated solutions of the radial equation (3.4).

In Fig. 3.4 we plot the power emitted by the rotating source at the RISCO as a function of the radius  $r_{isco}$  of the orbit. We can see that the power emitted decreases as  $r_{isco}$  increases, i. e., it decreases as  $a$  increases. This is compatible with the fact that for retrograde motions the modulus of angular velocity decreases as  $r_{isco}$  increases. We also see, from Fig. 3.4, that the power emitted decreases as  $l = m$  increases.

We shall now analyze the power emitted by the source in general circular orbits, including stable and unstable ones. In Figs. 3.5-3.8 we plot the power associated with  $in$  and  $up$  modes emitted by the rotating source in direct circular orbits as a function of  $\Omega$  and  $a$ , for two different choices of  $l = m$ . We can see that the  $in$  modes give the main contribution to the total emitted power, as we have already stated. From Fig. 3.5 we can see that for  $l = m = 1$  the maximum of the irradiated power by the  $in$  modes is larger for larger values of  $a$ . This does not occur for  $l = m = 5$ , in which the maximum of the irradiated power by the  $in$  modes, as  $a$  increases, initially increases, reaches a maximum and then decreases, as can be seen in Fig. 3.6. The  $up$  modes contribute only when  $\Omega > \Omega_+$ , as previously stated.

In Figs. 3.7 and 3.8 we plot the emitted power associated with the  $up$  modes for  $l = m = 1$  and  $l = m = 5$ , respectively. For a fixed value of  $a$ , the maximum of the power associated with the  $up$  modes, as  $a$  increases, initially increases, reaches a maximum and then decreases, for both  $l = m = 1$  and  $l = m = 5$ , as can be seen in Figs. 3.7 and 3.8, respectively. From these plots we can clearly see that the power emitted by a source in a relativistic orbit is considerably different for different values of the black hole rotation parameter.

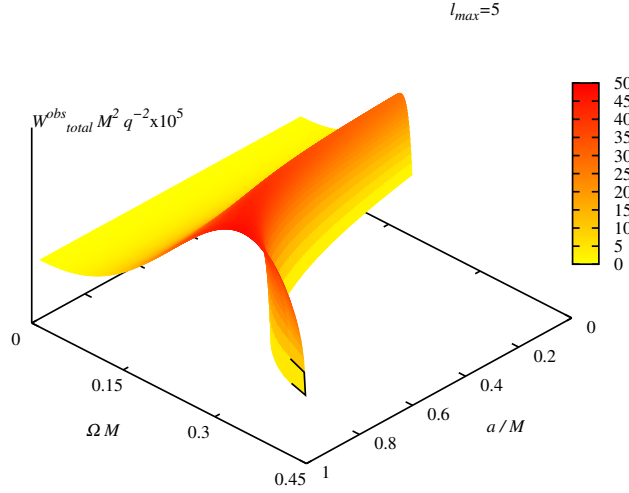


Figure 3.17: Total observed power for direct orbits, as a function of  $a$  and  $\Omega$ , considering angular momentum contributions in Eq. (3.27) up to  $l_{max} = 5$ . The vertical axis gives the intensity of the total observed power ( $W_{total}^{obs} M^2 q^{-2} \times 10^5$ ).

In Figs 3.9-3.12 we plot the power associated with  $in$  and  $up$  modes emitted by the rotating source in retrograde circular orbits as a function of  $\Omega$  and  $a$ . We see from these plots that the behavior of the emitted power in the case of a rotating black hole is very similar to the Schwarzschild case [114]. Moreover, we also see from Figs. 3.9-3.12 that, for a fixed value of  $l = m$ , the maximum of the emitted power always decreases as  $|a|$  increases.

In Figs. 3.13 and 3.14 we plot the total power emitted by the source in direct and retrograde orbits, respectively, considering different values of  $a$  and  $l_{max}$ , with  $l_{max}$  being the upper limit in the  $l$ -summation in Eq. (3.27). As a general behavior, the total emitted power initially grows with  $\Omega$ , reaches a maximum and then decreases as the radius of the orbit approach to the radius of the light-like circular orbit. In the bottom plot of Fig. 3.13 we can see the effect of high-frequency radiation-emission suppression for direct orbits in highly-rotating black holes.

In Figs. 3.15 and 3.16 we plot the ratio between the total power emitted by a source in Kerr spacetime (considering different values of  $a$  and  $l_{max}$ ) and the power emitted by a source in Minkowski spacetime considering Newtonian gravity [114] for direct and retrograde orbits, respectively. We see that this ratio presents a local maximum for high values of  $\Omega$  (and this maximum is bigger for bigger values of  $l_{max}$ ), except for direct orbits around highly-rotating black holes (bottom plot of Fig. 3.15), due to the high-frequency radiation-emission suppression in this case. For retrograde orbits (Fig. 3.16) we see basically the same behavior for all values of  $a$ , corroborating the fact that there is no radiation-emission suppression in the case of relativistic unstable retrograde orbits.

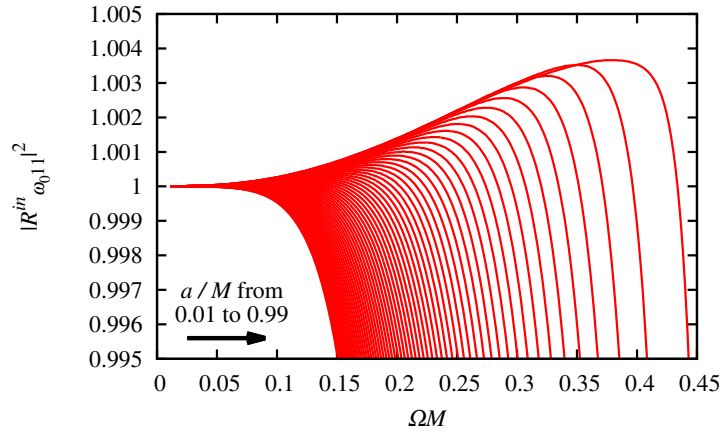


Figure 3.18: Reflection coefficients for  $l = m = 1$ , showing superradiance for the scalar geodesic synchrotron radiation in Kerr spacetime. Each curve corresponds to a reflection coefficient with different value of  $a$ . The maxima of the curves increase as  $a$  increases. The curve with the highest maximum in the plot is the one for  $a = 0.99M$ .

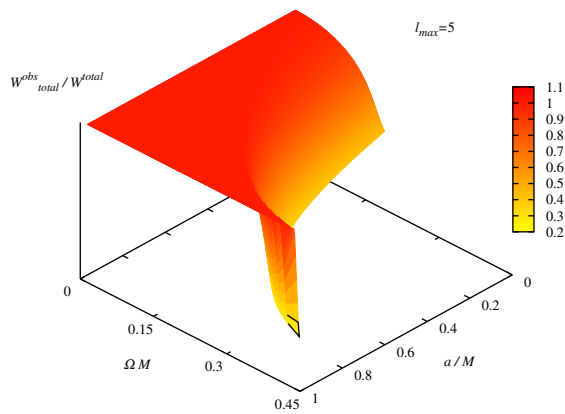


Figure 3.19: Ratio  $W_{total}^{obs}/W^{total}$  plotted as a function of  $\Omega$  and  $a$  for geodesic (stable and unstable) direct circular orbits, considering angular momentum contributions in Eqs. (3.27) and (3.34) up to  $l_{max} = 5$ .

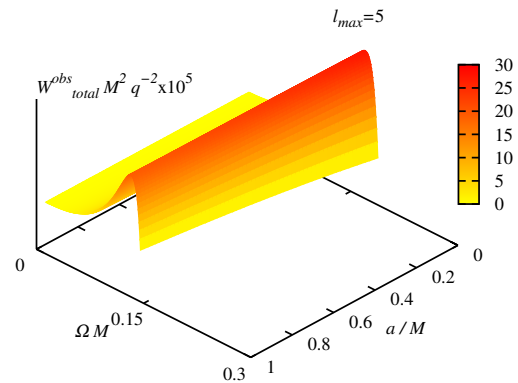


Figure 3.20: Total observed power for retrograde orbits, as a function of  $a$  and  $\Omega$ , considering angular momentum contributions in Eq. (3.27) up to  $l_{max} = 5$ .

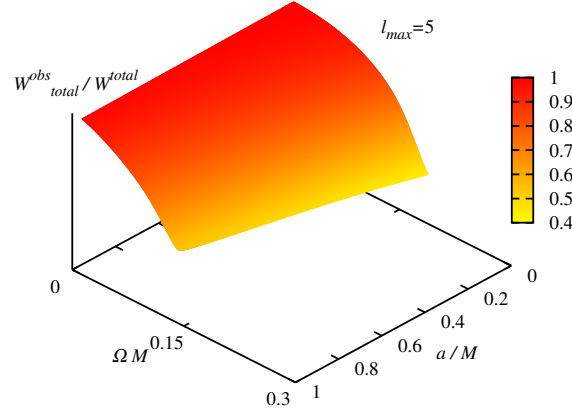


Figure 3.21: Ratio  $W_{total}^{obs}/W_{total}^{total}$  plotted as a function of  $\Omega$  and  $a$  for geodesic (stable and unstable) retrograde circular orbits, considering angular momentum contributions in Eqs. (3.27) and (3.34) up to  $l_{max} = 5$ .

### 3.4.4 Power observed asymptotically

The power which is observed asymptotically, for a fixed value of  $l$  and  $m$ , is given by

$$W_{lm}^{obs} = |\mathcal{R}_{\omega_0 lm}^{in}|^2 W_{lm}^{in} + |\mathcal{T}_{\omega_0 lm}^{up}|^2 W_{lm}^{up}, \quad (3.33)$$

and the total observed power at infinity is

$$W_{total}^{obs} = \sum_{l=1}^{\infty} \sum_{m=1}^l W_{lm}^{obs}. \quad (3.34)$$

In Fig. 3.17 we plot the total observed power for the source in direct orbits, with the summation in Eq. (3.34) performed up to  $l = m = 5$ . We can see that the observed power is larger for larger values of the black hole rotating parameter  $a$ .

One feature of bosonic fields in Kerr spacetime is superradiance [130, 131]. Due to this effect, the reflection coefficient  $|\mathcal{R}_{\omega_0 lm}^{in}|^2$  can be greater than 1 for some values of  $\Omega$ . In Fig. 3.18 we plot the reflection coefficient, for different values of  $a$ , as a function of  $\Omega$ . The superradiance effect is more evident for lower values of  $m$  (we recall that the lowest value for occurrence of this effect is  $m = 1$ ).

Let us now estimate how the superradiance effect affects the asymptotic power. As stated in the previous section, for some values of  $\Omega$  the dominant term of the emitted power is the one related with the  $in$  modes. By ignoring the contribution related with the  $up$  modes, which is negligible in these cases, we obtain

$$\frac{W_{lm}^{obs}}{W_{lm}^{in} + W_{lm}^{up}} \approx |\mathcal{R}_{\omega_0 lm}^{in}|^2, \quad (3.35)$$

resulting in the possibility for the power observed asymptotically to be greater than the power

emitted by the rotating source in direct orbits with  $\Omega < \Omega_+$ , as indeed occurs.

In Fig. 3.19 we show the ratio  $W_{total}^{obs}/W^{total}$ , as a function of  $a$  and  $\Omega$ , for the source rotating in direct orbits. It can be seen that for high enough values of the black hole rotation parameter, the observed power is bigger than the emitted power. It can also be seen that for highly-rotating black holes ( $a \approx M$ ), the absorbed power is only significant for orbits close to the light-like circular orbit.

In Fig. 3.20 we plot the total observed power for the source in retrograde orbits, with the summation in Eq. (3.34) performed up to  $l = m = 5$ . In Fig. 3.21 we show the ratio  $W_{total}^{obs}/W^{total}$ , as a function of  $a$  and  $\Omega$ , for retrograde orbits. When  $|a|$  grows, the portion of the emitted power which is observed asymptotically, related with relativistic orbits, also grows.

As it occurs for the total emitted power, for highly-rotating black holes the asymptotically observed power is negligible for the source in direct circular orbits close to the direct light-like circular orbit. However, for retrograde orbits this does not occur. The power observed at infinity for retrograde orbits grows as the source's orbit approaches the retrograde light-like circular orbit.

### 3.5 Final remarks

We have calculated the radiated power from a scalar source rotating around a Kerr black hole, using the framework of quantum field theory in curved spacetimes at tree level.

We have shown, with numerical calculations, that the black hole rotation considerably affects the power emitted by the orbiting source. The main contribution to the total emitted power comes from the emitted power associated with the  $in$  modes. For the DISCO, the emitted power presents local maxima for intermediate values of  $a$ , while the power emitted in the RISCO always decreases as  $a$  increases. We have also shown that the maxima of the emitted power associated with the  $in$  modes for  $l = m = 1$  increases as  $a$  increases. The emitted power associated with the  $in$  modes for higher values of  $l = m$ , as  $a$  increases, initially increases, reaches a maximum, and then decreases.

We have computed the total power emitted by the rotating source for different values of the black hole rotation parameter  $a$ . We have verified the classical result presented in Ref. [129], obtaining that there is no considerable power emitted by rotating sources in direct orbits in the high-frequency regime for  $a \rightarrow M$  (rapidly rotating black holes). We computed the total power emitted by a source in retrograde orbits, showing that there is no radiation-emission suppression in this case. We also plotted the ratio between the emitted power in the Kerr spacetime and the emitted power in Minkowski spacetime, assuming Newtonian gravity.

We have also computed the amount of power emitted by the rotating source that is observed at infinity. We have shown that most of the emitted radiation goes to infinity. For direct orbits, we obtained that the amount of radiation that escapes to infinity can be bigger than the total emitted power. This amplification of the emitted power is related to superradiance. For the electromagnetic and gravitational fields this effect would be more significant due to the fact that superradiance is more evident in those cases.

## Chapter 4

# On the quasinormal modes of relativistic stars and interacting fields

The study of the natural oscillations of physical systems is of much interest in astrophysics [109, 132]. For relativistic compact objects such as stars and black holes, these natural oscillations are referred to as quasinormal modes (QNMs). QNMs depend only on the system parameters. The waves emitted from the collapse of a star and in the coalescence of binaries have a close relation with the quasinormal modes of the final compact object. The composition of matter forming astrophysical objects is very important for the study of the spacetime oscillations. Indeed, many matter oscillations in Newtonian theory are also present in the general relativistic case [132]. Fluid modes can also be excited, for instance, by a particle moving around the star [133, 134], generating a large dephasing in the gravitational-wave signal (see Chapter 6).

It is also of great interest to study how matter and fields around black holes behave. The presence of matter around black holes can lead to resonances, which were analyzed in detail recently [135]. Scalar fields around rotating Kerr black holes can generate hairy configurations [136] (see also Ref. [137] for a recent review on black holes with scalar hair). Moreover, massive scalar fields can form quasibound states and develop scalar ‘clouds’ around black holes [138, 139]. Notwithstanding, relativistic stars can also present nontrivial gravitating field profiles. For instance, very strong magnetic fields in neutron stars — configurations known as magnetars [140] — have an influence on the shape of the star [141]. Neutron stars can also accrete dark matter, acquiring a core formed by an additional gravitating component [142]. Moreover, stars formed by fundamental fields, like boson stars [51, 143, 144], are also interesting examples of the outcomes of interacting fields within gravity scenarios.

All the above examples share a common feature: They are formed by components (matter and fields) coupled with each other, and such characteristic is crucial for its structure. At infinity, we may have that only gravity survives (through a power decay), or that all fields decouple. Moreover, the coupling between the components also has an effect in the analysis of linear perturbation in such spacetimes. Additional components describing perturbations of relativistic objects can enrich their oscillation spectra, generating distinctive signatures. For instance, the scalar field modes in boson stars can be excited by an orbiting particle (see Chapters 5 and

6). Notwithstanding, the scattering of massive scalar wave packets can carry information about the clouds around black holes [145]. However, it is difficult to analyze the mode behavior of such structures, basically due to the fact that the coupling between the components is highly nontrivial in most cases.

Here we shall discuss two distinct methods to compute the QNMs of field perturbations that interact only in a finite region: the direct integration method and the continued fraction method. The direct integration method discussed here is slightly different from the one presented in Ref. [146]. On the other hand, the continued fraction method is similar to the one discussed in Refs. [147, 148], but we extend it to deal with more general situations. We shall assume that the angular part of the perturbations can be separated so that we end up with a system of  $N$  coupled second order differential equations. Additionally, we assume that the perturbations depend in time as  $e^{-i\sigma t}$ . These assumptions are valid in a wide variety of astrophysical scenarios [109, 135].

The remainder of this chapter is organized as follows: In Sec. 4.1 we describe the direct integration and continued fraction methods to compute the QNMs modes of interacting fields. As an application, in Sec. 4.2 we compare the direct integration and continued fraction methods to compute the QNMs of boson stars. Moreover, we extend the results presented in Ref. [149] (see also Chapter 5) computing the QNMs of mini boson stars as function of the central field and compactness. We show that the  $l = 0$  modes becomes unstable beyond the critical point. In Sec. 4.3 we discuss our results and write our final remarks.

## 4.1 Methods

We generically assume that the perturbation functions can be described by the following set of equations

$$\frac{d^2}{dr_*^2}\Psi(r) + (\sigma^2 - \mathbf{V}(r))\Psi(r) = 0, \quad (4.1)$$

where  $r_*$  is a tortoise radial coordinate,  $\sigma$  is the frequency of the field,  $\Psi(r)$  is a  $N$ -dimensional vector representing the perturbations, and  $\mathbf{V}(r)$  is a  $N \times N$  matrix which can possibly depend on  $\sigma$ . If the components of the perturbation  $\Psi(r)$  are not coupled,  $\mathbf{V}(r)$  is a diagonal matrix. In some scenarios, it may be possible to obtain a set of uncoupled equations for the perturbations performing canonical perturbations within a Hamiltonian framework [150]. But here the only restriction to  $\mathbf{V}(r)$  is that it has a diagonal form for  $r > l_i$ , where  $l_i$  denotes the characteristic range of the interaction between the components of  $\Psi(r)$ .

### 4.1.1 Direct integration method

This method consists of integrating the differential equations from two different regions: near the origin and far from the star, with the proper QNM boundary conditions. The problem of finding the QNM frequencies reduces to find the proper values of  $\sigma$  for which the solutions

obtained integrating from the origin and from infinity are linearly dependent. This method was first used by Chandrasekhar and Detweiler [151], and then applied to uniform density stars to compute the least damped (lowest imaginary part) QNMs [152].

The boundary conditions at the origin, can be written as<sup>1</sup>

$$\Psi(r \sim 0) \sim r^l \sum_{j=0}^{N_0} \mathbf{x}_0^j r^j, \quad (4.2)$$

where  $\mathbf{x}_0^i$  are constant  $N$ -dimensional vectors and the upper summation limit  $N_0$  is chosen so that the boundary conditions converge. Substituting Eq. (4.2) into Eq. (4.1) and expanding around  $r \sim 0$  lead to a recursion relation for the coefficients  $\mathbf{x}_0^i$ , such that all of them can be written as functions of the coefficients  $\mathbf{x}_0^0$ , which is a collection of  $N$  independent numbers. In this way, since the system is linear, we can form a set of  $N$  independent solutions by integrating from the origin by choosing the vector  $\mathbf{x}_0^0$  to be, e.g.,  $(1, 0, \dots, 0)$ ,  $(0, 1, \dots, 0)$ , ..., and  $(0, 0, \dots, 1)$ . The general solution can be achieved by a linear combination of the  $N$  independent solutions, namely,

$$\Psi^-(r) = \sum_{n=1}^N \alpha_n^- \Psi_n^-(r), \quad (4.3)$$

where  $\Psi_n^-$  denotes the  $n$ -th independent solution of Eq. (4.1), obtained by integrating it from the origin. We note that, in the case of BHs, one generally deals with boundary conditions at the event horizon to describe the QNMs, imposing ingoing waves into the BH.

The boundary conditions at infinity, can be written as:

$$\Psi(r \sim \infty) \sim \exp(\pm k(\sigma) r_*) \sum_{j=0}^{N_0} \frac{\mathbf{x}_{\pm, \infty}^j}{r^j}, \quad (4.4)$$

where

$$k_j(\sigma) = \sqrt{V_{jj}(r \rightarrow \infty) - \sigma^2}. \quad (4.5)$$

Depending on  $V_{jj}(r \rightarrow \infty)$  and on the value of the frequency  $\sigma$ , we select the value of the  $\pm$  sign in Eq. (4.4) to suit the particular problem — e.g., for field components that are wavelike at infinity, we require purely outgoing waves  $\Psi_j \sim e^{k_j(\sigma) r_*}$ , and for field components that are bounded we require an exponential damping  $\Psi_j \sim e^{-k_j(\sigma) r_*}$  (see, e.g., Table II of Ref. [149]). Once again,  $\mathbf{x}_{\pm, \infty}^j$  are constant  $N$ -dimensional vectors and the upper summation limit  $N_0$  in Eq. (4.4) has to be chosen according to the precision required. In the same way as for the integration from the origin, we can form a set of  $N$  independent solutions integrated from infinity by choosing different values for  $\mathbf{x}_{\pm, \infty}^0$ . We have that the solution integrated from infinity

<sup>1</sup>The potential  $V(r)$  usually diverges at the origin due to a centrifugal term, and that is the reason of  $r^l$  term in Eq. (4.2), where  $l$  is the angular number of the waves. See, for instance, Chapter 7.

is

$$\Psi^+(r) = \sum_{n=0}^N \alpha_n^+ \Psi_n^+(r), \quad (4.6)$$

where  $\Psi_n^+$  denotes the  $n$ -th independent solution of Eq. (4.1). The QNM solutions are such that  $\Psi^-(r)$  and  $\Psi^+(r)$  are linearly dependent. We have that the QNM frequencies can be found through

$$\begin{aligned} \Psi^-(r)|_{r=R_{\text{ext}}} &= \Psi^+(r)|_{r=R_{\text{ext}}}, \\ \Psi^{-\prime}(r)|_{r=R_{\text{ext}}} &= \Psi^{+\prime}(r)|_{r=R_{\text{ext}}}, \end{aligned} \quad (4.7)$$

where  $R_{\text{ext}} > l_i$ . The conditions (4.7) generate a system of  $2N$  equations for the coefficients  $\alpha_n^\pm$ . Since the system is linear, we can set one of the  $\alpha_n^\pm$  to unity, say, for instance,  $\alpha_0^+ = 1$ . We then use the remaining  $2N - 1$  equations to find the rest of the coefficients as functions of  $\sigma$ . The remaining equation is then used to find the QNM frequencies.

### 4.1.2 Continued fraction method

The continued fraction method is a very powerful technique, with many applications in physics. In the case of QNMs computation, it was first used by Leaver [153], and extensively studied by many authors since then [109]. One of the main difficulties in computing QNMs in the frequency domain is the divergence of the wave functions at large distances. The continued fraction method works extremely well in some cases because it maps the divergent boundary behavior in a specific recurrence relation.

For stellar structures, the continued fraction method is actually a mixed method. Outside the star (vacuum region) we do have a continued fraction solution for the perturbations. However, in order to guarantee that all the proper boundary conditions are satisfied, we have to match continuously this outer solution with the one obtained by integrating the differential equations from the origin, so that the method is a sort of direct integration method from inside the star and a continued fraction method outside the star.

The method presented here is general, and it is very similar to the one shown in Ref. [146] (see also Ref. [154]), with the difference that we extend it to deal with any system of perturbations formed by fields that couple with each other only in a finite region in space. Once again, we shall assume that the system of equations can be described by Eq. (4.1).

Outside the star, the spacetime is described by the Schwarzschild metric. We shall assume that there exists an expansion of the components of the wave vector as follows:

$$\Psi_i^+(r) = \Xi_i(r) \sum_{n=0}^{\infty} a_{i,n} v^n, \quad (4.8)$$

where the index  $i$  denotes the  $i$ -th component of the vector functions and  $v \equiv (1 - b/r)$ , in which  $b$  is chosen such that the series solution (4.8) is convergent [147]. The vector function  $\Xi$  is chosen such that the vector  $\Psi^+$  satisfies the proper boundary conditions at infinity [155] — in general, its components are proportional to  $e^{\pm k_j(\sigma)r^*}$ . Substituting the expansion (4.8) into the differential equation (4.1) generically leads to recurrence relations for the coefficients

$a_{i,n}$  [146, 153]. These could in principle be  $n$ -term recurrence relations, which can be reduced to a three-term recurrence relation by recursive Gaussian elimination steps.

Let us illustrate this procedure by assuming that we end up with a four-term recurrence relation. We have

$$\alpha_n \mathbf{a}_{n+1} + \beta_n \mathbf{a}_n + \gamma_n \mathbf{a}_{n-1} + \delta_n \mathbf{a}_{n-2} = 0, \quad n > 1, \quad (4.9)$$

where  $\alpha_n$ ,  $\beta_n$ ,  $\gamma_n$  and  $\delta_n$  are  $N \times N$  invertible matrices.  $\mathbf{a}_n$  is the vector whose components are the coefficients  $a_{i,n}$  in the expansion (4.8). We can reduce the four-term recurrence relation to a three-term by using a matrix-valued Gaussian elimination step [146]. Using

$$\tilde{\alpha}_n = \alpha_n, \quad (4.10)$$

$$\tilde{\beta}_0 = \beta_0, \quad (4.11)$$

$$\tilde{\gamma}_0 = \gamma_0, \quad (4.12)$$

$$\tilde{\beta}_n = \beta_n - \delta_n [\tilde{\gamma}_{n-1} \tilde{\alpha}_{n-1}]^{-1}, \quad n > 0, \quad (4.13)$$

$$\tilde{\gamma}_n = \gamma_n - \delta_n [\tilde{\gamma}_{n-1} \tilde{\alpha}_{n-1}]^{-1}, \quad n > 0. \quad (4.14)$$

One can show through Eq. (4.9) that the tilde matrices satisfy the following three-term recurrence relation

$$\tilde{\alpha}_n \mathbf{a}_{n+1} + \tilde{\beta}_n \mathbf{a}_n + \tilde{\gamma}_n \mathbf{a}_{n-1} = 0, \quad n > 0. \quad (4.15)$$

Defining a ladder matrix  $\mathbf{R}_n^+$  with the following property

$$\mathbf{a}_{n+1} = \mathbf{R}_n^+ \mathbf{a}_n, \quad (4.16)$$

and using Eq. (4.15), we obtain the following equation:

$$\mathbf{R}_n^+ = - \left[ \tilde{\beta}_{n+1} + \tilde{\alpha}_{n+1} \mathbf{R}_{n+1}^+ \right]^{-1} \tilde{\gamma}_{n+1}. \quad (4.17)$$

Eq. (4.17) may be solved recursively. We can start at some large value of  $n$ , say  $N_0$ , impose  $\mathbf{R}_{N_0}^+ = 0$ , and then, moving backward in  $n$ , determine all  $\mathbf{R}_n^+$ . The result has a form of a continued fraction, justifying the name of the method <sup>2</sup>.

Using Eqs. (4.16) and (4.17), we obtain all  $\mathbf{a}_n$  as functions of  $N$  parameters, given by  $\mathbf{a}_0$ . The expansion (4.8), with the determined coefficients, gives the solution to be used outside the

<sup>2</sup>For instance, if we have just one second order equation, the solution of recurrence (4.17) takes the form

$$R_n^+ = - \frac{\tilde{\gamma}_{n+1}}{\tilde{\beta}_{n+1}-} \frac{\tilde{\alpha}_{n+1} \tilde{\gamma}_{n+2}}{\tilde{\beta}_{n+2}-} \frac{\tilde{\alpha}_{n+2} \tilde{\gamma}_{n+3}}{\tilde{\beta}_{n+3}-} \dots, \quad (4.18)$$

where we used the notation

$$\frac{a}{b-d} \frac{c}{d} \equiv \frac{a}{b-\frac{c}{d}}. \quad (4.19)$$

Table 4.1: Comparison of  $l = 2$  QNMs of boson stars computed through the direct integration and continued fraction methods. In this particular case, the direct integration method is the same as the one used in Ref. [156].

Configurations of Ref. [149]	DI		CF	
Mini-BS I, N=1	0.1195	$-5 \times 10^{-5}i$	0.1186	$-5.3 \times 10^{-5}i$
Mini-BS I, N=2	0.1316	$-2 \times 10^{-5}i$	0.1316	$-2.4 \times 10^{-6}i$
Mini-BS I, N=3	0.1404	$-8 \times 10^{-6}i$	0.1404	$-7.7 \times 10^{-6}i$
Massive-BS I, N=1	$4.03 \times 10^{-2}$	$-2 \times 10^{-5}i$	$4.029 \times 10^{-2}$	$-2.5 \times 10^{-5}i$
Massive-BS I, N=2	$7.16 \times 10^{-2}$	$-2 \times 10^{-6}i$	$7.158 \times 10^{-2}$	$-2.1 \times 10^{-6}i$
Massive-BS I, N=3	$9.47 \times 10^{-2}$	$-5 \times 10^{-7}i$	$9.465 \times 10^{-2}$	$-4.7 \times 10^{-7}i$

star. Therefore, there are  $N$  independent solutions of Eq. (4.1), and the general solution is a linear combination of them, similarly to Eq. (4.6).

We still have to impose that the wave function  $\Psi$  satisfies the proper boundary condition at the origin. For this, we can use the same procedure of Sec. 4.1.2, obtaining  $\Psi^-(r)$ , given by Eq. (4.3).

The QNM frequencies are found requiring that the wave functions obtained from inside and outside to be linearly dependent. Similarly to the direct integration method, we impose Eq. (4.7). Note that the difference between the two methods is that we construct the outer solutions  $\Psi^+$  through the continued fraction approximations. For relativistic fluid stars, in which we have the matter and gravitational components of the perturbations, by a suitable choice of  $b$ , the continued fraction method is basically the same as the one presented in Refs. [147, 148].

## 4.2 Application: Quasinormal modes of boson stars

Here we extend the calculations of Ref. [149], computing the quasinormal modes of boson stars through the continued fraction method. In the case of boson stars, outside an effective radius, the perturbations of the spacetime are well described by a decoupled system — two equations describing the polar and axial part of gravitational perturbations and two equations describing the perturbations of the complex scalar field<sup>3</sup>. The spacetime is described by the Schwarzschild geometry and, therefore, the continued fraction expressions for the wave functions outside the star are the same as in the Schwarzschild case. For the gravitational part of the perturbations, one can construct the continued fraction relation using the Regge-Wheeler equation, and use it to obtain the polar and axial gravitational perturbations [127, 153]. For the scalar field perturbations, we can use the results of Ref. [158].

For the axial sector of the perturbations, the application of the above method is direct, since the equation for the axial perturbations is already in the form (4.1). Moreover, the scalar field perturbations only couples with the polar sector of the perturbations [159, 160].

For the polar sector of the perturbations, the method can be applied using the first order differential equations for the gravitational perturbations presented in Ref. [149] in the following way:

<sup>3</sup>As apparent from [149], although the two equations describing the perturbations for the scalar field are coupled with each other even outside the star, one can always decouple them by a suitable change in the functions. See, e.g., Ref. [157].

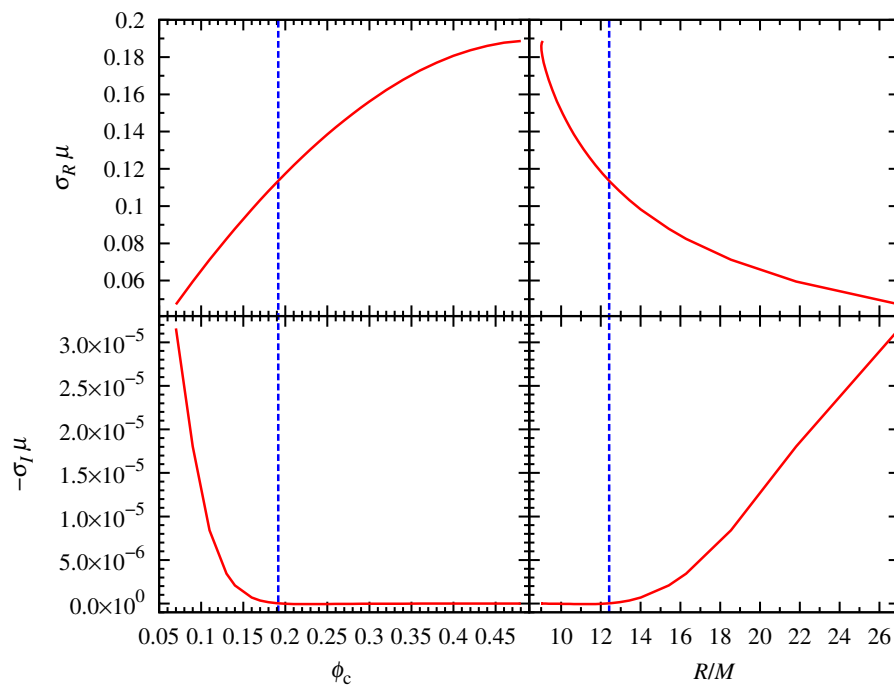


Figure 4.1: Real (top panels) and imaginary (lower panels) parts of the  $l = 0$  (monopole) mode of mini-BSs as a function of the central value of the scalar field (left panels) and of the star radius (right panels). The vertical dashed line indicates the maximum mass configuration.

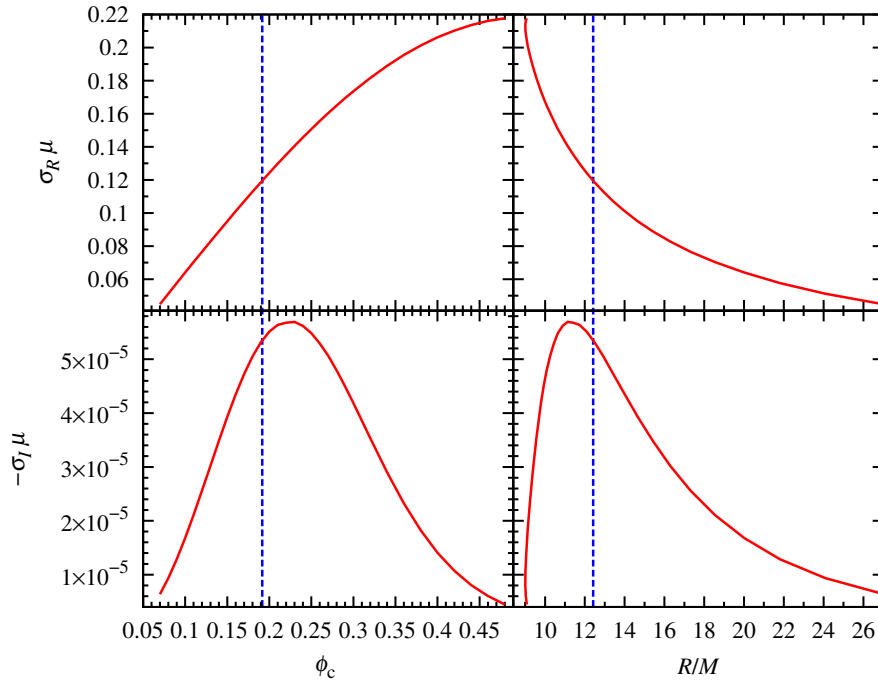


Figure 4.2: Same of Fig. 4.2, but for  $l = 2$  (quadrupole).

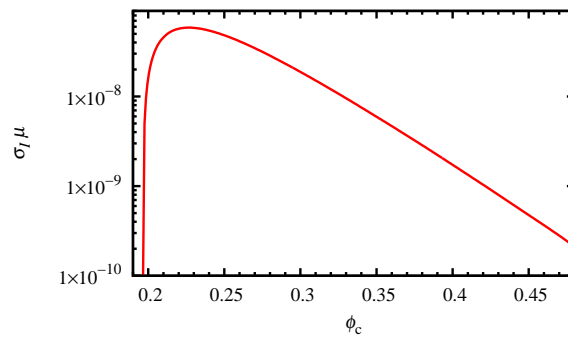


Figure 4.3: Zoom in the range of the unstable  $l = 0$  modes of mini-BSs.

- We solve the differential equations from the origin, choosing the three free parameters such that we obtain the three independent solutions for the metric and scalar field perturbations;
- Using the perturbations obtained by the procedure above, we construct the correspondent Zerilli function  $\Psi_Z$  (which describes the polar gravitational perturbations) of each independent solution. With the independent solutions  $(\Psi_Z, \phi_+, \phi_-)$ , we obtain  $\Psi^-(r)$  [Eq. (4.3)] (see [149] for more details);
- The vector  $\Psi^+(r)$  can be constructed using the continued fraction or the direct integration method. Since the gravitational and scalar part of the perturbations are independent, they can be computed separately;
- Finally, with the vector  $\Psi^+(r)$ , we find the QNMs by matching it with  $\Psi^-(r)$  through Eq. (4.7);

Note that for the polar case, since we are using the Zerilli function, the point  $R$  should be such that the background scalar field at that point is small.

We applied the above procedure and computed the QNMs of boson stars. A comparison between the direct integration procedure, as computed in [149], and the continued fraction method for some boson star configurations is exhibited in TABLE 4.1. Due to the low imaginary part of the modes, the divergence problem of the QNMs is weak and the agreement between the two methods is remarkable. In fact, most of the times, the direct integration method is suitable only to compute the least damped modes of the astrophysical object. Therefore, the very good agreement between the two methods is expected.

In the case of boson stars, the advantage of the continued fraction method over the direct integration one is in the construction of the background solutions. For the direct integration method to work properly, we need to integrate from a point in which  $V(r)$  has approximately a constant value (or zero). This integration from numerical infinity can get very contaminated with errors, such that one generally has to compute the sum in Eq. (4.4) up to typically  $N_0$  15, and the background solutions need to be constructed up to a point far away from the star. On the other hand, the only requirement for the continued fraction method to work properly is that the background scalar field is small enough, and therefore the continued fraction solutions can be constructed in a point relatively close to the star.

Using the continued fraction method, we computed the modes of mini boson stars as a function of the central density and radius of the star, defined as the radial point  $r$  which contains 99% of the star total mass [149]. The results are shown in Figs. 4.1 and 4.2. The monopole mode ( $l = 0$ , Fig. 4.1) exists due to the coupling between the scalar and gravitational perturbations [149, 160]. Interestingly, we can see that, from the behavior of the quadrupole mode ( $l = 2$ , Fig. 4.2), that this quadrupole mode is stable for the range of central densities we investigated. On the other hand, the monopole mode do become unstable for central densities  $\phi \gtrsim \phi_c^{\text{crit}}$ , where  $\phi_c^{\text{crit}}$  is the central density for the maximum mass configuration [51]. This is in accordance with previous works which considered stability of boson stars [161, 162].

### 4.3 Discussion and final remarks

We have analyzed two different methods to compute the QNMs of interacting fields. One of the methods is based on a direct integration of the differential equations and the other is based on an analytical continued fraction scheme to describe the perturbations. The methods can be applied in many astrophysical situations, as in computing relativistic stars modes or in studying stars with nontrivial fields profiles around it.

We applied the direct integration and continued fraction methods to compute the polar QNMs of boson stars. For the modes analyzed, the continued fraction method is in excellent agreement with the direct integration one. Moreover, we computed the modes as a function of the central value of the scalar field, showing that the monopole mode becomes unstable for configurations beyond the critical one.

The results methods presented in this chapter can be of great aid in the computation of QNMs of complicated astrophysical configurations. One limitation of the continued fraction method, however, is in dealing with less compact interacting field profiles, i.e. configurations with higher  $l_i$ . In that case, the integrations from the origin usually grow rapidly as  $r$  increases, and many numerical errors can appear in the matching of the solutions [cf. Eq. (4.7)]. One possible way to circumvent this problem is to mix the direction integration method with the continued fraction one — for instance, one can use the continued fraction expansion as an outer boundary condition for the integration from the infinity, decreasing the errors introduced when using the expansion (4.4).

# Chapter 5

## Astrophysical signatures of boson stars: Quasinormal modes and inspiral resonances

Boson stars (BSs) are compact configurations satisfying the Einstein-Klein-Gordon equations, prevented from total collapse through Heisenberg uncertainty principle (for reviews on the subject see [51, 144, 163]). They have been claimed in the literature as promising horizonless black hole (BH) mimickers, being a possible star candidate for supermassive objects. BSs can be classified [51] according to the scalar potential, namely  $V(\Phi)$  (see Sec. 5.1), in the Klein-Gordon Lagrangian. In this chapter, we shall discuss some of the most popular BS models, namely:

- *Mini boson stars*, for which the scalar potential is given by  $V(\Phi) = \mu^2|\Phi|^2$ , where  $\mu$  is the scalar field mass. The maximum mass for this BS model is given by the so-called Kaup limit  $M_{max} \approx 0.633m_{\text{P}}^2/\mu$ , with  $m_{\text{P}}$  being the Planck mass [143, 164]. For typical values of  $\mu$ , this mass limit is much smaller than the Chandrasekhar limit for a fermion star, approximately  $m_{\text{P}}^3/\mu^2$ . Nevertheless, despite their name, mini BSs may have a total mass compatible with that observed in active galactic nuclei [51]. This happens for ultralight boson masses  $\mu$ , as those motivated by string axiverse scenarios [165].
- *Massive boson stars*. In this model, the scalar potential has an additional quartic scalar field term,  $V(\Phi) = \mu^2|\Phi|^2 + \lambda|\Phi|^4/2$  [166]. Depending on the value of  $\lambda$ , the maximum mass can be comparable to the Chandrasekhar limit. For  $\lambda \gg \mu^2/m_{\text{P}}^2$  one can estimate  $M_{max} \approx 0.062\lambda^{1/2}m_{\text{P}}^3/\mu^2$ .
- *Solitonic boson stars*, for which  $V(\Phi) = \mu^2|\Phi|^2(1 - 2|\Phi|^2/\sigma_0^2)^2$ , where  $\sigma_0$  is a constant [167]. This potential supports confined nondispersive solutions with finite mass, even in absence of gravity. The total mass of the star depends on  $\sigma_0$  and  $M_{max} \approx 0.0198m_{\text{P}}^4/(\mu\sigma_0^2)$ . This model (also known in literature as nontopological solitonic stars)

allows for supermassive objects with  $M \sim 10^6 M_\odot$  even in presence of heavy bosons with  $\mu \sim \sigma_0 \sim 500 \text{ GeV}$ .

Other types of BSs can be obtained using different scalar self-potentials, see Ref. [51] for a more detailed list.

The emission spectra from a simple accretion disk model around BSs was studied in Refs. [168, 169]. It was shown that, depending on the BS model and on the compactness, spherically symmetric massive BSs can be indistinguishable from Schwarzschild BHs. In this sense, BS can supplant BHs as supermassive objects. Ways to discriminate BSs from BHs have been studied in the literature, such as, for instance, the  $K\alpha$  iron line profile from accretion disks [170] (see also [12] for other compact objects) and gravitational lensing [171] (see also Ref. [51]).

Despite the vast existing literature on its dynamical features (cf. the recent review [144]), a detailed study on the astrophysical signatures of BSs in fully relativistic setting is missing. The scope of the present chapter is to fill this gap. We study dynamical BSs in order to identify possible smoking guns of horizonless compact objects and of compact dark matter configurations, extending previous studies in several directions.

After laying down the necessary formalism in Sec. 5.1, we explore the three different types of BSs discussed above in section 5.2. The spacetimes are obtained using the full Einstein's equation, without any approximation scheme. Our results agree very well with the ones presented in the literature [164, 166, 167].

In Sec. 5.3, we characterize circular geodesics in BS spacetimes. In particular, even though a BS does not possess a well defined surface and stable circular geodesics may exist even *inside* the star, we find some upper bound on the angular frequency as measured by (static) asymptotic observers. In Sec. 5.4 we compute the fundamental quasinormal modes (QNMs) of various BS models and show that there exists a class of low-frequency modes. In Sec. 5.5 we show that these modes can be excited by a point-particle in quasicircular geodesic motion. This is a striking difference with the BH case, where QNMs can only be excited by particles plunging into the BH and not during the inspiral.

The results of Sec. 5.4 are complementary to those of Refs. [159, 160], where the QNMs of mini BS configurations were computed using a WKB approximation (see also Ref. [172] where the scalar QNMs of BS models in the probe limit were computed). We extend those results by considering several BS models and by computing the proper modes with more sophisticated methods that do not rely on any approximation scheme. More specifically, we focus on the quasi-bound state modes of the scalar field and we argue that these are generic features of any BS configuration supported by a massive scalar field.

The results of Sec. 5.5 are complementary to – and in fact extend – the work by Kesden *et al.* [173], who calculated the approximated waveforms for gravitational waves emitted by particle inspirals from the Schwarzschild exterior to the interior of a nontopological soliton star. As in Ref. [173] here we have the broad goal of studying gravitational-wave emission by EMRIs around generic horizonless objects. EMRIs are unique probes of the strong-curvature regime of GR and are also perfect testbeds to put constraints on modified theories of gravity (see, e.g., Refs. [174, 175]). In addition to computing the gravitational and scalar energy fluxes in a consistent and fully relativistic approach for several BS models, we find that the absence of the “one-way membrane” (event horizon) opens up the possibility that the free oscillation modes of a BS are measurably different from those of a BH and they can be even resonantly

excited by orbiting point particles. Indeed, we find that orbiting stellar-mass objects around BSs generically excite a multitude of resonant frequencies, *and* give rise to a signal which in its last stages bears no resemblance to chirp or ringdown signals typical of inspirals into BHs. We have discussed the detectability of these resonances in Ref. [156].

Our results might be interesting at various levels but, from a phenomenological standpoint, the main message is that gravitational waves do allow a discrimination between compact objects, in particular between BHs and BSs. In this chapter, we use the signature  $(-, +, +, +)$  for the metric and natural units  $\hbar = c = G = 1$ .

## 5.1 Einstein's equation for a particle orbiting a boson star

BSs are equilibrium self-gravitating solutions of the Einstein-Klein-Gordon theory:

$$S = \int d^4x \sqrt{-g} \left[ \frac{R}{2\kappa} - g^{ab} \partial_a \Phi^* \partial_b \Phi - V(|\Phi|^2) \right] + S_{\text{matter}},$$

where  $\kappa = 8\pi$  and  $S_{\text{matter}}$  denotes the action of any other matter field. From the action above, Einstein's equations read

$$R_{ab} - \frac{1}{2} g_{ab} R = \kappa (T_{ab}^\Phi + T_{ab}^{\text{matter}}), \quad (5.1)$$

where

$$T_{ab}^\Phi = \partial_a \Phi^* \partial_b \Phi + \partial_b \Phi^* \partial_a \Phi - g_{ab} (\partial^c \Phi^* \partial_c \Phi + V(|\Phi|^2)), \quad (5.2)$$

is the energy-momentum of the scalar field. The Klein-Gordon equation reads

$$\frac{1}{\sqrt{-g}} \partial_a (\sqrt{-g} g^{ab} \partial_b \Phi) = \frac{dV}{d|\Phi|^2} \Phi, \quad (5.3)$$

together with its complex conjugate.

### 5.1.1 Background solutions

We will focus exclusively on spherically symmetric BSs and consider the background line element

$$ds_0^2 = -e^{v(r)} dt^2 + e^{u(r)} dr^2 + r^2 (d\theta^2 + \sin^2 \theta d\varphi^2). \quad (5.4)$$

The ansatz for the background scalar field reads [144]

$$\Phi_0(t, r) \equiv \phi_0(r) e^{-i\omega t}, \quad (5.5)$$

where  $\phi_0(r)$  is a real function. Although the scalar field is time-dependent, the Einstein-Klein-Gordon system admits static and spherically symmetric metrics [51, 143, 157, 164, 166, 176]. With the ansatz above, the background field equations, obtained from (5.1)–(5.3), read

$$\frac{1}{r^2} (r e^{-u})' - \frac{1}{r^2} = -\kappa\rho, \quad (5.6)$$

$$e^{-u} \left( \frac{v'}{r} + \frac{1}{r^2} \right) - \frac{1}{r^2} = \kappa p_{\text{rad}}, \quad (5.7)$$

$$\phi_0'' + \left( \frac{2}{r} + \frac{v' - u'}{2} \right) \phi_0' = e^u (U_0 - \omega^2 e^{-v}) \phi_0, \quad (5.8)$$

where a prime denotes derivative with respect to  $r$ ,  $U_0 = U(\phi_0)$  and  $U(\Phi) = dV/d|\Phi|^2$ . In the equations above, the density  $\rho$ , the radial pressure  $p_{\text{rad}}$ , and the tangential pressure  $p_{\text{tan}}$  are given in terms of the stress-energy tensor of the scalar field,  $T^{\Phi}_{ab}$ . More specifically,

$$\rho \equiv -T^{\Phi}_t{}^t = \omega^2 e^{-v} \phi_0^2 + e^{-u} (\phi_0')^2 + V_0, \quad (5.9)$$

$$p_{\text{rad}} \equiv T^{\Phi}_r{}^r = \omega^2 e^{-v} \phi_0^2 + e^{-u} (\phi_0')^2 - V_0, \quad (5.10)$$

$$p_{\text{tan}} \equiv T^{\Phi}_\theta{}^\theta = \omega^2 e^{-v} \phi_0^2 - e^{-u} (\phi_0')^2 - V_0. \quad (5.11)$$

where  $V_0 = V(\phi_0)$ . Unlike the case of perfect fluid stars, the complex scalar field behaves like an anisotropic fluid,  $p_{\text{rad}} \neq p_{\text{tan}}$ . Equations (5.6)–(5.8) can be solved numerically with suitable boundary conditions (see Sec. 5.2) to obtain the background metric and scalar field configuration.

### 5.1.2 Perturbations

We are interested in the free oscillation spectrum of a BS as well as in the scalar field and metric perturbations induced by test-particles on geodesic motion in the spherically symmetric spacetime described above. At first order in the perturbations, the metric reads

$$g_{ab} = g_{ab}^{(0)} + h_{ab}, \quad (5.12)$$

where  $g_{ab}^{(0)}$  is given in Eq. (5.4). In the Regge-Wheeler gauge [177], using a Fourier expansion, the first order perturbation  $h_{ab}$  separates into the axial sector

$$h_{ab}^{\text{axial}} = \sum_{l \geq |m|} \int d\sigma \begin{pmatrix} 0 & 0 & -\frac{1}{\sin\theta} h_0(r) \partial_\varphi & \sin\theta h_0(r) \partial_\theta \\ \star & 0 & -\frac{1}{\sin\theta} h_1(r) \partial_\varphi & \sin\theta h_1(r) \partial_\theta \\ \star & \star & 0 & 0 \\ \star & \star & \star & 0 \end{pmatrix} \times Y^{lm} e^{-i\sigma t} \quad (5.13)$$

and polar sector

$$h_{ab}^{polar} = \sum_{l \geq |m|} \int d\sigma \begin{pmatrix} e^v H_0(r) & i\sigma H_1(r) & 0 & 0 \\ \star & e^u H_2(r) & 0 & 0 \\ \star & \star & r^2 K(r) & 0 \\ \star & \star & \star & r^2 \sin^2 \theta K(r) \end{pmatrix} \times Y^{lm} e^{-i\sigma t}, \quad (5.14)$$

where  $Y^{lm} \equiv Y^{lm}(\theta, \varphi)$  are the usual scalar spherical harmonics. Each metric and scalar field perturbation, e.g.  $h_0(r)$ , explicitly depends on the frequency  $\sigma$  and on the wave numbers  $l$  and  $m$ . The  $\star$ -symbol indicates the symmetric components, such that  $h_{ab} = h_{ba}$ .

At first order, the scalar field reads  $\Phi = \Phi_0 + \delta\Phi$  where  $\Phi_0$  is the background scalar field defined above and

$$\delta\Phi = \sum_{l \geq |m|} \int d\sigma \frac{\phi_+(r)}{r} Y^{lm} e^{-i(\sigma+\omega)t}, \quad (5.15)$$

$$\delta\Phi^* = \sum_{l \geq |m|} \int d\sigma \frac{\phi_-(r)}{r} Y^{lm} e^{-i(\sigma-\omega)t}. \quad (5.16)$$

Note that the ansatz above differs from that used in Refs. [159, 160]. The scalar field potential can be written as

$$V = V_0 + \sum_{l \geq |m|} \int d\sigma \delta V(r) Y^{lm} e^{-i\sigma t}. \quad (5.17)$$

Likewise, for the first derivative

$$\frac{dV}{d|\Phi|^2} = U_0(r) + \sum_{l \geq |m|} \int d\sigma \delta U(r) Y^{lm} e^{-i\sigma t}. \quad (5.18)$$

In the presence of matter fields other than the complex scalar, also  $T_{ab}^{\text{matter}}$  has to be expanded in tensorial harmonics [178, 179]. In the time domain, the matter stress-energy tensor of a particle in the  $\theta = \pi/2$  plane reads

$$T_{ab}^{\text{matter}} = \mu_p \frac{\dot{x}_a(t) \dot{x}_b(t)}{r_p(t)^2 \dot{x}^t(t)} e^{-\frac{1}{2}(v+u)} \times \delta(r - r_p(t)) \delta(\cos \theta) \delta(\varphi - \varphi_p(t)),$$

where  $\dot{x}^a \equiv (\dot{t}_p, \dot{r}_p, 0, \dot{\phi}_p)$  and  $\mu_p$  are the particle's four-velocity and mass, respectively.

### Axial Sector

As discussed in Ref. [159], perturbations of the scalar field have even parity, so they couple only with polar gravitational perturbations. Thus, gravitational axial perturbations decouple and they are described by the linearized Einstein's equations (5.1), namely:

$$e^{-u}h'_1 + i\sigma e^{-v}h_0 + \frac{1}{2}\kappa(p_{\text{rad}} - \rho)h_1 + \frac{2}{r^2}m(r)h_1 = P_{\sigma lm}, \quad (5.19)$$

$$-i\sigma h'_0 + \frac{2i\sigma}{r}h_0 - \left[ \sigma^2 - \frac{e^v}{r^2}(l(l+1) - 2) \right] h_1 = P_{\sigma lm}^r, \quad (5.20)$$

$$i\sigma h'_1 + h''_0 - \frac{1}{2}\kappa r e^u(\rho + p_{\text{rad}})(h'_0 + i\sigma h_1) + \frac{2i\sigma}{r}h_1 + h_0 e^u \left[ \kappa(p_{\text{rad}} + \rho) - \frac{l(l+1)}{r^2} + \frac{4m(r)}{r^3} \right] = P_{\sigma lm}^t, \quad (5.21)$$

where we have defined

$$e^{-u(r)} \equiv 1 - 2m(r)/r, \quad (5.22)$$

and  $m(r)$  is the mass function which denotes the total mass within a sphere of radius  $r$ . From Eq. (5.6), we get

$$m(r) = \frac{\kappa}{2} \int_0^r \rho(x) x^2 dx, \quad (5.23)$$

and the total mass of the star is given by  $M \equiv m(r \rightarrow \infty)$ . In the equations above, the  $P_{\sigma lm}$ 's are source terms which depend on the particle's stress-energy tensor and they are explicitly given, e.g., in Ref. [175]. We can also define  $h_1(r)$  in terms of the Regge-Wheeler function,

$$h_1(r) = -e^{\frac{1}{2}(u-v)} r \Psi_{RW}(r). \quad (5.24)$$

Substituting the relation above into Eq. (5.19), the function  $h_0(r)$  can be written in terms of  $\Psi_{RW}$  as

$$h_0(r) = -\frac{i}{\sigma} e^{\frac{1}{2}(v-u)} \frac{d}{dr} [r \Psi_{RW}(r)] - \frac{i}{\sigma} e^v P_{\sigma lm}(r). \quad (5.25)$$

Equations (5.19)-(5.21) are not all independent, due to the Bianchi identities. Indeed, they are equivalent to a single Regge-Wheeler equation for  $\Psi_{RW}$ , namely:

$$\left[ \frac{d^2}{dr_*^2} + \sigma^2 - V_{RW}(r) \right] \Psi_{RW}(r) = S_{RW}(r), \quad (5.26)$$

where  $r_*$  is the Regge-Wheeler coordinate, defined through  $dr_* = e^{(u-v)/2}dr$ ,  $V_{RW}(r)$  is the Regge-Wheeler potential

$$V_{RW}(r) = e^v \left[ \frac{l(l+1)}{r^2} - \frac{6m(r)}{r^3} - \frac{\kappa}{2}(p_{\text{rad}} - \rho) \right], \quad (5.27)$$

and  $S_{RW}(r)$  is the source term

$$S_{RW} = \frac{e^{\frac{1}{2}(v-u)}}{r} \left[ \frac{2e^v}{r} \left( 1 - \frac{rv'}{2} \right) P_{\sigma lm} - e^v P'_{\sigma lm} + P^r_{\sigma lm} \right].$$

Note that the homogeneous Regge-Wheeler equation (5.26) with the potential (5.27) is equivalent to that of a isotropic, perfect-fluid star with pressure equals to  $p_{\text{rad}}$  [132, 180, 181].

### Polar Sector

The equations for the polar sector are more involved. Following Zerilli [178], the linearized Einstein's equations read

$$\begin{aligned} & K' + \frac{K}{2r} (3 - e^u (1 + r^2 \kappa p_{\text{rad}})) + \frac{H_1}{2r^2} (l(l+1) - 2r^2 \kappa (p_{\text{tan}} + \rho)) - \frac{H_0}{r} \\ & + \frac{\kappa}{r^2 \sigma} [r((\sigma + \omega)\phi_+ + (\sigma - \omega)\phi_-)\phi'_0 + \omega\phi_0 (\phi_+ - \phi_- - r\phi'_+ + r\phi'_-)] \\ & = \frac{1}{\sigma} A^{(1)}(\sigma, r) - 2rF(\sigma, r), \end{aligned} \quad (5.28)$$

$$\begin{aligned} & H'_0 + \frac{K}{2r} (3 - e^u (1 + r^2 \kappa p_{\text{rad}})) - \frac{H_0}{r} (2 - e^u (1 + r^2 \kappa p_{\text{rad}})) \\ & + \frac{1}{2} H_1 \left( \frac{l(l+1)}{r^2} - 2e^{-v} \sigma^2 - 2\kappa (p_{\text{tan}} + \rho) \right) \\ & + \frac{\kappa}{r^2 \sigma} [r((\omega - \sigma)\phi_+ - (\omega + \sigma)\phi_-)\phi'_0 + \omega\phi_0 (\phi_+ - \phi_- - r\phi'_+ + r\phi'_-)] \\ & = \frac{1}{\sigma} A^{(1)}(\sigma, r) + B(\sigma, r) - rF(\sigma, r) (1 - e^u (1 + r^2 \kappa p_{\text{rad}})), \end{aligned} \quad (5.29)$$

$$\begin{aligned} & H'_1 + (H_0 + K)e^u + \frac{H_1}{r(r-2m)} (2m - r^3 \kappa V_0) - \frac{2\kappa}{r\sigma} e^u \omega \phi_0 (\phi_+ - \phi_-) \\ & = \frac{e^u}{\sigma} B^{(0)}(\sigma, r) + 2r^2 e^u F(\sigma, r), \end{aligned} \quad (5.30)$$

where the source terms  $A^{(1)}$ ,  $F$ ,  $B$  and  $B^{(0)}$  read

$$A^{(1)}(\sigma, r) = \frac{\kappa}{2\sqrt{2\pi}} \int dt A_{lm}^{(1)}(r, t) e^{i\sigma t}, \quad (5.31)$$

$$F(\sigma, r) = \frac{\kappa}{2\pi} \sqrt{2 \frac{(l-2)!}{(l+2)!}} \int dt F_{lm}(r, t) e^{i\sigma t}, \quad (5.32)$$

$$B(\sigma, r) = \frac{\kappa r}{\sqrt{2l(l+1)\pi}} \int dt B_{lm}(r, t) e^{i\sigma t}, \quad (5.33)$$

$$B^{(0)}(\sigma, r) = \frac{\kappa r}{\sqrt{2l(l+1)\pi}} \int dt B_{lm}^{(0)}(r, t) e^{i\sigma t}, \quad (5.34)$$

and the functions  $A_{lm}^{(1)}(r, t)$ ,  $F_{lm}(r, t)$ ,  $B_{lm}(r, t)$  and  $B_{lm}^{(0)}(r, t)$  for the Schwarzschild background are explicitly given in Ref. [179]. In the background (5.4), these functions can be computed in a similar fashion and they reduce to those in Ref. [179] in the vacuum case. We have also used that

$$H_2 = H_0 - 2r^2 F(\sigma, r), \quad (5.35)$$

which is obtained from the Einstein's equations. The scalar field perturbations are governed by the following inhomogeneous equations:

$$\left[ \frac{d^2}{dr_*^2} + (\sigma \pm \omega)^2 - \tilde{V} \right] \phi_{\pm}(r) = -\tilde{S}_{\pm} \quad (5.36)$$

where

$$\begin{aligned} \tilde{V} &= e^v \left( \frac{l(l+1)}{r^2} + \frac{2m}{r^3} + U_0 - \kappa V_0 \right), \\ \tilde{S}_{\pm} &= \frac{e^{-u}\sigma}{2} [2r(\sigma \pm 2\omega)\phi'_0 \pm \omega(4 - e^u r^2 \kappa(p_{\text{rad}} + \rho))\phi_0] H_1 \\ &\pm r\omega\phi_0 [(\sigma \pm 2\omega)H_0 + \sigma K + e^{-u}\sigma H'_1] \\ &+ e^v r [e^{-u}(K' - H'_0)\phi'_0 - (U_0 H_0 + \delta U)\phi_0] \\ &+ r^3 F \left[ \phi_0(2e^v U_0 - \omega(2\omega \mp \sigma)) + e^{v-u}\phi'_0 \left( \frac{2}{r} + \frac{F'}{F} \right) \right]. \end{aligned}$$

Therefore, the polar sector is described by three first-order Einstein equations coupled to two second-order scalar equations. There exists an algebraic relation between  $K$ ,  $H_0$  and  $H_1$  that can be used to eliminate one of the gravitational perturbations. Finally, the system can be reduced to three coupled second order differential equations. This is in contrast with the case of perfect-fluid stars, where the polar sector is described by a system of two second-order equations [132, 182, 183]. Here, rather than working with three second order equations, we shall use the system

of equations given by Eqs. (5.28)–(5.30) and (5.36).

## 5.2 Solving the background equations

In this section we construct spherically symmetric BS models by solving numerically the background equations (5.6)–(5.8). After imposing suitable boundary conditions, the background equations form an eigenvalue problem for the frequency  $\omega$ , which we solve using a standard shooting method [184]. We integrate Eqs. (5.6)–(5.8) from the origin, where we require regularity

$$u(r \sim 0) = 0, \quad (5.37)$$

$$v(r \sim 0) = v_c, \quad (5.38)$$

$$\phi_0(r \sim 0) = \phi_c, \quad (5.39)$$

$$\phi'_0(r \sim 0) = 0. \quad (5.40)$$

The value  $v_c$  is arbitrary because it can be adjusted by a time-reparametrization in order to impose asymptotic flatness, i.e.  $v(r \rightarrow \infty) = 0$ . In practice, to increase accuracy of the numerical integration, we have considered a higher order expansion near the origin which, at first order, reduces to the equations above. At infinity, we impose the metric to be Minkowski and the scalar field to be vanishing:

$$\phi_0(r \rightarrow \infty) = 0. \quad (5.41)$$

For each value of  $\phi_c$ , the boundary condition above is satisfied by a discrete set of eigenfrequencies  $\omega$ . We focus here on BS background solutions in the ground state, which correspond to the scalar profile having no nodes and to the lowest eigenfrequency  $\omega$ . The overtones correspond to excited states that would decay to the ground state through emission of scalar and gravitational radiation [185]. Note that, depending on the specific BS model, the shooting procedure can be challenging, due to singularities that appear in the integration if the trial frequency  $\omega$  is not sufficiently close to the eigenfrequency. In many cases, a precise and tedious fine tuning is necessary. Furthermore, due to the presence of a mass term in the scalar potential, the scalar field has a Yukawa-like behavior,  $(e^{-\sqrt{\mu^2 - \omega^2} r_*})/r$  at large distances  $r_* \mu \gg 1$  [51]. This makes the integration particularly challenging at large distances.

By adopting the procedure above, we can obtain a one-parameter family of solutions, the parameter being the central value of the scalar field  $\phi_c$ . For each configuration, the total mass of the BS is  $M = m(r \rightarrow \infty)$ . Contrarily to the case of perfect-fluid stars, BSs do not possess a well defined surface as the scalar field spreads all over the radial direction. However, due to the exponential suppression, the configuration is highly localized in a radius  $\sim 1/\mu$ . It is thus useful to define an effective radius for the compact configuration. We shall define the effective radius  $R$  such that  $m(R)$  corresponds to 99% of the total mass  $M$ . Other inequivalent definitions have been considered in the literature, see e.g. Ref. [51] for a discussion.

In the following, we describe each of the BS models we have considered, namely: mini

Table 5.1: (Adapted from Ref. [156]) BS models used in this chapter. For massive BS configurations we used  $\tilde{\lambda} = 100$ , whereas both solitonic BS models have  $\sigma_0 = 0.05$ . The significant digits of  $\tilde{\omega}$  do not represent the numerical precision, but they show the fine tuning needed to achieve the solutions.

	$\tilde{\phi}_c$	$\tilde{\omega}$	$\tilde{M}$	$\tilde{R}$	$M\omega$	$R/M$
mini BS I	0.1916	0.853087	0.63300	7.86149	0.54000	12.4194
mini BS II	0.4101	0.773453	0.53421	4.52825	0.41319	9.03368
massive BS I	0.094	0.82629992558783	2.25721	15.6565	1.86513	6.9362
massive BS II	0.155	0.79545061700675	1.92839	11.3739	1.53394	5.8981
solitonic BS I	1.05	0.4868397896964082036868178070	1.847287	5.72982	0.89933	3.1017
solitonic BS II	1.10	0.4931624243761699601334882568	1.698627	5.08654	0.83770	2.9945

BSs, massive BSs and solitonic BSs. A summary of the configurations used in this chapter is presented in Table 5.1 (adapted from Ref. [156]). For each BS model, we have selected two stellar configurations. The first configuration corresponds to the maximum total mass of the model, which corresponds to the critical point diving stable and unstable configurations. The second configuration corresponds to the maximum compactness, defined as  $M/R$ . Note that the maximum compactness configuration generally occurs for values of  $\phi_c$  which are larger than those corresponding to the maximum mass. Therefore, the second configuration is usually in the unstable branch of solutions (cf. e.g. Ref. [69]).

### 5.2.1 Mini boson stars

In this model the scalar potential reads

$$V(|\Phi|^2) = \mu^2 |\Phi|^2. \quad (5.42)$$

This is one of the simplest potentials that can support self-gravitating configurations. The name comes from the fact that the maximum mass achieved in this model is smaller than the Chandrasekhar limit for the same particle mass although, for ultralight bosonic fields [165], it can still reproduce supermassive astrophysical objects. In order to compare with Refs. [159, 160], we rescale the equations as:

$$r \rightarrow \frac{\tilde{r}}{\mu}, \quad m(r) \rightarrow \frac{\tilde{m}(\tilde{r})}{\mu}, \quad \omega \rightarrow \tilde{\omega}\mu, \quad \phi_0(r) \rightarrow \frac{\tilde{\phi}_0(\tilde{r})}{\sqrt{4\pi}}.$$

The rescaled background profiles (metric functions and the scalar field) for the two configurations listed in Table 5.1 are shown in the left panels of Fig. 5.1. The metric functions for these configurations are also compared with the Schwarzschild black hole ones.

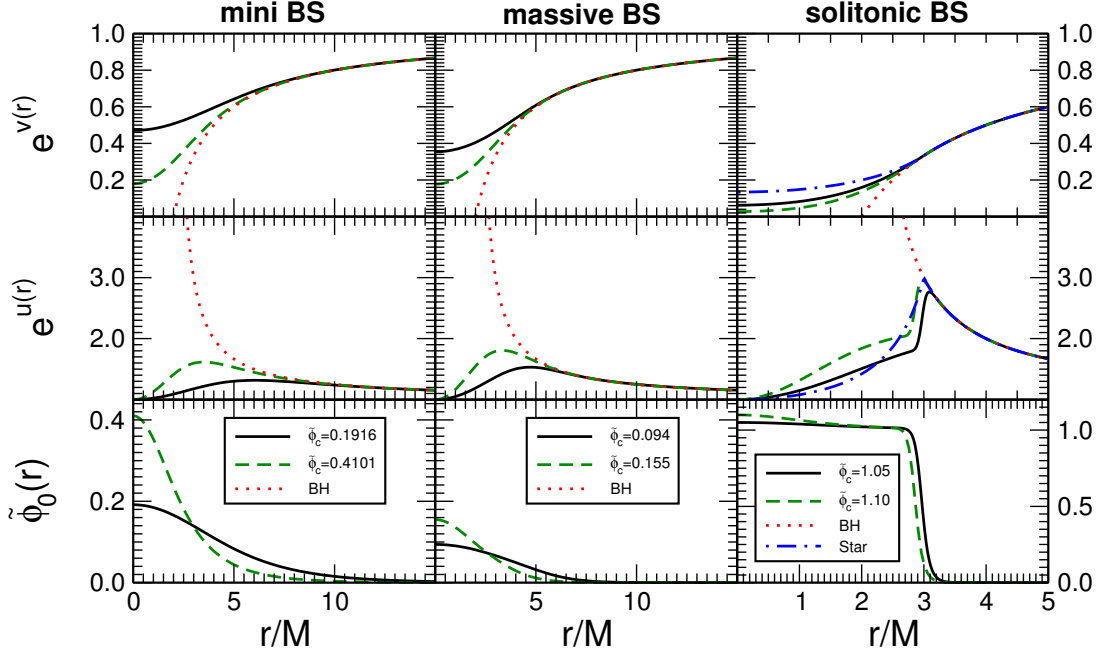


Figure 5.1: Rescaled background profiles for different BS models and configurations (cf. Table 5.1). In the top, middle and lower row we show the metric elements  $e^v$ ,  $e^u$  and the scalar profile  $\tilde{\phi}_0$ , respectively. Each column refers to a different BS model. From left to right: mini BS, massive BS and solitonic BS. For each model, we compare the metric profiles to those of a Schwarzschild BH and for the solitonic BS model we also compare to the metric elements of a uniform density star with  $R = 3M$ .

## 5.2.2 Massive boson stars

For this model the potential has a quartic interaction:

$$V(|\Phi|^2) = \mu^2 |\Phi|^2 + \frac{\lambda}{2} |\Phi|^4, \quad (5.43)$$

where  $\lambda$  is a constant. This potential was studied in Ref. [166], where it was shown that the model may differ considerably from the mini BS case, even when  $\lambda \ll 1$ . Also, the maximum mass increases with  $\lambda$ , being comparable with the Chandrasekhar limit. For the case of massive BSs, in order to facilitate the comparison with the results in Ref. [166], we have performed the following rescaling:

$$\begin{aligned} r &\rightarrow \frac{\tilde{r}}{\mu}, & m(r) &\rightarrow \frac{\tilde{m}(\tilde{r})}{\mu}, & \omega &\rightarrow \tilde{\omega}\mu, \\ \lambda &\rightarrow 8\pi\mu^2\tilde{\lambda}, & \phi_0(r) &\rightarrow \frac{1}{2\sqrt{2\pi}}\tilde{\phi}_0(\tilde{r}). \end{aligned} \quad (5.44)$$

The maximum compactness for solutions of this model increases with  $\lambda$ , and we found results in agreement with previous calculations [169, 186]. Here, we fixed  $\tilde{\lambda} = 100$  and considered two configurations as summarized in Table 5.1. The metric and scalar field profiles for this model

are shown in the middle panels of Fig. 5.1.

### 5.2.3 Solitonic boson stars

The scalar potential for this configuration is given by

$$V(|\Phi|^2) = \mu^2 |\Phi|^2 (1 - 2|\Phi|^2/\sigma_0^2)^2, \quad (5.45)$$

where  $\sigma_0$  is a constant, generically taken to be of the same order as  $\mu$  [167, 187]. This is the simplest potential that can generate, in the absence of gravity, nontopological solitonic solutions, i.e., nondispersive scalar field solutions. In this case, it is convenient to rescale the equations in units of  $\Lambda\mu$ , with  $\Lambda = \kappa^{1/2}\sigma_0$ . We use [167, 173]

$$\begin{aligned} r &\rightarrow \frac{\tilde{r}}{\Lambda\mu}, & m(r) &\rightarrow \frac{\tilde{m}(\tilde{r})}{\Lambda\mu}, \\ \omega &\rightarrow \tilde{\omega}\Lambda\mu, & \phi_0(r) &\rightarrow \frac{\sigma_0\tilde{\phi}_0(\tilde{r})}{\sqrt{2}}. \end{aligned}$$

The field equations for the solitonic potential are stiff and the scalar field has a very steep profile across a surface layer of thickness  $\sim \mu^{-1}$ . This stiffness makes the numerical integration particularly challenging and, in Refs. [167, 173], spherically symmetric solutions to this model were constructed only perturbatively, in the limit  $\sigma_0 \ll m_{\text{p}}$  and considering a step-function profile for the scalar field. One advantage of that approach is that the approximate solution has a well-defined radius and that, because the scalar profile is given, only the metric equations have to be solved numerically in the interior of the star. The solution is then matched with a Schwarzschild exterior.

However, besides the challenging technicalities in the integration, there is no real need to obtain approximate solutions, which neglect the backreaction between metric functions and the scalar field. Here, we have constructed solitonic BS solutions to the *full* nonlinear system (5.6)–(5.8), i.e. without any approximation (cf. also Refs. [188] where similar solutions were constructed using relaxation methods). This requires high-precision numerical schemes and an extremely fine-tuned shooting method, as shown by the fine tuning needed to find a solution (cf. Table 5.1). In the small  $\sigma_0$  limit, our results agree remarkably well with the approximate solutions presented in Refs. [167, 173] and they extend those results to generic values of the parameters in the scalar potential (5.45).

Unlike the other cases explored in this chapter, solitonic BSs can be very compact, with the radius of the star comparable to or smaller than the Schwarzschild light-ring [167, 173]. In the right panels of Fig. 5.1 we compare the metric components to those of a Schwarzschild spacetime and of the uniform density stars with  $R = 3M$  and we show the steep profile of the scalar field. The scalar field approximates a step function, in agreement with the approximate solution of Refs. [167, 173]. In that case,  $e^{u(r)}$  is discontinuous at the star surface. In our case there is no actual radius, and  $e^{u(r)}$  is continuous, although it has a sharp peak close to the effective radius of the star.

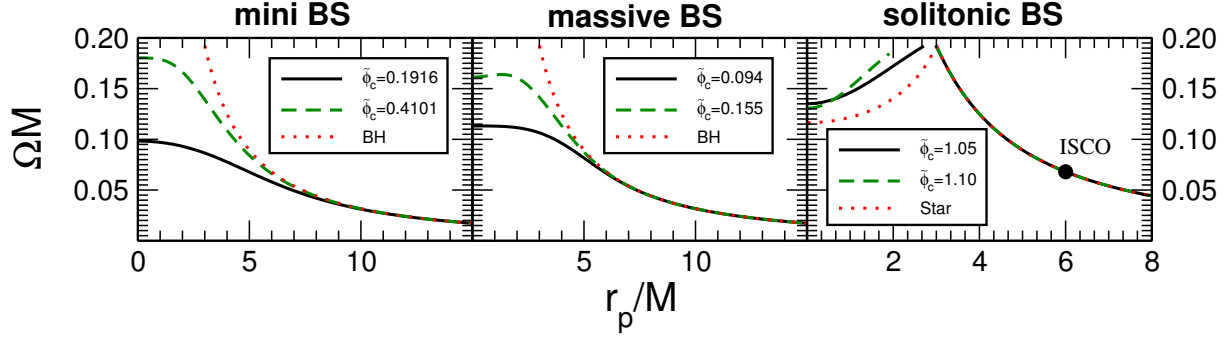


Figure 5.2: (Adapted from Ref. [156]) Angular velocity for timelike circular geodesic motion for the different BS models and configurations specified in Table 5.1. Each plot refers to a different BS model. From left to right: mini BS, massive BS and solitonic BS. For mini and massive BSs, we compare the angular velocity to those of a Schwarzschild BH and for the solitonic BS model we compare to the case of a uniform density star with  $R = 3M$ . In the solitonic case, the marker indicates the innermost stable circular orbit for the Schwarzschild BH, which is given by  $r = 6M$  and  $M\Omega_{isco} \approx 0.068$ .

### 5.3 Geodesics around boson stars

Stellar-size objects gravitating around supermassive BSs have a small back-reaction on the geometry and to leading order in the object's mass move along geodesics of the BS background. Accordingly, gravitational-wave emission by such binaries requires a knowledge of the geodesic motion, in which we now focus. We will also concentrate exclusively on circular, geodesic motion. The reasoning behind this is that it makes the calculations much simpler, while retaining the main features of the physics. Furthermore, it can be shown that generic eccentric orbits get circularized by gravitational-wave emission in vacuum [189] and in the presence of accretion and gravitational drag [156], on a time scale that depends on the mass ratio.

We follow the analysis by Chandrasekhar [127] (see also Ref. [190], where the formalism for a generic background is presented, and Ref. [191] for a recent work on geodesics in BS spacetimes). Following previous studies [168, 169, 173], we assume that the point-particle is not directly coupled to the background scalar field. We start by defining the Lagrangian of the particle motion on the  $\theta = \pi/2$  plane:

$$2\mathcal{L}_p = \dot{s}^2 = -e^v \dot{t}^2 + e^u \dot{r}^2 + r^2 \dot{\varphi}^2. \quad (5.46)$$

The conserved energy  $E$  and angular momentum parameter per unit rest mass  $L$  and can be obtained via

$$E = -\frac{\partial \mathcal{L}_p}{\partial \dot{t}} = e^v \dot{t}, \quad L = \frac{\partial \mathcal{L}_p}{\partial \dot{\varphi}} = r^2 \dot{\varphi}. \quad (5.47)$$

From these equations, we get the following equation of motion

$$e^{u+v} \dot{r}^2 = E^2 - V_{eff}(r) = E^2 - e^v \left( 1 + \frac{L^2}{r^2} \right). \quad (5.48)$$

The energy and angular momentum of the particle in circular orbits follow from Eq. (5.48) by imposing  $\dot{r}|_{r=r_p} = 0$  and  $\ddot{r}|_{r=r_p} = 0$  resulting:

$$E_c = \left[ e^v \frac{2(r-2m)}{2r - \kappa r^3 p_{\text{rad}} - 6m} \right]_{r=r_p}^{1/2} \quad (5.49)$$

$$L_c = \left[ r^2 \frac{(\kappa r^3 p_{\text{rad}} + 2m)}{2r - \kappa r^3 p_{\text{rad}} - 6m} \right]_{r=r_p}^{1/2}, \quad (5.50)$$

where the background Einstein's equations were used to eliminate metric derivatives. Circular null geodesics correspond to  $2r - \kappa r^3 p_{\text{rad}} - 6m = 0$ . Finally, the orbital frequency of circular geodesics reads

$$\Omega = \left[ \frac{e^v (\kappa r^3 p_{\text{rad}} + 2m)}{2r^2 (r - 2m)} \right]_{r=r_p}^{1/2}. \quad (5.51)$$

The angular velocity of circular geodesics in BS spacetimes are shown in Fig. 5.2. Up to the innermost stable circular orbit of a Schwarzschild spacetime,  $r = 6M$ , the angular velocities are very close to their Schwarzschild counterpart with the same total mass, as might be expected since these are very compact configurations. For geodesics at  $r < 6M$  the structure can be very different. A striking difference is that stable circular timelike geodesics exist for BSs even well deep into the star [156, 168, 169].

Solitonic BSs can become truly relativistic gravitating objects. For these objects, an outer last stable circular orbit exists at  $r \approx 6M$  and  $M\Omega_{\text{isco}} \approx 0.068$ . This is expected, as the spacetime is very close to Schwarzschild outside the solitonic BS effective radius. We also find a first (unstable) light-ring at roughly  $r_{l_+} \approx 3M$ . The unexpected feature is the presence of a second *stable* light-ring at  $r_{l_-} < r_{l_+}$ , together with a family of stable timelike circular geodesics all the way to the center of the star. These light-rings are genuine relativistic features, which was not reported in previous studies, as far as we are aware. Uniform density stars, depending on their compactness, also present two light-ring and stable circular timelike orbits in their interior. In the right panel of Fig. 5.2 it is also shown the case of a uniform density star with radius  $R = 3M$ . In that case, the two light-rings degenerate in the star surface. What makes solitonic BSs stand out is the possibility that inspiralling matter couples weakly to the solitonic BS scalar field and therefore has access to these geodesics, although as we showed in Ref. [156] (also in Chapter 6), inspiralling BHs in principle do *not* follow these geodesics. Furthermore, we found no circular orbits between the outer and the inner light-ring, whereas all circular orbits are stable inside the inner light-ring.

Finally, deep inside the BSs, the circular geodesics are non-relativistic. In fact, the velocity as measured by static observers at infinity and by static observers at fixed  $r$ , decreases to zero as the radius approaches zero. In this regime, other dissipative effects such as gravitational drag and accretion onto the small compact object have to be considered [156].

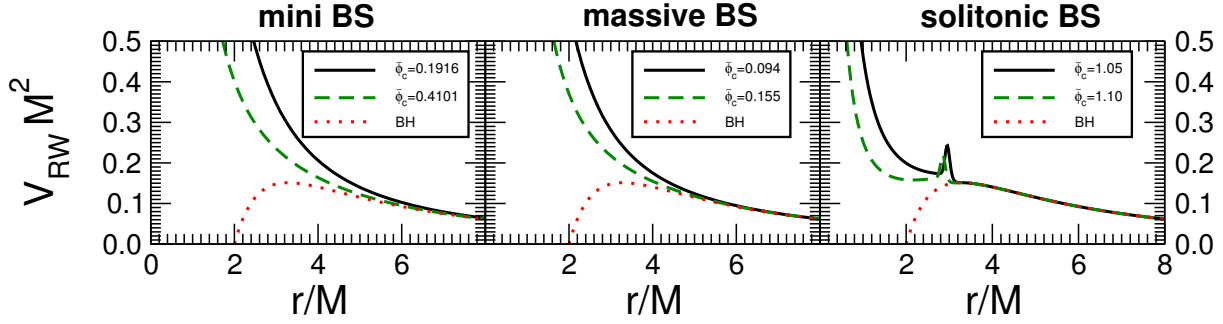


Figure 5.3: Regge-Wheeler potential for the mini BS, massive BS and solitonic BS models compared to that of the Schwarzschild BH for  $l = 2$ .

## 5.4 Quasinormal modes of boson stars

In this section we discuss the quasinormal modes (QNMs) of the BS models presented in the previous sections. QNMs are complex eigenfrequencies  $\sigma = \sigma_R + i\sigma_I$  of the linearized homogeneous perturbation equations supplied with physically motivated boundary conditions (see e.g. [109, 132]). Since the perturbations of a spherically symmetric spacetime naturally divide into an axial and a polar sector, there exist two different classes of modes, which we shall refer to as axial and polar modes, respectively.

Unlike the case of a Schwarzschild BH [127], the axial and the polar BS modes are not isospectral. As we shall discuss, the BS QNMs can be understood in analogy to the modes of ordinary stars, with the background scalar field playing the role of an anisotropic fluid. The main difference with the case of ordinary stars is that a BS does not have a proper surface and that scalar perturbations, unlike their fluid counterpart, can propagate to infinity. In the following, we shall treat axial and polar modes separately.

### 5.4.1 Axial quasinormal modes

As discussed in Sec. 5.1.2, the source-free ( $S_{RW} = 0$ ) axial perturbations can be reduced to the homogeneous Regge-Wheeler equation

$$\left[ \frac{d^2}{dr_*^2} + \sigma^2 - V_{RW}(r) \right] \Psi_{RW}(r) = 0, \quad (5.52)$$

where  $V_{RW}$  is defined in Eq. (5.27) and it is shown in Fig. 5.3 for some BS model and for the case of a Schwarzschild BH. Note that Eq. (5.52) does not involve scalar field perturbations, in analogy to the fluid perturbations of an ordinary star, which are only coupled to the polar sector. This decoupling led Yoshida et al. [160] to assume that the axial sector of BSs is “not coupled to gravitational waves” and therefore not interesting. However, we show here that BS models generically admit axial QNMs, in analogy to the  $w$ -modes of ordinary stars which are in fact curvature modes similar to those of a BH (see Ref. [132] for a review). Moreover, for ultracompact stars ( $R < 3M$ ), a potential well appears in the Regge-Wheeler potential,

generating the possibility of having trapped QNMs, which are long-lived modes [152, 192]. In Sec. 5.5, we shall also show that axial perturbations with odd values of  $l + m$  are sourced by point-particles orbiting the BS and therefore they contribute to the gravitational-wave signal emitted during the inspiral.

At the center of the star, we require regularity of the Regge-Wheeler function,

$$\Psi_{RW}(r \approx 0) \sim r^{l+1} \sum_{i=0}^N a_0^{(i)} r^i, \quad (5.53)$$

where the coefficients  $a_0^{(i)}$  can be obtained by solving the Regge-Wheeler equation order by order near the origin. At infinity, the solution of Eq. (5.52) is a superposition of ingoing and outgoing waves. QNMs are defined by requiring purely outgoing waves at infinity, i.e.

$$\Psi_{RW}(r \rightarrow \infty) \sim e^{i\sigma r_*} \sum_{i=0}^N \frac{a_\infty^{(i)}}{r^i}, \quad (5.54)$$

where again the coefficients  $a_\infty^{(i)}$  can be obtained perturbatively. In the following we discuss two different methods to compute BS axial modes.

### Axial quasinormal modes via continued fractions

In Ref. [160], the polar modes of some mini BS configurations were computed using a WKB approximation. Here, we resort to a continued fraction method [153] adapted from the studies of ordinary stars as showed in Refs. [147, 193] (see also Ref. [154] in which the same method was applied to gravastars).

First, we write the solution of the homogeneous Regge-Wheeler equation in a power-series expansion of the form

$$\Psi_{RW}(r) = (r - 2M)^{2iM\sigma} e^{i\sigma r} \sum_{n=0}^{\infty} a_n z^n, \quad (5.55)$$

where  $z \equiv 1 - R_2/r$ , and  $r = R_2$  is some point outside the stellar object (in our case will be outside the effective radius). The expansion coefficients  $a_n$  are found to satisfy a four-term recurrence relation of the form:

$$\begin{aligned} \alpha_1 a_2 + \beta_1 a_1 + \gamma_1 a_0 &= 0, & n = 1, \\ \alpha_n a_{n+1} + \beta_n a_n + \gamma_n a_{n-1} + \delta_n a_{n-2} &= 0, & n \geq 2, \end{aligned} \quad (5.56)$$

where:

$$\begin{aligned}
\alpha_n &= n(n+1)(R_2 - 2M), \quad n \geq 1, \\
\beta_n &= 2n(-3Mn + R_2(n - iR_2\sigma)), \quad n \geq 1, \\
\gamma_n &= 6M((n-1)n - 1) + (1+l-n)(l+n)R_2, \\
\delta_n &= 2M(3-n)(1+n), \quad n \geq 2.
\end{aligned} \tag{5.57}$$

Since the Regge-Wheeler equation is homogeneous, the coefficient  $a_0$  is an arbitrary normalization constant. The ratio  $a_1/a_0$  can be determined by imposing the continuity of  $\Psi_{RW}$  and  $\Psi'_{RW}$  at  $r = R_2$ . From Eq. (5.55) it follows that:

$$\frac{a_1}{a_0} = \frac{R_2}{\Psi_{RW}(R_2)} \left[ \Psi'_{RW}(R_2) - \frac{i\sigma R_2}{R_2 - 2M} \Psi_{RW}(R_2) \right]. \tag{5.58}$$

As in the case of ordinary stars, the values of  $\Psi_{RW}(R_2)$  and  $\Psi'_{RW}(R_2)$  are obtained by integrating numerically the Regge-Wheeler equation in the interior. Leaver [194] has shown that the four-term recurrence relation (5.56) can be reduced to a three-term recurrence relation by a gaussian elimination step and solved by standard methods [109] (see also Ref. [154] for a more detailed discussion). The complex roots of the continued fraction relation are the QNMs of the BS.

### Axial quasinormal modes via direct integration

In some cases, QNMs can be computed via direct integration [146, 151]. This method is not particularly well-suited, because radial QNM functions grow exponentially as  $r \rightarrow \infty$  and become very sensitive to numerical errors [109]. However, it is possible to integrate Eq. (5.52) up to moderately large values of  $r$  and to minimize the truncation errors by considering a large number of terms in the series expansion (5.54). In our code, we typically considered  $N = 15$  in Eq. (5.54) and integrated up to  $r \sim 30M$ . This would suppress truncation errors at the level of  $10^{-15} \sim 10^{-22}$ .

The method is a simple extension of the case of uniform density stars [151, 152, 192]. We perform two integrations of Eq. (5.52): one from the center of the star with the boundary condition (5.53) up to  $r_m$ , and another from  $r_\infty$  with the boundary condition (5.54) until  $r_m$ . The wavefunctions constructed this way have the correct boundary conditions both at the origin and at infinity. However, for generic values of the frequency  $\sigma$  the Regge-Wheeler function is not continuous at the matching point  $r = r_m$ . We define the jump at  $r_m$  as [151]

$$\Delta_m(\sigma) \equiv \left[ \frac{d\Psi_{RW}/dr_*}{\Psi_{RW}} \right]_- - \left[ \frac{d\Psi_{RW}/dr_*}{\Psi_{RW}} \right]_+, \tag{5.59}$$

where the “minus” and “plus” subscripts denote evaluation at  $r = r_m$  from the left and from the right, respectively. The axial QNMs are obtained as the roots of  $\Delta_m(\sigma)$ . Due to the numerical inaccuracies discussed above, this procedure becomes less accurate for modes with large

imaginary part. For example it can be used to obtain only the first few tones of a Schwarzschild BH [151].

A similar procedure can be adopted in the case of ordinary stars, this time by requiring that the Wronskian of the two solutions (those constructed by integrating from the center and from infinity) is vanishing at the star surface. This is equivalent to requiring continuity of the wavefunction and of its first derivative. To test our code, we successfully found some of the modes presented in Refs. [152, 192] for constant density stars, whose background metric coefficients can be determined analytically (see Appendix C). For all modes computed by direct integration, we have checked the stability of the results under variation of the parameters  $r_m$  and  $r_\infty$ . We stress that, at variance with continued fraction techniques, the direct integration is only accurate when  $\sigma_I \ll \sigma_R$ , mainly because of the exponential radial divergence of the QNMs.

### 5.4.2 Polar quasinormal modes

As discussed in Sec. 5.1.2, the polar sector can be reduced to a system of three coupled second order differential equations: two for the scalar field perturbations  $\phi_\pm$  and one for gravitational perturbations described by a modified Zerilli equation. In practice, in the interior of the object it is more convenient to solve directly for the polar perturbation functions,  $K$ ,  $H_0$  and  $H_1$ , which are described by three first order differential equations and by an algebraic relation.

As in the axial case, at the origin we require regularity of the perturbations and we can expand them in powers of  $r$  as

$$X(r \approx 0) \sim r^l \sum_{i=0}^N x_0^i r^i, \quad (5.60)$$

where  $X$  collectively denotes  $H_2 = H_0, K, H_1$  and  $\phi_\pm$ . It is straightforward to show that this expansion near the center only depends on three free parameters.

At infinity, the background scalar field vanishes and gravitational and scalar perturbations decouple [160].

Let us now discuss the asymptotic behavior of the gravitational field. In vacuum, all polar metric perturbations can be written in terms of one single function which obeys the Zerilli equation,

$$\left[ \frac{d^2}{dr_*^2} + \sigma^2 - V_Z(r) \right] \Psi_Z = 0, \quad (5.61)$$

where  $dr/dr_* = 1 - 2M/r$ ,

$$V_Z(r) = \frac{dr}{dr_*} \frac{2\tilde{\Lambda}^2 r^2 (3M + (\tilde{\Lambda} + 1)r) + 18M^2 (\tilde{\Lambda}r + M)}{r^3 (\tilde{\Lambda}r + 3M)^2}, \quad (5.62)$$

and  $\tilde{\Lambda} = (l-1)(l+2)/2$ . The generic solution at infinity is a superposition of outgoing and incoming waves:

$$\Psi_Z(r \rightarrow \infty) \sim A_{\text{out}} e^{i\sigma r_*} + A_{\text{in}} e^{-i\sigma r_*}, \quad (5.63)$$

and again the standard QNM condition requires  $A_{\text{in}} = 0$  [109]. The metric perturbations can be written in terms of the Zerilli function through the following equations:

$$\begin{aligned} H_1 &= -\frac{\tilde{\Lambda}r^2 - 3\tilde{\Lambda}Mr - 3M^2}{(r-2M)(\tilde{\Lambda}r+3M)}\Psi_Z - r^2\frac{d\Psi_Z/dr_*}{r-2M}, \\ K &= \frac{\tilde{\Lambda}(\tilde{\Lambda}+1)r^2 + 3M\tilde{\Lambda}r + 6M^2}{r^2(\tilde{\Lambda}r+3M)}\Psi_Z + \frac{d\Psi_Z}{dr_*}, \\ H_0 &= H_2 = \frac{\tilde{\Lambda}r(r-2M) - \sigma^2r^4 + M(r-3M)}{(r-2M)(\tilde{\Lambda}r+3M)}K \\ &\quad + \frac{M(\tilde{\Lambda}+1) - \sigma^2r^3}{r(\tilde{\Lambda}r+3M)}H_1. \end{aligned}$$

The asymptotic behavior of the scalar field perturbations is more involved. In vacuum, the equations for the scalar perturbations (5.36) reduce to

$$\left[ \frac{d^2}{dr_*^2} + (\sigma \pm \omega)^2 - V_\phi(r) \right] \phi_\pm = 0, \quad (5.64)$$

where

$$V_\phi(r) = \left(1 - \frac{2M}{r}\right) \left(\mu^2 + \frac{l(l+1)}{r^2} + \frac{2M}{r^3}\right). \quad (5.65)$$

The asymptotic solution for the scalar perturbations reads

$$\phi_\pm(r \rightarrow \infty) \sim B_\pm e^{-k_\pm r_*} r^{\nu_\pm} + C_\pm e^{k_\pm r_*} r^{-\nu_\pm}, \quad (5.66)$$

where we have defined  $\nu_\pm = M\mu^2/k_\pm$  and

$$k_\pm = \sqrt{\mu^2 - (\sigma \pm \omega)^2}. \quad (5.67)$$

Without loss of generality, we choose the root such that  $\text{Re}[k_\pm] > 0$ . Different physically motivated boundary conditions are possible for the scalar field, depending on the sign of the imaginary part of  $k_\pm$ ,  $\text{Im}[k_\pm] \sim -(\sigma_R \pm \omega)\sigma_I$ . As usual, a purely outgoing-wave boundary condition at infinity, i.e.  $\phi_\pm \sim e^{i|\text{Im}[k_\pm]|r_*}$ , defines the QNMs. On the other hand, due to the presence of the mass term it is possible to have quasi bound-state modes, i.e. states that are spatially localized within the vicinity of the compact object and decay exponentially at spatial infinity [195–197]. Therefore, quasi bound-states are simply defined by  $C_\pm = 0$ . In the case at hand, the QNM conditions depend on  $\sigma_R$  and on  $\sigma_I$ , as shown in Table 5.2 where all cases are listed. In the following, we detailed the QNM condition for stable and unstable modes.

Let us start discussing the boundary conditions for stable modes ( $\sigma_I < 0$ ). When  $\sigma_R > \omega$  the QNM condition is the same for both scalar perturbations,  $B_\pm = 0$ . However, if  $\sigma_R < \omega$ , the QNM condition for the scalar fields perturbations is different, being  $B_+ = 0$  and  $C_- = 0$ . Note

Table 5.2: Possible boundary conditions at infinity for the scalar field perturbations  $\phi_{\pm}$  with eigenfrequency  $\sigma = \sigma_R + i\sigma_I$ .

	$\sigma_I$	$\sigma_R$	$\text{Im}[k_{\pm}]$	QNM condition	Bound-state condition
I	stable, $\sigma_I < 0$	$\sigma_R > \omega$	$\text{Im}[k_+] > 0, \text{Im}[k_-] > 0$	$B_+ = 0, B_- = 0$	$C_+ = 0, C_- = 0$
II	stable, $\sigma_I < 0$	$\sigma_R < \omega$	$\text{Im}[k_+] > 0, \text{Im}[k_-] < 0$	$B_+ = 0, C_- = 0$	$C_+ = 0, C_- = 0$
III	unstable, $\sigma_I > 0$	$\sigma_R > \omega$	$\text{Im}[k_+] < 0, \text{Im}[k_-] < 0$	$C_+ = 0, C_- = 0$	$C_+ = 0, C_- = 0$
IV	unstable, $\sigma_I > 0$	$\sigma_R < \omega$	$\text{Im}[k_+] < 0, \text{Im}[k_-] > 0$	$C_+ = 0, B_- = 0$	$C_+ = 0, C_- = 0$

that in this case the stable QNMs of  $\phi_-$  decay exponentially and degenerate with the bound-state modes.

For unstable modes ( $\sigma_I > 0$ ) the situation is different. In this case when  $\sigma_R > \omega$ , the QNM condition is the same for both scalar perturbations,  $C_{\pm} = 0$  and coincide with the bound-state conditions. However, when  $\sigma_R < \omega$  the QNM conditions read  $C_+ = 0$  and  $B_- = 0$ , so that only the unstable QNM of  $\phi_+$  degenerate with the bound-state condition.

This peculiar behavior is due to the presence of a mass term (which allows for bound states) *and* of a complex background scalar field,  $\omega \neq 0$ , which essentially shifts the real part of the frequency of the scalar perturbations. Note that in the case of probe complex scalars around a Schwarzschild BH, the terms introduced by  $\omega$  can be eliminated by a simple shift of the wave frequency, but in the case at hand this term is physical because of the coupling to the gravitational perturbations.

### Polar QNMs via direct integration

Computing the polar modes of a BS is particularly challenging. To compute the polar QNMs of perfect fluid stars the usual continued fraction method proved to be very robust. However, unlike the case of ordinary stars, BSs do not possess a surface where fluid perturbations vanish. In order to understand this issue, let us briefly review the case of ordinary stars [147, 193]. In that case polar QNMs are found by first solving a boundary problem in the interior of the star, requiring the perturbations to be regular at the center and the pressure perturbations to be vanishing at the surface of the star. For any given frequency, this procedure singles out one solution that satisfies the correct boundary condition in the interior and it allows to construct the Zerilli function  $\Psi_Z$  at the radius of the star. Then, Chandrasekhar transformations [127] are used to transform the Zerilli function into the Regge-Wheeler function  $\Psi_{RW}$  and, finally, the continued fraction method can be implemented as explained above for the axial case.

Contrarily to the case of fluid perturbations in ordinary stars, in the BS cases the matter perturbations (scalar field perturbations) propagate in vacuum and, strictly speaking, there is no exterior Schwarzschild solution in which the linear dynamics is simply governed by a single Regge-Wheeler equation. This prevents a direct extension of this method.

To circumvent this problem, we opted for direct integration techniques, which we now describe. The system of linearized perturbation equations can be written as a first order system for the sixth dimensional vector  $\Psi = (H_1, K, \phi_+, \phi_-, \phi'_+, \phi'_-)$ . We perform two integrations: one from the origin and one from infinity, in both cases imposing suitable boundary conditions as discussed above. It is easy to show that, for each integration, there exists a three-parameter family of solutions, corresponding to three independent parameters of the near-origin and near-

infinity expansions. Then, we construct the linear combinations

$$\Psi_- = \alpha_1^{(-)}\Psi_1^{(-)} + \alpha_2^{(-)}\Psi_2^{(-)} + \alpha_3^{(-)}\Psi_3^{(-)}, \quad (5.68)$$

$$\Psi_+ = \alpha_1^{(+)}\Psi_1^{(+)} + \alpha_2^{(+)}\Psi_2^{(+)} + \alpha_3^{(+)}\Psi_3^{(+)}, \quad (5.69)$$

where  $\alpha_i^{(\pm)}$  are constants and  $\Psi_-$  and  $\Psi_+$  refer to the integration from the origin and from infinity, respectively. The subscripts 1, 2 and 3 refer to three linear independent solutions of the homogeneous system. Since the system of equations is linear, we have the freedom to set one of the coefficients  $\alpha_i^{(\pm)}$  of the linear combination to unity. The other five coefficients can be obtained by requiring  $\Psi_- = \Psi_+$  at some arbitrary matching point. For a generic frequency, only five out of the six components of  $\Psi$  can be matched smoothly. Finally, the eigenfrequency of the problem is obtained by requiring that also the remaining component is continuous. In practice, for each frequency  $\sigma$  we can perform six numerical integrations of the linear system, construct the linear combinations above, obtain the coefficients  $\alpha_i^{(\pm)}$  and compute the jump of the only discontinuous component of  $\Psi$  at the matching point. Then, a standard shooting method can be implemented to obtain the complex eigenfrequency. Similarly to the direct integration discussed in the axial case, this method provides accurate results only when  $\sigma_I \ll \sigma_R$ .

### 5.4.3 Results for boson star quasinormal modes

Using the methods described above, we have computed axial and polar modes of several BS models in a fully relativistic setting, i.e. without using any approximation method. As shown in Table 5.2, the spectrum of BS polar modes is fairly rich. Here, we focus on the least damped modes, i.e. those with the smallest imaginary part, which are expected to dominate the ringdown waveform at late time [109]. Note that, for all BS models we have investigated, there exists a class of much longer lived modes than that considered in Ref. [160]. We also shown the modes in units of  $M$ , for future comparisons. In the tables,  $N \geq 1$  is the overtone number.

For the axial modes, we have used the continued fraction method and, for the modes with  $\sigma_I \ll \sigma_R$ , we independently confirmed the results by using a direct integration method. The direct integration works better for compact configurations like the solitonic BSs, which share many similarities with compact uniform density stars. The least damped axial QNMs of solitonic BSs are presented in Table 5.3, comparing the results of the two different methods.

Note that this class of BS modes is qualitatively similar to the  $w$ -modes of constant density stars with comparable compactness [132]. Computing the modes for the mini BS and massive BS models is more challenging, because the imaginary part of these modes is comparable to the real part. In this case, a direct integration method becomes inaccurate. On the other hand, for these cases, we have successfully implemented the continued fraction method discussed above. Some modes for the mini BS model and the massive BS model are presented in Table 5.4. We note that, according to Ref. [147], the value of  $R_2$  in the expansion (5.55) cannot be completely arbitrary. In fact, it has to be slightly larger than the BS effective radius, in order to obtain a stable mode. This introduces an intrinsic inaccuracy in the BS QNMs computed with the continued fractions. Indeed, at  $r = R_2$  the background scalar field is not exactly vanishing

Table 5.3: Axial QNMs for solitonic BS configuration I and II for  $l = 1$  and  $l = 2$ . Here we compare the results obtained through the continued fraction and the direct integration methods.

Continued fraction						Direct integration	
Model	N	$\text{Re}(\sigma) [\Lambda^2 \mu]$	$-\text{Im}(\sigma) [\Lambda^2 \mu]$	$\text{Re}(M\sigma)$	$-\text{Im}(M\sigma)$	$\text{Re}(\sigma) [\Lambda^2 \mu]$	$-\text{Im}(\sigma) [\Lambda^2 \mu]$
$l = 1$							
solitonic BS I	1	0.22328867	0.08370555	0.412478	0.154628	0.22329050	0.08370789
solitonic BS I	2	0.38509593	0.10287792	0.711383	0.190045	0.38509593	0.10287792
solitonic BS I	3	0.55353269	0.11432831	1.022530	0.211197	0.55353269	0.11432831
solitonic BS II	1	0.20007784	0.06608236	0.339858	0.112249	0.20007454	0.06608373
solitonic BS II	2	0.32840222	0.08229700	0.557833	0.139792	0.32840223	0.08229700
solitonic BS II	3	0.46744415	0.09216367	0.794014	0.156552	0.46744415	0.09216367
$l = 2$							
solitonic BS I	1	0.25636868	0.05347247	0.47358	0.098779	0.25636863	0.05347248
solitonic BS I	2	0.32633835	0.10252772	0.60284	0.189398	0.32633833	0.10252773
solitonic BS I	3	0.47822011	0.10629265	0.88341	0.196353	0.47822011	0.10629266
solitonic BS II	1	0.26620716	0.02511717	0.452187	0.0426647	0.26620715	0.02511717
solitonic BS II	2	0.32967926	0.08729943	0.560002	0.148289	0.32967925	0.08729944
solitonic BS II	3	0.41859619	0.08681748	0.711039	0.147471	0.41859618	0.08681749

Table 5.4: Axial QNMs of mini BS and massive BS configurations for  $l = 1$  and  $l = 2$ , computed by a continued fraction method.

$l = 1$						$l = 2$			
Model	N	$\text{Re}(\sigma) [\mu]$	$-\text{Im}(\sigma) [\mu]$	$\text{Re}(M\sigma)$	$-\text{Im}(M\sigma)$	$\text{Re}(\sigma) [\mu]$	$-\text{Im}(\sigma) [\mu]$	$\text{Re}(M\sigma)$	$-\text{Im}(M\sigma)$
mini BS I	1	0.136	0.254	0.085	0.160	0.277	0.388	0.175	0.246
mini BS I	2	0.316	0.388	0.200	0.245	0.456	0.374	0.289	0.237
mini BS II	1	0.297	0.296	0.158	0.158	0.452	0.552	0.242	0.295
mini BS II	2	0.725	0.457	0.387	0.244	0.721	0.456	0.385	0.244
massive BS I	1	0.228	0.207	0.515	0.468	0.225	0.197	0.507	0.444
massive BS I	2	0.416	0.184	0.940	0.415	0.375	0.180	0.847	0.408
massive BS II	1	0.264	0.213	0.508	0.410	0.260	0.204	0.502	0.395
massive BS II	2	0.473	0.190	0.913	0.366	0.437	0.182	0.844	0.351

and the recursion relations (5.56) are not exactly satisfied. This error decreases for compact configurations, because the scalar field decays faster. In our calculations, we used  $R_2 = 1.4R$  and checked the accuracy of the method by changing the location of  $R_2$  in the range  $1.3M$  to  $1.5M$ . We estimate an error of a few percents in the values presented in Table 5.4.

Let us now discuss the polar modes, which show a much richer structure due to the coupling between gravitational and scalar perturbations. Some of these modes were computed in Ref. [160] using a WKB approximation, for the cases in which  $\mu < (\sigma \pm \omega)$  (cf. Eq. (5.67)). In this case, both gravitational and scalar perturbations behave as outgoing waves at infinity. However, this restriction prevents the existence of quasi-bound state modes for the scalar field perturbations, which are expected to dominate in the late time signal. Here we focus on this complementary regime, where scalar perturbations admit localized states (cf. Table 5.2). We have obtained the fundamental modes of our BS models using the direct integration method described above. A selection of the results is presented in Table 5.5. For the solitonic BS polar modes, due to the precision needed for the background, a precise root finder method was not possible, making the modes more inaccurate than the mini and massive BS cases.

In Tables 5.4–5.5 we also show the  $l = 1$  axial modes and the  $l = 0$  polar modes, respectively. Given the quadrupolar nature of GR, in the Schwarzschild case the  $l = 0, 1$  perturbations are simply associated to infinitesimal changes in the mass and in the angular momentum, respectively [177, 178]. However, due to the coupling with the scalar field, for BSs these modes become part of the spectrum and are associated to monopole and dipole emission.

Finally, by comparing the real part of the polar modes shown in Table 5.5 with the orbital

Table 5.5: Polar QNMs of mini BS, massive BS and solitonic BS configurations for  $l = 0$  (left), and  $l = 2$  (right), computed by a direct integration method.

Model	N	$l = 0$				$l = 2$			
		$\text{Re}(\sigma) [\mu]$	$-\text{Im}(\sigma) [\mu]$	$\text{Re}(M\sigma)$	$-\text{Im}(M\sigma)$	$\text{Re}(\sigma) [\mu]$	$-\text{Im}(\sigma) [\mu]$	$\text{Re}(M\sigma)$	$-\text{Im}(M\sigma)$
mini BS I	1	0.001416	$1 \times 10^{-11}$	0.0009	$7 \times 10^{-12}$	0.1195	$5 \times 10^{-5}$	0.0757	$3 \times 10^{-5}$
mini BS I	2	0.11356	$1 \times 10^{-13}$	0.0719	$9 \times 10^{-14}$	0.1316	$2 \times 10^{-5}$	0.0833	$1 \times 10^{-5}$
mini BS I	3	0.12958	$9 \times 10^{-15}$	0.0820	$5 \times 10^{-15}$	0.1404	$8 \times 10^{-6}$	0.0888	$5 \times 10^{-6}$
massive BS I	1	0.0197	$1 \times 10^{-4}$	0.04460	$4 \times 10^{-4}$	0.0403	$2 \times 10^{-5}$	0.0909	$6 \times 10^{-5}$
massive BS I	2	0.0636	$1 \times 10^{-11}$	0.1436	$4 \times 10^{-11}$	0.0716	$2 \times 10^{-6}$	0.1616	$5 \times 10^{-6}$
massive BS I	3	0.0896	$5 \times 10^{-13}$	0.2023	$4 \times 10^{-13}$	0.0947	$5 \times 10^{-7}$	0.2136	$1 \times 10^{-7}$
solitonic BS I	1	$3 \times 10^{-4}$	$2 \times 10^{-5}$	0.002	$1 \times 10^{-4}$	0.0348	$1 \times 10^{-4}$	0.3137	$1 \times 10^{-3}$
solitonic BS I	2	0.063	$9 \times 10^{-6}$	4.631	$7 \times 10^{-5}$	0.0769	$3 \times 10^{-5}$	0.6928	$2 \times 10^{-4}$
solitonic BS I	3	0.103	$2 \times 10^{-10}$	7.601	$2 \times 10^{-9}$	0.1127	$4 \times 10^{-6}$	1.0156	$3 \times 10^{-5}$

frequency of circular geodesics shown in Fig. 5.2, we observe that such modes can be potentially excited by a quasicircular EMRI [134, 198] in the point-particle limit. We investigate this effect in the next section.

## 5.5 Point-particle orbiting a boson star

The gravitational and the scalar wave emission by a particle in a circular geodesic motion around a BS is governed by the inhomogeneous system of equations (5.26) and (5.28)-(5.30) and (5.36). The solutions can be constructed via Green's function techniques. Once again we shall treat the axial and polar separately.

### 5.5.1 Axial sector

The axial sector is fully described by Eq. (5.26). The general solution can be constructed from two independent solutions of the associated homogeneous equations:

$$\Psi_{RW} = \frac{1}{W_Z} \left[ Z_+(r) \int_0^r dr_* Z_- S_{RW} + Z_-(r) \int_r^\infty dr_* Z_+ S_{RW} \right], \quad (5.70)$$

where  $Z_\pm$  are solutions of the homogeneous associated equation with the following boundary conditions

$$Z_+(r \rightarrow \infty) \sim e^{i\sigma r_*}, \quad (5.71)$$

$$Z_-(r \rightarrow 0) \sim r^{l+1}, \quad (5.72)$$

and  $W_Z = Z_-(dZ_+/dr_*) - Z_+(dZ_-/dr_*)$  is the Wronskian. At large distance, the solution (5.70) reads

$$\Psi_{RW}(r \rightarrow \infty) \sim \frac{e^{i\sigma r_*}}{W_Z} \int_0^\infty dr_* Z_- S_{RW}. \quad (5.73)$$

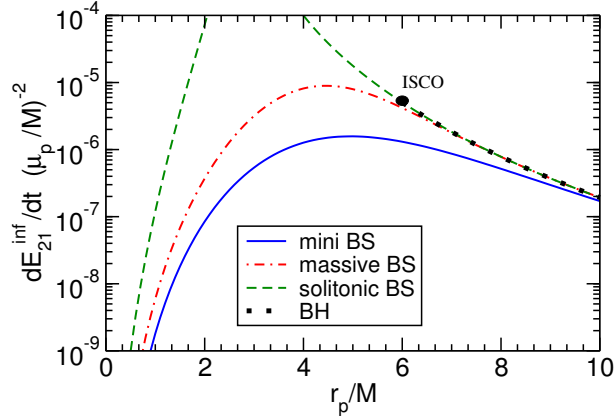


Figure 5.4: (Adapted from Ref. [156]) Dominant  $l = 2$ ,  $m = 1$  contribution to the axial gravitational flux emitted by a point-particle orbiting a BS for the stable BS configurations used in this chapter, compared to that of a Schwarzschild BH. The solitonic configuration for  $r > 3M$  have basically the same values of the BH case.

For circular orbits the source terms generically contain Dirac's delta terms  $\delta(r - r_p)$  and their derivative, namely:

$$S_{RW} = [G_{RW}\delta(r - r_p) + F_{RW}\delta'(r - r_p)]\delta(\sigma - m\Omega),$$

so that the solution (5.73) can be rewritten as

$$\Psi_{RW} \sim \bar{\Psi}_{RW}\delta(\sigma - m\Omega)e^{i\sigma r_*}, \quad (5.74)$$

where [199]

$$\bar{\Psi}_{RW} = \frac{e^{\frac{1}{2}(u-v)}}{W_Z} \left[ G_{RW}Z_- - \frac{d}{dr_*} \left( e^{\frac{1}{2}(u-v)} F_{RW}Z_- \right) \right] \Big|_{r=r_p}.$$

Finally, the energy flux at (null) infinity due to the axial part of the perturbations is given by [199, 200]

$$\dot{E}_{lm}^{\text{inf,axial}} = \frac{1}{16\pi} \frac{(l+2)!}{(l-2)!} |\bar{\Psi}_{RW}|^2.$$

Due to the explicit form of the source term, the axial flux is vanishing for even values of  $l + m$ . In Fig. 5.4, we show the dominant  $l = 2$ ,  $m = 1$  contribution of the axial flux for various stable BS models as well as that of a Schwarzschild BH. The deviations from the BH case are basically indistinguishable at large distances. As expected, more compact configurations like the solitonic BS model are closer to the BH case.

### 5.5.2 Polar sector

The polar sector is described by the inhomogeneous system of coupled equations (5.28)–(5.30). A general method to solve this class of problems was presented in Ref. [175], which we shall closely follow. The polar equations can be written as

$$\frac{d\Psi}{dr} + \mathbf{V}\Psi = \mathbf{S}, \quad (5.75)$$

where we introduced the 6-dimensional vectors

$$\Psi = (H_1, K, \phi_+, \phi_-, \phi'_+, \phi'_-), \quad (5.76)$$

and the vector  $\mathbf{S}$  describes the source terms. The matrix  $\mathbf{V}$  can be straightforwardly constructed from Eqs. (5.28)–(5.30). In order to solve Eq. (5.75), let us define the  $6 \times 6$  matrix  $\mathbf{X}$ , whose columns are formed by independent solutions of the associated homogeneous problem. It is easy to show that

$$\frac{d\mathbf{X}}{dr} + \mathbf{V}\mathbf{X} = 0. \quad (5.77)$$

The general solution can be written in terms of the homogeneous solutions by [175]

$$\Psi = \mathbf{X} \int dr \mathbf{X}^{-1} \mathbf{S}. \quad (5.78)$$

The matrix  $\mathbf{X}$  can be constructed in the following way [30, 175]: the solution close to the origin is defined by three independent parameters, say  $(\psi_0^{or}, \phi_+^{or}, \phi_-^{or})$ . Likewise, the solution close to infinity is characterized by  $(\psi_0^\infty, \phi_+^\infty, \phi_-^\infty)$ . We can construct three independent solutions integrating the equations from the origin by setting the triad to  $(1, 0, 0)$ ,  $(0, 1, 0)$  and  $(0, 0, 1)$ . Using the same for the integration from infinity, we construct the set of six independent solutions which form  $\mathbf{X}$ .

The boundary conditions for the problem are analogous to those described in the previous sections. For the gravitational functions, we require regularity at the origin and outgoing waves at infinity. For the scalar field, we require regularity at the origin, but the condition of outgoing waves is not satisfied for all values of  $\Omega$ . In fact, for sufficiently small frequency, when  $k_\pm^2 > 0$  (cf. Eq. (5.67)), the perturbations of the scalar field are localized near the star and form quasi-bound states. If  $k_\pm^2 < 0$ , the orbital frequency is larger than the potential well and the perturbations are wave-like at infinity. The value of  $\Omega$  for which this transition occurs depends on the specific model through  $\mu$  and  $\omega$  and on the azimuthal number  $m$  (cf. Eq. (5.67) and recall that, for a circular orbit,  $\sigma = m\Omega$ ).

To compute the polar gravitational part of the flux we construct the Zerilli function at infinity, using the solutions for  $K$  and  $H_1$  obtained by solving the coupled system. Then, the polar

gravitational flux is the sum of the multipolar contributions [175, 199, 200]:

$$\dot{E}_{lm}^{\text{inf},Z} = \frac{1}{64\pi} \frac{(l+2)!}{(l-2)!} (m\Omega_p)^2 |\Psi_Z(r \rightarrow \infty)|^2, \quad (5.79)$$

which, by virtue of the specific source term, are nonvanishing only for even values of  $l+m$ .

The scalar flux can be computed through the energy momentum tensor of the scalar field [175, 201] (see also Refs. [113, 114] for other approach). It reads

$$\dot{E}_{lm}^{\text{inf},\phi_{\pm}} = 2(m\Omega_p)^2 |\phi_{\pm}(r \rightarrow \infty)|^2. \quad (5.80)$$

The total energy flux for the polar sector is the sum of the two contributions, i.e.

$$\dot{E}_{lm}^{\text{inf,polar}} = \dot{E}_{lm}^{\text{inf},Z} + \dot{E}_{lm}^{\text{inf},\phi_{\pm}}. \quad (5.81)$$

In the next subsection, we give the details of the polar part of the flux.

### 5.5.3 Emitted polar flux and inspiral resonances

Adopting the procedure explained above, we have evaluated the total scalar and polar gravitational flux emitted by a test-particle orbiting a BS in several BS models. In some cases, the numerical integration is challenging. Indeed, for sufficiently small orbital frequency the scalar perturbations decay exponentially at infinity, but they are nonetheless coupled to the gravitational perturbation which instead propagate to infinity as waves. To achieve good accuracy, the numerical domain of integration should extend up to many wavelengths, i.e.  $r_{\infty}\sigma \gg 1$ , where  $r_{\infty}$  is our numerical value for the infinity. On the other hand, the typical lengthscale of the scalar perturbation is given by the Yukawa-like term, i.e.  $1/\mu$ . Due to the exponential decay, it is challenging to integrate the scalar field if  $r_{\infty}\mu \gg 1$  and this sets a limit to the values of  $r_{\infty}$  that can be used. To circumvent this problem, we have constructed the large distance solution perturbatively using many terms (typically 20) in the series expansion of the solutions at the infinity. This allows to reduce numerical truncation errors. Note that this problem becomes more severe when the mass of the scalar field is large,  $\mu \gg \sigma$ .

An interesting phenomenon that occurs for test-particles orbiting relativistic stars is the appearance of resonances in the flux (see, e.g., Ref. [134]). The resonance condition reads

$$m\Omega = \sigma_R, \quad (5.82)$$

where  $m$  is the azimuthal number and  $\sigma_R$  is the real part of the QNM frequency. In other words, if the characteristic frequency of the BS matches (multiples of) the orbital frequency of the particle, sharp peaks appear in the emitted flux. This is consistent with a simple harmonic oscillator model, where the orbiting particle acts as an external force and where  $\sigma_R$  is the proper frequency of the system. In this picture, the imaginary part of the frequency  $\sigma_I$  is related to the

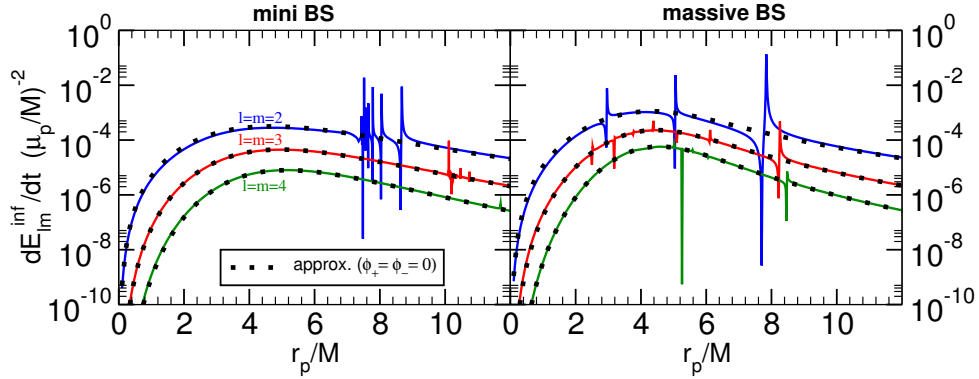


Figure 5.5: (Adapted from Ref. [156]) Main multipole contributions to the polar flux,  $l, m = 2, 3$  and  $4$ , for the mini and massive BS configurations I. The dots indicate the approximated results obtained by setting the scalar perturbations to zero.

damping of the oscillator and it is roughly proportional to the width of the resonance, while the quality factor  $\sigma_R/\sigma_I$  is proportional to the square root of the height [134].

The appearance of these resonances seems to be a generic feature of BSs. As shown in Fig. 5.5, the resonant frequencies may correspond to a stable circular orbit located *outside* the BS effective radius (as for the rightmost resonance of the massive BS case in the right panel of Fig. 5.5) or may correspond to stable circular orbits *inside* the BS (as in the mini BS case shown in the left panel of Fig. 5.5). While resonant circular orbits also occur around outside perfect-fluid stars [134] and gravastars [198], the existence of resonant geodesics *inside* the compact object is peculiar to BSs, due to the absence of a well-defined surface and due to the existence of *stable* circular orbits inside the star [156]. We shall address the solitonic BS case later, due to its complexity.

The existence of these inner resonances is intriguing, because they appear to be a generic feature of compact objects supported solely by the self-gravity of a scalar field. Indeed, any sufficiently compact object can support bound and quasi-bound modes in its interior. In Appendix C, we show that constant density stars can support bound-state modes (i.e. modes with purely real frequency) for massive scalar perturbations with  $l > 0$  and they can also support quasi-bound modes (i.e. modes with small but nonvanishing imaginary part) for massless scalar and for gravitational perturbations. In the case of ordinary stars, these modes cannot be excited because their frequency is higher than the frequency of the innermost stable circular orbit. However, the same class of modes exist also for BSs which, however, admit stable circular orbits in their interior. In the case of a BS, even the massive scalar modes are quasi-bound. The small imaginary part of the frequency is related to the coupling between scalar and gravitational perturbations: even if the scalar flux is zero for bound-state modes, part of the energy carried by the scalar field can be converted into gravitational energy that is then dissipated at infinity through gravitational waves. This also explains qualitatively why the imaginary part of these modes is small (i.e. why the resonances are generically narrow), because the dissipation mechanism is not efficient.

The structure of the resonances is fairly rich and it depends on the values of  $l, m$  and on the specific BS model. We can gain some insight by looking at the analog problem for a Schwarzschild BH. In that case, the location and width of the resonances can be computed

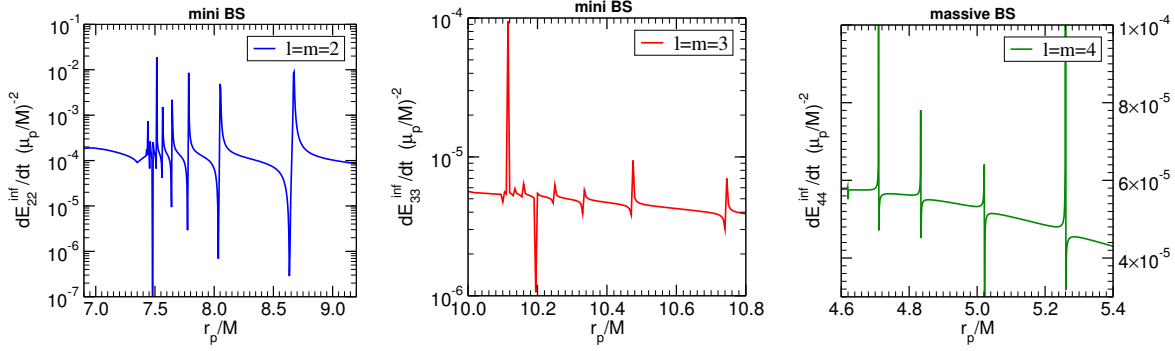


Figure 5.6: Zoom of the main multipole contributions to the polar flux for orbital frequencies close to the interface condition (5.83). Left panel: mini BS configuration I for  $l = m = 2$ . In this case the interface condition corresponds to  $r_p = 7.3624M$ . Middle panel: mini BS configuration I for  $l = m = 3$ ; the interface condition corresponds to  $r_p = 10.0292M$ . Right panel: massive BS configuration I for  $l = m = 4$ ; the interface condition corresponds to  $r_p = 3.8540M$ .

analytically in the small mass limit [202, 203]. For the Schwarzschild BH case, the real and imaginary part of the quasi-bound modes read

$$\sigma_R \approx \mu \left( 1 - \frac{M^2 \mu^2}{2(n+l+1)} \right),$$

$$\sigma_I \approx -\frac{4^{1-2l} \pi^2 (M\mu)^{4l+6}}{M(1+l+n)^{2(2+l)}} \left[ \frac{(2l+n+1)!}{\Gamma[\frac{1}{2}+l]^2 \Gamma[\frac{3}{2}+l]^2 n!} \right],$$

where  $n \geq 0$  is the overtone number. Therefore, as  $\sigma$  approaches  $\sigma_R$  there is a multitude of modes that can be excited and their separation in orbital frequency vanishes in the large  $l$  or large  $n$  limit. However, in the same limit the imaginary part (and hence the width of the resonances) of the modes decreases very rapidly, as shown by the last equation above. Our results for the resonances appearing in the flux from a BS inspiral are in qualitative agreement with this behavior. This is shown in Fig. 5.6, where we show the polar flux in a restricted region of the orbital radius for some BS model. Due to the complex scalar field, the resonance condition is shifted:  $\sigma \pm \omega \approx \mu$  and corresponds to  $k_{\pm} \approx 0$  in Eq. (5.67), i.e. to the interface between quasi-bound states and QNMs. In the left panel of Fig. 5.6, we show the main  $l = m = 2$  contribution for our mini BS configuration I. In this case, the interface condition  $k_+ = 0$  occurs at  $r_p \approx 7.3624M$  and, even for  $l = 2$ , several resonances appear when the particle approaches this peculiar orbit. Similar results hold for the contribution to the flux  $l = m = 3$  for the mini-BS configuration I and  $l = m = 4$  for the massive BS configuration I. In these case, the interface condition reads  $r_p \approx 10.0292M$  and  $r_p \approx 3.8540M$ , respectively. Note that the width of the resonances decreases very rapidly for large values of  $l$ , so that the resonances of higher multipoles are more difficult to resolve and the corresponding modes have a smaller quality factor.

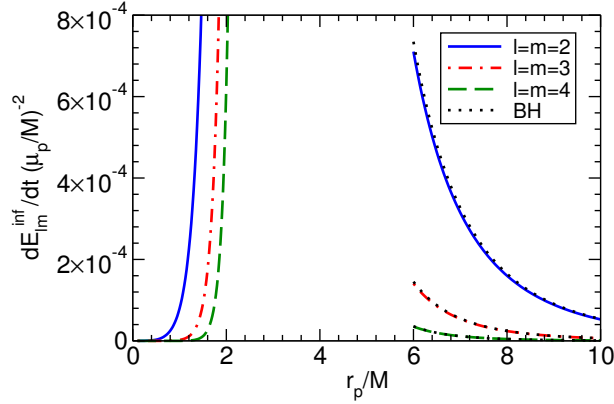


Figure 5.7: Polar flux for the stable (solitonic BS I configuration, cf. Table 5.1), compared with the Schwarzschild BH case.

Our analysis generically shows that the orbital frequency

$$\Omega_{\text{res}} \sim \frac{\mu \mp \omega}{m}, \quad (5.83)$$

plays a special role in the gravitational and scalar flux emitted in a quasicircular inspiral around a BS. The detectability and some observational implications of these resonant frequencies are discussed in Chapter 6 (see also Ref. [156]).

The presence of the scalar field perturbations is crucial for the resonances. In order to illustrate this point, we have considered a decoupling limit, where gravitational and scalar perturbations do not couple to each other. Although this approximation is not fully consistent, it is nevertheless useful to separate the features of the flux computed for the full coupled system. In this limit, scalar perturbations are described by two coupled second-order equations, which support *normal* modes, i.e. modes with purely real part. These modes are very close to the real part of the slowly-damped modes found in the full system and they roughly coincide with the resonant frequencies of the point-particle quasicircular inspiral. Likewise, we have computed the gravitational flux after having artificially set the scalar perturbations to zero. In Fig. 5.5 we show a comparison between the fluxes in the decoupling limit and those obtained by solving the full equations for mini BSs and massive BSs. Away from the resonances, the gravitational flux is in very good agreement with the exact result. This is consistent with the picture presented above: in absence of gravito-scalar coupling, the system would admit normal bound scalar modes. The latter however acquire a small imaginary part due to the coupling with the gravitational sector and can be dissipated at infinity as gravitational waves. Thus, the real part of the QNMs is mainly governed by the scalar sector, whereas the generic aspects of the flux away from the resonant modes is mainly driven by the gravitational sector.

Supported by the good agreement of the decoupling of the scalar field and gravitational perturbations, we have adopted it to compute the flux in the solitonic BS configurations. In this case, the large mass of the background scalar field makes it challenging to solve the full system. This is due to the presence of two different length scales: the BS mass  $M$  which regulates the gravitational sector, and the scalar-field mass  $\mu M \gg 1$  which regulates the decay of the scalar

field.

In Fig. 5.7 we show the flux obtained in the decoupling limit, compared to its (exact) Schwarzschild counterpart. We only show the stable circular orbits located roughly at  $r > 6M$ . For these orbits, the difference is small. This is expected because the external spacetime is very close to Schwarzschild. On the other hand, unlike the other BS models, highly energetic stable circular orbits exist close to the stable light-ring inside the star. In Fig. 5.7 we have neglected the resonance structure of the flux. However, as shown in Tab. 5.5, resonant frequencies for this model correspond to relativistic high-energy orbits and they are not excited by the quasicircular inspiral. Furthermore, since the mass coupling of these configurations is higher than the other models, scalar field radiation is only emitted for very high multipoles, which are subdominant. Thus, for solitonic compact configurations the main distinctive feature of such compact horizonless configurations with respect to a Schwarzschild BH is the possibility of having stable geodesics in the core of the object, which are also associated to large gravitational fluxes. We refer the reader to Chapter 6 (also Ref. [156]), where other features of the inner inspiral are discussed.

## 5.6 Conclusions and outlook

In this chapter we constructed three different BS models, namely mini, massive and solitonic BSs. The spacetimes were constructed using the full Einstein's equations, without any approximation method. Moreover, we discussed circular geodesic motion in the BS spacetime, showing some specific features that are also present in the case of circular motion in uniform density stars in general relativity, like the presence of two light-rings, depending on the compactness of the star. We computed the QNMs of the BS configurations, extending the results of Ref. [160], showing that generically they would be excited by the motion of a point particle in circular orbits. The energy fluxes emitted by the particle were calculated, showing the distinctive characteristic of the resonances in the flux. The analysis made here also extends the results of Ref. [173]. The discussion on the detectability and observational consequences of the resonances will be given in the following chapter.

The results presented in this chapter offer an answer to the question of whether or not one can distinguish BSs from BHs, from the gravitational point of view. We conclude that the motion of stellar-size objects would leave characteristic imprints in the signal that are intrinsically connected with the BS models. The mass of the bosonic particle forming the star has to be light enough in order to reproduce supermassive objects. The studies presented here for the gravitational flux are for point particles in circular orbits, and are most applicable in the region where the scalar field  $\phi_0$  is small enough, i.e., outside an effective BS radius. Inside the star other effects like accretion and dynamical friction should be considered (these are analyzed in the next Chapter). In particular, these effects in a head-on collision could lead to interesting features. Also, the study of eccentric orbits is a direct and important generalization of the present work.

Another possible extension of the present study is the investigation of EMRIs in rotating BS spacetimes. Rotating BSs were analyzed in the literature, in both Newton's and Einstein's gravity context [204]. Perturbation theory around non-spherically symmetric spacetimes is still a challenge, and some cases were studied only within approximation schemes, like in slowly

rotating BHs [146, 197, 205]. The study presented here serves as a reference for further studies of BSs systems.

# Chapter 6

## Into the lair: Gravitational wave signatures of dark matter

The Universe is populated with a plethora of different gravitationally-bound objects in dynamical equilibrium. Luminous, hydrogen-fueled stars like our Sun are supported against collapse by radiation and gas pressure, whereas darker, compact and quiescent objects like neutron stars are prevented from full collapse by degeneracy pressure. Although evidence has been mounting for decades, only in recent years has it become apparent that a completely different class of objects may, or *must*, also abound. Dark matter (DM) makes up a large fraction of galaxies and even though its exact nature is not known, it conglomerates into huge halos around the center of galaxies [206]. Because all forms of matter gravitate, compact self-gravitating DM configurations could therefore be a substantial component of our own galaxy.

Compact DM objects have also been occasionally invoked as an alternative to one of the most intriguing predictions of general relativity, namely the existence of black holes (BHs). Very massive main-sequence stars are dynamically unstable, a feature which is shared by most of the known compact configurations. Thus, “standard” stars cannot explain the dark, compact and supermassive objects lurking at the center of most galaxies, like the  $\sim 10^6 M_{\odot}$  object in our own Milky Way [207]. It is widely accepted that BHs are the most natural explanation for these supermassive compact objects. Nevertheless, although actual observations support the BH hypothesis, experiments showing the direct existence of an event horizon are still missing. In fact, some argue that an observational proof of the event horizon based only on electromagnetic observation is fundamentally impossible [208]. In an attempt to test the BH paradigm, exotic forms of matter which possibly collapse to form supermassive horizonless objects, have been proposed. Besides their relevance for testing fundamental aspects of gravity, these objects may contribute to the dark matter content of the Universe [206], being thus relevant for particle physics and cosmology. The exact nature of the object at the center of our galaxy will soon be strongly constrained by observations [209–211], making this an exciting time to theoretically model and understand alternatives.

Common approaches to probe DM in astrophysical settings are based on model-dependent interactions between the DM and the baryonic sector. Such approaches usually focus on the

imprints these interactions leave on the evolution and equilibrium structures of astrophysical objects. However, the equivalence principle guarantees that all forms of matter gravitate as predicted by Einstein's general relativity, regardless of the (non)baryonic nature of the constituent particles. As such, model-independent signatures of DM can arise from the study of gravitational self-interacting effects, like the existence of supermassive DM configurations. See [212] for a very recent proposal in this direction.

It is widely believed that measurements of gravitational waves (GWs) from inspiralling stellar-mass objects into supermassive compact objects will map the entire spacetime geometry [213, 214] and will carry imprints of the nature of the central object. Thus, GW measurements are in principle able to test the existence of compact DM objects and to discriminate between BHs and other types of horizonless objects [173, 215].

With the above as motivation, we study distinctive features of the extreme mass-ratio inspiral (EMRI) around supermassive scalar-field configurations. In this system, a small compact object with mass  $\mu_p \in (1, 10)M_\odot$  spirals into a supermassive object with mass  $M \in (10^4, 10^7)M_\odot$ . The late-time inspiral of this system is of interest to future space-based GW detectors [216, 217]. The typical orbital period is  $(10^2, 10^4)$  seconds and low-frequency GWs are emitted in the  $(10^{-4}, 10^{-2})$  Hz frequency band. In the EMRI limit, the inspiral can last tens to hundreds of years in the detector band. In one year of observation, millions of radians are contained in the signal, encoding rich information about the spacetime dynamics [213]. For this reason EMRIs are exceptional probes of strong-field gravity [218], modifications of general relativity [174, 175, 203, 219] and of the nature of supermassive objects.

Here we argue that the GW signal from an EMRI can be also used to probe the existence of exotic fields that constitute the dark content of the Universe. If the central object is a BH, the inspiral terminates with a merger and subsequent ringdown [109]. Instead, if the central object is formed by some compact DM configuration that interacts very weakly with baryonic stars, the EMRI proceeds also in the interior of the object, contributing significant amounts of signal-to-noise ratio to the signal [173]. EMRIs are relatively clean systems that can be described with great accuracy within a perturbative approach. During most of the inspiral the stellar-mass object can be considered as a test particle moving on a fixed background. The timescale for merger is much longer than the orbital period and the evolution can be described by an adiabatic approximation. At each instant, we consider that the particle follows a geodesic of the background spacetime and the secular evolution of the geodesic parameters can be computed by solving the linearized Einstein's equations. In this way one finds the inspiralling orbit and the corresponding gravitational waveform. This procedure takes into account the main dissipative effects of the back-reaction. A more detailed analysis, which would also consider conservative effects [220, 221] is beyond the scope of this chapter.

Among other models for self-gravitating exotic fields (e.g. axion stars [222], boson-fermion stars [223], etc...), boson stars (BSs) are particularly interesting because they arise as simple solutions of the Einstein-Klein-Gordon equations, without requiring any exotic matter other than a massive bosonic field (for reviews on the subject see [51, 144, 163]). BSs are compact stars configurations that may be thought of as a natural realization of Wheeler's geons [224] for scalar fields. Unlike the original geons, BSs can admit stable configurations which share many features with central galactic objects, without having singularities nor horizons [169, 225], being indistinguishable from BHs in certain regimes. Formation of BSs has been studied extensively in the literature [51, 185, 226–231]. The recent discovery of the Higgs boson [232] is of course

a further motivation to study this type of solutions.

BSs can be classified [51] according to the scalar potential in the Klein-Gordon Lagrangian. Depending upon the scalar self-interactions, the maximum mass of a BS spans the entire range from one to billions of solar masses.

Rather than working on a case-by-case analysis, here we focus on generic features that can leave a characteristic imprint on the waveform. The inspiral can be divided into two different regimes: the motion in the exterior of the supermassive object and the motion in the interior. In Section 6.1 we discuss EMRIs *inside* generic DM configurations. We show that the inspiral is mostly driven by accretion of the scalar field onto the small compact object and by dynamical friction [233, 234], rather than by GW emission. We include these effects in a Newtonian analysis and compute the signal emitted in GWs. The signal is markedly different from that arising during the merger into a supermassive BH and it also deviates substantially from the evolution obtained when accretion and gravitational drag are neglected [173]. While our results of Section 6.1 are fairly generic, to discuss the outer evolution we need to specify some relativistic model. This is done in Section 6.2, where we describe the EMRI around a spherically symmetric BS. We show that the evolution is driven by the emission of gravitational and scalar waves, which we describe at fully relativistic level. We show that, during a quasi-circular evolution, the energy flux can be resonantly excited. This leads to a large dephasing with important observational consequences for GW detection. We conclude in Section 6.3 by discussing possible extensions of our approach. We use the signature  $(-, +, +, +)$  for the metric and in most of the chapter we adopt natural units  $\hbar = c = G = 1$ , unless otherwise stated.

## 6.1 GW-signatures of EMRIs inside compact DM configurations

We are interested in discussing simple models that can capture the salient features of the inspiral through a DM medium in the extreme mass-ratio limit. There is a variety of situations in which such inspiral can occur. The most obvious one is the existence of self-gravitating, compact DM objects. Another is the inspiral around Kerr BHs surrounded by bosonic clouds [235–238]. Very recently, the GW signatures of intermediate mass BHs with DM mini-halos has also been considered [212].

Despite the multitude of models one can conceive, two of the most important generic features of these configurations are: (i) they interact with standard baryonic matter by purely gravitational effects and (ii) they are typically supported by self-interactions of a massive bosonic field, whose mass can range between  $\mathcal{O}(10^{-20})$  eV (or smaller) and  $\mathcal{O}(1)$  TeV (or larger). In fact, as far as purely gravitational effects are considered, many dynamical aspects do not even depend on the nature of the DM particles (e.g. spin, mass, coupling constants,...), but solely on their mass-energy distribution.

Although compact DM configurations usually require relativistic effects to support their selfgravity, many features of the inspiral can be captured by a simple Newtonian model. In this section, we consider compact Newtonian objects which are characterized by some nonvanishing

density profile  $\rho(r)$  when  $r < R$  and zero outside. The simplest model is a constant-density star<sup>1</sup> supported by purely radial pressure, but more realistic nonconstant profiles are also possible. The crucial point here is to assume that these objects do not couple with standard matter in any way other than through gravitational interactions. In particular, the small orbiting perturber can penetrate the stellar surface and move *inside* the object. Our main interest here is to understand this motion and the corresponding GW emission.

### 6.1.1 Accretion- and gravitational drag-driven inspiral

While the motion in the exterior is driven by radiation-reaction only, when the particle penetrates the stellar surface other effects must be taken into account, namely the accretion of the nonbaryonic mass onto the small compact object and the drag force due to the gravitational interaction of the orbiting perturber with its own wake. In the context of EMRIs, these effects have been taken into account to study the imprints of matter surrounding supermassive BHs [240] on the GW emission. We will show that in the interior of compact nonbaryonic matter configurations, these processes are actually dominant and the inspiral is mostly driven by DM accretion rather than by GW emission.

#### Accretion: Collisionless versus Bondi-Hoyle

Accretion of the scalar field onto the small compact object produces external forces that contribute to the secular evolution. As long as the accreted mass is much smaller than the total mass of the orbiting object, the assumption of quasi-stationary motion should provide a fairly accurate description. Let us start by some simple estimates, assuming the accretion cross section is roughly the geometrical one of the small compact object. For head-on collisions, the small compact object of mass  $\mu_p$  traverses the entire diameter  $2R$  of the star, accreting a tube of length  $2R$  and radius  $R_p$ . Therefore,

$$\frac{M_{\text{accreted}}}{\mu_p} \sim \frac{3}{2} \frac{\mu_p M}{R^2} \sim 0.02 \frac{\mu_p}{M} \ll 1, \quad (6.1)$$

where we used  $R_p \approx \mu_p$ ,  $R \sim 10M$  and we have assumed constant density. Thus, during a single passage, the accreted matter has a negligible effect for head-on collisions. On the other hand, during the inspiral from the surface, the orbiting object can accrete much more as it sweeps through the equatorial plane, tearing a disk-gap of width  $\mu_p$  and area  $\sim R^2$ . In this case we get

$$\frac{M_{\text{accreted}}}{\mu_p} \sim \frac{3M}{4R} \sim \mathcal{O}(1), \quad (6.2)$$

for compact central objects. Thus, inspirals have to be carefully considered.

---

<sup>1</sup>Constant density solutions exist – both in Newtonian gravity and in general relativity – also when the fluid is anisotropic, as in the case of selfgravitating scalar fields [239]. However, we will show that possible anisotropies in the fluid are not important to model the inspiral, because accretion and dragging are mostly insensitive to pressure in the extreme mass-ratio limit.

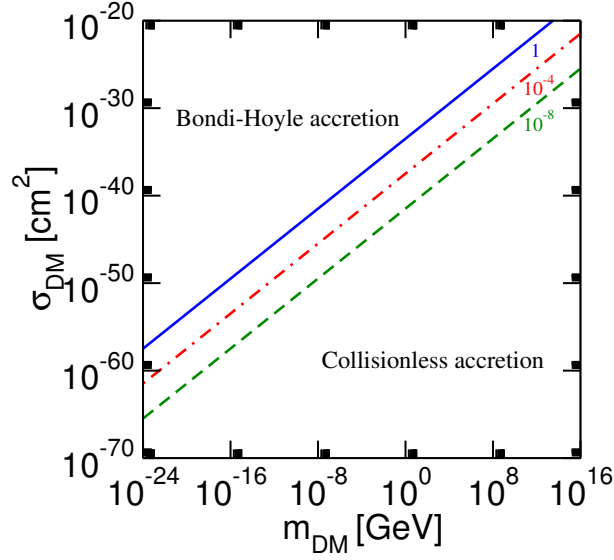


Figure 6.1: Level plots corresponding to the ratio  $R_p/\ell = 1, 10^{-4}, 10^{-8}$  in the  $(\sigma_{\text{DM}}, m_{\text{DM}})$  plane, where  $\sigma_{\text{DM}}$  is the total self-interaction cross section for DM and  $m_{\text{DM}}$  is the mass of the DM particle. In the left-uppermost part of the parameter space the radius of the small compact object  $R_p$  is much larger than the mean free path  $\ell$  and accretion occurs at the Bondi-Hoyle rate (6.6). In the lower-rightmost part of the diagram  $R_p \ll \ell$  and accretion is governed by Eq. (6.5). Straight lines refer to  $\mu_p/M = 10^{-6}$  and  $R = 2M$ , but they have a simple scaling with the inverse of the mass ratio and with the compactness of the central object.

In a more rigorous treatment, dynamical effects and the nature of the small compact object must be included. Accretion is described by

$$\dot{\mu}_p = \sigma \rho v, \quad (6.3)$$

where  $\rho$  is the density of the DM configuration,  $v$  is the modulus of the velocity of the small object with respect to distant static observers and  $\sigma$  is the accretion cross section. The latter strongly depends on the physical processes involved in the accretion and on the nature of the perturber. If the small compact object is a BH, whose radius  $R_p$  is much smaller than the mean free path  $\ell = (\sigma_{\text{DM}} n)^{-1}$  ( $\sigma_{\text{DM}}$  and  $n$  being the DM self-interaction total cross section and the particle density, respectively), then an approximate formula is  $\sigma = \pi R_{\text{eff}}^2$  where [69, 241]

$$R_{\text{eff}} \sim \frac{R_p}{v}. \quad (6.4)$$

is the effective capture radius. Therefore, as  $v \rightarrow 0$ , any particle that forms the supermassive object will eventually fall into the small BH even when orbiting at large distance. Clearly, there exists a cutoff distance given by the radius  $R$  of the supermassive star and which corresponds to a minimum velocity,  $v_{\text{min}} = R_p/R$ . In the small mass-ratio limit  $v_{\text{min}} \sim \mu_p/M \ll 1$ . Therefore, for any  $v > v_{\text{min}}$  we get

$$\dot{\mu}_p = \frac{\pi \rho R_p^2}{v} \quad R_p \ll \ell. \quad (6.5)$$

If the small compact object is a neutron star, the effective cross section is the minimum between the geometrical cross section and sum of the cross sections upon the individual nuclei of the star (see, e.g., [142,242]). Provided the scattering cross section between DM particles and the stellar nucleons is larger than  $10^{-45}\text{cm}^2$ , Eq. (6.5) is still a good approximation for the accretion rate at nonrelativistic velocities. If the small object is a white dwarf, the geometrical cross section is typically larger than the individual scattering contributions, so that the effective cross section is given by the sum of the individual nuclei cross sections [142]. In this case the accretion rate will depend on the details of the microphysics and on the type of DM particles that make up the supermassive object. However, white dwarfs are not compact enough to sustain tidal forces and are likely to be tidally disrupted during the latest stage of the external inspiral. Thus, we shall restrict our attention to accretion onto relatively slow BHs and neutron stars only, both governed by Eq. (6.5).

On the other hand, if the radius of the object is comparable to or larger than the mean free path,  $R_p \gg \ell$ , then accretion becomes a macroscopic process and cohesion forces and matter compressibility must be taken into account [69,241]. When the small compact object is a BH, this type of accretion is described by the Bondi-Hoyle formula [69,243,244]

$$\dot{\mu}_p = 4\pi\lambda \frac{\rho\mu_p^2}{(v^2 + c_s^2)^{3/2}} \quad R_p \gg \ell, \quad (6.6)$$

where  $c_s$  is the speed of sound and  $\lambda$  is a number of order unity which depends on the details of the fluid. In our numerical simulations we have assumed  $\lambda = 1$ , but the results depend on  $\lambda$  very mildly. In Fig. 6.1, we show the straight lines in the DM cross section-mass ( $\sigma_{\text{DM}}-m_{\text{DM}}$ ) plane corresponding to  $R_p/\ell = 1, 10^{-4}, 10^{-8}$  for a mass ratio  $\mu_p/M = 10^6 M_\odot$  and  $R = 2M$ . In the upper-leftmost part of the parameter space  $R_p \gg \ell$  and accretion occurs at the Bondi-Hoyle rate (6.6). In the lower-rightmost part of the diagram  $R_p \ll \ell$  and accretion is governed by Eq. (6.5). In the rest of this chapter, we shall consider the two regimes separately.

### Drag force

Another important effect is the gravitational drag which results in a dynamical friction force on the small compact object traveling through the DM distribution [233,234]. The gravitational field of the small perturber is felt universally, including by the DM making up the compact configuration. Thus, a portion of this material is “dragged” along the inspiral, being tantamount to a net decelerating force acting on the perturber. In the EMRI limit, at the scale of the small compact object, the density of the medium is nearly constant, so that we can adopt the theory of dynamical friction for motion through constant-density media. For linear motion, the dynamical force friction reads [234]

$$F_{\text{DF}} = -\frac{4\pi\mu_p^2\rho}{v^2}I_v, \quad (6.7)$$

with

$$I_v = \begin{cases} \frac{1}{2} \log \left( \frac{1+v/c_s}{1-v/c_s} \right) - v/c_s, & v < c_s \\ \frac{1}{2} \log \left( 1 - \frac{c_s^2}{v^2} \right) + \log \left( \frac{vt}{r_{\min}} \right), & v > c_s \end{cases} \quad (6.8)$$

where  $r_{\min}$  is the effective linear size surrounding the small compact object.

The gravitational drag force in the case of circular motion has been derived in [245], where it is shown that the curvature of the orbit will bend the wake at large distances from the perturber. However, it is found that the subsonic motion is remarkably similar to the linear case, whereas the supersonic motion deviates from the linear case when the size of the small perturber is not parametrically smaller than the orbital radius. Within the extreme mass-ratio assumptions, the size of the perturber is always much smaller than the orbital radius, i.e.  $r_{\min} \ll r$ , so that we expect the linear-motion analysis to approximate well the generic orbital case. We have confirmed this expectation by checking the results obtained using Eq. (6.7) with those obtained by implementing the fitting formulae given in [245] for the gravitational drag force in subsonic circular motion.

If the central object is very compact, the speed of sound is comparable to the speed of light, and, in the nonrelativistic limit we focus on, the motion is likely to be subsonic. On the other hand, supersonic motion is in principle allowed close to the surface and depending on the particular model at hand. Supersonic motion produces a sharp enhancement of the drag force when  $v \approx c_s$  [234, 245]. In particular, the supersonic drag force depends on  $r_{\min}$  and effects related to the circular motion must be taken into account if  $r_{\min} \gtrsim \mathcal{O}(r/10)$ . Even when  $v \gg c_s$ , in the extreme-mass ratio limit  $r_{\min} \ll r$ , the results obtained for the linear motion are in remarkably good agreement with the exact ones [245]. In our models we have assumed  $r_{\min} \equiv R_{\text{eff}} \ll r$ .

Dynamical friction might be very important during the inspiral. Indeed, since the force due to accretion reads  $F_a = \dot{\mu}_p v$ , we obtain

$$\frac{|F_{\text{DF}}|}{F_a^{\text{collisionless}}} \sim \begin{cases} \frac{1}{3} \frac{c^3}{c_s^3} \frac{v}{c} & v \ll c_s \\ \log \left( \frac{vt}{r_{\min}} \right) \frac{c^2}{v^2} & v \gg c_s \end{cases}, \quad (6.9)$$

for the accretion rate (6.5) and

$$\frac{|F_{\text{DF}}|}{F_a^{\text{Bondi}}} \sim \begin{cases} (3\lambda)^{-1} & v \ll c_s \\ \lambda^{-1} \log \left( \frac{vt}{r_{\min}} \right) & v \gg c_s \end{cases}, \quad (6.10)$$

for the Bondi rate (6.6), respectively. In Eq. (6.9) we have considered  $R_p \sim 2\mu_p/c^2$  and we have reintroduced the speed of light  $c$  for clarity. Thus, in the case of collisionless accretion, if the motion is supersonic but nonrelativistic,  $c_s \ll v \ll c$ , dynamical friction dominates over accretion. In the subsonic regime, if  $c_s \sim \mathcal{O}(c)$ , the drag force is subdominant in the nonrelativistic limit and we expect the late stages of the inner inspiral to be dominated by collisionless accretion effects. Nonetheless, depending upon the ratio  $c_s/c$ , there exists a crossover regime

in which both effects are equally important. On the other hand, if accretion is governed by the Bondi rate, it is comparable to the gravitational drag force in the subsonic regime and it is negligible in the supersonic one. The results presented in the next section are obtained by including both the accretion and the drag force during the inspiral and considering both types of accretion separately.

### Gravitational radiation backreaction

In addition to accretion and gravitational drag, the motion inside compact DM configurations is also driven by gravitational radiation reaction, similarly to the usual inspiral around compact objects in vacuum. Neglecting radiation-reaction, the motion of the perturber is governed by the gravitational force  $F_g(r) = m(r)\mu_p/r^2$ . For simplicity, in this chapter we consider the following mass function and DM density profile:

$$m(r) = M \left( \frac{r}{R} \right)^\alpha, \quad \rho(r) = \frac{\alpha M}{4\pi R^\alpha} r^{\alpha-3}, \quad (6.11)$$

but our results extend straightforwardly to more realistic profiles. Note that the equation above reduce to the case of constant-density DM configuration when  $\alpha = 3$  and to the vacuum case (briefly discussed in Appendix D) when  $\alpha = 0$ .

Neglecting radiation-reaction, the energy and angular momentum of the perturber are conserved quantities [212]:

$$E = \frac{1}{2}\mu_p \dot{r}^2 + \frac{L^2}{2\mu_p r^2} - \frac{M\mu_p}{(1-\alpha)R^\alpha r^{1-\alpha}}, \quad (6.12)$$

$$L = \mu_p r^2 \dot{\varphi}. \quad (6.13)$$

In the case of circular orbits of radius  $r$ , we get

$$E = \mu_p \frac{M(1+\alpha)}{R^\alpha r^{1-\alpha} 2(\alpha-1)}, \quad (6.14)$$

$$L^2 = \mu_p^2 \frac{M}{R^\alpha} r^{1+\alpha}. \quad (6.15)$$

and the Keplerian frequency reads

$$\Omega = \sqrt{\frac{m(r)}{r^3}}. \quad (6.16)$$

For circular orbits the radius and the orbital frequency are constant and, therefore, these orbits dissipate energy through the standard quadrupolar formula [246]:

$$\dot{E}_{\text{GW}} = \frac{32\mu_p^2 M^3 r^{3\alpha-5}}{5R^{3\alpha}}, \quad (6.17)$$

where we have used Eq. (6.16). Finally, differentiating Eq. (6.14) and using the energy balance law,  $\dot{E} = -\dot{E}_{\text{GW}}$ , we obtain the evolution equation of the orbital radius

$$\dot{r} = -\frac{64M^2\mu_p}{5(\alpha+1)r^{3-2\alpha}R^{2\alpha}}, \quad (6.18)$$

whose solution reads

$$r(t) = R(1+t/\tau_0)^{-\frac{1}{2(\alpha-2)}}, \quad (6.19)$$

with  $(\alpha-2)\tau_0 = 5(1+\alpha)R^4/(128M^2\mu_p)$ . Note that the late time behavior of the solution above strongly depends on  $\alpha$ : for  $\alpha < 2$  the radius drops to zero in a finite time  $|\tau_0|$ , whereas for  $\alpha > 2$  the radius approaches zero asymptotically. In the singular case  $\alpha = 2$  the behavior is exponentially suppressed.

Let us now show that radiation-reaction effects are small compared to accretion. Simply by angular momentum conservation and using Eq. (6.16), we obtain, for the secular evolution of the radius under accretion,

$$\dot{r}_{\text{accretion}} = -\frac{2}{1+\alpha} \frac{r(t)\dot{\mu}_p}{\mu_p(t)}. \quad (6.20)$$

By comparing with Eq. (6.18), we obtain

$$\frac{\dot{r}_{\text{collisionless}}}{\dot{r}_{\text{reaction}}} \sim \frac{5\alpha}{32} \left(\frac{R}{M}\right)^{3/2} \left(\frac{R}{r(t)}\right)^{\frac{3(\alpha-1)}{2}}, \quad (6.21)$$

$$\frac{\dot{r}_{\text{Bondi}}}{\dot{r}_{\text{reaction}}} \sim \frac{5\alpha\lambda}{32c_s^3} \frac{R}{M} \left(\frac{R}{r(t)}\right)^{\alpha-1}, \quad (6.22)$$

for collisionless and subsonic Bondi accretion, respectively. Interestingly, in both cases and for any  $\alpha > 1$ , the late-time inspiral in the interior of DM compact configurations is generically dominated by accretion and not by radiative dissipation.

### 6.1.2 Numerical evolution of the inspiral in the interior

In this section we describe the secular evolution of the small perturber inside a spherically-symmetric DM configuration as driven by DM accretion and gravitational drag. As proved in the previous section, gravitational radiation reaction is a small effect compared to accretion, so we can safely neglect it here. In Newtonian theory, the accretion- and gravitational drag-driven inspiral is described by the following system:

$$\dot{\mu}_p \dot{r} + \mu_p (\ddot{r} - r\dot{\phi}^2) = -\frac{\mu_p m(r)}{r^2} + F_{\text{DF},r}, \quad (6.23)$$

$$r\dot{\mu}_p \dot{\phi} + \mu_p (r\ddot{\phi} + 2\dot{r}\dot{\phi}) = F_{\text{DF},\phi}, \quad (6.24)$$

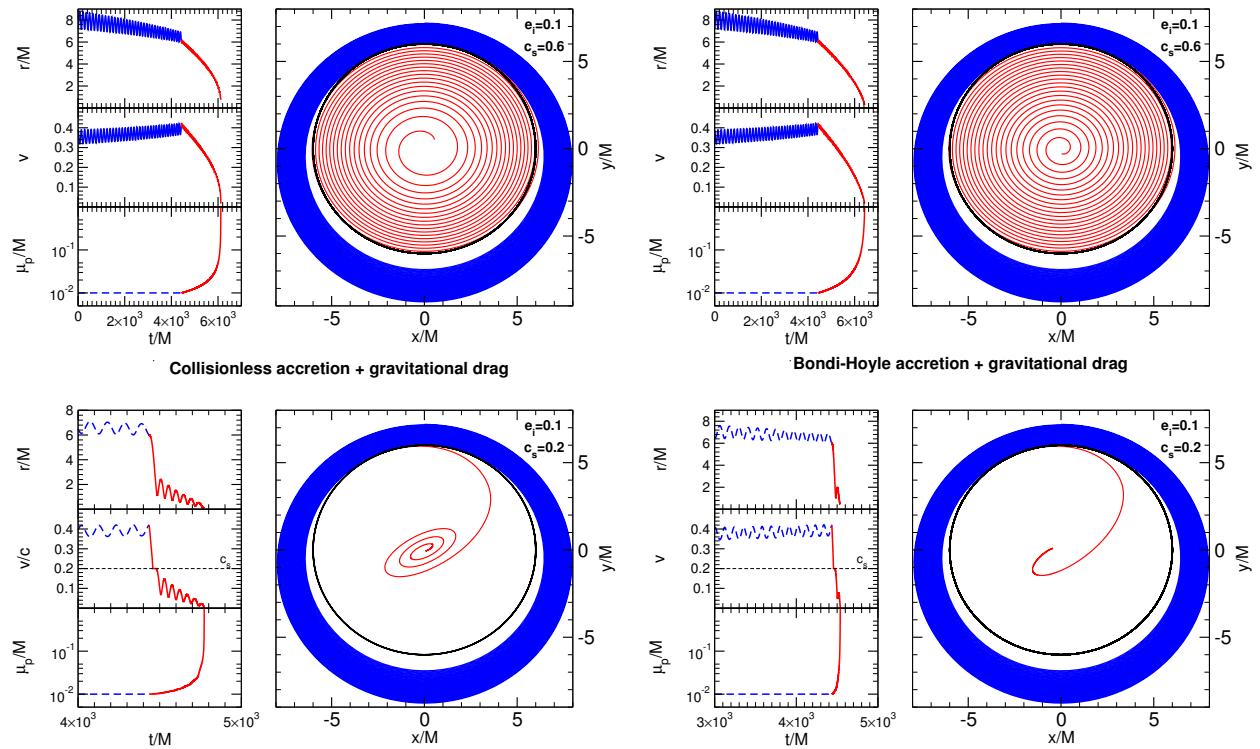


Figure 6.2: Secular evolution of the orbital parameters of a point particle orbiting a constant density, Newtonian star with radius  $R = 6M$ . The particle starts at  $r(0) = 8M$  with initial eccentricity  $e_i \equiv e(t = 0) = 0.1$ . When  $r > R$  (blue curves), the evolution is radiation-driven through the quadrupole formula (cf. Appendix D). When  $r < R$  (red curves) the evolution is driven by dynamical friction and by (i) collisionless accretion (left panels, cf. Eq. (6.5)) or ii) Bondi-Hoyle accretion (right panels, cf. Eq. (6.6)). Upper panels:  $c_s = 0.6$  and the motion is always subsonic. In the interior the orbits circularize quickly. Lower panels:  $c_s = 0.2$ ; the inspiral in the interior starts supersonic and the evolution is dominated by dynamical friction. When  $v < c_s$ , the evolution proceeds qualitatively as in the upper panel. In the small left panels we show (from top to bottom): the radial position in polar coordinates, the module of the particle's velocity and the time evolution of the mass-ratio. The evolution does not qualitatively depend on the accretion rate formula used.

together with Eq. (6.5) or Eq. (6.6) for the evolution of  $\mu_p(t)$ . In the equations above  $F_{\text{DF},r}$  and  $F_{\text{DF},\varphi}$  are the two components of the gravitational drag force. Namely,

$$F_{\text{DF},r} = F_{\text{DF}} \frac{\dot{r}}{v}, \quad F_{\text{DF},\varphi} = F_{\text{DF}} \frac{r\dot{\varphi}}{v}. \quad (6.25)$$

where  $v^2 = \dot{r}^2 + r^2\dot{\varphi}^2$  and  $F_{\text{DF}}$  is the linear dynamical force friction, Eq. (6.7). As discussed above, using the formula for linear motion is well justified in the extreme-mass ratio limit [245].

Equation (6.24) can be directly integrated in two extremal limits. Neglecting gravitational drag, and for *any* accretion rate, we get

$$r\Omega \equiv r\dot{\varphi} = \frac{L}{r\mu_p}, \quad (6.26)$$

which can be also obtained from the conservation of the angular momentum  $L$ . On the other hand, if we neglect accretion ( $\mu_p = \text{const}$ ) and in the limit  $v \ll c_s$ , we get

$$r\Omega \equiv r\dot{\varphi} = \frac{L}{r\mu_p} \exp\left(-\frac{4\pi\rho}{3c_s^3}\mu_p t\right), \quad (6.27)$$

where we have assumed constant density.

In the general case, the system (6.23)-(6.24) has to be integrated numerically for a given density profile  $\rho(r)$  and some initial conditions. The latter are chosen at the time the particle reaches the radius of the object at the end of the quasi-elliptical, radiation-driven inspiral in the exterior.

Some results are shown in Fig. 6.2. As an example, we have considered a constant-density, Newtonian star with radius  $R = 6M$  and a point-like particle located at  $r = 8M$  at  $t = 0$ . The initial eccentricity is  $e_i = e(t = 0) = 0.1$ . Similar results can be obtained for other choices of the parameters and for nonconstant density profiles<sup>2</sup>.

In absence of dissipative effects, the motion inside constant-density distributions is worked out in Appendix E, where we show that the small body moves on ellipses centered at the origin. The quasi-elliptical evolution is then governed by Eqs. (6.23)-(6.24). Figure 6.2 summarizes the quasi-elliptical evolution of the orbital parameters in the subsonic (upper panels) and in the supersonic (lower panels) cases, both for collisionless accretion (left panels) and for Bondi accretion (right panels), respectively. In the top panels, we show the evolution of the orbital parameters for the case  $c_s = 0.6$  (in units of the speed of light), i.e. the motion in the interior of the object is always subsonic. In the large panels we show the orbit in cartesian coordinates. The small panels refer to the evolution of the orbital radius, the velocity and the mass of the small object, respectively. To help visualization, we have considered the unrealistic initial mass ratio  $\mu_p(t = 0) = 10^{-2}M$  and the number of cycles grows with the inverse of  $\mu_p/M$ . In the interior, accretion is very efficient and the mass-ratio becomes of order unity during the inspiral,

<sup>2</sup>Nonetheless, in the deep interior of stellar configurations the density is nearly constant, so that we expect constant-density profiles to be a good approximation for the latest stages of the inner inspiral inside more complicated matter configurations.

so that our approximation breaks down.

In the interior (red curves) the orbit circularizes, regardless the details of the accretion rate. This can be proved analytically in the case of accretion-driven inspiral. Indeed, using the results of Appendix E, together with conservation angular momentum conservation and the energy balance law, it is easy to derive the secular evolution of the semi-major axis  $b$  and of the eccentricity in the small-eccentricity limit:

$$\dot{b}_{\text{accretion}} = -b \left( \frac{1}{2} + \frac{e^2}{8} \right) \frac{\dot{\mu}_p}{\mu_p} + \mathcal{O}(e^4). \quad (6.28)$$

$$\dot{e}_{\text{accretion}} = -\frac{e}{4} \frac{\dot{\mu}_p}{\mu_p} + \mathcal{O}(e^3). \quad (6.29)$$

The equation above shows the important result that circular motion remains circular. Because  $\dot{\mu}_p > 0$ , orbits which are slightly eccentric will tend to circularize. Therefore, as clearly shown in Fig. 6.2, circular inspiral is an attractor of the motion. Remarkably, this result is independent of the specific accretion process.

In the bottom panels of Figure 6.2, we show the same quantities as in the top panels but for the case  $c_s = 0.2$ , i.e. the motion in the interior starts supersonic and, as the velocity decreases, the inspiral enters the subsonic regime. As expected, during the supersonic phase the motion is dominated by dynamical friction and the velocity decreases abruptly. As the particle enters the subsonic regime, the evolution proceeds qualitatively as in Fig. 6.2. However, the inspiral in the supersonic case is much faster and the orbits do not have time to circularize. Note that the evolution does not qualitatively depend on the accretion rate formula used: the results shown in the left and right panels of Figure 6.2 are qualitatively similar.

Finally, note that the accretion can be extremely efficient. In the latest stages of the inspiral, the orbiting object will start accreting very fast [cf. (6.36) below] and an arbitrarily small initial mass will accrete an amount of matter  $M$  in a finite amount of time. Therefore, our small mass-ratio hypothesis will eventually break down. If the orbiting object is a neutron star, during the inspiral it will develop a DM core and it will likely collapse to form a BH [142]. The signal emitted during the collapse is another distinctive feature that must be quantified by a relativistic analysis.

### 6.1.3 Gravitational waveforms

Here we present the waveforms emitted during the inspiral shown in Fig. 6.2. Once the orbital radius, angular velocity and perturber mass are obtained as functions of time, we can use the standard quadrupole formula to compute  $h_+(t)$  and  $h_\times(t)$  for a distant observer located at  $\tilde{r}$  with an angle view of  $(\iota, 0)$  [cf. Eq. (3.72) in [246]].

In Figure 6.3 we consider  $\iota = \pi/2$ , so that only  $h_+$  is nonvanishing and the wave is linearly polarized. The motion in the exterior is driven by the classical radiation-reaction mechanism, briefly summarized in Appendix D for completeness. In panel a) we have neglected accretion and dynamical friction, so that the evolution proceeds only through the radiation-backreaction. In panel b) we have considered accretion but neglected gravitational drag and the signal has a constant amplitude and constant frequency. We discuss this case in detail in the next section.

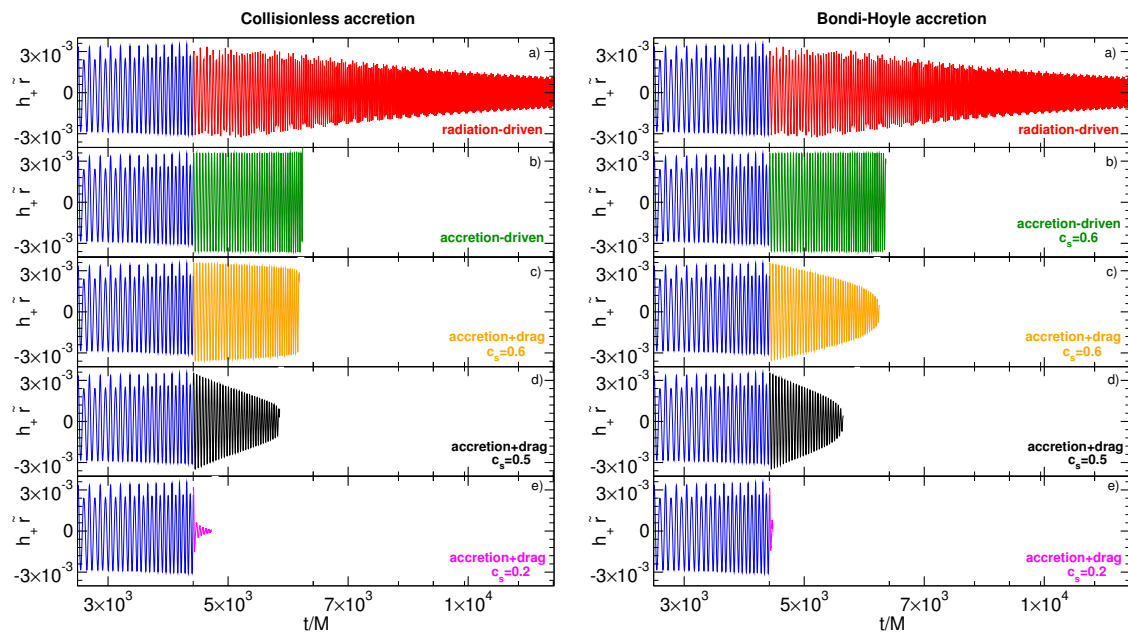


Figure 6.3: Gravitational-wave amplitude  $h_+ \tilde{r}$  along  $(\iota, 0) = (\pi/2, 0)$  as a function of time when collisionless accretion (left panels) and Bondi accretion (right panels) are considered, respectively. Small panels refer to: a) usual radiation-driven inspiral (neglecting accretion and dynamical friction); b) accretion-driven inspiral (neglecting radiation and dynamical friction); c) inspiral driven by accretion and dynamical friction (neglecting radiation) with  $c_s = 0.6$ , which corresponds to the orbits shown in the top panels of Fig. 6.2; d) same as panel c) but with  $c_s = 0.5$ ; e) supersonic regime with  $c_s = 0.2$ , which corresponds to the orbits shown in the bottom panels of Fig. 6.2. Remaining parameters as in Fig. 6.2.

In panels c)-e) we have included both accretion and dynamical friction with different constant values of  $c_s$ .

The last panel shows the supersonic case described in the lower set of panels of Figure 6.2. As expected, the contribution of dynamical friction becomes dominant as  $c_s \ll c$  and we observe two effects: (i) the amplitude of the signal decreases in time and (ii) the total time of the inspiral in the interior quickly decreases for smaller values of  $c_s$ . The latter effect is simply due to the extra dissipative channel during the evolution.

These features would be completely missed by an evolution purely driven by radiative effects. Our analysis does not include relativistic effects, but provides a strong case for including accretion and gravitational drag effects in the inspiral inside compact DM configurations.

### 6.1.4 Analytical Fourier waveforms in the stationary-phase approximation

Some of the qualitative features of the waveforms presented in Figure 6.3 can be analytically captured by a toy model in which we consider a small object of mass  $\mu_p$  on a quasi-circular orbit inside a Newtonian star and whose secular evolution is driven by a single dissipative effect. At Newtonian order, it is possible to obtain analytical templates of the waveforms in Fourier domain in the case of accretion-driven and radiation-driven inspiral. To lowest order,  $\mu_p$ ,  $r$  and  $\Omega$  are constant and the Newtonian waveforms simply read:

$$h_+(t) = \frac{Gr^2\mu\omega_{\text{GW}}^2}{c^4\tilde{r}} \left( \frac{1 + \cos^2 \iota}{2} \right) \cos(\omega_{\text{GW}}t), \quad (6.30)$$

$$h_\times(t) = \frac{Gr^2\mu\omega_{\text{GW}}^2}{c^4\tilde{r}} \cos \iota \sin(\omega_{\text{GW}}t), \quad (6.31)$$

where  $\omega_{\text{GW}} = 2\Omega$ . Then, dissipative effects can be included by replacing the constant parameters  $\omega_{\text{GW}}$ ,  $r$  and  $\mu_p$  by  $\omega_{\text{GW}}(t)$ ,  $r(t)$  and  $\mu_p(t)$ , where the secular time evolution is governed by the specific dissipative mechanism [246]. In the next sections, we shall treat collisionless accretion, Bondi accretion and radiation-reaction separately.

#### Collisionless accretion, $R_p \ll \ell$

In order to isolate the effects of accretion, let us neglect GW reaction and gravitational drag. As we discussed above, if  $c_s = \mathcal{O}(c)$ , the gravitational drag is a small effect compared to accretion, at least in the nonrelativistic regime and for collisionless accretion. Let us then consider the orbital evolution driven by accretion only. Because the system is in isolation, the total angular momentum is constant, even when accretion is included. On the other hand, the binding energy evolves during accretion. A simple and powerful result can be obtained solely by angular momentum conservation,

$$\mu_p(t)r(t)^2 = \frac{L}{\Omega(t)}. \quad (6.32)$$

For quasi-circular orbits,  $v = r\Omega$  and the orbital frequency reads as in Eq. (6.16). Using Eq. (6.32), we obtain

$$\mu(t) = \frac{L}{\sqrt{Gm(r)r(t)}}, \quad (6.33)$$

where, here and in the rest of the section, we restore factors  $G$  and  $c$  for clarity. Finally, using Eq. (6.5) we get:

$$\dot{r} = -\frac{8\pi LG}{c^2} \frac{\rho(r)r(t)}{m(r) + 4\pi\rho(r)r(t)^3} \quad R_p \ll \ell. \quad (6.34)$$

Once a density profile is specified, the equation above can be solved for  $r(t)$ . Then, the other dynamical quantities  $\mu(t)$  and  $\Omega(t)$  respectively read as in Eqs. (6.33) and (6.16).

To be concrete, let us consider the density profile given in Eq. (6.11). In this case, Eq. (6.34) can be directly integrated:

$$r(t) = R(1 - t/t_{\text{insp}})^{\frac{1}{3}}, \quad (6.35)$$

$$\mu_p(t) = \mu_p^{(i)}(1 - t/t_{\text{insp}})^{-\frac{\alpha+1}{6}}, \quad (6.36)$$

$$\Omega = \Omega_i(1 - t/t_{\text{insp}})^{\frac{\alpha-3}{6}}, \quad (6.37)$$

where  $\mu_p^{(i)}$  is the mass of the particle at the time  $t = 0$ , with  $R = r(0)$  and  $\Omega_i = \Omega(0)$ , and we have introduced the duration of the inspiral,

$$t_{\text{insp}} = \frac{c^2 R^3 (1 + \alpha)}{6G\alpha L} = \frac{c^2 (1 + \alpha)}{8\pi G^{3/2} \alpha \langle \rho \rangle \mu_p^{(i)}} \sqrt{\frac{M}{R}}, \quad (6.38)$$

where  $\langle \rho \rangle = 3M/(4\pi R^3)$ .

With this solution at hand, we can compute the corresponding gravitational waveforms [246]. Standard treatment allows to write Eqs. (6.30) and (6.31) to lowest order as

$$h_+(t) = A_+(t_{\text{ret}}) \cos \varpi(t_{\text{ret}}), \quad (6.39)$$

$$h_\times(t) = A_\times(t_{\text{ret}}) \sin \varpi(t_{\text{ret}}), \quad (6.40)$$

where  $t_{\text{ret}}$  is the retarded time and  $\varpi = 2 \int_{t_i}^t dt' \Omega(t')$ . In the case at hand, we get

$$\varpi = \varpi_0 - \frac{12t_{\text{insp}}}{3 + \alpha} \sqrt{\frac{GM}{R^3}} \left( \frac{\tau}{t_{\text{insp}}} \right)^{\frac{3+\alpha}{6}}, \quad (6.41)$$

where  $\tau = t_{\text{insp}} - t$  and  $\varpi_0 = \varpi(t_{\text{insp}})$ . Note that the orbital frequency  $\Omega$  is constant when the density is homogeneous. When the density is nonconstant it is relevant to compute the Fourier

transform of the waveform. Adopting a stationary phase approximation [246], we obtain

$$\tilde{h}_+ = \mathcal{A}_+ e^{i\Psi_+}, \quad \tilde{h}_\times = \mathcal{A}_\times e^{i\Psi_\times}, \quad (6.42)$$

where

$$\begin{aligned} \mathcal{A}_+ &= \frac{4\sqrt{3}i\mu_p^{(i)}}{c^4\tilde{r}} \sqrt{\frac{t_{\text{insp}}}{2(\alpha-3)} \frac{1+\cos^2\iota}{2}} \\ &\times \left[ G^{\frac{3(\alpha-4)}{2}} \pi^\alpha M^{\frac{\alpha-6}{2}} R^{\frac{6+\alpha}{2}} f^{\frac{3+\alpha}{2}} \right]^{\frac{1}{\alpha-3}}, \end{aligned} \quad (6.43)$$

$$\mathcal{A}_\times = \frac{2\cos\iota}{1+\cos^2\iota} \mathcal{A}_+, \quad (6.44)$$

$$\begin{aligned} \Psi_+ &= \frac{12t_{\text{insp}}}{3+\alpha} \left( \frac{R^3}{GM} \right)^{\frac{3}{\alpha-3}} (\pi f)^{\frac{3+\alpha}{\alpha-3}} \\ &+ 2\pi f \left( t_c + \frac{r}{c} \right) - \varpi_0 - \frac{\pi}{4}, \end{aligned} \quad (6.45)$$

$$\Psi_\times = \Psi_+ + \pi/2. \quad (6.46)$$

where  $f = 2\Omega/(2\pi)$ . Therefore, for  $\alpha > 0$  the amplitude and the phase increase with the frequency.

### Bondi-Hoyle accretion, $R_p \gg \ell$

In this case, from Eq. (6.6) we get

$$\dot{r} = -\frac{8\pi LG\lambda}{c_s^3} \frac{\rho(r)\sqrt{Gm(r)r(r)}}{m(r) + 4\pi\rho(r)r(t)^3} \quad R_p \gg \ell, \quad (6.47)$$

which, for the density profile given in Eq. (6.11), can be directly integrated

$$r(t) = R \left( 1 - t/t_{\text{insp}}^{(B)} \right)^{\frac{2}{7-\alpha}}, \quad (6.48)$$

$$\mu_p(t) = \mu_p^{(i)} \left( 1 - t/t_{\text{insp}}^{(B)} \right)^{-\frac{\alpha+1}{7-\alpha}}, \quad (6.49)$$

$$\Omega = \Omega_i \left( 1 - t/t_{\text{insp}}^{(B)} \right)^{\frac{\alpha-3}{7-\alpha}}, \quad (6.50)$$

where we have assumed  $\alpha \neq 7$  and

$$t_{\text{insp}}^{(B)} = \frac{c_s^3 MR^{7/2}(1+\alpha)}{(7-\alpha)\alpha\lambda L(GM)^{3/2}} = \frac{c_s^3(1+\alpha)}{4\pi G^2\alpha(7-\alpha)\langle\rho\rangle\lambda\mu_p^{(i)}}.$$

Similarly to the previous case, using the solution above we can perform a stationary phase approximation to compute the amplitude and the phase in the frequency domain. The relevant ones read

$$\mathcal{A}_+ = \frac{2i\mu_p^{(i)}}{c^4\tilde{r}} \sqrt{\frac{t_{\text{insp}}^{(B)}(7-\alpha)}{\alpha-3} \frac{1+\cos^2\iota}{2}} \times \left[ G^{\frac{7\alpha-25}{4}} \pi^{\frac{1+\alpha}{2}} M^{\frac{3\alpha-13}{4}} R^{\frac{15-\alpha}{4}} f^2 \right]^{1/(\alpha-3)}, \quad (6.51)$$

$$\Psi_+ = \frac{7-\alpha}{2} t_{\text{insp}}^{(B)} \left( \frac{R^3}{GM} \right)^{\frac{7-\alpha}{2(\alpha-3)}} (\pi f)^{\frac{4}{\alpha-3}} + 2\pi f \left( t_c + \frac{r}{c} \right) - \varpi_0 - \frac{\pi}{4}. \quad (6.52)$$

### Gravitational radiation-reaction

The motion driven solely by gravitational radiation reaction has been worked out in Section 6.1.1. Using Eqs. (6.19) and (6.16) we obtain, to lowest order,

$$\mathcal{A}_+ = \frac{4i\mu_p^{(i)}}{c^4\tilde{r}} \sqrt{\frac{\tau_0(\alpha-2)}{\alpha-3} \frac{1+\cos^2\iota}{2}} \times \left[ G^{2\alpha-7} \pi^2 M^{\alpha-4} R^{6-\alpha} f^{\frac{7-\alpha}{2}} \right]^{1/(\alpha-3)}, \quad (6.53)$$

$$\Psi_+ = \frac{8(\alpha-2)}{5-3\alpha} \tau_0 \left( \frac{GM}{R^3} \right)^{\frac{2(\alpha-2)}{\alpha-3}} (\pi f)^{\frac{5-3\alpha}{\alpha-3}} + 2\pi f \left( t_c + \frac{r}{c} \right) - \varpi_0 - \frac{\pi}{4}. \quad (6.54)$$

where  $\tau_0$  is defined below Eq. (6.19).

Comparing the waveform amplitudes and phase in Fourier space shows that each specific dissipative mechanism produces a very peculiar signal. In particular, the signal produced by accretion-driven inspiral is dramatically different from that arising in the classical radiation-driven inspiral, already at Newtonian level. Our analysis can be easily extended to more realistic density profiles. In general, the signal strongly depends on the DM profile and the waveform parameters are also sensitive to the type of accretion process. Thus, the GW signal can be used to constrain the nature and the properties of compact DM configurations.

## 6.2 Relativistic analysis for the external inspiral

A self-consistent relativistic analysis of the inspiral around scalar-field compact configuration is fairly involved already at first order in the mass ratio. Indeed, due to the coupling between gravitational and scalar perturbations and to the presence of a background scalar field, a small perturber will also source scalar waves, even if it is formed by purely baryonic mass. On the

	$V_s( \Phi ^2)$	$\phi_0(r=0)$	$\omega/\mu$	$M\mu$	$R\mu$	$M\omega$	$R/M$
mini-BS I	$\mu^2 \Phi ^2$	0.0541	0.853087	0.63300	7.86149	0.54000	12.4194
mini-BS II		0.1157	0.773453	0.53421	4.52825	0.41319	9.03368
massive-BS I	$\mu^2 \Phi ^2 + \frac{\lambda}{2} \Phi ^4$	0.0188	0.82629992558783	2.25721	15.6565	1.86513	6.9362
massive-BS II		0.0309	0.79545061700675	1.92839	11.3739	1.53394	5.8981
solitonic BS I	$\mu^2 \Phi ^2(1 - 2 \Phi ^2/\sigma_0^2)^2$	0.0371	0.1220326382068426831501347644	7.36961	22.8587	0.89933	3.1017
solitonic BS II		0.0389	0.1236174876926880171453994576	6.77654	20.2924	0.83770	2.9945

Table 6.1: Boson-star models used in this chapter. The quantities  $M$ ,  $R$  and  $\mu$  represent the mass of the solution, its radius and the mass of the scalar field. For massive-BS and solitonic-BS configurations we used the fiducial values  $\lambda = 800\pi\mu^2$  and  $\sigma_0 = 0.05$ . The labels ‘‘I’’ and ‘‘II’’ respectively refer to stable and unstable configurations with respect to radial perturbations. The significant digits of the eigenvalue  $\omega$  do not represent the numerical precision, but they show the fine tuning needed to obtain the solution.

other hand, this property allows for a much richer phenomenology that would be missed if a fully relativistic analysis is not properly performed. To be concrete, in this section we focus on specific models for selfgravitating DM objects. We investigate the emission of gravitational and scalar waves sourced by a test-particle in circular orbit around a boson star (BS). In this section we discuss the main features of this process. The mathematical procedure is standard but technically involved. A detailed analysis will appear elsewhere [149].

### 6.2.1 Relativistic models of supermassive DM objects

For concreteness, in the following we focus on BS configurations [144] which are relativistic solutions of the Einstein-Klein-Gordon theory but most of our results hold at a qualitative level for different models.

We consider the Einstein-Klein-Gordon theory:

$$S = \int d^4x \sqrt{-g} \left[ \frac{R}{2\kappa} - g^{ab} \partial_a \Phi^* \partial_b \Phi - V_s(|\Phi|^2) \right] + S_{\text{matter}},$$

where  $\kappa = 8\pi$  and  $S_{\text{matter}}$  denotes the action of any baryonic matter field. The Einstein-Klein-Gordon equations read

$$R_{ab} - \frac{1}{2} g_{ab} R = \kappa (T_{ab}^\Phi + T_{ab}^{\text{matter}}), \quad (6.55)$$

$$\frac{1}{\sqrt{-g}} \partial_a (\sqrt{-g} g^{ab} \partial_b \Phi) = \frac{dV_s}{d|\Phi|^2} \Phi, \quad (6.56)$$

where

$$T_{ab}^\Phi = \partial_a \Phi^* \partial_b \Phi + \partial_b \Phi^* \partial_a \Phi - g_{ab} (\partial^c \Phi^* \partial_c \Phi + V_s(|\Phi|^2)),$$

is the energy-momentum of the scalar field. For a complex scalar field, Eq. (6.56) is supplied by its complex conjugate. We will focus on spherically symmetric selfgravitating objects, whose line element is

$$ds_0^2 = -e^{v(r)} dt^2 + e^{u(r)} dr^2 + r^2 (d\theta^2 + \sin^2 \theta d\varphi^2), \quad (6.57)$$

whereas the background scalar field reads

$$\Phi_0(t, r) \equiv \phi_0(r)e^{-i\omega t}, \quad (6.58)$$

with  $\phi_0(r)$  being a real function. The field equations for  $v(r)$ ,  $u(r)$  and  $\phi_0(r)$  form an eigenvalue problem for  $\omega$  and they can be solved by standard methods, see e.g. [51, 143, 157, 164, 166, 176]. The equations can be recast in the form of Einstein gravity coupled to an anisotropic, nonbarotropic fluid, whose energy density and pressure are defined in terms of the stress-energy tensor of the scalar field,  $T_{ab}^\Phi$ . Namely,

$$\rho \equiv -T_t^\Phi{}^t = \omega^2 e^{-v} \phi_0^2 + e^{-u} (\phi_0')^2 + V_s^0, \quad (6.59)$$

$$p_r \equiv T_r^\Phi{}^r = \omega^2 e^{-v} \phi_0^2 + e^{-u} (\phi_0')^2 - V_s^0, \quad (6.60)$$

$$p_t \equiv T_\theta^\Phi{}^\theta = \omega^2 e^{-v} \phi_0^2 - e^{-u} (\phi_0')^2 - V_s^0. \quad (6.61)$$

where  $V_s^0 = V_s(\phi_0)$  and  $\rho$ ,  $p_r$  and  $p_t$  are the density, radial pressure and tangential pressure of the fluid, respectively. Using a standard shooting method, we have constructed spherically symmetric compact BSs which are solutions of three different models, presented in Table 6.1.

## 6.2.2 Geodesics around boson stars

Stellar-size objects gravitating around supermassive BSs have a small back-reaction on the geometry and to first order in the object's mass move along geodesics of the BS background. Accordingly, GW emission by such binaries requires a knowledge of geodesic motion together with the consequent perturbative expansion of the gravitational field. Many features of the gravitational radiation can be understood from the geodesic motion, in which we now focus. We will also focus exclusively on circular, geodesic motion. The rationale behind this is that it makes the calculations much simpler while retaining the main features of the physics. Furthermore, it can be shown that generic eccentric orbits get circularized by GW emission in vacuum [189], on a time scale that depends on the mass ratio.

We follow the analysis by [127], the formalism for a generic background is presented in [190]. Following previous studies, we assume that the point-particle is not directly coupled to the background scalar field [168, 169, 173]. The conserved energy  $E$ , the angular momentum parameter per unit rest mass  $L$ , and the orbital frequency of circular geodesics read

$$E_c = \left( \frac{2A(r_c)^2}{2A(r_c) - r_c A'(r_c)} \right)^{1/2} \quad (6.62)$$

$$L_c = \left( \frac{r_c^3 A'(r_c)}{2A(r_c) - r_c A'(r_c)} \right)^{1/2}, \quad (6.63)$$

$$\Omega = \frac{\dot{\varphi}}{\dot{t}} = \left( \frac{A'(r_c)}{2r_c} \right)^{1/2}. \quad (6.64)$$

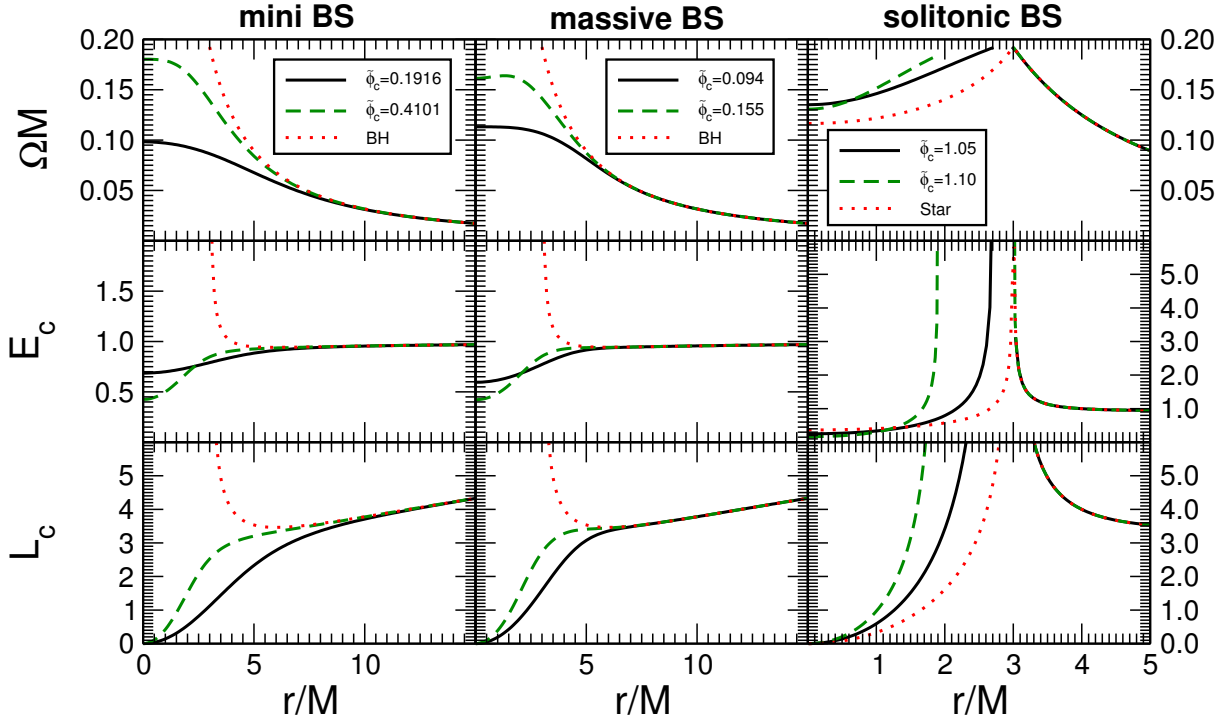


Figure 6.4: Circular geodesic motion for different BS models and configurations (cf. Table 6.1). In the top, middle and lower row we show the orbital frequency  $\Omega$ , the energy  $E_c$  and the specific angular momentum  $L_c$ , respectively. Each column refers to a different BS model. From left to right: mini-BS, massive-BS and solitonic BS. For each model, we compare the geodesic quantities to those of a Schwarzschild BH and for the solitonic BS model we also compare to the metric elements of a uniform density star with  $R = 3M$ . In the last column, the markers indicate the outer last stable orbit for solitonic BS configurations, which is approximately given by  $r \approx 6M$  and  $M\Omega_{isco} \approx 0.06804$ . The light-rings are given by  $r_{l-} \approx 2.72093M$  and  $r_m \approx 2.9812M$ , with  $M\Omega_{l-} \approx 0.188818$  and  $M\Omega_{l+} \approx 0.192453$ , for the first configuration and  $r_{l-} \approx 1.91163M$  and  $r_m \approx 2.99883M$ , with  $M\Omega_{l-} \approx 0.184590$  and  $M\Omega_{l+} \approx 0.192452$ , for the second one.

with  $A(r) = e^v$  as defined in Eq. (6.57). A summary of the geodesic quantities corresponding to the BS models in Table 6.1 is presented in Fig. 6.4. Up to the innermost stable circular orbit of a Schwarzschild spacetime,  $r = 6M$ , geodesic quantities are very close to their Schwarzschild counterpart with same total mass, as might be expected for very compact configurations. However, the geodesic structure at  $r < 6M$  can be very different [173]. A striking difference is that stable, circular timelike geodesics exist for BSs even well deep into the star [168, 169, 173].

For less compact configurations – namely mini BSs and massive BSs – stable circular geodesics exist *all the way down* the center of the star. This is an important feature because, if radiative effects and external forces are small, the inspiral will proceed through a secular evolution of these orbits. Furthermore, the orbital frequency  $\Omega$  is roughly constant close to the origin. This also implies that the circular geodesics deep inside the BS are nonrelativistic, as the velocity measured by static observers at infinity vanishes as the radius approaches zero. In this case, our previous Newtonian analysis should provide reliable results. Therefore, we expect that even the circular orbits in the interior of the object will be accessible to a quasi-circular evolution that, as we previously discussed, is mainly driven by accretion and gravitational drag effects.

More compact configurations such as solitonic BSs may show truly relativistic effects. For these models  $R \sim 3M$  and an innermost stable circular orbit exists at  $r \approx 6M$  with  $M\Omega_{isco} \approx 0.06804$ . This is to be expected, as the background scalar field is exponentially suppressed and the spacetime is very close to Schwarzschild outside the solitonic-BS effective radius. Like in the case of a Schwarzschild BH, there exists an unstable light ring at roughly  $r_m \approx 3M$ . The unexpected feature is the presence of a second *stable* light ring at  $r_{l-}$ , together with a family of stable timelike circular geodesics all the way to the center of the star. This is clearly a relativistic feature, which is similar to the case of uniform density stars. The latter may also present two light-ring and stable circular time-like orbits in their interior, depending on their compactness. The bottom panels of Fig. 6.4 depicts a uniform density star with radius  $R = 3M$ . In this case, the two light-rings degenerate in the star surface. It has been argued [173] that, for these very compact models, the orbiting particle plunges when it reaches the innermost stable circular orbit and, due to radiation effects, the eccentricity of the orbits in the interior of the BS will increase. However, as we have discuss, accretion effects are dominant in the interior of the star and they also contribute to circularize the orbit. Our results are based on a Newtonian analysis, which is nonetheless accurate well deep inside the star, where the velocity is small. It is therefore possible that, after the initial plunge, the particle will have access to these circular geodesics, whose evolution is governed by accretion, rather than by radiative effects.

### 6.2.3 Point-particle orbiting a boson star, resonant fluxes and quasinormal modes

The gravitational and scalar energy fluxes emitted during the quasi-circular inspiral of a test-particle around a compact BS can be derived at fully relativistic level. The emission is governed by an inhomogeneous system of equations, whose regular solutions can be constructed via standard Green's function techniques. We present here the main results, whereas a detailed analysis will appear elsewhere [149].

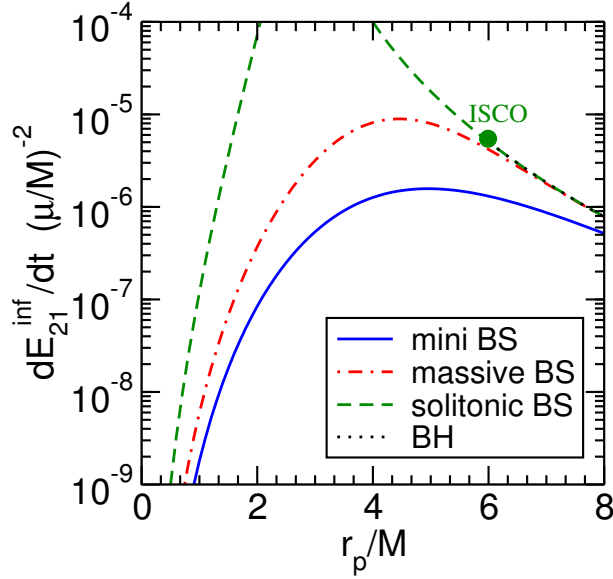


Figure 6.5: Dominant  $l = 2$ ,  $m = 1$  contribution to the axial gravitational flux emitted by a point-particle orbiting a BS for the stable BS configurations used in this chapter, compared to that of a Schwarzschild BH. The most compact configurations are closer to the BH case, and both solitonic configurations for  $r > 3M$  have basically the same values of the BH case.

The axial sector is governed by a single equation which does not involve scalar perturbations. Due to the explicit form of the source term, the axial flux is vanishing for even values of  $l + m$ . In Fig. 6.5, we show the dominant  $l = 2$ ,  $m = 1$  contribution of the axial flux for various BS models and compared to that of a Schwarzschild BH.

The polar sector is described by an inhomogeneous system of coupled equations. A general method to solve this class of problems was presented in [175] (see also [30]). The contribution of the polar radiation to the total energy flux is nonvanishing only when  $l + m$  is even and it is maximum when  $l = m$ . The dominant contributions is shown in Fig. 6.6 as a function of the orbital distance for mini BSs and massive BSs. The axial and polar sector present similar features: at large distance the deviations from the BH case are basically indistinguishable, whereas for stable circular orbits inside the BS the energy flux quickly decreases as the orbit shrinks. In this limit, the orbital velocity is nonrelativistic and our results agree with a simple quadrupole formula [246].

However, the polar flux shows some sharp peaks which correspond to specific resonant frequencies. This interesting phenomenon occurs quite generically for small objects orbiting relativistic compact stars (see, e.g. [134, 247]) and it is related to the excitation of the quasi-normal mode (QNM) frequencies. For a point-particle with orbital frequency  $\Omega$ , the resonance condition reads

$$m\Omega = \sigma_R, \quad (6.65)$$

where  $m$  is the azimuthal number and  $\sigma_R$  is the real part of the QNM frequency. In other words, if the characteristic frequency of the BS matches (multiples of) the orbital frequency of the particle, sharp peaks appear in the emitted flux. This can be modeled in terms of a simple harmonic oscillator, where the orbiting particle acts as an external force and where the  $\sigma_R$  is the

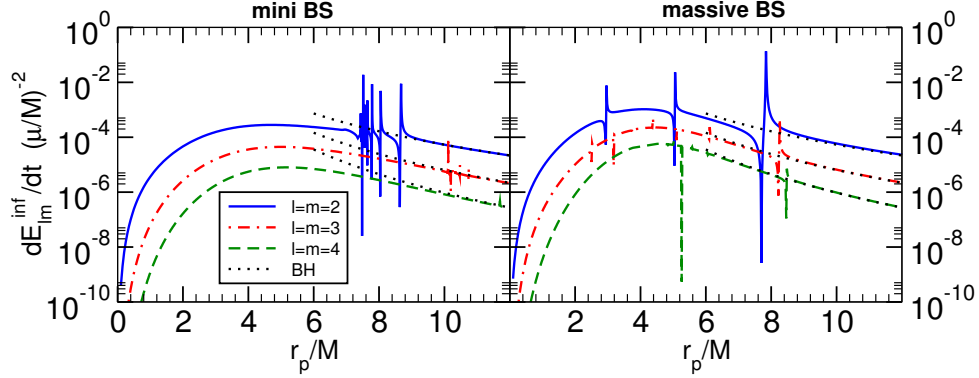


Figure 6.6: Main multipole contributions,  $l, m = 2, 3$  and  $4$ , for the mini and massive-BS configurations.

Model	$\sigma_R M$	$-\sigma_I M$	$h/\nu^2$	$\delta\phi_{\text{GW}}$ [rads]
mini-BS I	0.0757	$3 \times 10^{-5}$	0.01	$6 \times 10^3$
massive-BS I	0.0909	$6 \times 10^{-5}$	0.13	$9 \times 10^4$
massive-BS I	0.1616	$5 \times 10^{-6}$	0.02	$2 \times 10^2$
massive-BS I	0.2136	$1 \times 10^{-7}$	0.007	$4 \times 10^{-1}$

Table 6.2: Polar quasi-bound modes  $\sigma = \sigma_R + i\sigma_I$  of mini-BS and massive-BS configurations corresponding to the resonances shown in Fig. 6.6 for  $l = 2$  and computed by a direct integration method [149]. We also present the height of the resonance normalized by the mass ratio,  $h/\nu^2$ , and the total GW dephasing  $\delta\phi_{\text{GW}}$  as computed in Eq. (6.68) for  $T_{\text{obs}} = 1\text{yr}$  and  $M = 10^5 M_{\odot}$ .

proper frequency of the system. In this picture, the imaginary part of the frequency  $\sigma_I$  is related to the damping of the oscillator and it is roughly proportional to the width of the resonance, while the quality factor  $\sigma_R/\sigma_I$  is proportional to the square root of the resonance height [134]. In agreement with this model, the resonances shown in Fig. 6.6 correspond to the lowest damped QNMs, which are presented in Table 6.2. The QNM spectrum of a BS is rich and comprises several classes of modes [160]. Here we have found a novel class of lowest damped modes, which can be excited during the inspiral due to their low frequency. A complete analysis of the QNM spectrum was presented in Chapter 5.

As shown in Fig. 6.6, the resonant frequencies may correspond to a stable circular orbit located *outside* the BS radius (as for the rightmost resonance in the right panel of Fig. 6.6) or may correspond to stable circular orbits *inside* the BS (as in the mini-BS case shown in the left panel of Fig. 6.6). While resonant circular orbits also occurs around perfect-fluid stars [134] and other BH mimickers [198], the existence of resonant geodesics inside the compact object is peculiar of BSs, due to the absence of a well-defined surface and due to the existence of stable circular orbits inside the star. Similar results as those shown in Fig. 6.6 may be derived for other choices of the parameters and for higher values of  $l$ .

The existence of these resonances is intriguing, because they appear to be a generic feature of compact objects supported solely by the self-gravity of a scalar field. For BSs, this novel class of modes corresponds to the scalar perturbations being localized close to the BS radius and decaying exponentially at infinity, while the gravitational perturbations propagate to infinity as plane waves. These modes are usually named “quasi-bound” states [195–197] and they are supported by the mass of the scalar field. In fact, any sufficiently compact object can support

this class of modes in its interior. Constant density stars can support bound-state modes (i.e. modes with purely real frequency) for massive scalar perturbations with  $l > 0$  [149]. In the case of a BS, these modes acquire a small imaginary part which is related to the coupling between scalar and gravitational perturbations: even if the scalar flux is zero for bound-state modes, part of the energy carried by the scalar field can be converted into gravitational energy that is then dissipated at infinity through GWs. This also explains qualitatively why the imaginary part of these modes is small (i.e. why the resonances are generically narrow), because the dissipation mechanism is not efficient.

The overall structure of the resonances is fairly rich and it depends on the values of  $l$ ,  $m$  and on the specific models. However, in line with the case of a Schwarzschild BH, the modes have a hydrogenic-like spectrum. In that case, the location and width of the resonances can be computed analytically in the small mass limit [202, 203]. For a Schwarzschild BH the quasi-bound modes  $\sigma = \sigma_R + i\sigma_I$  read

$$\begin{aligned}\sigma_R &\approx \mu \left( 1 - \frac{M^2 \mu^2}{2(n+l+1)} \right), \\ \sigma_I &\approx -\frac{4^{1-2l} \pi^2 (M\mu)^{4l+6}}{M(1+l+n)^{2(2+l)}} \frac{(2l+n+1)!}{\Gamma[\frac{1}{2}+l]^2 \Gamma[\frac{3}{2}+l]^2 n!},\end{aligned}$$

where  $n \geq 0$  is the overtone number. Therefore, as  $\sigma$  approaches  $\sigma_R$  there is a multitude of modes that can be excited and their separation in orbital frequency vanishes in the large  $l$  or large  $n$  limit. In the same limit the imaginary part (and hence the width of the resonances) of the modes decreases very rapidly, as shown by the last equation above. Our results are in qualitative agreement with this behavior, although in the BS models we considered the scalar field mass is not small, cf. Table 6.1. Indeed, in the opposite regime when  $\mu M \ll 1$  the imaginary part is exponentially suppressed, at least when the background spacetime is a BH [248]. We have found the same exponential behavior in the case of solitonic BSs (which have  $\mu M = \mathcal{O}(10)$ , cf. Table 6.1). This makes it extremely challenging to compute the polar flux for solitonic BSs and the corresponding flux would show extremely narrow resonances. This is the reason why we do not show the polar flux for solitonic BSs in Fig. (6.6) However, the effective mass for a complex scalar field also depends on  $\omega$  and, correspondingly, the resonance condition is shifted [149]. Our analysis generically shows that the resonant frequencies are of the order

$$\Omega_{\text{res}} = \frac{\mu \mp \omega}{m}, \quad (6.66)$$

and the width of the resonances decreases quickly for large values of  $m$  and for the overtones. It would be interesting to derive an analytical formula similar to the one above, for BSs. Remarkably, the resonant frequencies only depend on the parameters of the theory – namely on the scalar field mass and on  $\omega$  – so that possible detection of resonant fluxes can be used to discriminate among different models and to tell a BS from a supermassive BH.

Let us now estimate the prospects of observing such effects. A generic framework to study the detectability of narrow resonances has been developed by [174]. While the orbiting body crosses the resonance, the emitted energy flux increases by orders of magnitude and the inspiral

proceeds faster. Therefore, the main observational consequence is a dephasing of the GW signal induced by the orbital acceleration at the resonance. Following [174], we model the energy flux as a top-hat function<sup>3</sup>:

$$\dot{E} = \dot{E}_0 + h(t)\mathcal{H} [\delta t_{\text{res}}^2 - (t - t_{\text{res}})^2], \quad (6.67)$$

where  $\dot{E}_0$  is the flux in absence of the resonance which is well approximated by the quadrupole formula at large distance,  $h(t)$  is a time-dependent height of the resonance occurring at  $t = t_{\text{res}}$ ,  $\delta t_{\text{res}}$  is its duration and  $\mathcal{H}$  is the Heaviside function. In our case  $\delta t_{\text{res}}$  is much shorter than the orbital period, thus the leading-order formula for the dephasing induced by the resonance reads [174]

$$|\delta\phi_{\text{GW}}| \sim \frac{5h}{16\nu^2} \frac{M\Delta\Omega_{\text{res}}}{(M\Omega_{\text{res}})^{10/3}} \frac{T_{\text{obs}}}{M}, \quad (6.68)$$

where  $h = h(t_{\text{res}})$ ,  $\nu = \mu_p/M \ll 1$  and  $\Delta\Omega_{\text{res}}$  is the width of the resonance in the frequency space. We estimate  $\Delta\Omega_{\text{res}} \approx 2\sigma_I$  and  $\Omega_{\text{res}} \approx \sigma_R$ , where  $\sigma_R$  and  $\sigma_I$  are the real and the imaginary part of the QNM frequency. Finally, we obtain

$$\begin{aligned} |\delta\phi_{\text{GW}}| &\approx 8.6 \times 10^3 \text{rads} \left[ \frac{10^5 M_\odot}{M} \right] \left[ \frac{T_{\text{obs}}}{1\text{yr}} \right] \\ &\times \left[ \frac{h/\nu^2}{10^{-2}} \right] \left[ \frac{\sigma_I M}{10^{-5}} \right] \left[ \frac{0.1}{\sigma_R M} \right]^{10/3}, \end{aligned} \quad (6.69)$$

where we have rescaled all quantities by typical values as obtained for the peak of the resonance and for the QNM frequencies (cf. Table 6.2). Space-based observatories like eLISA/NGO will be sensitive to variations in the GW phase of the order of one radian [216, 217]. The estimate above shows that the dephasing induced by the flux resonance can easily be larger by orders of magnitude. In fact, such large dephasing implies that a matched-filtering search for EMRIs that uses general relativistic templates would likely miss the signal or detect it but extracting completely wrong physical parameters. Depending on the parameters of the model, the height and the width of the resonance can be smaller and, for very narrow resonances, the dephasing will be negligible. Nonetheless, the bottom line of our analysis is that the quasi-circular inspiral of small compact objects around supermassive BSs will leave potentially detectable imprints that would be missed if the central object is *a priori* assumed to be a BH.

Once the energy fluxes are computed, the evolution of an EMRI can be modeled using an adiabatic approximation and a Teukolsky evolution [249, 250]. This procedure will include dissipative effects to all Post-Newtonian orders, but it is valid only at first order in the mass ratio. While such relativistic approach (together with including self-force effects [220, 221]) is crucial for generating accurate templates, no qualitatively new features will arise with respect to the case of inspiral around a massive BH. Our goal here is to point out new effects that can be used as a smoking gun for scalar-field configurations. One effect is the appearance of

---

<sup>3</sup>Note that, as shown in Fig. 6.6 and consistently with a simple harmonic oscillator model [134], the resonant flux consists of a resonance and an antiresonance. Both can be modelled by a top-hat function as in Eq. (6.67), but they would have opposite sign. However, the height of the antiresonance is of the order of the Newtonian flux or less, whereas the height of the resonance is large by orders of magnitude. Therefore, we can safely neglect the contribution from the antiresonance and focus on a single top-hat function as in Eq. (6.67).

resonances discussed above. Another effect is the existence of stable circular orbits inside the BS and the possibility that the small compact object proceeds all the way down to the origin, without plunging. This was discussed in Section 6.1 within a much simpler – although more general – Newtonian analysis.

## 6.3 Conclusions and outlook

According to general relativity, if self-interacting fundamental scalar fields exist in nature they may collapse to form compact self-gravitating configurations whose mass ranges from one to billions of solar masses, depending upon the scalar potential. Future GW detectors will be sensitive to the signal emitted by neutron stars and solar-mass BHs orbiting supermassive objects like those powering active galactic nuclei. In this chapter, we have investigated several distinctive features of the inspiral around supermassive scalar-field configurations in the extreme mass-ratio regime. Rather than working on a case-by-case analysis, we focused on generic features that can leave a characteristic imprint on the gravitational waveform and which are fairly independent from the microphysics of DM particles.

Working in a Newtonian approximation, we have discussed the inspiral in the interior of very generic DM configurations. If the small compact object interacts purely gravitationally with the scalar field, its motion will be described by quasi-elliptical orbits whose secular evolution is driven by DM accretion and by gravitational drag. These effects dominate the inspiral and are responsible for a peculiar GW signal. If accretion dominates over dynamical friction, the signal has a nearly constant amplitude and nearly constant frequency at late times. This is markedly different from the classical plunge which would occur if the central object were a BH and it might be used to discriminate the supermassive objects in galactic nuclei and to probe DM. We have shown that, already at Newtonian level, the waveforms in the Fourier space are strongly sensitive on the DM density profile.

As an aside application, our results may also be relevant to study the GW signal from the inspiral of putative primordial BHs [5] in the interior of neutron stars or to study the inspiral around Kerr BHs endowed with bosonic clouds [235–238].

Secondly, the motion of the small compact object in the exterior of the supermassive configuration is driven by the emission of gravitational and scalar waves, which are coupled to each other. Due to this coupling, a baryonic test-particle in quasi-circular motion can resonantly excite the scalar QNMs of the central DM object. We have demonstrated this by considering some specific models of relativistic BSs in spherical symmetry. These resonances appear as sharp peaks in the energy flux emitted in GWs and would result in a faster inspiral, leading to a dephasing which can have observational consequences for future detectors. The resonant frequencies are largely insensitive to the details of the system, and they mainly depend only on the mass of the scalar particle. We have shown that the resonances correspond to the excitation of a novel class of QNMs, which have a much longer lifetime and should therefore dominate the late-time signal during the gravitational collapse and during the ringdown. We have discussed the QNM spectrum and the linear response of the system at fully relativistic level.

The plethora of DM candidates, modified gravitational theories and models for BH mimickers makes it mandatory to select generic features such as those described here. More rigorous

case-by-case analysis might be performed if some of these signatures are eventually detected. Indeed, our work can be extended in several directions. A rigorous treatment of the accretion and drag effects in the interior beyond the Newtonian approximation is lacking. Relativistic effects might be important at the interface close to the radius, where velocities may be moderately relativistic and the motion could be supersonic. Special relativity effects were included in [251] and it would be interesting to extend our work by using those results and also by including Post-Newtonian corrections to the accretion-driven inspiral. On the other hand, the late-time inspiral close to the origin is intrinsically nonrelativistic and we expect our results to be accurate in that regime. Furthermore, a simple extension of our analysis is to include noncircular motion at fully relativistic level (see e.g. [199], where the same extension has been performed for the inspiral around a BH). Our results also show that a relativistic analysis as that performed by [173] should be extended to include the effects of accretion and dynamical friction. Finally, we focused here on nonspinning solutions, while spin will certainly play a crucial role. In particular, possible superradiance instabilities [252], which affect horizonless and spinning compact objects, can be considered together with their possible imprint on the GW signal emitted during the inspiral.

While this study was in its last stages, a related work appeared in the literature [212]; while the assumptions of both works are different, and our framework more general, the broad conclusions are both optimistic: gravitational waves can be an efficient tool to study DM.

## Chapter 7

# Light rings as observational evidence for event horizons: Long-lived modes, ergoregions and nonlinear instabilities of ultracompact objects

Our current understanding of stars and stellar evolution strongly suggests that sufficiently compact, massive objects are unstable against gravitational collapse. Neutron stars, with compactness  $2GM/c^2R \sim 1/3$  cannot sustain masses larger than  $\sim 3M_\odot$ , whereas giant stars with masses  $M \gtrsim 10M_\odot$  have compactnesses orders of magnitude smaller. In other words, ordinary matter cannot support the enormous self-gravity of a massive and ultracompact object, so that the latter is naturally expected to be a black hole (BH).

The above picture has been challenged by the construction of exotic objects relying on different support mechanisms. For example, boson stars made up of fundamental massive scalar fields can be as compact as a neutron star and as massive as the BH candidate at the center of our galaxy [144, 156]. Several other – albeit more artificial – objects such as gravastars [253], superspinars, etc, share similar properties [252, 254] and have been proposed as prototypical alternatives to stellar and massive BHs.

The observation – or lack thereof – of a surface would be bullet-proof indication that compact dark objects have star-like properties or are instead endowed with an event horizon. Such tests are extremely challenging to perform in the optical window, but will become available with the advent of gravitational-wave astronomy: the oscillation modes of BHs have a very precise and well-known structure, which can be tested against observations [10, 109, 255], while the presence of a surface should be imprinted also on the gravitational waves generated during the merger of two objects [154, 156, 173] (but see the discussion in Sec. 7.3.3).

Fortunately, general relativity also comes to the rescue in helping to discriminate the nature of compact objects. Very compact and highly spinning objects with an ergoregion but without

a horizon are unstable [256]. Thus, rapidly-spinning compact objects must, in principle, be black holes [252, 254]. However, observations of these objects are marred with uncertainties and not all of them are highly spinning. Furthermore, depending on the compactness and the spin, the instability time scale might be longer than the age of massive objects [257], making it an ineffectual mechanism.

Very recently, a new mechanism was put forward that could exclude *any* ultracompact star configuration on the grounds that such object would be nonlinearly unstable [258]. If correct, this mechanism would close the “BH paradigm” project: within general relativity, the observation of an ultracompact object would be an observation of a BH <sup>1</sup>. The relevance of such corollary calls for a detailed analysis of the decay of linear perturbations in the spacetime of ultracompact configurations, and of the nonlinear evolution of such objects. Here, we wish to take a first step in this direction by studying linear perturbations.

We show that linear perturbations of *any* ultracompact star do become arbitrarily long-lived in the eikonal regime, and correspond to fluctuations trapped between the outer, unstable light ring and the origin. Such modes are peaked at the location of a *stable* light ring, whose existence is a peculiar property of these ultracompact objects. Already at the linear level, these long-lived modes turn unstable against the ergoregion instability [256] when a small amount of rotation is added to the star. Furthermore, at the nonlinear level, we provide evidence that the outer layers of the star may fragment and subsequently fallback on the star’s core, making it dynamically resemble a “boiling object”. Consequent emission of gravitational radiation will cause mass loss and a decrease in compactness, leading to stable stars without light rings. Depending on the star structure, fragmentation could even be due to BH formation, in which case the end-state is a BH.

## 7.1 Ultracompact objects

We define an ultracompact object as one possessing a light ring (in addition, we will be working mostly with horizonless objects). We focus here on static, spherically symmetric spacetimes described by (henceforth we use geometrical units  $G = c = 1$ )

$$ds^2 = -f(r)dt^2 + B(r)dr^2 + r^2d\Omega_2^2. \quad (7.1)$$

If we use coordinates where the spacetime is manifestly asymptotically flat, then  $f(r)$ ,  $B(r) \rightarrow 1$  at large distances. Moreover, the requirement that the spacetime be locally flat and regular implies that  $f(r)$  and  $B(r)$  be finite at the origin  $r = 0$  for any object.

The radial equation for null geodesics in this geometry reads [190]

$$B(r)f(r)\dot{r}^2 = E^2 - V_{\text{geo}} \equiv E^2 - L^2 \frac{f(r)}{r^2}, \quad (7.2)$$

---

<sup>1</sup>We are assuming that the instability time scale is short enough to dominate the dynamical evolution of the compact object, see below for a discussion.

where  $V_{\text{geo}}$  is the geodesic potential<sup>2</sup> and  $E$  and  $L$  are the conserved specific energy and angular momentum of the geodesic. The existence of one (unstable) light ring for ultracompact objects – at roughly  $r_{\text{LR}} \sim 3M$  for spherically symmetric configurations – means that  $V_{\text{geo}}$  has a local maximum at that point. Because  $V_{\text{geo}}$  diverges and is positive at the origin for ultracompact stars, this also implies the existence of a local minimum and therefore of a *second* – stable – light ring, typically within the star.

The existence of a stable light ring is thus an unavoidable feature of any ultracompact star and has dramatic consequences for the dynamics of the latter. Indeed, a stable light ring suggests that some modes can become very long-lived [135, 190, 259, 260]. When this happens, nonlinear effects can become important and destabilize the system. In a nutshell, this was the argument recently put forward to suggest that ultracompact configurations might be nonlinearly unstable [258]<sup>3</sup>.

In the following we will test some of these consequences by computing the modes of ultracompact configurations and the time evolution of wavepackets in the vicinities of such objects. We consider two different ultracompact objects – constant density stars and “gravastars” – briefly described below. Our results apply also to ultracompact boson stars, which have been recently built in Ref. [156], or to any other ultracompact object, as will become apparent from the technical details we present.

### 7.1.1 Constant-density stars

Constant-density stars are excellent idealized models to explore the properties of ultracompact objects. Because of the simplicity of the model, the metric is known analytically in the entire space. Outside the star, the spacetime is described by the Schwarzschild metric. Inside the star, the metric coefficients are given by [69]

$$f(r) = \frac{1}{4R^3} \left( \sqrt{R^3 - 2Mr^2} - 3R\sqrt{R - 2M} \right)^2, \quad (7.3)$$

$$B(r) = \left( 1 - \frac{2Mr^2}{R^3} \right)^{-1}, \quad (7.4)$$

where  $R$  is the radius of the star. The pressure is given by

$$p(r) = \rho_c \frac{\sqrt{3 - 8\pi R^2 \rho_c} - \sqrt{3 - 8\pi r^2 \rho_c}}{\sqrt{3 - 8\pi r^2 \rho_c} - 3\sqrt{3 - 8\pi R^2 \rho_c}}, \quad (7.5)$$

where  $\rho_c = 3M/(4\pi R^3)$  is the density of the uniform star.

<sup>2</sup>To simplify the comparison with the effective potential for wave propagation, here we defined the geodesic potential  $V_{\text{geo}} = E^2 - B(r)f(r)V_r$ , where  $V_r$  is the effective potential adopted in Eq. (29) of Ref. [190].

<sup>3</sup>Similar arguments have also been recently used to suggest that the superradiant instability could lead to turbulent states [261].

### 7.1.2 Thin-shell gravastars

“Gravitational condensate stars”, or gravastars, have been devised to mimic BHs [253]. In these models, the spacetime is assumed to undergo a quantum phase transition in the vicinity of the would-be BH horizon. The latter is effectively replaced by a transition layer and the BH interior by a segment of de Sitter space [262]. The effective negative pressure of the de Sitter interior contributes to sustain the self-gravity of the object for any compactness. In the static case these models have been shown to be thermodynamically [253] and dynamically [154, 263, 264] stable for reasonable equations of state.

Here we focus on the simplest static thin-shell gravastar model, whose exterior metric for  $r > R$  is identical to Schwarzschild whereas the interior,  $r < R$ , is described by a de Sitter metric,

$$f(r) = B(r)^{-1} = 1 - \frac{2M}{R} \frac{r^2}{R^2}, \quad (7.6)$$

where  $M$  is the gravastar mass measured by an observer at infinity and the effective cosmological constant of the de Sitter region is  $\Lambda \equiv 6M/R^3$ . The junction conditions at  $r = R$  surface have already been partially chosen by requiring the induced metric to be continuous across the shell (cf. Ref. [154] for details). Israel’s junction conditions [265] then relate the discontinuities in the metric coefficients to the surface energy  $\Sigma$  and surface tension  $\Theta$  of the shell as [263]

$$[[B^{-1/2}]] = -4\pi R\Sigma, \quad \left[ \left[ \frac{f' B^{-1/2}}{f} \right] \right] = 8\pi(\Sigma - 2\Theta). \quad (7.7)$$

where the symbol “[[ ...]]” denotes the “jump” in a given quantity across the spherical shell. In the simplest model considered here, the coefficient  $B$  is continuous across the shell, and therefore  $\Sigma = 0$ , whereas the surface tension is nonzero.

## 7.2 Perturbations of ultracompact objects

Various classes of perturbations of the metric (7.1) are described by a master equation

$$\left[ \frac{\partial^2}{\partial t^2} - \frac{\partial^2}{\partial r_*^2} + V_{sl}(r) \right] \Psi(r, t) = 0, \quad (7.8)$$

where  $\frac{\partial^2}{\partial r_*^2} = \frac{f}{B} \frac{\partial^2}{\partial r^2} + \frac{f}{2B} \left( \frac{f'}{f} - \frac{B'}{B} \right) \frac{\partial}{\partial r}$  and

$$V_{sl}(r) = f \left[ \frac{l(l+1)}{r^2} + \frac{1-s^2}{2rB} \left( \frac{f'}{f} - \frac{B'}{B} \right) + 8\pi(p_{\text{rad}} - \rho)\delta_{s2} \right], \quad (7.9)$$

where the prime denotes derivative with respect to the coordinate  $r$ , which is related to the tortoise coordinate  $r_*$  through  $dr/dr_* = \sqrt{f/B}$ . In the potential (7.9)  $l \geq s$ ,  $s = 0, 1$  for test Klein-Gordon and Maxwell fields, respectively, whereas  $s = 2$  for axial perturbations of

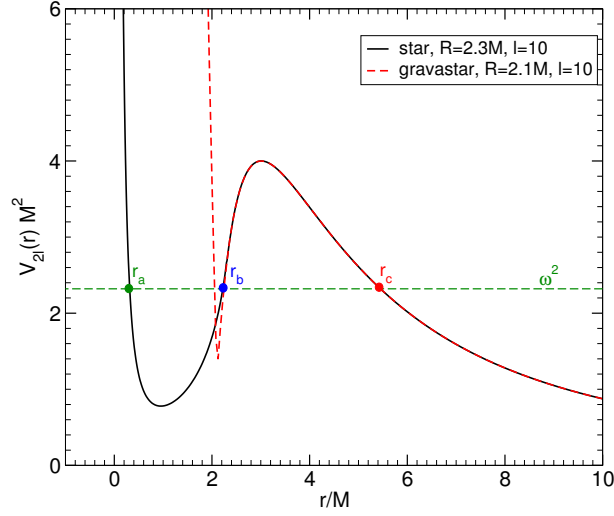


Figure 7.1: Examples of the potential governing linear perturbations of a static ultracompact star. The black solid line and the red dashed line correspond to  $l = 10$  gravitational axial perturbations of a uniform star with  $R = 2.3M$  and of a gravastar with  $R = 2.1M$ , respectively.

a (generically anisotropic) fluid in general relativity (where  $p_{\text{rad}} = T_r^r$  and  $\rho = -T_t^t$  are the radial pressure and the energy density of the fluid, respectively). In the latter case, using the field equations, the potential above reduces to

$$V_{2l}(r) = f \left[ \frac{l(l+1)}{r^2} - \frac{6m(r)}{r^3} - 4\pi(p_{\text{rad}} - \rho) \right], \quad (7.10)$$

where  $m(r)$  is defined through  $B(r) = (1 - 2m(r)/r)^{-1}$ . Clearly, assuming a time dependence  $\Psi(r, t) = \psi(r)e^{-i\omega t}$ , the radial function  $\psi$  satisfies a Schrodinger-like equation,  $d^2\psi/dr_*^2 + [\omega^2 - V_{sl}(r)]\psi = 0$ .

For a thin-shell gravastar, the gravitational perturbations in the interior of the star are described by the potential (7.10), with  $-p_{\text{rad}} = \rho = \Lambda/(8\pi)$  and  $m(r) = M(r/R)^3$ . In this case the Schrodinger-like problem in the interior simplifies considerably and can be solved analytically in terms of hypergeometric functions  $F[a, b, c; z]$  [154]

$$\psi(r) = r^{l+1} (1 - C(r/2M)^2)^{i\frac{M\omega}{\sqrt{C}}} F \left[ \frac{l+2 + i\frac{2M\omega}{\sqrt{C}}}{2}, \frac{l+1 + i\frac{2M\omega}{\sqrt{C}}}{2}, l + \frac{3}{2}; \frac{Cr^2}{4M^2} \right], \quad (7.11)$$

where  $C = (2M/R)^3$ . The master function above describes *both* gravitational axial and polar perturbations of the gravastar interior and has to be matched with the Regge-Wheeler or Zerilli function in the Schwarzschild exterior using suitable junction conditions [154].

## 7.3 Long-lived modes of ultracompact objects

### 7.3.1 A WKB analysis

As previously discussed, ultracompact stars have two light rings. From a point of view of massless fields, which propagate as null particles in the eikonal regime, the light rings effectively confine the field and give rise to long-lived modes. Before analyzing in some detail each of the specific geometries, let us perform a WKB analysis of these trapped modes.

The effective potential for wave propagation,  $V_{sl}(r)$ , shares many similarities with the geodesic potential  $V_{\text{geo}}(r)$  to which it reduces in the eikonal limit [190]: it has a local maximum, diverges at the origin and is constant at infinity. Examples of the effective potential  $V_{sl}(r)$  are shown in Fig. 7.1, corresponding to  $l = 10$  gravitational axial perturbations of a uniform star with compactness  $M/R \sim 0.435$  (black solid curve) and of a thin-shell gravastar with compactness  $M/R \sim 0.476$  (dashed red curve), respectively.

Because the potential necessarily develops a local minimum, it is possible to show that in the eikonal limit ( $l \gg 1$ ) the spectrum contains long-lived modes whose damping time grows exponentially with  $l$ . In order to do so, we follow closely the analysis by Festuccia and Liu [266, 267]<sup>4</sup>.

In the eikonal limit the potential can be approximated as  $V_{sl}(r) \sim l^2 f/r^2$ . Let us define  $r_a$ ,  $r_b$  and  $r_c$  to be the three real turning points of  $\omega_R^2 - V_{sl}(r) = 0$  as shown in Fig. 7.1 for the black solid curve. When such turning points exist, the real part of the frequency of a class of long-lived modes in four spacetime dimensions is given by the WKB condition (see also Ref. [268])

$$\int_{r_a}^{r_b} \frac{dr}{\sqrt{f/B}} \sqrt{\omega_R^2 - V_{sl}(r)} = \pi(n + 1/2), \quad (7.12)$$

where  $n$  is a positive integer and we have used the fact that  $dr_* = dr/\sqrt{f/B}$ . The imaginary part of the frequency  $\omega_I$  of these modes is given by

$$\omega_I = -\frac{1}{8\omega_R\gamma} e^{-\Gamma}, \quad (7.13)$$

where

$$\Gamma = 2 \int_{r_b}^{r_c} \frac{dr}{\sqrt{f/B}} \sqrt{V_{sl}(r) - \omega_R^2}, \quad (7.14)$$

$$\gamma = \int_{r_a}^{r_b} \frac{dr}{\sqrt{f/B}} \frac{\cos^2 \chi(r)}{\sqrt{\omega_R^2 - V_{sl}(r)}}, \quad (7.15)$$

$$\chi(r) = -\frac{\pi}{4} + \int_{r_a}^r \frac{dr}{\sqrt{f/B}} \sqrt{\omega_R^2 - V_{sl}(r)}. \quad (7.16)$$

<sup>4</sup>These authors study the Schwarzschild-anti-de Sitter geometry, for which  $V_{sl}(r)$  shares many of the properties above: it diverges at the boundaries, vanishes near the horizon and always displays a maximum at the unstable light ring.

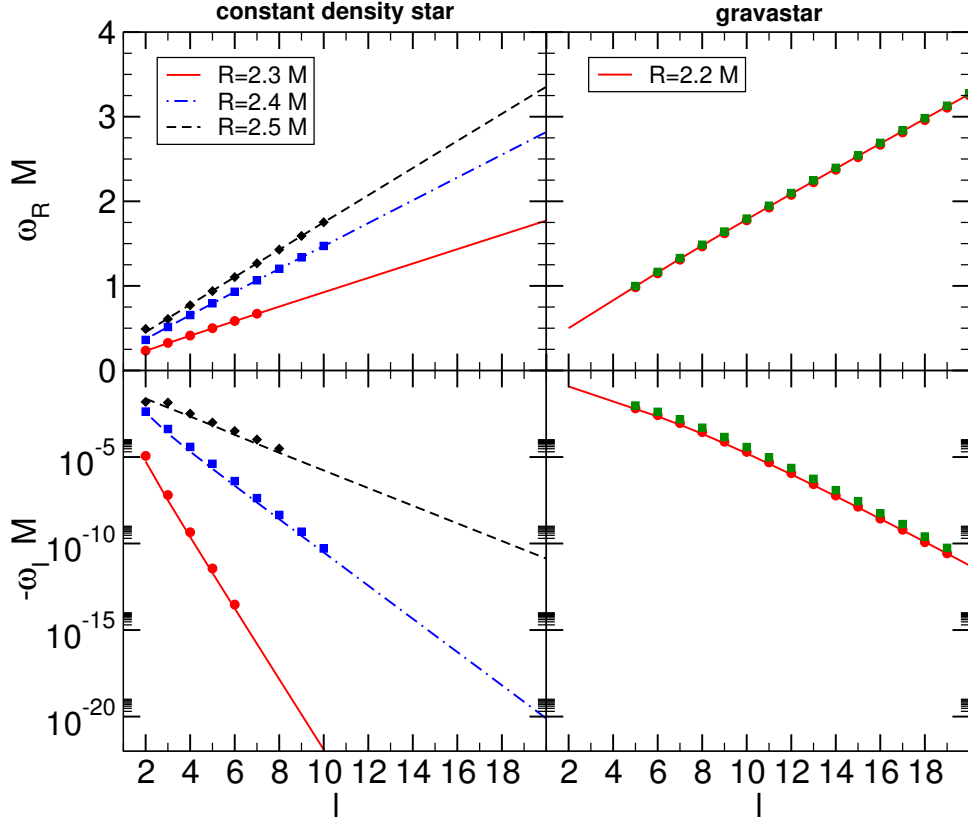


Figure 7.2: Real and imaginary parts of the long-lived modes of a uniform star for different compactness (left panels) and for a gravastar with  $R = 2.2M$  (right panels). The lines are the WKB results, whereas markers show the numerical points (when available) obtained using direct integration or continued fractions. For uniform stars we show gravitational axial modes, whereas for gravastar we show both axial modes (red circles) and gravitational polar modes with  $v_s = 0.1$  (green squares), where  $v_s$  is related to the speed of sound on the shell [154]. Note that the modes of a static gravastar become isospectral in the high-compactness regime [154].

By expanding Eqs. (7.12) and (7.13), one can show that, to leading order in the eikonal limit, the mode frequency reads

$$\omega \sim a l - i b e^{-cl} \quad l \gg 1, \quad (7.17)$$

where  $a$ ,  $b$  and  $c$  are positive constants. By expanding Eq. (7.12) near the minimum of the potential displayed in Fig. 7.1, it is possible to show that

$$a \sim \Omega_{\text{LR2}} \equiv \frac{\sqrt{f(r_{\text{LR2}})}}{r_{\text{LR2}}}, \quad (7.18)$$

where  $\Omega_{\text{LR2}}$  is the angular velocity of the *stable* null geodesic at the light-ring location  $r = r_{\text{LR2}}$ . For constant-density stars this orbital frequency reads

$$\Omega_{\text{LR2}} = \frac{2\sqrt{M(R - 9M/4)}}{R^2}, \quad (7.19)$$

and is vanishing in the Buchdahl limit  $R \rightarrow 9M/4$ . For gravastars

$$\Omega_{\text{LR2}} = \frac{\sqrt{R - 2M}}{R^{3/2}}, \quad (7.20)$$

and is vanishing at the Schwarzschild limit  $R \rightarrow 2M$ .

### 7.3.2 Numerical results: the spectrum of linear perturbations

A numerical computation of the quasinormal mode (QNM) frequencies [109] shows that long-lived modes are indeed part of the spectrum, as indicated by the WKB analysis. In Fig. 7.2 we present some of these modes for constant-density ultracompact stars with  $R/M = 2.3, 2.4, 2.5$  (left panels) and for a thin-shell gravastar with  $R = 2.2M$  (right panels). The exact numerical values obtained via direct integration and continued fractions (cf. e.g. Ref. [109] for details) are denoted by markers and are compared against the WKB prediction (lines). These independent computations are in very good agreement, validating each other.

For uniform stars (left panels of Fig. 7.2) we present the gravitational axial modes which are governed by the effective potential in Eq. (7.10). The existence of trapped modes in ultracompact stars was discovered in Ref. [269] (see also [270, 271] and [132] for a review). Our analysis perfectly agrees with previous results and extends the latter in the case of large values of  $l$ .

For gravastars (right panels of Fig. 7.2) we present both gravitational axial and gravitational polar perturbations. The latter depends on the equation of state of the thin-shell through the parameter  $v_s^2 \equiv \partial\Sigma/\partial\Theta$ , which is related to the speed of sound on the shell. To compute the gravastar modes we matched the exact solution (7.11) to the Regge-Wheeler or the Zerilli function in the Schwarzschild exterior for axial or polar modes, respectively, as discussed in detail in Ref. [154].

We note that the critical value of  $l$  for which the behavior (7.17) sets in depends strongly on the compactness: the larger the star radius (constrained to  $R/M \lesssim 3$ ) the larger the critical value of  $l$ . Nonetheless, the qualitative behavior is largely independent of the compactness, the nature of the modes and even the nature of the ultracompact object, as long as the latter is compact enough to support long-lived modes. In particular, our results show that trapped modes also exist in the polar sector of gravitational perturbations, which are coupled to the fluid perturbations [132] and that dominate the linear response of the object to external sources.

In the top panel of Fig. 7.3 we show a representative example of the eigenfunctions corresponding to the long-lived modes of an ultracompact object. This plot refers to a uniform star with  $R = 2.3M$ , but different choices of the compactness and different models give similar results. The eigenfunctions are confined within the unstable light ring and within the star. Furthermore, they peak close to the location of the stable light ring and high- $l$  eigenfunctions are more and more localized around  $r \sim r_{\text{LR2}}$ . It will be important in the following (cf. Sec. 7.5) to observe that the eigenfunctions spread over a distance  $R/l$  in the angular direction and  $\sim l^{-1/2}$  in the radial direction.

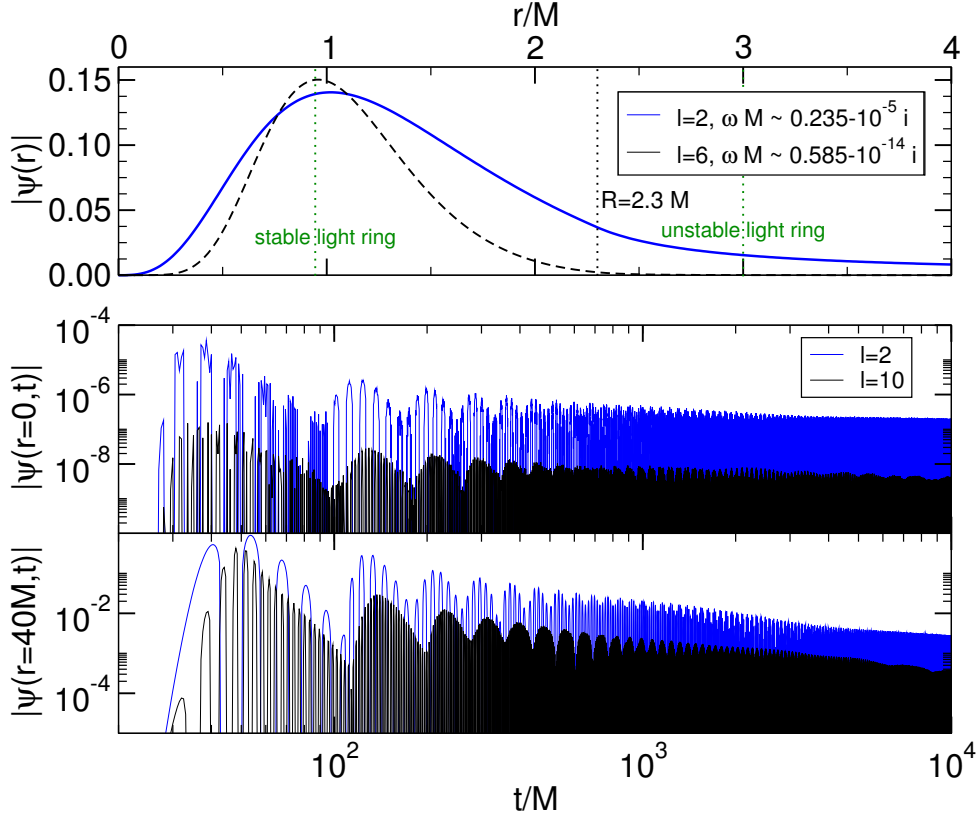


Figure 7.3: Top panel: gravitational axial eigenfunctions of an ultracompact star for  $l = 2$  and  $l = 10$ . The radius of the star,  $R = 2.3M$ , is marked by a vertical line. High- $l$  modes correspond to eigenfunctions which are localized near the stable light ring. Middle and bottom panels: time evolution of a scalar Gaussian wavepacket with width  $\sigma = 4M$  centered at  $r_0 = 6M$  in the background of a constant-density star of radius  $R = 2.3M$  for  $l = 2$  and  $l = 10$ . The waveform extracted at  $r = 0$  (middle panel) and  $r = 40M$  (bottom panel). Note that the Schwarzschild ringdown phase lasts until  $t \sim 60M$ .

### 7.3.3 Numerical results: time evolution of wavepackets

In the middle and bottom panels of Fig. 7.3 we summarize the evolution of a Gaussian scalar wavepacket in the background of an ultracompact constant-density star. Initially the wavepacket is localized outside the star and has the form

$$\dot{\Psi}(0, r) = \exp \left[ -\frac{(r + 2 \log(r - R) - r_0)^2}{\sigma^2} \right]. \quad (7.21)$$

where  $r_0$  and  $\sigma$  denote the initial position and the width of the packet. The overdot denotes time derivative.

#### Imprints of the Schwarzschild BH geometry on ultracompact stars

As shown in Fig. 7.3, the signal initially consists of a damped sinusoid, whose frequency and damping time match closely the quasinormal frequencies of the *Schwarzschild BH* space-

time [109, 255]. Thus, although the QNMs of Schwarzschild BHs are *not* part of the spectrum of this ultracompact star, they are still excited at early times and are an important part of the response of this system. Such interesting “mode camouflage” phenomenon was observed earlier in the context of BHs surrounded by matter [135, 260]. In the present context, it also has a natural interpretation: the modes of BHs “live” on the external null circular geodesic [190], which is also present for ultracompact stars. Accordingly, we expect the BH ringdown stage to dominate until other scales become important, in our case, after fluctuations cross the star.

This feature has two important consequences for gravitational-wave astronomy and for attempts at proving or ruling out the existence of BHs. Any spacetime which – close to the unstable null circular geodesic – resembles the Kerr geometry is expected to ringdown like a Kerr BH at early times. In other words, both dirty BHs and ultracompact stars will show a dominant ringdown stage which is indistinguishable from that of vacuum Kerr BHs. This was observed for dirty BHs in Ref. [135, 260] and our results show that it holds even for ultracompact objects, which can be looked at as a deformed BH with no horizon. Thus, current gravitational-wave ringdown searches which *assume* the source is described by the Kerr geometry [272, 273] are most likely to perform well under any circumstances.

These results also have an impact on proposed methods to discriminate between BHs and other objects. These proposals typically hinge on the no-hair theorem and the characteristic oscillation modes of these objects [10]. The argument is that different objects have different oscillation modes, and the modes of BHs are known very accurately; thus, the measurement of these modes can be used to infer which object is oscillating. While the reasoning is correct, in practice the ringdown mode of any object which is compact enough will be dominated at early times by a universal ringdown: it is a superposition of the QNMs of a vacuum BH.

Furthermore, it is commonly believed that different boundary conditions (for example due to the presence of an event horizon instead that of a surface) would drastically change the spectrum of ringdown modes. While it is true that the full QNM spectrum (as obtained in the frequency domain) is strongly affected by the boundary conditions, nonetheless the early-time behavior of the waveforms is mostly dominated by the macroscopic “local” properties of the object (i.e. by the geometry near the unstable light ring), irrespectively of the existence of a horizon [135, 260]. It is still possible – though probably more challenging – to dig out the signal in the late-time stage, which will contain the object’s true modes, but this would require large signal-to-noise detections [135, 260].

### Long-lived perturbations

The mode camouflage phase we just described lasts roughly  $60M$ , which corresponds to the (roundtrip) light-crossing time for the star under consideration. The light crossing time seems to be decisive in the low-frequency modulation of the signal. At very late times, the modes of the system set in and the field decays very slowly. The decay rate depends on the initial conditions and on the model, but it is always slower than  $1/t$ . For example, for the case shown in the bottom panels of Fig. 7.3 we estimate the decay to be at most  $\sim t^{-0.4}$  inside the star for the  $l = 10$  mode *assuming* it is a power-law decay. The results are equally well described, at late-times, by a  $1/\log t$  behavior. The reason why the signal decays so slowly at late-times is apparent from the top panel of Fig. 7.3 and also in Fig. 7.4: the corresponding eigenfunctions in the frequency domain are trapped inside the star and localized near the stable light ring.

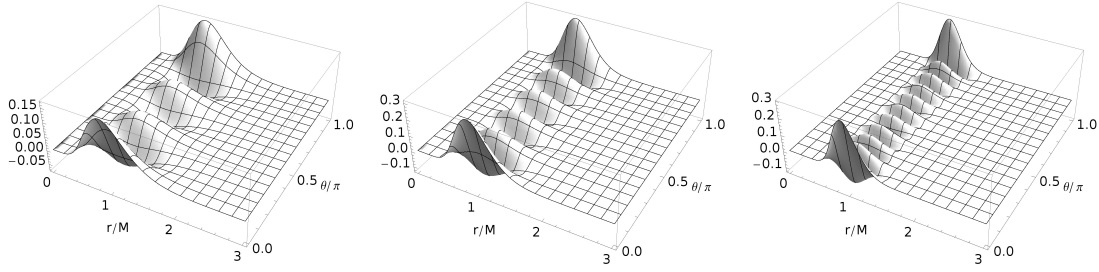


Figure 7.4: Scalar eigenfunctions of an ultracompact star with  $R = 2.3M$  for  $m = 0$  and  $l = 6, 10, 20$  (from left to the right). We find that the eigenfunctions have a typical width that scales as  $l^{-1}$  in the angular direction and a width in the radial direction that depends on the model used for the star, but typically ranges between  $l^{-0.4} - l^{-0.8}$ . Therefore, the “aspect ratio” of the perturbation  $\sim l^{0.6} - l^{0.2}$  grows in the large- $l$  limit and the perturbation becomes more and more elongated along the radial direction.

## 7.4 Spinning ultracompact objects and the ergoregion instability

The long-lived modes that generically exist for any static ultracompact star can turn unstable when the star is spinning. This instability is related to the *ergoregion instability* which affects any spacetime possessing an ergoregion but not a horizon [256]. The ergoregion is defined as the spacetime region in which observers must be dragged along with rotation and cannot remain at rest. This corresponds to the timelike Killing vector  $\xi_t$  becoming spacelike, i.e.

$$\xi_t \cdot \xi_t = g_{tt}(r, \theta) > 0. \quad (7.22)$$

In fact, the existence of long-lived modes in the static limit is *the* underlying reason of the ergoregion instability. This has been first discussed by Comins and Schutz, who studied a scalar field propagating in a slowly-rotating background in the eikonal limit [259]. They considered the line element

$$ds^2 = -F(r)dt^2 + B(r)dr^2 + r^2d\theta^2 + r^2\sin^2\theta(d\phi - \varpi(r)dt)^2, \quad (7.23)$$

which, although not being a solution of Einstein’s equations coupled to a fluid, should approximate the exact metric describing a spinning star in the case of slow rotation and high compactness [259]. In such metric, the ergoregion is defined by

$$\varpi(r) \sin \theta > \frac{\sqrt{F(r)}}{r}, \quad (7.24)$$

and its boundary, the ergosphere, is topologically a torus. In the eikonal limit, the Klein-Gordon equation in the background (7.23) can be written in the form [259]

$$\psi'' + m^2 \frac{B}{F} (\bar{\omega} + V_+) (\bar{\omega} + V_-) \psi = 0, \quad (7.25)$$

where  $\bar{\omega} = \omega/m$  is a rescaled frequency,  $m$  is the azimuthal number associated to the axisymmetry of the background, and

$$V_{\pm} = -\varpi \pm \frac{\sqrt{F}}{r}, \quad (7.26)$$

are the effective potentials that describe the motion of (counter-rotating for the plus sign and co-rotating for the minus sign) null geodesics in the equatorial plane of the geometry (7.23).

Now, the boundary of the ergoregion (if it exists) corresponds to two real roots of  $V_+ = 0$  and  $V_+ < 0$  inside the ergoregion. Because  $V_+ \rightarrow +\infty$  at the center and attains a positive finite value in the exterior, it is clear that the ergoregion must contain a point in which  $V_+$  displays a (negative) local minimum. This simple argument shows the important result that the presence of an ergoregion in a horizonless object implies the existence of *stable* counter-rotating photon orbits.

Furthermore, Eq. (7.25) supports unstable modes whose instability time scale in the eikonal limit grows exponentially,  $\tau \equiv 1/\omega_I \sim 4\alpha e^{2\beta m}$ , where  $\alpha$  and  $\beta$  are two positive constants [259]. This instability can be understood from the fact that the corresponding modes are localized near the stable photon orbit, which is situated within the ergosphere, and are confined within the star. This confinement provides the arena for the instability to grow through the negative-energy states that are allowed within the ergoregion [256]. Likewise, this argument also explains why spinning BHs – that also possess a light ring and an ergoregion – are linearly stable, because the presence of the horizon forbids the existence of trapped modes.

Although the analysis of Ref. [259] is approximate, such result has been subsequently extended to low values of  $(l, m)$  [274] and to gravitational axial perturbations [275]. In both cases, the instability time scale has been found to be much shorter, ranging from seconds to minutes for low- $m$  gravitational perturbations of uniform constant stars [275]. The conclusion of these studies is that, if long-lived modes exist in the static case, they become unstable for sufficiently high rotation rates. The onset of the instability precisely corresponds to the appearance of an ergoregion in the interior of an ultracompact star [275]. The same picture applies to other ultracompact objects such as gravastars and boson stars, which become linearly unstable when they possess an ergoregion [252] with an instability time scale that depends strongly on the compactness [257]. The same instability affects also Kerr-like BH geometries spinning above the Kerr bound (so-called superspinars [254]) when the dissipation at the horizon is not enough to quench the negative-energy states trapped within the ergoregion [276]. Finally, the ergoregion instability of acoustic geometries was recently reported [277, 278].

## 7.5 The nonlinear regime

The argument for nonlinear instability given earlier is anchored on the large lifetimes of linear fluctuations. This argument carries over equally to other more familiar contexts, e.g. to conservative systems with normal modes. Generically however, normal-mode systems are an idealization and neglect *any* form of dissipation. The outstanding feature of ultracompact stars is that gravitational-wave dissipation is already included and is negligible.

We can foresee at least two possible outcomes for the nonlinear development of ultracompact stars; which one is actually chosen depends on the details of the object's composition:

**I. Other dissipation mechanisms are relevant**, in which case the star is stable. Loss of energy through gravitational-wave emission is suppressed for ultracompact stars, but this is not the only dissipation mechanism. For example, viscosity in neutron stars plays an important role on relatively short time scales, and may quench possible nonlinear instabilities for very compact stars. Simple expressions for the dissipative time scales as functions of the angular number  $l$  and the parameters of a neutron star were derived in Ref. [279]:

$$\tau_\eta = \frac{10}{(l-1)(2l+1)} \rho_{14}^{-5/4} T_5^2 \left( \frac{R}{4.5 \text{ km}} \right)^2 \text{ s}, \quad (7.27)$$

$$\tau_\kappa = 10^{14} \tau_\eta \frac{(l-1)^2}{l^3} \rho_{14}^{19/12} T_5^{-2} \left( \frac{R}{4.5 \text{ km}} \right)^2, \quad (7.28)$$

$$\tau_\zeta > 61 \tau_\eta \frac{\eta}{\zeta}, \quad (7.29)$$

where  $\rho_{14} = \rho/(10^{14} \text{ g/cm}^3)$ ,  $T_5 = T/(10^5 \text{ K})$ ,  $T$  is the neutron-star temperature,  $\tau_\eta$ ,  $\tau_\kappa$  and  $\tau_\zeta$  are the time scales for shear viscosity, thermal conductivity and bulk viscosity, respectively, whereas  $\eta$ ,  $\zeta$  and  $\kappa$  are dissipation coefficients.

These are order-of-magnitude estimates, valid in principle only for neutron stars. Any hypothetical ultracompact star will however also be affected by dissipation of this nature, whose time scale becomes shorter at shorter scales, i.e., larger  $l$ . Note, however, that some modes are only weakly coupled with the fluid perturbations (e.g. gravitational axial modes and  $w$ -modes in general [132]) so that only a small fraction of the energy contained in such modes can be dissipated through viscosity. Furthermore, the interior of exotic ultracompact stars could be made of a superfluid as in self-gravitating Bose-Einstein condensates [144] and also in this case viscosity is expected to be negligible.

**II. Nonlinear effects become relevant.** Let us now assume that there is no dissipation mechanism strong enough to damp linear perturbations on realistic time scales. Recent studies of gravitational collapse of small scalar-field wavepackets in anti-de Sitter geometries (which are another example of conservative systems with normal modes at linear level), suggest that broad classes of initial data *always* collapse to form BHs, through a “weakly turbulent” mechanism [280]. The process, still not well understood, involves blueshift of initial perturbations which eventually collapse to a small BH. Although originally discovered in anti-de Sitter, the mechanism works also in flat spacetime [281] if the boundary conditions prevent leakage of energy to infinity. Generically, one expects nonlinear effects to play a role whenever the linear fluctuations are longer lived than any nonlinear timescale. It is unknown whether certain extra

conditions on the resonant frequencies of the system have to be met [282, 283], but it is likely that the mechanism is always active at *finite* amplitude-perturbations. Ultracompact stars trap high multipole wave very effectively, and we therefore argue that these modes are potentially subject to the weakly turbulent instability.

If active for ultracompact stars, it most likely involves a growth of curvature close to the stable null geodesic and consequent collapse to small BHs. The number of such small BHs would be tied to the angular number of the mode in question and would scale as  $l$ . For large enough initial fluctuation, the BHs that would form can be large enough to swallow the star in less than a Hubble time.

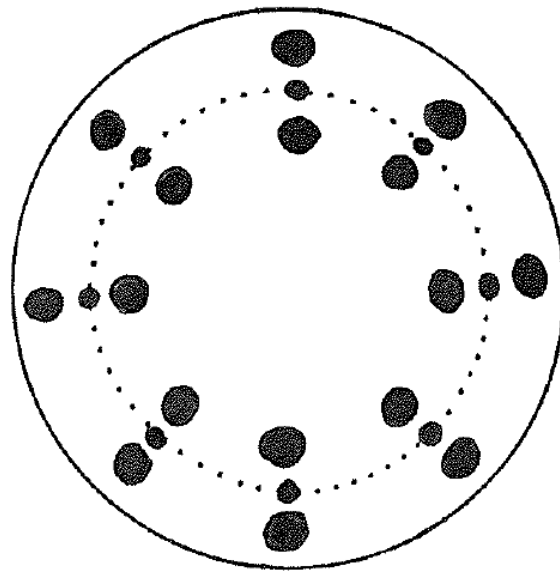


Figure 7.5: Pictorial description of the nonlinear evolution of a perturbed ultracompact object. The figure represents the equatorial density profile of the object. The solid circumference represents the unperturbed surface, whereas the dashed line represents the stable light ring at its interior. Solid circles represent condensation of nonlinear-growth structures which are the bi-product of the DCF instability. The core is left unperturbed and is now a less compact – and therefore stable – configuration. Likewise, the the solid circles are also stable and subsequent time evolution presumably leads to a fall-back on the core. Gravitational radiation, generated during this and subsequent repetitions of this process will lead to loss of mass and possibly a reduction of the star’s compactness.

Do nonlinear effects always conspire to produce catastrophic results? The answer is no. Recent studies show that there exist initial datas which are nonlinearly stable against such weakly turbulent mechanism [282–284]. How generic such initial conditions are is unclear at the present time. Nevertheless, a plethora of other nonlinear effects might play a role and one in particular is likely to be dominant: fragmentation via a “Dyson-Chandrasekhar-Fermi” (DCF) mechanism, which is akin to the Rayleigh-Plateau fragmentation of fluid cylinders [285–288]. To show this point we observe that, at linear level, the eigenfunctions have a width  $\sim l^{-1}$  in the angular direction  $\theta$  and a width  $\sim l^{-\chi}$  in the radial direction, where  $\chi < 1$  depends on the star model (cf. Figs. 7.3 and 7.4 for a representative example of a constant-density star). Therefore the perturbations are asymmetric, elongated along the radial direction and their elongation grows with  $l$ .

Let us now assume for simplicity that we are dealing with axisymmetric modes. Axisymmetric distributions of matter such as these elongated, long-lived modes are unstable against the same DCF mechanism that affects thin cylinders or rings of matter [285–288]. The minimum growth time scale of this instability scales as  $\tau_{\text{DCF}} \sim \delta\rho^{-1/2}$ , where  $\delta\rho$  is the density fluctuation. The requirement that nonlinearities take over is that  $\tau_{\text{DCF}}$  be much smaller than the lifetime of linear fluctuations. Because the latter grows exponentially with  $l$  for an ultracompact object, it is easy to show that fragmentation becomes important already at moderately small values of  $l$  even for  $\delta\rho/\rho \sim 10^{-16}$  or smaller. In other words, we are arguing that even though “weak turbulence” may be negligible, fragmentation instabilities are not.

The fragmentation of the linear eigenfunction leads to a configuration which can look like that depicted in Fig. 7.5 (see also nonlinear results for fragmentation of black strings [289]): it consists on a spherically symmetric core surrounded by droplets of the star fluid, whose sizes are much smaller than that of the original star. It is easy to see that these smaller droplets, although of the same material as the original star, are much less compact because they are much smaller and are therefore expected to be themselves stable. Likewise, the core of the star is also less compact and stable. On longer time scales, these droplets re-arrange and fall into the core, and the process continues. The dynamical picture looks like that of a “boiling” fluid, and radiates a non-negligible amount of radiation. If this scenario is correct, a sizable fraction of the object’s initial mass can be dispersed to infinity, possibly reducing the compactness of the final object to values which no longer allow for the existence of light rings.

## 7.6 Conclusions

Strong and growing evidence suggests that supermassive compact objects in our Universe are BHs. Nevertheless, incontrovertible proofs are hard to come by and would likely require detection of Hawking radiation from the event horizon, the latter being negligible for astrophysical objects. As such, fundamental mechanisms that forbid the existence of ultracompact stars are mostly welcome and would automatically imply that (the much more easily achievable) observations of a light ring are detections of BHs in fact. There are at least two known mechanisms that might do just that. One such mechanism is the possible nonlinear instability of any ultracompact star, which have one unstable light ring in its exterior (and another stable light ring in its interior). We have provided additional evidence that such objects have long-lived fluctuations which may fragment the star and make it less compact on long time scales. Alternatively, weak turbulence might lead to collapse of the star into a BH. Whether or not the instability is actually relevant depends on possible additional dissipation mechanisms.

When rotation is added, long-lived fluctuations become unstable already at the *linear* level. This is also known as ergoregion instability, and has been used to exclude highly spinning, compact objects [252, 254, 276]. Taken together, these results suggest that the observation of the light ring alone – a challenging task which is nevertheless within the reach of next facilities such as, for instance, the Event Horizon Telescope [290] – is evidence enough for the existence of BHs, a truly remarkable consequence.

Clearly, future work should consider the difficult but fundamental problem of following long-lived fluctuations through the nonlinear regime, to understand the role of dissipation, the

time scale associated with possible nonlinear instabilities, and the issue of the final state.

## **Part III**

# **Absorption and scattering of planar scalar waves**

# Chapter 8

## Absorption of planar massless scalar waves by Kerr black holes

Black holes (BHs) [127] are among the most intriguing predictions of general relativity (GR) [124]. In electrovacuum, BHs are described by the Kerr-Newman family of solutions, which are governed by just three parameters: mass, spin and electric charge. The no-hair theorem [108] implies that black holes cannot support additional degrees of freedom, which suggests that in essence black holes are rather simple objects, even if their astrophysical environments are likely to be extremely complex.

BHs are believed to populate the galaxies [291]. The realization that supermassive rotating BHs reside at the center of active galactic nuclei has had a profound impact [292]. Some of these rotating BHs are expected to be spinning very close to their upper rotating limit [293,294], and so the phenomenology around rotating BHs is of major importance to astrophysics. This motivates careful study of the nature and observational consequences of the Kerr metric, which describes a rotating BH in GR. An improved understanding of the Kerr BH will also help us to understand more complicated structures, such as rotating BHs in modified theories of gravity [8,26,295,296].

One aspect of Kerr phenomenology is the absorption and scattering of particles by BHs. Particles are described by (quantum and fluid) field theories, and so the absorption and scattering of particles is naturally related to the absorption and scattering of fields, which may have spin, mass and charge. Spinless (i.e. scalar) fields are particularly important, both as a particle model (e.g., for pseudoscalar mesons) and as a first model for bosonic fields with spin (e.g., the electromagnetic field). In theories that seek to go beyond the Standard Model, light scalar bosons may play important roles; for instance, in axiverse models [165,235] and in scalar field dark matter models [297]. The discovery of a Higgs-like particle by the ATLAS and CMS collaborations has given extra motivation to the study of scalar fields [232].

The absorption and scattering cross sections of planar waves by black holes have been extensively studied. Recently, a unified picture of the scattering of massless planar waves by Schwarzschild BHs was presented [298]. This builds upon the work of many authors in investigating the absorption cross section of planar waves by the Schwarzschild black hole [299–303].

Various studies have also been made considering charged black holes as central scatterers [304–307]. Despite their physical relevance, rotating BHs have received less attention in the literature, with several notable exceptions [308–310]. Absorption and scattering cross sections by acoustic BH analogues have also been recently investigated [311–314].

In this chapter, we analyze the absorption cross section of a planar massless scalar wave impinging upon a Kerr BH, giving emphasis to the general case in which the direction of incidence is not aligned with the axis of rotation. The chapter is ordered as follows. In Sec. 8.1 we describe the separation of variables for the massless scalar field in the Kerr spacetime in Boyer-Lindquist coordinates, and the physical boundary conditions for planar wave scattering. In Sec. 8.2 we give expressions for the absorption cross section in the Kerr spacetime, and identify the co and counterrotating contributions. We describe the low- and high-frequency regimes, and present a new asymptotic formula for the absorption cross section arising from the complex angular momentum method. In Sec. 8.3 we present a selection of numerical results, considering different values of the incident angle, and of the BH rotation parameter. We conclude with a discussion in Sec. 8.4. Throughout, we use natural units ( $c = G = \hbar = 1$ ), and the metric signature  $(+, -, -, -)$ .

## 8.1 Scalar field in the Kerr spacetime

In the standard Boyer-Lindquist coordinate system  $(t, r, \theta, \varphi)$ , the Kerr BH is described by the line element [107]

$$ds^2 = \left(1 - \frac{2Mr}{\rho^2}\right) dt^2 + \frac{4Mar \sin^2 \theta}{\rho^2} dt d\varphi - \frac{\rho^2}{\Delta} dr^2 - \rho^2 d\theta^2 - \left(r^2 + a^2 + \frac{2Mra^2 \sin^2 \theta}{\rho^2}\right) \sin^2 \theta d\varphi^2, \quad (8.1)$$

in which  $\Delta = r^2 - 2Mr + a^2$  and  $\rho^2 = r^2 + a^2 \cos^2 \theta$ . From the asymptotic behavior, one may infer that  $M$  is the mass of the Kerr BH and  $a$  its angular momentum per unit mass ( $a = J/M$ ). Here we restrict ourselves to the regime in which the Kerr metric describes a BH spacetime, i.e.,  $a \leq M$ . For  $a < M$  the Kerr BH has two horizons. The inner (Cauchy) horizon is at  $r_- = M - \sqrt{M^2 - a^2}$  and the outer (event) horizon is at  $r_+ = M + \sqrt{M^2 - a^2}$ . If  $a = M$  we have an extreme Kerr BH with an event horizon at  $r_+ = r_- = M$ . The case  $a > M$  corresponds to a naked singularity.

A massless scalar field  $\Phi(x^\mu)$  in a curved background is governed by

$$\frac{1}{\sqrt{-g}} \partial_\mu (\sqrt{-g} g^{\mu\nu} \partial_\nu \Phi) = 0, \quad (8.2)$$

where  $g_{\mu\nu}$  are the covariant metric components of the Kerr spacetime,  $g$  the metric determinant and  $g^{\mu\nu}$  are the contravariant metric components. Here we shall be interested in monochromatic wave-like solutions of Eq. (8.2), which can be obtained by separation of variables [119, 120],

so that we may write:

$$\Phi = \frac{U_{\omega lm}(r)}{\sqrt{r^2 + a^2}} S_{\omega lm}(\theta) e^{im\varphi - i\omega t}. \quad (8.3)$$

The functions  $S_{\omega lm}(\theta)$  are the standard oblate spheroidal harmonics [121], which will be normalized according to

$$2\pi \int d\theta \sin \theta |S_{\omega lm}(\theta)|^2 = 1. \quad (8.4)$$

The radial functions  $U_{\omega lm}(r)$  obey the following differential equation

$$\left( -\frac{d^2}{dx^2} + V_{\omega lm}(x) \right) U_{\omega lm}(x) = \omega^2 U_{\omega lm}(x), \quad (8.5)$$

with an effective potential given by

$$V_{\omega lm}(x) = -\frac{1}{(r^2 + a^2)^2} [m^2 a^2 - 4Mma\omega r + \Delta(\lambda_{lm} + \omega^2 a^2)] + \Delta \frac{\Delta + 2r(r - M)}{(r^2 + a^2)^3} - \frac{3r^2 \Delta^2}{(r^2 + a^2)^4}. \quad (8.6)$$

In Eq. (8.5) we made use of the tortoise coordinate  $x$  of the Kerr spacetime, defined through

$$dx = \frac{r^2 + a^2}{\Delta} dr. \quad (8.7)$$

The constants  $\lambda_{lm}$  are the eigenvalues of the oblate spheroidal harmonics (cf., e.g., Ref. [315]). The independent solutions of Eq. (8.5) are usually labeled as *in*, *up*, *out* and *down* (see, e.g., Ref. [123]). Here we will be interested in the *in* modes, since they characterize purely incoming waves from the past null infinity, obeying the following boundary conditions

$$U_{\omega lm}(x) \sim \begin{cases} \mathcal{A}_{\omega lm} R_I + \mathcal{R}_{\omega lm} R_I^* & (x/M \rightarrow \infty), \\ \mathcal{T}_{\omega lm} R_{II} & (x/M \rightarrow -\infty). \end{cases} \quad (8.8)$$

The functions  $R_I$  and  $R_{II}$  are given by

$$R_I = e^{-i\omega x} \sum_{j=0}^N \frac{A_{\infty}^j}{r^j}, \quad (8.9)$$

$$R_{II} = e^{-i\tilde{\omega} x} \sum_{j=0}^N (r - r_+)^j A_{r_+}^j, \quad (8.10)$$

where  $\tilde{\omega} \equiv \omega - ma/(2Mr_+)$ , and the coefficients  $A_{\infty}^j$  and  $A_{r_+}^j$  are obtained by requiring

that the functions  $R_I$  and  $R_{II}$  are solutions of the differential equation (8.5) far from the BH and close to the outer horizon, respectively. The coefficients  $\mathcal{R}_{\omega lm}$  and  $\mathcal{T}_{\omega lm}$  are related to the reflection and transmission coefficients, respectively, and obey the following relation

$$\left| \frac{\mathcal{R}_{\omega lm}}{\mathcal{A}_{\omega lm}} \right|^2 = 1 - \frac{\tilde{\omega}}{\omega} \left| \frac{\mathcal{T}_{\omega lm}}{\mathcal{A}_{\omega lm}} \right|^2. \quad (8.11)$$

When  $\omega\tilde{\omega} < 0$ , it follows that  $|\mathcal{R}_{\omega lm}|^2 > |\mathcal{A}_{\omega lm}|^2$ , due to a phenomenon known as superradiance [316].

## 8.2 Absorption cross section

The partial absorption cross section of an asymptotic plane scalar wave propagating in the direction  $\mathbf{n} = (\sin \gamma, 0, \cos \gamma)$  is given by [309, 310]

$$\sigma_{lm} = \frac{4\pi^2}{\omega^2} |S_{\omega lm}(\gamma)|^2 \Gamma_{\omega lm}, \quad (8.12)$$

where the transmission factors are

$$\Gamma_{\omega lm} = \left( 1 - \left| \frac{\mathcal{R}_{\omega lm}^{in}}{\mathcal{A}_{\omega lm}^{in}} \right|^2 \right), \quad (8.13)$$

and the total absorption cross section is

$$\sigma = \sum_{l=0}^{\infty} \sum_{m=-l}^l \sigma_{lm}. \quad (8.14)$$

The cross section is invariant under  $\gamma \rightarrow \pi - \gamma$ . When the direction of incidence is parallel to the spin axis of the BH ( $\gamma = 0$ ), we have  $\sigma_{lm} = 0$  for  $m \neq 0$ . When the direction of incidence lies in the equatorial plane of the BH ( $\gamma = 90$  degrees) we have  $\sigma_{lm} = 0$  for odd values of  $l + m$ , because  $S_{\omega lm}(\pi/2) = 0$  in this case. The total absorption cross section can be decomposed in the following way:

$$\sigma = \sigma^+ + \sigma^-, \quad (8.15)$$

where

$$\sigma^{\pm} = \frac{1}{2} \sum_{l=0}^{\infty} \sigma_{l0} + \sum_{l=1}^{\infty} \sum_{m=1}^l \sigma_{l\pm m}. \quad (8.16)$$

In this way we may separate the absorption cross section into corotating ( $\sigma^+$ ) and counterrotating ( $\sigma^-$ ) contributions.

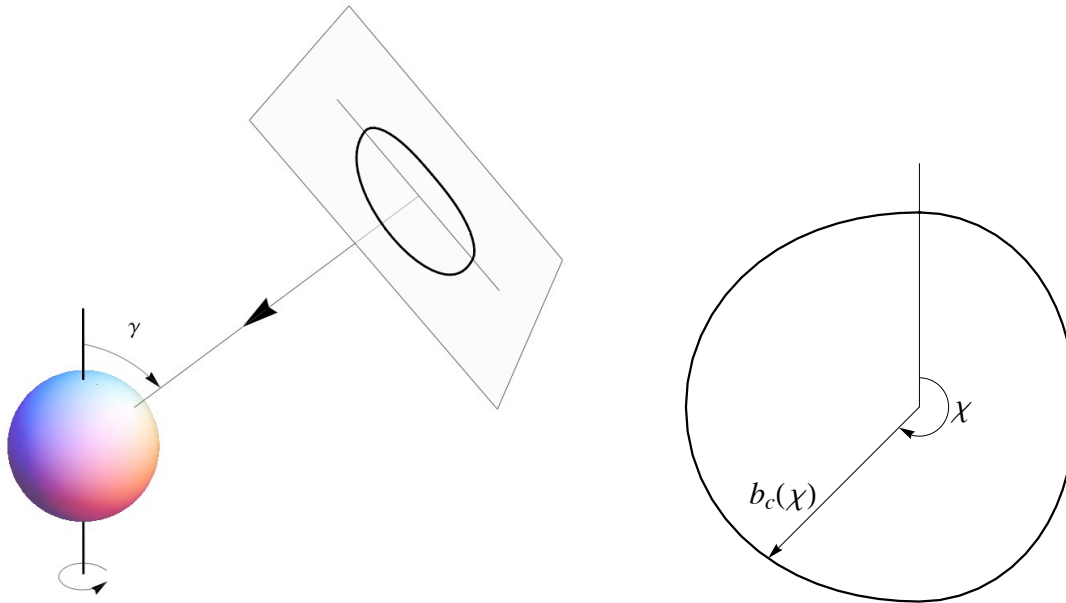


Figure 8.1: Illustrating a planar wave impinging upon a Kerr black hole. The left plot shows a segment of planar wave impinging upon a black hole at angle of incidence  $\gamma$  (where  $\gamma$  is angle between the black-hole rotation axis and the direction of incidence). The right plot shows the locus of absorption, corresponding to that part of the wavefront which is absorbed in the geometric-optics limit. The locus is described by  $b_c(\chi)$ , where  $\chi$  is the angle between a point on the surface and the projection of the BH rotation axis, and  $b_c$  is the critical impact parameter.

### 8.2.1 Low-frequency regime

In the low-frequency regime, it has been shown that the absorption cross section for stationary BHs equals the area of the BH event horizon [317, 318]. This result is quite general and does not depend on the direction of the incident wave. We have checked our numerical results in this limit, computing numerically the absorption cross section for low values of  $\omega$ . Sample values for the area of the horizon are presented in TABLE 8.1. In Sec. 8.3 we compare these low-frequency limits of the absorption cross section with the numerical results for the quantity (8.14), obtaining excellent agreement.

### 8.2.2 High-frequency regime

At high frequencies, under the eikonal approximation, the wave propagates along null geodesics which pass orthogonally through the initial wavefront. Hence, an analysis of absorption can be made by computing the capture cross section of null geodesics impinging on a Kerr BH from infinity. Calculations of the capture cross section may be found in Refs. [127, 319]. Below, we develop a complementary approach which emphasises the geometrical aspects of the calculation.

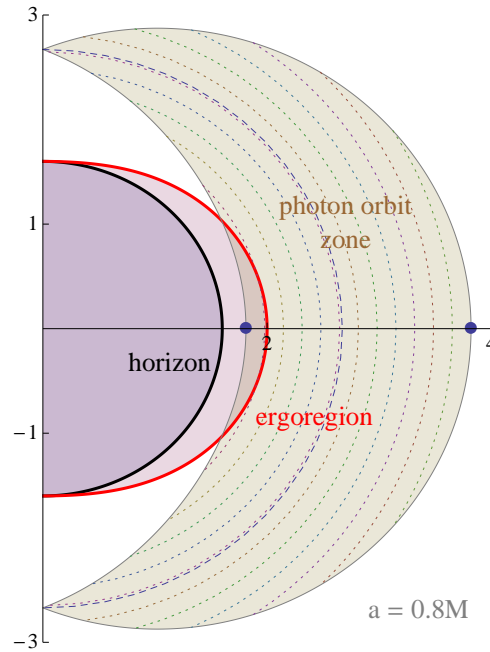


Figure 8.2: Schematic illustration of a slice of a Kerr black hole. Here,  $M = 1$ ,  $a = 0.8M$  and the event horizon [black] and ergoregion [red] are shown as solid lines. The photon orbit zone, marked in beige, is spanned by the family of constant-radius null geodesics, shown as dotted lines. Special cases include the polar orbit, which runs from pole to pole (and precesses around the black hole), shown as a dashed line at  $r/M \approx 2.67$ ; and the co and counterrotating equatorial orbits marked by purple points at  $r/M \approx 1.81$  and  $3.82$ , respectively.

### Capture cross section

Figure 8.1 illustrates the scenario: a planar wavefront impinges upon a rotating black hole, at an angle of incidence  $\gamma$ . The capture cross section  $\sigma_{\text{geo}}$  is the area of the ‘locus of absorption’ which is traced on the incident planar surface. We may write

$$\sigma_{\text{geo}} = \int_{-\pi}^{\pi} \frac{1}{2} b_c^2(\chi, \gamma) d\chi, \quad (8.17)$$

where  $\chi$  an angle defined on the planar surface, measured from the rotation axis in a corotating sense. Here,  $b_c(\chi, \gamma)$  is the ‘critical’ impact parameter, which corresponds to the marginal case of a null geodesic that asymptotically approaches a constant-radius photon orbit.

For a Schwarzschild black hole, the constant-radius photon orbit occurs at  $r = 3M$  (the ‘light-ring’), and the set of such orbits defines a 2D ‘photon sphere’. In the Kerr case, the radius of the orbit depends on the azimuthal angular momentum. Figure 8.2 shows that the set of all constant-radius photon orbits defines a ‘photon orbit zone’. Each point in this zone is associated with a constant-radius null geodesic, which is the asymptote of a null ray encroaching from spatial infinity.

To find  $b_c(\chi, \gamma)$  we solve the geodesic equations which are obtained with Hamilton-Jacobi methods. Geodesics on Kerr are governed by four first-order equations, and three constants of motion: energy  $E$ , azimuthal angular momentum  $L_z$  and Carter constant  $Q$ . The first step is to establish the relationship between the constants of motion and the values of  $b$  and  $\chi$  for the null

ray passing orthogonally through the planar wavefront. Without loss of generality, let us assume that the wave is impinging along the  $\phi = 0$  direction. We may introduce an ‘impact vector’  $\mathbf{b}$  with Cartesian components  $\mathbf{b} = [b \cos \gamma \cos \chi, b \sin \chi, -b \sin \gamma \sin \chi]$ . This corresponds to a ray with the following constants of motion:

$$\hat{L}_z \equiv L_z/E = b \sin \chi \sin \gamma, \quad (8.18)$$

$$\hat{Q} \equiv Q/E^2 = b^2 \cos^2 \chi + (b^2 \sin^2 \chi - a^2) \cos^2 \gamma. \quad (8.19)$$

The next step is to find the critical radius and impact parameter,  $r_c$  and  $b_c$ , for the direction  $\chi$ , by solving

$$R(r_c) = 0, \quad \frac{\partial R(r_c)}{\partial r} = 0, \quad (8.20)$$

where

$$R(r) = \left( (r^2 + a^2) - a \hat{L}_z \right)^2 - \Delta \left( (\hat{L}_z - a)^2 + \hat{Q} \right). \quad (8.21)$$

By solving Eq. (8.20) we get a pair of values  $(r_c(\chi, \gamma), b_c(\chi, \gamma))$ , corresponding to the radius of the photon orbit and the critical impact parameter for a null ray that passes through the incident wavefront at an angle  $\chi$  relative to the rotation axis, as shown in Fig. 8.1. The capture cross section is computed by inserting  $b_c(\chi, \gamma)$  into Eq. (8.17).

Figure 8.3 shows the geodesic capture cross section as a function of angle of incidence  $\gamma$  for a variety of black hole spins  $a$ . Some values for the capture cross section in the special case of on-axis incidence ( $\gamma = 0$ ) are presented below in TABLE 8.1. These values will be compared with the numerical results for the absorption cross section exhibited in Sec. 8.3.

Table 8.1: Low- and high-frequency limits of the absorption cross section for the different choices of  $a$  exhibited in the plots of the Sec. 8.3. The high-frequency results presented here are for on-axis incident null geodesics.

$a [M]$	0.00	0.30	0.60	0.90	0.99
$\sigma(\omega \approx 0) [\pi M^2]$	16.000	15.631	14.400	11.487	9.128
$\sigma(\omega \gg M) [\pi M^2]$	27.000	26.726	25.855	24.168	23.409

### Sinc approximation

In the 1970s, Sanchez [300] found that, at high frequencies, the absorption cross section for a Schwarzschild BH oscillates around the geometric capture cross section with a peak-to-peak period of  $\Delta\omega = 1/\sqrt{27}M$ . In one sense, oscillations arise from the contributions of successive partial waves to Eq. (8.14). In a complementary sense, as recently shown in Refs. [320, 321] using complex angular momentum (CAM) methods, the oscillations are related to the properties of the unstable photon orbit. For a scalar field absorbed by a spherically-symmetric BH, it was shown that [320]

$$\sigma/\sigma_{\text{geo}} \sim 1 - 8\pi\beta e^{-\pi\beta} \text{sinc}(2\pi\omega/\Omega), \quad (8.22)$$

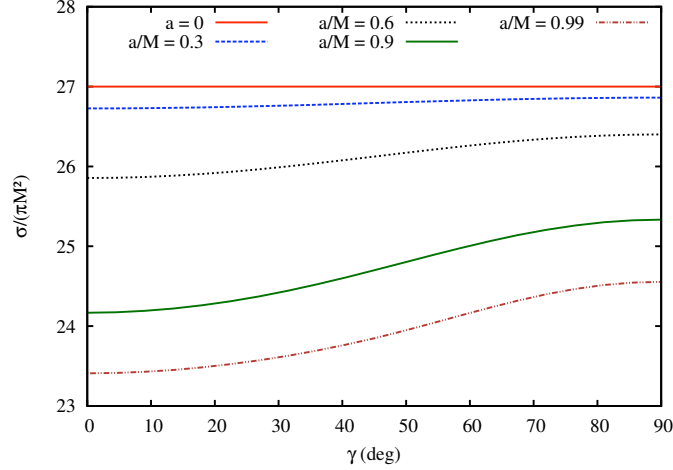


Figure 8.3: Geodesic capture cross section  $\sigma$  as a function of angle of incidence  $\gamma$ , where  $\gamma = 0$  corresponds to incidence along the black hole's axis of rotation (and  $\sigma$  is symmetric under  $\gamma \rightarrow \pi - \gamma$ ). The geodesic capture cross section is the high-frequency asymptote for the planar wave absorption cross section.

where  $\beta \equiv \Lambda/\Omega$ , with  $\Omega$  the frequency of the null orbit, and  $\Lambda$  the associated Lyapunov exponent. In the Schwarzschild case,  $\sigma_{\text{geo}} = \pi b_c^2$  is the geodesic capture cross section and  $\Omega = 1/(\sqrt{27}M) = 1/b_c$  with  $\beta = 1$ . The oscillatory term arises from a (high-frequency approximation to) a sum over Regge poles. Regge poles are characteristic resonances of the spacetime closely related to the quasinormal modes. The idea that oscillations in absorption cross sections provide information about the properties of the null orbits is an intriguing one, which surely deserves further investigation in non-spherically-symmetric cases, such as Kerr.

In Sec. 8.3 we show that oscillations around the capture cross section are also present in the Kerr context, and, for general angles of incidence, these oscillations exhibit a richer spectrum. The oscillations arise from the superposition of partial contributions which now depend on azimuthal number  $m$  as well as on  $l$ . From the complementary viewpoint, these oscillations are related to the spectrum of Regge poles, which also depend on both  $l$  and  $m$ .

In the special case in which the plane wave is incident along the axis of rotation ( $\gamma = 0$  or  $\pi$ ), a slightly-modified version of Eq. (8.22) is still valid, even though the BH itself is not spherically symmetric. One subtlety is that we need to take account of the spheroidal harmonics in Eq. (8.12). Progress can be made with an asymptotic relation, obtained using the WKB techniques of Ref. [322]:

$$|S_{\omega l 0}(\gamma = 0)|^2 = \frac{1}{4\pi^2} \frac{\partial A}{\partial L}. \quad (8.23)$$

Here  $L = l + 1/2$  and  $A$  is the angular eigenvalue of the spheroidal equation for  $m = 0$ . We may then use the following expansion

$$\frac{A}{L^2} = 1 - \frac{1}{2}\alpha^2 + \frac{1}{32}\alpha^4 + \frac{5}{8192}\alpha^8 + \mathcal{O}(\alpha^{12}), \quad (8.24)$$

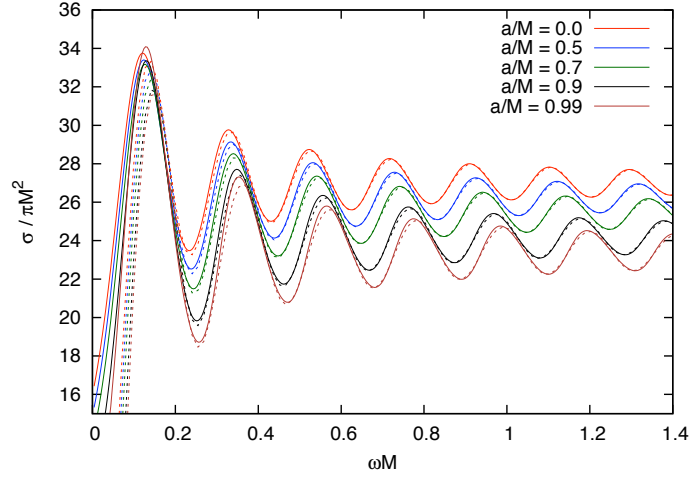


Figure 8.4: The sinc approximation for on-axis incidence ( $\gamma = 0$ ). The solid lines show the numerically-determined cross section (cf. Fig. 8.6), and the dashed lines show the sinc approximation, Eq. (8.25), for a range of  $a/M$  and  $\omega M$ .

which is valid in the regime  $\alpha \equiv a\omega/L < 1$ . It follows that  $2\pi^2|S_{\omega lm}(\gamma)|^2 = L - \frac{\alpha^4 L}{32} + \dots$ , and the subdominant term is very small near the Regge pole, and may be neglected. The other steps in the derivation of Ref. [320] follow through unchanged, and we arrive at

$$\sigma/\sigma_{\text{geo}} \sim 1 - \frac{8\pi\beta e^{-\pi\beta}}{\Omega^2 b_c^2} \text{sinc}(2\pi\omega/\Omega), \quad (8.25)$$

where again  $\beta = \Lambda/\Omega$ . In the on-axis case,  $b_c$ ,  $\Omega$  and  $\Lambda$  can be written in closed form; the relevant expressions are found in Eqs. (18), (22) and (24), respectively, of Ref. [323]. Note that now  $b_c \neq 1/\Omega$ , for  $a > 0$ . In Fig. 8.4 we plot a selection of results obtained through Eq. (8.25), and compare with numerically-determined cross sections.

### Semi-analytic approximation

In the high frequency regime, the behaviour of the transmission factors are closely linked to the properties of null orbits, via

$$\Gamma_{\omega lm} \sim [1 + \exp(-2\pi(\omega - \Omega_R L)/\Omega_I)]^{-1} \quad (8.26)$$

(cf. Eq. (15) in Ref. [320]). Here  $\Omega_R(a/M, \mu)$  and  $\Omega_I(a/M, \mu)$  are, respectively, the orbital frequency and Lyapunov exponent associated with a null orbit with angular momentum ratio  $\mu \equiv m/L$ . Accurate semi-analytic approximations for  $\Omega_R$  and  $\Omega_I$  are given in Ref. [322]: see Eq. (2.35), (2.36) and Eq. (2.40).

Figure 8.5 shows the transmission factors  $\Gamma_{\omega lm}$  as a function of frequency  $M\omega$ , for the case  $l = 5$ ,  $a = 0.9M$ , and  $-l \leq m \leq l$ . It shows that Eq. (8.26) provides an excellent approximation in the regime  $\omega \sim \Omega_R L$ .

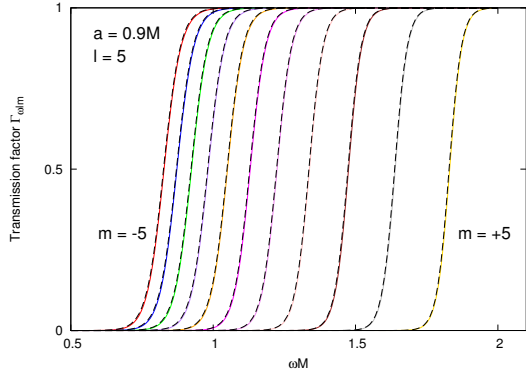


Figure 8.5: Transmission factors  $\Gamma_{\omega lm}$  for angular multipoles  $l = 5$  and  $-l \leq m \leq l$ . The solid lines show numerical solutions of Eq. (8.13), and the dashed lines show the semi-analytic approximation, Eq. (8.26).

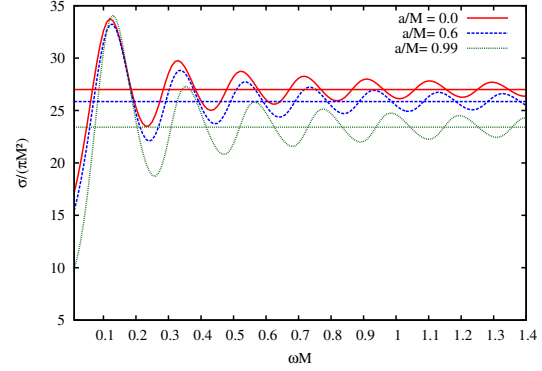


Figure 8.6: On-axis ( $\gamma = 0$ ) absorption cross section for  $a/M = 0.00, 0.60$  and  $0.99$ . The horizontal lines represent the high-frequency limits. We see that the general pattern of the on-axis absorption cross section, even for rapidly rotating BHs, is similar to the case of spherical ( $a = 0$ ) BHs.

### 8.3 Numerical results

In this section we present our numerical results for the scalar absorption cross section of the Kerr BH. We give particular attention to the off-axis absorption cross section, i.e., the  $\gamma \neq 0$  cases, which exhibit many distinct features when compared to the spherically symmetric case.

As for the numerical precision, we have considered the summation in Eqs. (8.9) and (8.10) until the next term contributes less than  $10^{-3}$  of the total value. This makes the computation more efficient, as we do not need to integrate to very large radii in order to obtain convergent results. In our case, the maximum radius  $r_\infty$  is typically  $r_\infty/r_+ \sim 10^2$  and the numerical outer horizon  $r_h$  is such that  $(r_h/r_+ - 1) \sim 10^{-2}$ .

The numerical upper limit in the  $l$  summation in Eq. (8.14),  $l_{max}$ , should be considered carefully, in order to properly compute the total absorption cross section. The convergence of Eq. (8.14) depends strongly on the value of the wave frequency  $\omega$ . For higher values of  $\omega$  one should take higher values of  $l_{max}$ . For the results presented here, which are in the frequency range  $0 < \omega M < 1.4$ , we performed the summation until  $l_{max} = 8$ . Additional terms coming from  $l > 8$  would contribute less than  $10^{-6}$  of the total value, being unnoticeable in the data plots presented here. Our results were checked using independent codes, which increases their reliability.

In Fig. 8.6 we show the total on-axis absorption cross section for  $a/M = 0.00$  (Schwarzschild case),  $0.60$ , and  $0.99$ . In the on-axis case, as the frequency is increased, the absorption cross section increases from the area of the event horizon and then oscillates regularly around the high-frequency limit given by the capture cross section of null geodesics (see Fig. 8.3), which is represented by horizontal lines in Fig. 8.6.

In Fig. 8.4 we compare the numerically-determined cross section with the ‘sinc approximation’ of Eq. (8.25). We see that the agreement is excellent in the moderate-to-large  $M\omega$  regime, which confirms the validity of Eq. (8.25).

In Fig. 8.7 we show the absorption cross section for a range of rotation parameters ( $a/M = 0.30, 0.60, 0.90,$  and  $0.99$ ) and incidence angles ( $\gamma = 0, 30, 60,$  and  $90$  degrees). We see that, as we move away from the on-axis case ( $\gamma = 0$ ), by increasing the incidence angle  $\gamma$ , and

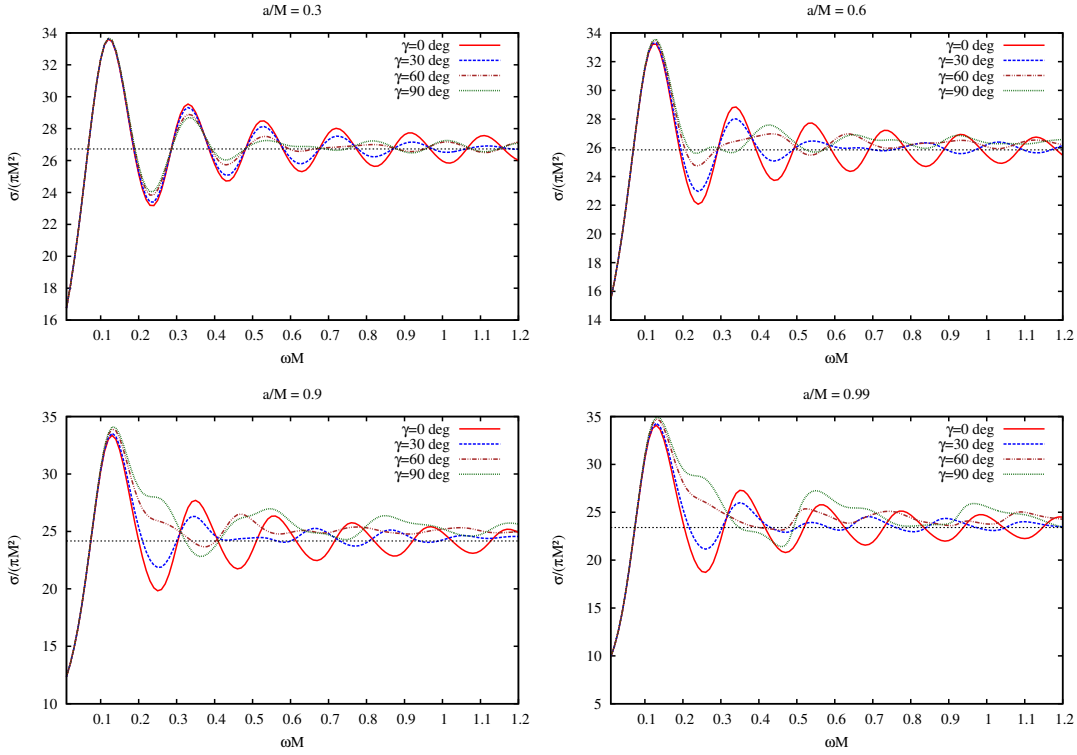


Figure 8.7: Off-axis absorption cross section for  $a/M = 0.30, 0.60, 0.90$  and  $0.99$ . For comparison, we also exhibit the on-axis case ( $\gamma = 0$ ), and its high-frequency limit (horizontal lines). We see that the oscillation pattern for the off-axis cases differs considerably from the regular one exhibited in the on-axis case.

increasing the rotating parameter  $a$ , the absorption cross section starts to differ considerably from the regular behavior shown in Fig. 8.6. In the high-frequency regime,  $\sigma$  oscillates in an irregular way around the geodesic capture cross section. This irregular oscillatory behavior arises as a consequence of breaking the azimuthal degeneracy, so that the transmission factor becomes strongly dependent on  $m$ , as shown in Fig. 8.5. In other words, there is a coupling between the BH rotation and the azimuthal number  $m$ , which may be interpreted as the result of frame-dragging [308].

The azimuthal number  $m$  may be positive, which corresponds to corotating modes, or negative, which corresponds to counterrotating modes. In order to see their contribution separately, we computed the absorption cross sections,  $\sigma^+$  and  $\sigma^-$ , as defined in Eq. (8.16). The results are shown in Fig. 8.8. When we split the absorption cross section into co ( $\sigma^+$ ) and counterrotating ( $\sigma^-$ ) contributions, we see that the oscillating pattern becomes more regular. Furthermore, we see that the counterrotating contributions for the total absorption cross section are bigger than the corotating ones. This agrees with the null geodesic approach, where the critical radius for retrograde orbits is bigger than the one for direct orbits [127]. We note that  $\sigma^+$  and  $\sigma^-$  move further apart as the rotation rate increases. The difference between the co and counterrotating absorption cross sections is more pronounced for  $\gamma = 90$  deg, as a consequence of the increased importance of frame-dragging in the equatorial plane.

In Fig. 8.9 we show the main partial contributions for the total absorption cross section for fixed values of  $|m|$ , varying  $l$ , according to Eq. (8.12). We see from Fig. 8.9 that corotating ( $am > 0$ ) and counterrotating ( $am < 0$ ) contributions to the partial absorption cross section

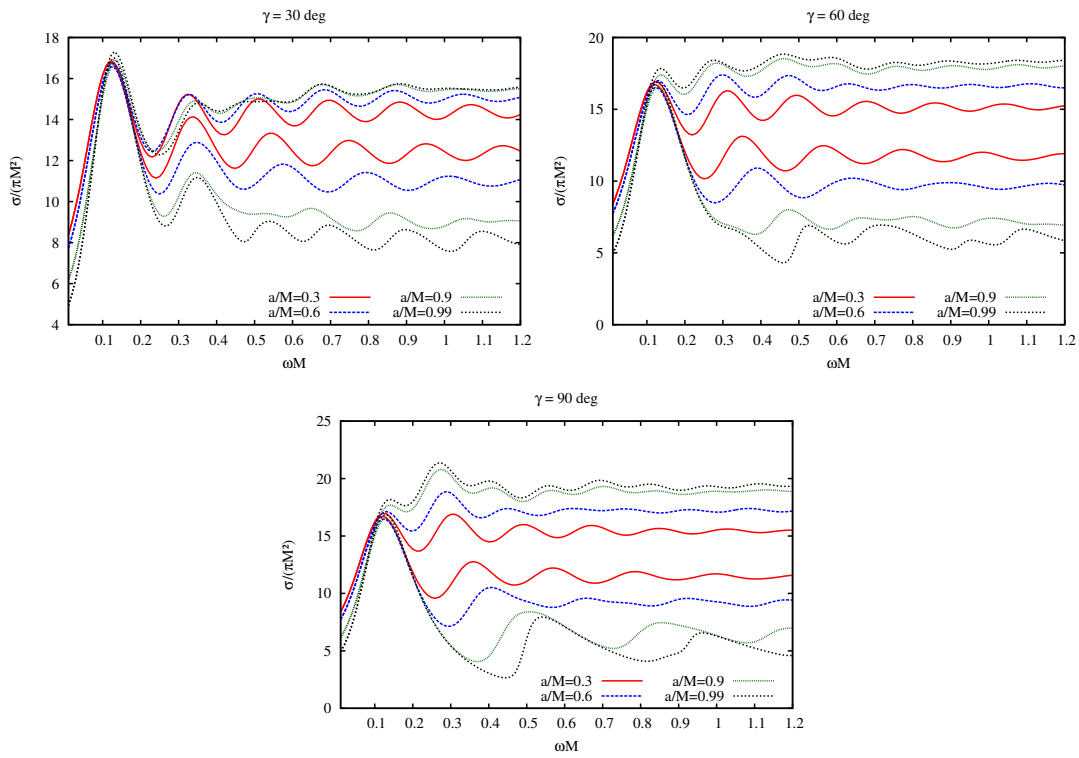


Figure 8.8: Co ( $\sigma^+$ ) and counterrotating ( $\sigma^-$ ) absorption cross section for  $\gamma = 30, 60,$  and  $90$  degrees. The curves are plotted for different BH rotation parameters, namely  $a/M = 0.30, 0.60, 0.90,$  and  $0.99$ . The counterrotating absorption cross sections are bigger than the correspondent corotating ones, and their separation becomes larger as  $a$  increases.

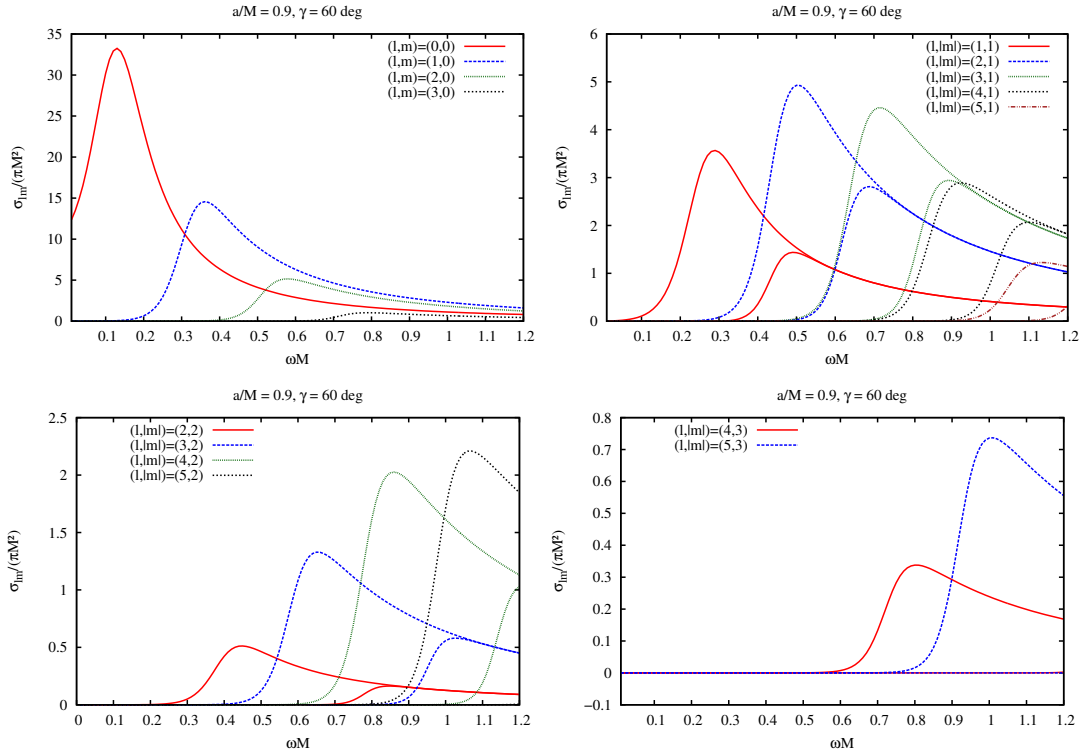


Figure 8.9: Partial absorption cross sections for  $a/M = 0.90$  and  $\gamma = 60$  degrees. We plot the main contributions for fixed values of  $l$  and  $m$ , both for corotating (curves with lower peaks) and counterrotating (higher peaks) cases.

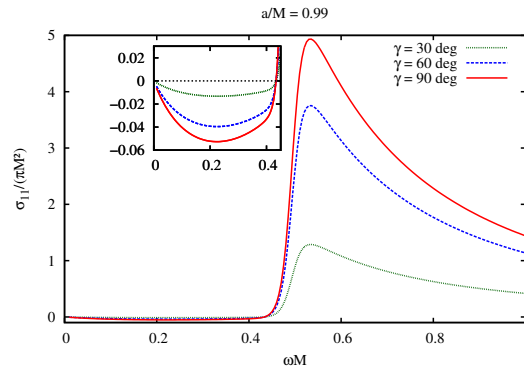


Figure 8.10: Zoom at the mode with  $l = m = 1$  for  $\gamma = 30, 60,$  and  $90$  degrees, with  $a/M = 0.99$ . Superradiance is more evident for this mode, although being very small even in this case.

with the same value of  $|m|$  become equal after a certain value of the frequency. This occurs once both waves are completely absorbed, i.e.  $|\mathcal{R}_{\omega lm}^{in}/\mathcal{A}_{\omega lm}^{in}|^2 = 0$ , and the sign of  $m$  in Eq. (8.12) becomes irrelevant. The approximate value of the frequency at which absorption becomes significant is determined by  $\Omega_R L$ , where  $\Omega_R$  is the frequency of the corresponding null orbit, which depends on both  $m/L$  and  $a/M$  (see Sec. 8.2.2).

Due to superradiance [316], the reflection coefficient can actually exceed unity for some values of  $(\omega, m)$ . See, for instance, Ref. [315], where the reflection coefficient is computed for different values of  $a$ . For these values, as can be seen in Fig. 8.10, the transmission factor and partial absorption cross section are negative, although the total absorption cross section remains positive. We recall that there is no superradiance for  $m = 0$ , and that it is most evident for the  $l = m = 1$  mode.

## 8.4 Conclusion

We have numerically computed the absorption cross section of plane massless scalar waves incident upon Kerr BHs, for general angles of incidence, revealing the effect of black hole rotation. In the special case of on-axis incidence, we showed that the absorption cross sections are well-described by a simple ‘sinc’ approximation. Our result was obtained by extending the complex angular momentum method of Ref. [320]. In the general case of arbitrary incidence, we showed that the absorption cross section of a Kerr BH exhibits an irregular oscillation pattern, which is in contrast to the regular oscillations shown by a Schwarzschild BH. We have taken steps to explain this effect in terms of the coupling between the azimuthal angular momentum of the field and the angular momentum of the BH. In Sec. 8.2.2 we gave a semi-analytic approximation to relate the transmission of partial waves to the properties of the null photon orbits. To explore the coupling, we have compared the corotating ( $am > 0$ ) and counterrotating ( $am < 0$ ) contributions to the absorption cross section. We have shown that, due to superradiance in the Kerr spacetime, the partial absorption cross section becomes negative for some values of  $(\omega, m)$ .

Some of the features observed in the scalar absorption by Kerr BH have also been observed in the absorption of sound waves by the draining bathtub: an (inexact) analogue of Kerr BH in (2+1)-dimensions [314] which is amenable to a full analysis using the complex angular momentum approach [313]. The results presented here represent a significant step towards understanding the absorption by axially-symmetric BHs, for waves impinging at general angles. Possible themes for future work could include (i) an extension of the complex angular momentum approach of Sec. 8.2.2 to waves impinging at arbitrary angles of incidence, which would require careful asymptotic analysis of the spheroidal harmonics, and (ii) analysis of higher-spin (e.g. Dirac [309] or electromagnetic) planar waves, where there will be an additional coupling between black hole rotation and the spin of the field.

## Chapter 9

# Scalar waves impinging in a dirty black hole: Schwarzschild black holes surrounded by thin spherical shells

In the year of 2015, the Theory of general relativity (GR) reaches 100 years of existence. In its centenary history, GR has been submitted to many experimental tests [1, 9], and has obtained remarkable success in all of them. Among the predictions of GR, the existence black holes (BHs) [124] arises as one of the most curious and fascinating ones, due to the features presented by these objects. In GR, one may assure that in electrovacuum, isolated black holes are governed by just three parameters [108]: angular momentum, charge, and mass. However, in an astrophysical environments, BHs are likely to be surrounded by other field sources [291].

The surroundings of BHs have a major importance in many of their observational features. Indeed, the accretion of matter into BHs is associated to characteristic signatures of the event horizon itself, through, for instance, the  $K\alpha$  iron line emission [12, 324]. Accretion can play a very important role in the evolution of supermassive BHs and therefore in the galactic evolution as well [292, 325, 326]. However, accreting matter into a BH can be very difficult to quantify: In general, one has to solve the time-independent, multidimensional, relativistic, magneto-hydrodynamic equations with coupled radiative transfer [69, 327]. Notwithstanding, many simplifying assumptions can be made in order to obtain the main features of accreting models. For instance, one can assume a non-interacting fluid flowing spherically into the BH, which can be solved analytically for some equation of state [69].

Most of the features of the accreting matter into BHs are obtained kinematically: given a fixed gravitational background one can in principle compute all relevant observational quantities. This reasoning is based on the assumption that the accreting matter has a density which is much smaller than the supermassive black hole itself, and therefore one can safely neglect its gravitational influence, and treat the system *adiabatically*. Despite that, some gravitational features considering matter environment surrounding BHs were studied in the past years. Configurations known as *dirty* BHs were considered to analyze the influence of environmental mat-

ter fields around BHs [328–330]. In Ref. [331, 332] a perturbative formula to study quasinormal modes of BHs with surrounding matter was proposed, where it was shown that the presence of an environment can modify the quasinormal modes of the BHs. More recently, in Ref. [260], the BH environment influence in the gravitational wave phenomenology was studied in a broad class of scenarios, some of them in which the whole configuration resembles an isolated BH. Additionally, in Ref. [333] Gürlebeck showed that the presence of matter surrounding a Schwarzschild BH has no influence on the multipole moments of the distorted BH, within generic assumptions on the matter.

Studies of BHs with surrounding matter can also be interesting in the context of dark matter. It is known that dark matter can form halo structures surrounding galactic disks. Also, clouds of dark matter can be formed in the BH vicinity [138, 139], in some cases this may lead to BH hairy configurations [136]. The effect of dark matter halos in the scattered light of the galaxies was studied recently in Ref. [334], setting an upper limit on the dark matter-photon cross section using observation data. The dark matter can be accreted by BHs, which would have an influence on its evolution. Therefore, it is interesting to study cases where the matter surrounding the BH couples very weakly to the interacting fields (i.e., interacts only gravitationally), for which the gravitational effects of the matter surrounding BHs can be seen more clearer.

The scattering/absorption of fields by isolated BHs have been widely investigated [298–304, 306–308, 310, 335–339], and helped us to understand many of the BH phenomenological features. Although planar wave scattering seems to be a very peculiar phenomenon, many interesting outcomes may be analyzed through it, like the accretion of dark matter by compact objects [149, 156]. Also, planar wave absorption shares many features with the accretion of a uniform velocity fluid into a BH [340]. Moreover, the scattering of light by the BHs may cast a shadow [341–343], that should be visible with near-future telescopes.

Within the literature on BHs planar wave scattering, the consideration of the gravitational effect exerted by the environment in the absorption spectrum is still missing. A review on wave propagation, taking into account the coupling with matter including effects of coupling with other matter fields, can be seen in Ref. [344]. However, the study of the gravitational backreaction of the matter surrounding the BH in its absorption is still lacking in the literature. In this chapter, we analyze the case of Schwarzschild BHs surrounded by a thin spherical shell [345], which we shall call dirty black hole (DBH). More specifically, we analyze the absorption cross section of planar massless scalar waves impinging upon a Schwarzschild BH surrounded by a thin shell of matter.

The remaining of this chapter is organized as follows. In Sec. 9.1 we review some features of a Schwarzschild BH surrounded by a thin spherical shell. In Sec. 9.2 we investigate the massless scalar field in the spacetime of interest, and the suitable boundary conditions for planar wave scattering. In Sec. 9.3 we provide expressions for the absorption cross section of a Schwarzschild BH with a thin spherical shell. Also, we describe the low- and high-frequency regimes, and show a sinc approximation for the absorption cross section. In Sec. 9.4 we show a selection of our numerical results, considering different values of the shell position, and of the BH and shell masses. We finalize pointing out some remarks in Sec. 9.5. Throughout the chapter, we use natural units ( $c = G = \hbar = 1$ ).

## 9.1 Black holes with surrounding spherical shells

Spherically symmetric spacetimes can be described by the following line element:

$$ds^2 = -A(r)dt^2 + \frac{1}{B(r)}dr^2 + r^2d\Omega^2, \quad (9.1)$$

where  $A$  and  $B$  are functions of the radial coordinate  $r$  only and  $d\Omega^2$  denotes the unit 2-sphere line element. We want to describe the metric functions  $A$  and  $B$  correspondent to a thin spherical shell outside of a Schwarzschild BH. In GR, (isotropic) fluid configurations are described by the Tolman-Openheimer-Volkoff (TOV) equations [69], i.e.,

$$\frac{d\mu}{dr} = 4\pi r^2 \rho(r), \quad (9.2)$$

$$\frac{dA}{dr} = 2 \frac{\mu + 4\pi r^3 p}{r^2 - 2r\mu} A, \quad (9.3)$$

$$\frac{dp}{dr} = - \frac{\mu + 4\pi r^3 p}{r(r - 2\mu)} (p + \rho), \quad (9.4)$$

where  $p$  and  $\rho$  are the pressure and density of the fluid, respectively, and  $\mu$  is the mass function, defined through

$$B(r) = 1 - \frac{2\mu}{r}. \quad (9.5)$$

The vacuum solutions (i.e.  $\rho = p = 0$ ) of the TOV equations are given by

$$A = a_1 \left( 1 - \frac{2a_2}{r} \right) \quad (9.6)$$

$$\mu = a_2, \quad (9.7)$$

where  $a_1$  and  $a_2$  are constants. From Eq. (9.2) we can see that  $a_2$  accounts for the total mass-energy of the configuration, within the radius  $r$ . Moreover, we note that the vacuum solution can always be brought to its Schwarzschild form, both inside and outside of the spherical shell, by absorbing the constant  $a_1$  in a time re-parametrization [345]. However, here we choose to keep the constant  $a_1$  for the solution inside the shell.

Now let us restrict ourselves to the case of a spherical thin shell surrounding a Schwarzschild BH [346]. Let  $R_S$  denote the radial position of the sphere. We have that, for  $r > R_S$ , the metric function can be written in the Schwarzschild form:

$$A(r) = B(r) = 1 - \frac{2M}{r}, \quad (9.8)$$

where  $M$  is the Arnowitt–Deser–Misner (ADM) mass. This mass,  $M$ , accounts for the mass of the spherical shell and also of the BH inside it. In the region between the BH event horizon

and the spherical shell, we can see from Eq. (9.7) and the behavior of  $B(r)$ , that the constant  $a_2 = M_{\text{H}}$  is the BH event horizon mass. The only remaining constant is  $a_1$ , which we choose such that  $A(r)$  is continuous across the spherical shell. We have that

$$a_1 \equiv \alpha = \frac{(1 - 2M/R_S)}{(1 - 2M_{\text{H}}/R_S)}. \quad (9.9)$$

Therefore, the full solution is given by

$$A(r) = \begin{cases} \alpha(1 - 2M_{\text{H}}/r), & r < R_S \\ (1 - 2M/r), & r > R_S \end{cases}, \quad (9.10)$$

$$B(r) = \begin{cases} (1 - 2M_{\text{H}}/r), & r < R_S \\ (1 - 2M/r), & r > R_S \end{cases}. \quad (9.11)$$

Using the metric discontinuities, we can evaluate the surface energy  $\Sigma$  and the surface tension  $\Theta$  of the spherical shell. The surface energy and tension are obtained through the following relations [154, 345]

$$\sqrt{B(R_S)_+} - \sqrt{B(R_S)_-} = -4\pi R_S \Sigma, \quad (9.12)$$

$$\left[ \frac{A'(R_S)\sqrt{B(R_S)}}{A(R_S)} \right]_+ - \left[ \frac{A'(R_S)\sqrt{B(R_S)}}{A(R_S)} \right]_- = 8\pi(\Sigma - 2\Theta), \quad (9.13)$$

where the subscript signs  $+$  and  $-$  indicate the limit  $r \rightarrow R_S$  from  $r > R_S$  and  $r < R_S$ , respectively. Using the metric coefficient (9.11), we find

$$\Sigma = \frac{1}{4\pi R_S} \left( \sqrt{1 - \frac{2M_{\text{H}}}{R_S}} - \sqrt{1 - \frac{2M}{R_S}} \right). \quad (9.14)$$

Moreover, using Eq. (9.13), the surface tension is given by

$$\Theta = \frac{1}{16\pi} \left( 8\pi\Sigma - \left[ \frac{A'(R_S)\sqrt{B(R_S)}}{A(R_S)} \right]_+ + \left[ \frac{A'(R_S)\sqrt{B(R_S)}}{A(R_S)} \right]_- \right), \quad (9.15)$$

hereafter the prime denotes derivative with respect to the coordinate  $r$ , inserting (9.10) and (9.11) in (9.15), we obtain

$$\Theta = \frac{1}{8\pi R_S} \left( \frac{1 - \frac{M_{\text{H}}}{R_S}}{\sqrt{1 - \frac{2M_{\text{H}}}{R_S}}} - \frac{1 - \frac{M}{R_S}}{\sqrt{1 - \frac{2M}{R_S}}} \right). \quad (9.16)$$

## 9.2 Scalar field

The massless scalar field  $\Phi$  is described by the Klein-Gordon equation, namely

$$\frac{1}{\sqrt{-g}}\partial_a(\sqrt{-g}g^{ab}\partial_b\Phi) = 0. \quad (9.17)$$

Monochromatic scalar waves in spherically symmetric spacetimes can be decomposed in the following way:

$$\Phi_{\omega lm}(t, r, \theta, \phi) = \sum_{lm} \frac{U_{\omega l}(r)}{r} e^{-i\omega t} Y_{lm}(\theta, \phi), \quad (9.18)$$

and, using Eq. (9.17), we obtain the following radial equation for  $U_{\omega l}(r)$

$$\begin{aligned} & \sqrt{AB} \left( \sqrt{AB} U' \right)' \\ & + \left\{ \omega^2 - A \left[ \frac{l(l+1)}{r^2} + \frac{(AB)'}{2Ar} \right] \right\} U = 0, \end{aligned} \quad (9.19)$$

where the prime denotes derivative with respect to the coordinate  $r$ .

Introducing the Regge-Wheeler coordinate  $x$ , which can be defined through

$$x = \int dr \frac{1}{\sqrt{AB}}, \quad (9.20)$$

we can rewrite Eq. (9.19) in the form of an one-dimensional Schrödinger-like equation, given by

$$\left[ -\frac{d^2}{dx^2} + V_l - \omega^2 \right] U_{\omega l}(x) = 0, \quad (9.21)$$

where  $V_l(r)$  is the effective potential, namely

$$V_l(r) = A \left[ \frac{l(l+1)}{r^2} + \frac{(AB)'}{2Ar} \right]. \quad (9.22)$$

We can note, from FIG. 9.1, that at the event horizon  $r = 2M_H \equiv r_H$  the effective potential vanishes, and goes as  $1/r^2$  for  $r \gg r_H$ . These characteristics of the potential are shared with the case of an isolated Schwarzschild BH. However, for DBHs the potential presents a discontinuity at the shell radius  $R_S$  (cf. FIG. 9.1).

The independent solutions of Eq. (9.21) are usually labeled as *in* and *up*. For absorption/scattering, the one of interest will be the *in* modes, which denote purely ingoing waves impinging from the past null infinity. The *in* modes obey the following boundary conditions:

$$U_{\omega l}(x) \sim \begin{cases} \mathcal{A}_{\omega l} R_I + \mathcal{R}_{\omega l} R_I^* & (x/M \rightarrow \infty), \\ \mathcal{T}_{\omega l} R_{II} & (x/M \rightarrow -\infty). \end{cases} \quad (9.23)$$

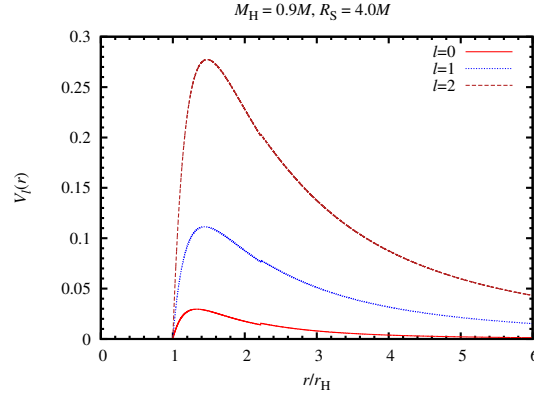


Figure 9.1: The effective potential,  $V_l(r)$ , plotted for the modes  $l = 0, 1, 2$ , at the shell radius  $R_S = 4.0M$  with the BH mass  $M_H = 0.9M$ .

The functions  $R_I$  and  $R_{II}$  can be written as

$$R_I = e^{-i\omega x} \sum_{j=0}^N \frac{A_{\infty}^j}{r^j}, \quad (9.24)$$

$$R_{II} = e^{-i\omega x} \sum_{j=0}^N (r - r_+)^j A_{r_+}^j, \quad (9.25)$$

and the coefficients  $A_{\infty}^j$  and  $A_{r_+}^j$  are obtained by requesting the functions  $R_I$  and  $R_{II}$  to be solutions of the differential equation (9.21), far from the BH and close to the event horizon, respectively. The coefficients  $\mathcal{R}_{\omega l}$  and  $\mathcal{T}_{\omega l}$  in Eq. (9.23) are related to the reflection and transmission coefficients, respectively, and obey the following relation

$$\left| \frac{\mathcal{R}_{\omega l}}{\mathcal{A}_{\omega l}} \right|^2 = 1 - \left| \frac{\mathcal{T}_{\omega l}}{\mathcal{A}_{\omega l}} \right|^2. \quad (9.26)$$

In order to obtain the coefficients  $\mathcal{R}_{\omega l}$  and  $\mathcal{T}_{\omega l}$ , we integrate the differential equation from the horizon up to a point far from the configuration (BH + shell). In the integration procedure, one must carefully choose the boundary conditions at the spherical shell. We impose that the scalar field is continuous at the shell location, i.e.,

$$U_{\omega l}(R_S)_+ = U_{\omega l}(R_S)_-, \quad (9.27)$$

where the  $+$  and  $-$  signs indicate the limit  $r \rightarrow R_S$  from  $r > R_S$  and  $r < R_S$ , respectively. Integrating the differential equation (9.19) across the shell location  $r = R_S$ , we find the jump

condition [135]:

$$\begin{aligned} & \left[ \sqrt{AB} U'_{\omega l}(R_S) \right]_+ - \left[ \sqrt{AB} U'_{\omega l}(R_S) \right]_- \\ &= \frac{U_{\omega l}(R_S)}{R_S} \left( \sqrt{AB_+} - \sqrt{AB_-} \right). \end{aligned} \quad (9.28)$$

Using the metric functions (9.10) and (9.11), the jump condition can be rewritten as [135]

$$\begin{aligned} & \left( 1 - \frac{2M}{r} \right) U'_{\omega l}(R_S)_+ - \sqrt{\alpha} \left( 1 - \frac{2M_H}{r} \right) U'_{\omega l}(R_S)_- \\ &= -2 \frac{(M - M_H) U(R_S)}{R_S^2 (1 + 1/\sqrt{\alpha})}. \end{aligned} \quad (9.29)$$

In practice, one integrates the differential equation (9.19) up to the spherical shell, using the inner solution, extracting  $U_{\omega l}(R_S)_-$  and  $U'_{\omega l}(R_S)_-$ . With these values, we use the jump condition to determine  $U'_{\omega l}(R_S)_+$ , and then integrate again the differential equation (9.19) from the shell to a point far away from the configuration which corresponds to the numerical infinity. The reflection and transmission coefficients can be obtained by comparing the numerical solution with the asymptotic forms (9.23).

## 9.3 Absorption cross section

In this Section we show the procedure to compute the absorption cross section for arbitrary frequencies, which uses the solutions from the numerical integration scheme described in Sec. 9.2. We also show analytical approximate results in the low- and high-frequency regimes.

### 9.3.1 Partial-waves approach

Using the standard partial wave method [347], one may show that the total absorption cross section  $\sigma$  of planar massless scalar waves impinging on a Schwarzschild BH surrounded by a spherical shell is given by

$$\sigma = \sum_{l=0}^{\infty} \sigma_l, \quad (9.30)$$

with

$$\sigma_l = \frac{\pi}{\omega^2} (2l + 1) \left| \frac{\mathcal{T}_{\omega l}}{\mathcal{A}_{\omega l}} \right|^2, \quad (9.31)$$

being the partial absorption cross section <sup>1</sup>, where  $\mathcal{T}_{\omega l}$  and  $\mathcal{A}_{\omega l}$  are the coefficients appearing on Eq. (9.23). This expression is algebraically the same as the one for a Schwarzschild BH

<sup>1</sup>The partial absorption cross section,  $\sigma_l$ , corresponds to the absorption cross section with a fixed value of  $l$ .

without surrounding shells [300]. From Eq. (9.31) we see that the main ingredient to determine the absorption cross section for arbitrary frequencies is  $|\mathcal{T}_{\omega l}/\mathcal{A}_{\omega l}|^2$  obtained using the procedure explained in Sec. 9.2.

### 9.3.2 Low-frequency regime

In the low-frequency regime, there is a general result which shows that for spherically symmetric BHs the absorption cross section for minimally coupled non-massive scalar field is given by the area of the event horizon [348]. We have computed numerically the absorption cross section in the low-range of  $\omega$ , and the results present large agreement.

### 9.3.3 Null geodesics: high-frequency

In the high-frequency limits, one can show that the scalar field propagates along null geodesics. Therefore, the absorption can be studied through null geodesics.

Without loss of generality, let us focus on null geodesics on the equatorial plane of spherically symmetric spacetimes. The Lagrangian associated to our problem is given by

$$\mathcal{L} = \frac{1}{2} \left( -A\dot{t}^2 + \frac{1}{B}\dot{r}^2 + r^2\dot{\phi} \right), \quad (9.32)$$

where the overdot indicates derivative with respect to the proper parameter of the curve. From the Lagrangian (9.32), we have the following conserved quantities

$$E = -\frac{\partial \mathcal{L}}{\partial \dot{t}} = A(r)\dot{t}, \quad (9.33)$$

$$L = \frac{\partial \mathcal{L}}{\partial \dot{\phi}} = r^2\dot{\phi}. \quad (9.34)$$

Therefore, Eq. (9.32) can be rewritten as

$$\frac{A}{B}\dot{r}^2 + L^2\frac{A}{r^2} = \frac{A}{B}\dot{r}^2 + V_e(r) = E^2, \quad (9.35)$$

where

$$V_e \equiv L^2 A/r^2, \quad (9.36)$$

is the effective potential of the geodesic. When compared to a Schwarzschild BH, the effective potential  $V_e$  has some interesting new features. From FIG. 9.2 we see that, due to the spherical shell, the potential is discontinuous at the shell's position. Moreover, depending on the shell's location we can have two maxima, which indicates the existence of two unstable light rings (see bellow).

With Eq. (9.32), one can show that the radius of circular null geodesics  $r_l$  and the ratio

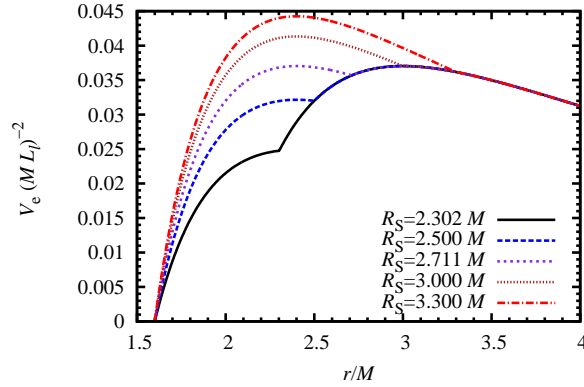


Figure 9.2: Effective potential  $V_e$ , normalized by the angular momentum, as a function of the radial coordinates for some values of the shell radius. Here, we assume  $M_H = 0.8M$ .

$L_l/E_l$  are given by <sup>2</sup>

$$r_l A'(r_l) - 2A(r_l) = 0, \quad (9.37)$$

$$b_l \equiv \frac{L_l}{E_l} = r_l A(r_l)^{-1/2}, \quad (9.38)$$

respectively. For a Schwarzschild BH,  $b_l$  is the critical impact parameter for which a massless particle coming from the infinity stays in an unstable circular orbit. For  $b = L/E < b_l$  the particle gets absorbed by the black hole and for  $b > b_l$  the particle is scattered to infinity. However, in the case of a DBH, as we shall see, this is not always true.

The presence of surrounding matter modifies the light ring structure. For the case of the DBH described in Sec. 9.1, depending on the position of the spherical shell, we have three possibilities, namely

$$r_l = \begin{cases} 3M, & \text{if } R_S < 3M_H, \\ 3M \text{ and } 3M_H, & \text{if } 3M_H < R_S < 3M, \\ 3M_H, & \text{if } R_S > 3M. \end{cases} \quad (9.39)$$

Accordingly, we may have two different constants  $b_l$  associated to unstable circular orbits. Since we are interested in the absorption properties, we shall be concerned with the critical impact parameter. The critical impact parameter  $b_c$  is such that for  $b < b_c$  the light rays get captured by the BH. The only situation which there can be ambiguities is the case  $3M_H < R_S < 3M$ . For this case, the critical impact parameter will be

$$b_c = \min(b_{l+}, b_{l-}), \quad (9.40)$$

where  $b_{l+}$  and  $b_{l-}$  are related to the unstable circular orbits  $3M$  and  $3M_H$ , respectively. The situation is illustrated in FIG. 9.3, where we have fixed the shell radius at  $R_S = 2.8M$  and the

<sup>2</sup>The index  $l$  denotes quantities related to the light ring.

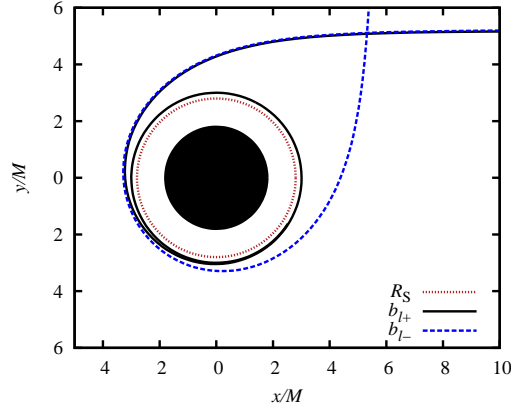


Figure 9.3: Null geodesics impinging from infinity with different impact parameters, namely,  $b_{l-}$  and  $b_{l+}$ . The geodesics are plotted for  $R_S = 2.8M$  and  $M_H = 0.9M$ , in this case we have that the critical impact parameter corresponds to  $b_{l+}$ , since  $b_{l+} < b_{l-}$  and the geodesic with the impact parameter  $b_{l-}$  is scattered to infinity (dashed line).

BH mass to  $M_H = 0.9M$ , one can show that for these parameters  $b_{l-} > b_{l+}$ , then we have that  $b_c = b_{l+}$ .

The capture cross section, which corresponds to the high-frequency limit of the absorption cross section, is given by

$$\sigma_{\text{geo}} = \pi b_c^2. \quad (9.41)$$

We shall explore the three possibilities described by Eq. (9.39). Additionally, we can impose energy conditions to the shell, and this would naturally restrict the shell position. In Appendix F we show how the dominant energy condition (DEC) and strong energy condition (SEC) impose a minimum radius to the location of the shell. In FIG. 9.4 we plot the lower acceptable value for the shell position  $r_{\text{min}}$  as a function of the BH mass, according to DEC and SEC, and compare with the position of the inner light ring  $3M_H$ . Interestingly, DEC enables all three cases listed in Eq. (9.39), while for SEC we only have two possibilities (those for which  $R_S > 3M_H$ ). We note that the radius of the shell is always bigger than  $2M$ , despite the energy conditions imposed, otherwise the whole configuration would collapse into a BH.

We are interested in the effect of the spherical shell in the scattering/capture of null geodesics. From Eq. (9.35), we have that the geodesics can be described by

$$\left(\frac{du}{d\phi}\right)^2 - \frac{B}{b^2 A} + Bu^2 = 0, \quad (9.42)$$

where we have defined  $u \equiv r^{-1}$ . We have integrated Eq. (9.42) subject to the boundary condition  $u(0) = 0$ . We detail our results bellow.

In order to understand the influence of the shell mass in the geodesic motion, we integrate three different geodesics for  $R_S = 4.0M$  (top) and  $R_S = 2.9M$  (bottom), with  $M_H = 0.899, 0.900, \text{ and } 0.901M$ . The impact parameter of the geodesics is chosen to be the one related to the case  $M_H = 0.9M$ , such that the geodesic ends up in unstable circular motion (dark solid line). The results are shown in the left panels of FIG. 9.5, where we show cases for  $3M_H < R_S < 3M$  (bottom) and  $R_S > 3M$  (top). The case  $R_S < 3M_H$  is similar to the

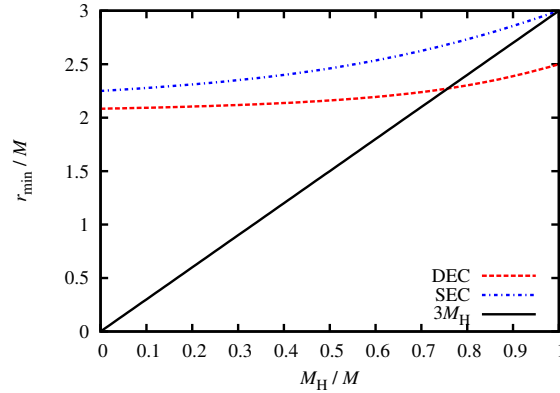


Figure 9.4: The minimum value for the shell position  $r_{\min}$ , according to DEC and SEC, as a function of the black hole mass  $M_H$ . For SEC, the minimum value allowed for the shell position is always larger than the inner light ring  $3M_H$ . However, if one considers DEC, the shell can be placed inside the unstable circular orbit  $3M_H$  for some values of the BH relative mass.

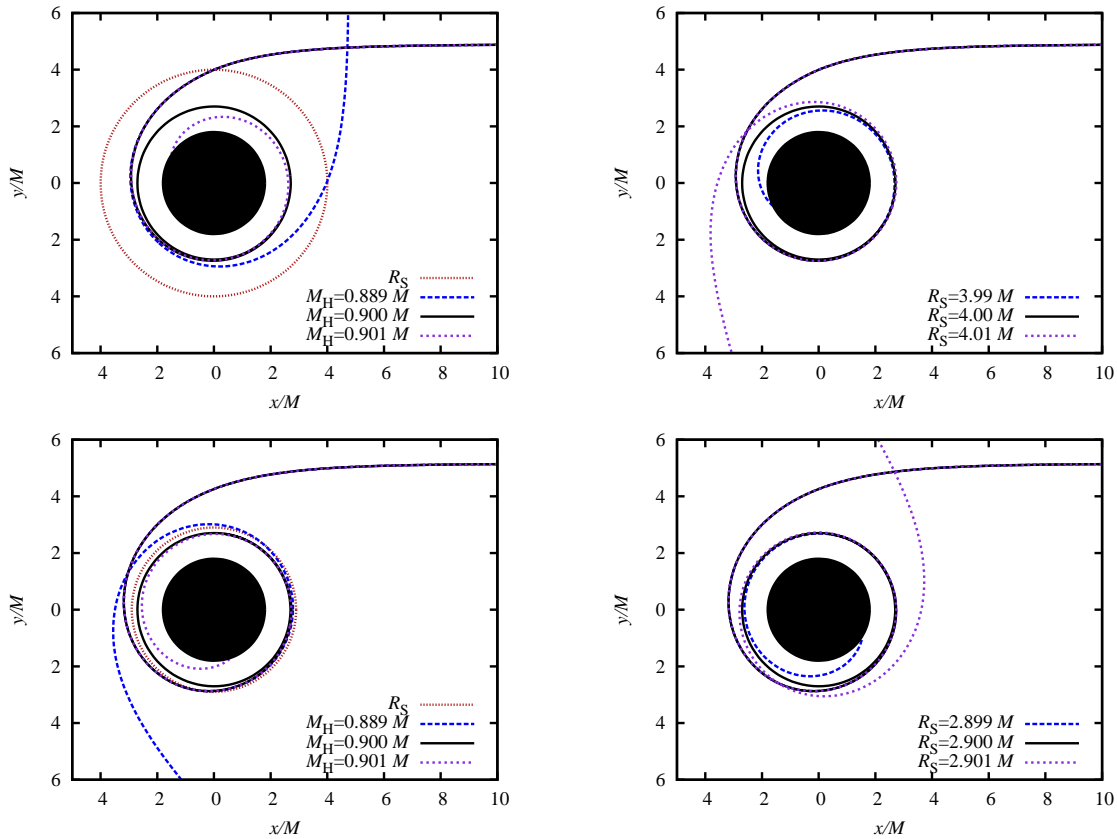


Figure 9.5: Null geodesics coming from infinity with a fixed impact parameter. LEFT PANELS: We fix the shell position, and change the BH mass. In the top and bottom images we choose  $R_S = 4M$  and  $R_S = 2.9M$ , respectively and the impact parameter  $b$  to be the one for the critical case for  $M_H = 0.9M$ . RIGHT PANELS: we fix the BH mass, and change the shell position. In the top and bottom images we choose  $M_H = 0.9M$ , and  $b$  to be the critical one for  $R_S = 4.00M$  (top) and  $R_S = 2.900M$  (bottom).

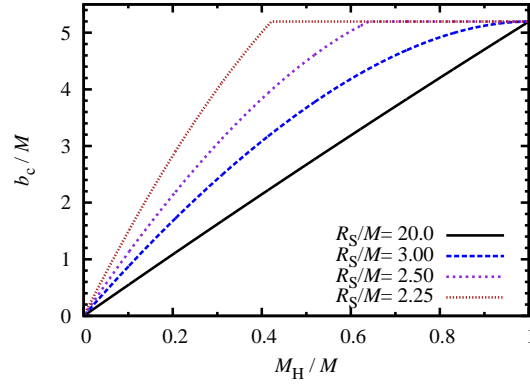


Figure 9.6: Critical impact parameter as a function of the BH mass  $M_H$ , for some values of the shell radius  $R_S$ .

Schwarzschild BH case with mass  $M$ . For a bigger shell mass, or equivalently a smaller  $M_H/M$  ratio, the geodesic is scattered to infinity (dashed line). For a smaller shell mass, the geodesic is captured by the BH (dotted line). Therefore, we conclude that the more massive the shell is the higher are the chances of a geodesic being scattered.

Another possibility is to let free the shell radius, fixing the horizon mass  $M_H = 0.9M$ . We can chose the impact parameter to be the one related to the unstable circular geodesic (dark solid line) associated with the shell radius  $R_S = 4M$  (top), and  $R_S = 2.9M$  (bottom). The results for these choices are shown in the right panels of FIG. 9.5. For a smaller shell radius, the geodesic is captured by the BH (dashed line). For a bigger shell radius, the geodesic is scattered to infinity (dotted line). Therefore, bigger the shell radius is, more the configuration scatterers light.

The above features can be confirmed by analyzing how the critical impact parameter varies with  $R_S$  and  $M_H$ . In FIG. 9.6 we plot the critical impact parameter as a function of the BH mass, for some values of the shells radius. As we can see, the impact parameter increases with the mass of the BH, up to a point in which  $b_{l-} = b_{l+}$ , then it goes as  $b_{l+} = 3\sqrt{3}M$ , regardless of  $M_H$ . This is in agreement with Eq. (9.40). Moreover, the critical impact parameter increases with the radius of the shell. For  $R_S < 3M_H$ , the impact parameter depends only on the ADM mass  $M$ , and the system behaves as a single BH with mass  $M$ . When the mass of the BH is set to zero, we see that the critical impact parameter also goes to zero. This is expected, since there would be no absorption if there was no BH.

Another interesting feature arises when the spherical shell is far away from the BH. When this happens, the whole system behaves as a single BH with a mass  $M_H$ . This can be seen directly from the metric function, since

$$A(r) \sim 1 - \frac{2M_H}{r} + \mathcal{O}(R_S^{-1}), \quad (9.43)$$

when  $R_S \gg M_H$ . This can be understood in terms of the density of the spherical shell, which decays quickly with its position, c.f. Eq. (9.14). Moreover, FIG. 9.6 also shows the case  $R_S = 20M$ , for which the critical impact parameter behaves almost as a straight line  $b_c \sim 3\sqrt{3}M_H$ , characteristic of the BH case.

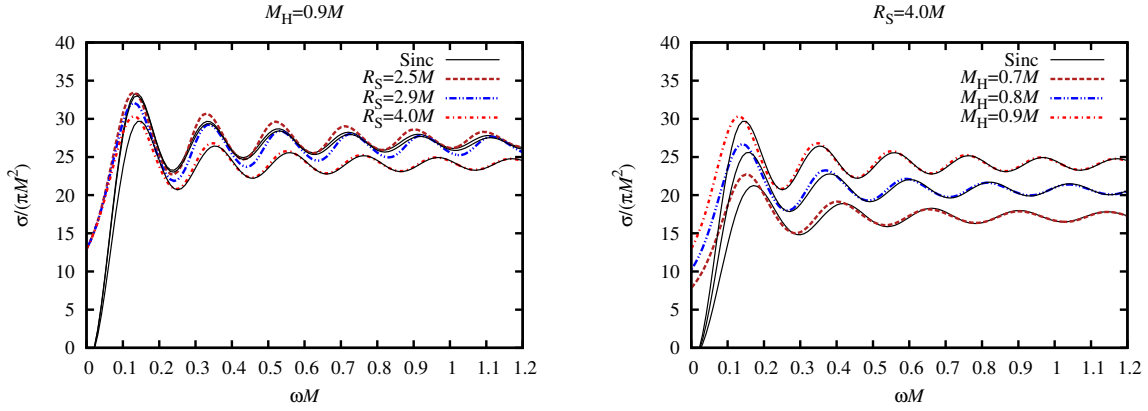


Figure 9.7: LEFT: Sinc approximation for fixed BH mass,  $M_{\text{H}} = 0.9M$ , and different shell positions, namely,  $R_{\text{S}} = 2.5, 2.9$ , and  $4.0M$ . RIGHT: Sinc approximation for fixed shell position  $R_{\text{S}} = 4.0M$  and different BH masses, namely,  $M_{\text{H}} = 0.7, 0.8$ , and  $0.9M$ . The dashed lines show the sinc approximation (9.44), and the solid lines represent the numerical results of the absorption cross section.

### Sinc approximation

At high values of  $\omega$ , the absorption cross section presents a regular oscillatory pattern around its capture cross section. Using complex angular momentum methods, some authors have shown that these oscillations are related to the features of the unstable null orbit [321, 349]. It has been shown that for a spherically symmetric BHs [349]

$$\sigma/\sigma_{\text{geo}} \sim 1 - 8\pi e^{-\pi\beta} \text{sinc}(2\pi\omega/\Omega) \quad (9.44)$$

in which  $\beta \equiv \Lambda/\Omega$ , where  $\Omega$  is the frequency of the null circular orbit and  $\Lambda$  the associated Lyapunov exponent [190]. For the DBH case explored here, the capture cross section  $\sigma_{\text{geo}}$  is given by  $\sigma_{\text{geo}} = \pi b_c^2$ , with  $\Omega = 1/b_c$ , and  $\beta = 1$ . In FIG. 9.7, we show a sample of results obtained through Eq. (9.44) and compare with the numerical results we obtained for the absorption cross section obtaining very good agreement.

## 9.4 Results

In this section we present our numerically results for the scalar absorption of a Schwarzschild BH surrounded by a thin spherical shell of matter. As a general behavior, we note that the total absorption cross section, similarly to the case of an isolated Schwarzschild BH, presents a regular oscillatory behavior around its high-frequency limit.

In the left plot of FIG. 9.8, we show the total absorption cross section for a fixed black hole mass  $M_{\text{H}} = 0.9M$  and positions of the shell at  $R_{\text{S}} = 2.5, 2.9$ , and  $4M$ . By increasing the frequency, we note that the total absorption cross section increases from the area of the event horizon and then oscillates regularly around the high-frequency limit given by the capture cross section of null geodesics (provided in Subsection 9.3.3), which is represented by a horizontal line. When we keep the same value for the BH mass, we see that the absorption decreases as the shell is positioned further away from the BH. We should point out that, for this case, DEC

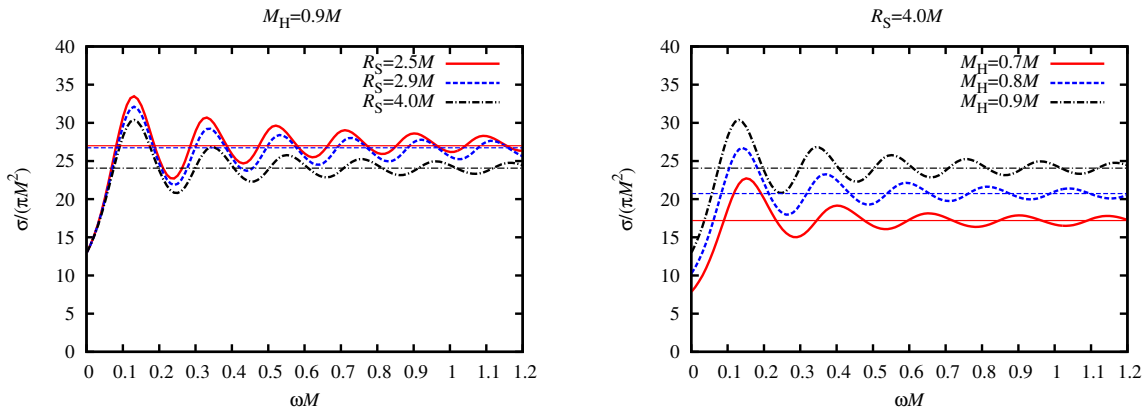


Figure 9.8: LEFT: Total absorption cross with  $M_H = 0.9M$  and  $R_S = 2.5, 2.9,$  and  $4.0M$ . RIGHT: Total absorption cross section for a fixed shell position  $R_S = 4.0M$  and different BH masses  $M_H = 0.7, 0.8,$  and  $0.9M$ . The horizontal lines correspond to the high-frequency limit in each case.

is fulfilled while SEC does not allow the shell to be located at  $R_S = 2.5M$  with  $M_H = 0.9M$ , as it can be seen in FIG. 9.4. Furthermore, according to the right image at plot of FIG. 9.8, when we consider the same value for the shell position  $R_S = 4.0M$  and different BH masses  $M_H = 0.7, 0.8,$  and  $0.9M$ , we note that the absorption decreases as the mass rate increases. In this case, both DEC and SEC are satisfied.

In FIG. 9.9, we show the results for the partial ( $\sigma_l$ ) and total absorption ( $\sigma$ ) cross sections for Schwarzschild BHs surrounded by a thin spherical shell of matter (DBHs), and compare with the results for an isolated Schwarzschild BH. The units are such that we can compare directly the DBH against isolated BH with the same ADM mass. We note that for the BH mass  $M_H = 0.9M$ , as we increase the shell radius  $R_S$ , the partial and total cross sections for DBHs become closer to the results for an isolated Schwarzschild BH with mass  $M_H$ . This occurs because for a large value of the shell radius the DBH behaves as an isolated BH with mass  $M_H$ , as shown by Eq. (9.43). Also, we see that when the shell is closer to the BH, the cross sections for DBHs approach the ones for a Schwarzschild BH with mass  $M_H = M$ . This is in agreement with the fact that, when the shell is near to the BH, the whole system behaves as a BH with mass  $M$ .

## 9.5 Final remarks

We have considered planar massless scalar waves impinging upon a Schwarzschild BH surrounded by a thin spherical shell of mass, and determined numerically its absorption spectrum. Our numerical results are in full agreement with the null geodesics analysis (c.f. Sec. 9.3.3). In the low-frequency regime, we have seen from our numerical results that the total absorption cross section is given by the area of the event horizon, in accordance with analytical results.

We show that for the same shell mass the absorption is bigger when the shell is closer to the BH, and for a fixed shell position, the absorption cross section increases as the shell mass decreases. Also, when we compare the absorption of a DBH with an isolated one, we have shown that as the shell is placed further away from the black hole the absorption cross section

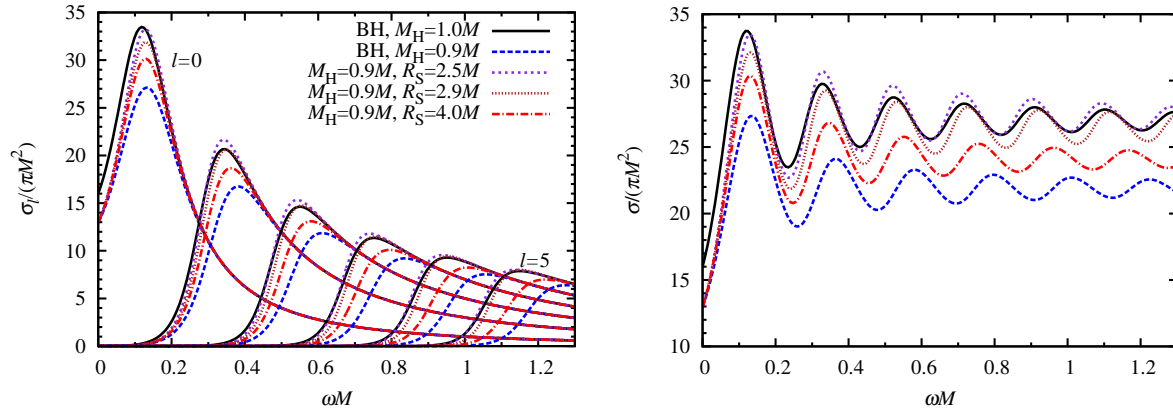


Figure 9.9: LEFT: Comparison between the partial absorption cross sections,  $\sigma_l$ , for DBHs and Schwarzschild BHs. RIGHT: The total absorption cross sections for DBHs compared, with the ones of Schwarzschild BHs with the same ADM mass.

of the DBH tends to the result of an isolated Schwarzschild BH with the same mass of the BH inside the shell. In accordance with the fact that as the shell is positioned away from the BH, the entire configuration (BH + shell) starts to behave as a single BH with mass  $M_H$ . Otherwise, if we approximate the shell to the BH, we note that the absorption rate approaches to case of a single BH with mass equal to the whole system (BH + shell).

The results presented in this chapter generically shows that the presence of matter around black holes can modify their absorption properties. The influence of the surrounding matter intensifies for higher density of the shell. Configurations of comparable amount of masses of the BH and the surrounding matter can occur, for instance, in stellar BH binaries [350]. Therefore, we expect that the analysis described here may be used to estimate the absorption properties of these systems. Considering very massive BHs, in which the surrounding matter is expected to have lesser influence on absorption properties, our analysis could be applied in cases of BHs hosted in dwarf galaxies [351].

Another interesting feature that arises due to the matter surrounding the black hole is the appearance of a second light ring. The existence of two light rings happens when the thin shell is properly placed, but we expect that other matter configurations would also share this feature, like, for instance, when considering thick shells. Between the two light rings positions there is a local minimum of the potential, similar to the one that appears in the case of gravastars [154, 262]. In the thick shell case, this minimum point is related to the existence of a *stable* light ring. Moreover, stable light rings support long-lived modes in the eikonal limit [352]. There are some studies that suggest that these long-lived modes can source nonlinear instabilities [352, 353], and therefore any kind of exotic matter that allows the existence of such feature may eventually collapse to the black hole. This could put further constraints on the matter surrounding BHs.

# Chapter 10

## Absorption of planar massless scalar waves by Bardeen black holes

One of the most intriguing predictions of general relativity (GR) is the existence of black holes (BHs). BHs became a paradigm in physics, and are believed to populate the galaxies [291]. Within standard GR, black holes are simple objects, described only by their mass, angular momentum and charge [354]. However, standard black holes suffer from one of the main problems of GR: the presence of singularities. Our physical knowledge breaks down at singularities. Although generally hidden by a horizon, and protected by the Penrose conjecture [355] (see also [356] for a review), singularities are expected to exist within GR, according to the singularity theorems developed by Hawking and collaborators [357].

Singularities are expected to be better understood with an improved theory of gravity (whether an extension or a modification of GR) [8]. Notwithstanding, within GR it is possible to obtain BH solutions without singularities. Bardeen presented a BH solution without singularities that satisfies the weak energy condition in GR [358]. Although Bardeen's solution has its theoretical motivation in the studies of BH spacetimes with no singularities, a stronger physical motivation for it was missing until it was shown that the Bardeen BH is a solution of GR with a nonlinear magnetic monopole, i.e., a solution of the Einstein's equations coupled to a nonlinear electrodynamics [359]. Apart from this, further works with other physically motivated regular BHs can be found in the literature (see, e.g., Refs. [360, 361]).

One way to test the physics of BHs is analyzing test fields around them. In this context, there are the quasinormal modes: natural oscillation frequencies of the fields with physically motivated boundary conditions [109, 148]. An extensive survey of quasinormal modes of test charged scalar fields around different types of regular BHs was presented in Ref. [362]. Quasinormal modes of the Dirac field were investigated in Ref. [363] and of the massive scalar fields in Hayward regular BHs in Ref. [364]. Quasinormal modes have an interesting relation with scattering processes in BH spacetimes. This relation can be seen, for instance, in the scattering of Gaussian packets by BHs [365, 366].

Another important aspect of BHs is how they absorb matter and fields around them, i.e., their accretion rate. Accretion has an important role in the phenomenology of active galactic

nuclei, and can be considered as an important agent to the mass growth of their BH hosts (see, e.g., Refs. [292, 325, 326] and the references therein). Along more than 45 years, absorption of scalar fields has been studied extensively in many BH scenarios (see, e.g., Refs. [300, 304, 317, 318, 338, 347, 367, 368] and the references therein). The initial field configuration is usually taken to be plane waves at infinity and the problem is often directed to compute the absorption cross section of the field. Also, in the classical (high-frequency) limit, absorption cross sections are directly related with the shadows of BHs [341–343]. Moreover, the case of planar waves absorption has many features in common with the case of accretion of a fluid moving with constant velocity toward a BH (see, e.g., Ref. [340]), which turns out to be important in the phenomenology of extreme mass-ratio inspirals [149, 156].

In this chapter we address the problem of how regular BHs absorb fields, focusing in the analysis of the absorption cross section of planar massless scalar waves by a Bardeen regular BH. Generically, the line element of spherically symmetric BH spacetimes can be written in the standard spherical coordinate system as

$$ds^2 = -f(r)dt^2 + f(r)^{-1}dr^2 + r^2d\Omega^2, \quad (10.1)$$

where the function  $f(r)$  depends on the particular BH under consideration. As we shall see, the Bardeen BH has a structure very similar to that of a standard electrically charged BH within GR, i.e., of a Reissner–Nordström (RN) BH. Because of that, we shall compare our results with the RN BH ones [304, 305].

The remainder of this chapter is organized as follows. In Sec. 10.1 we review some aspects of the Bardeen regular BHs. In Sec. 10.2 we revisit the main aspects of the absorption cross section of planar massless scalar waves in spherically symmetric BH spacetimes. We also present the results in the low- and high-frequency regimes for the massless scalar absorption cross section of Bardeen BHs. In Sec. 10.3 we exhibit a selection of our numerical results. We compare our results for the Bardeen regular BH with the results for the RN BH. Also, we discuss the possibility of having a Bardeen BH with a similar absorption cross section of a RN BH. We present our final remarks in Sec. 10.4. Throughout the chapter we use natural units, for which  $G = c = \hbar = 1$ .

## 10.1 Bardeen regular black holes

As mentioned in the Introduction, the Bardeen BH was one of the first regular BH solutions presented in the literature [358]. Later, it received the physical interpretation of a BH with a nonlinear magnetic monopole [359]. Nonlinear electrodynamics theories within GR are generically described by the action

$$S = \int d^4x \sqrt{-g} \left[ \frac{1}{16\pi} R - \frac{1}{4\pi} \mathcal{L}(F) \right], \quad (10.2)$$

where  $R$  is the Ricci scalar;  $\mathcal{L}$  is the Lagrangian of the electromagnetic field;  $F = \frac{1}{4}F_{ab}F^{ab}$ ; with  $F_{ab}$  being the standard electromagnetic field strength; and  $g$  is the determinant of the metric  $g_{ab}$ . For the theory that generates the Bardeen regular BH, we have that

$$\mathcal{L}(F) = \frac{3}{2s q^2} \left( \frac{\sqrt{2q^2 F}}{1 - \sqrt{2q^2 F}} \right)^{5/2}, \quad (10.3)$$

where  $s = |q|/(2M)$ ,  $q$  is the magnetic charge and  $M$  is the mass of the configuration [359]. The line element of the Bardeen BH is given by Eq. (10.1), with

$$f(r) = 1 - \frac{2Mr^2}{(r^2 + q^2)^{3/2}}. \quad (10.4)$$

The Bardeen solution has a structure similar to the RN spacetime, presenting two horizons up to some value of the BH charge. For  $q = q_{\text{ext}} = 4M/(3\sqrt{3})$ , the two horizons coincide and we have the so-called extremal BH. In this chapter, we shall consider  $0 \leq q \leq q_{\text{ext}}$ .

For later comparison, it is instructive to mention explicitly the RN solution. The line element of the RN spacetime is given by Eq. (10.1), with

$$f(r) = 1 - \frac{2M}{r} + \frac{q^2}{r^2}, \quad (10.5)$$

where, in this case,  $q$  is the electric charge of the BH. The extreme case of the RN BH is given by  $q_{\text{ext}} = M$ . Note that we are using the same symbol ( $q$ ) for both magnetic (Bardeen BH) and electric (RN BH) charge. To better compare both spacetimes, we shall present our results in terms of the normalized charge  $Q \equiv q/q_{\text{ext}}$ .

## 10.2 Absorption cross section

### 10.2.1 Partial-waves approach

A massless scalar field  $\Phi$  is described by the Klein–Gordon equation, namely,

$$\frac{1}{\sqrt{-g}} \partial_a (\sqrt{-g} g^{ab} \partial_b \Phi) = 0. \quad (10.6)$$

Here we are considering a minimally coupled scalar field.

A monochromatic wave with frequency  $\omega$  in a spherically symmetric background can be written as

$$\Phi = \sum_{lm} \frac{\phi(r)}{r} Y_l^m(\theta, \varphi) e^{-i\omega t}, \quad (10.7)$$

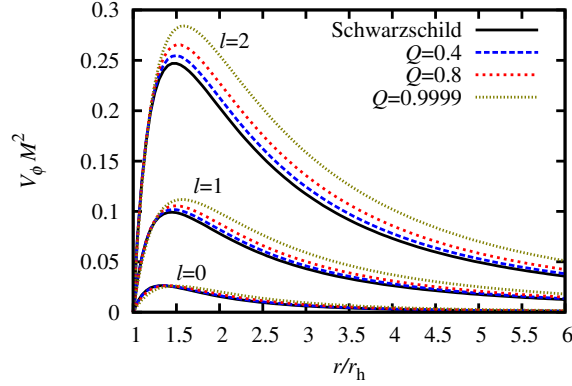


Figure 10.1: Scalar field potential ( $V_\phi$ ) as function of the radial coordinate in units of the event horizon radius ( $r_h$ ). Here we compare the Bardeen BHs with the Schwarzschild case, and we see that the shape of the potential is similar in all cases.

where  $Y_l^m(\theta, \varphi)$  are the standard scalar spherical harmonics. Substituting the expansion (10.7) in Eq. (10.6), and using the properties of the spherical harmonics, we get the following radial equation for  $\phi(r)$ :

$$\left(-\frac{d}{dx^2} + V_\phi(r) - \omega^2\right) \phi(r) = 0, \quad (10.8)$$

in which  $x$  is the tortoise coordinate, defined through  $dx = f(r)^{-1} dr$ , and

$$V_\phi(r) = f \left( \frac{l(l+1)}{r^2} + \frac{f'}{r} \right) \quad (10.9)$$

is the scalar field potential. Plots of  $V_\phi$  for Bardeen and Schwarzschild BHs are shown in Fig. 10.1. The scalar field potential  $V_\phi$  is localized, in the sense that it goes to zero at the event horizon and at infinity [369]. We are interested in a solution that represents a wave coming from the past null infinity. Such a solution can be written using the so-called *in* modes, i.e.

$$\phi(r) \sim \begin{cases} R_I + \mathcal{R}_{\omega l}^{in} R_I^* & x \rightarrow +\infty (r \rightarrow +\infty), \\ \mathcal{T}_{\omega l}^{in} R_{II} & x \rightarrow -\infty (r \rightarrow r_h), \end{cases} \quad (10.10)$$

with

$$R_I = e^{-i\omega x} \sum_{j=0}^N \frac{A_\infty^j}{r^j}, \quad (10.11)$$

$$R_{II} = e^{-i\omega x} \sum_{j=0}^N (r - r_h)^j A_{r_h}^j, \quad (10.12)$$

where the coefficients  $A_\infty^j$  and  $A_{r_h}^j$  are obtained by requiring the functions  $R_I$  and  $R_{II}$  to be solutions of Eq. (10.8) far from the BH and close to the event horizon, respectively.  $|\mathcal{R}_{\omega l}^{in}|^2$  and

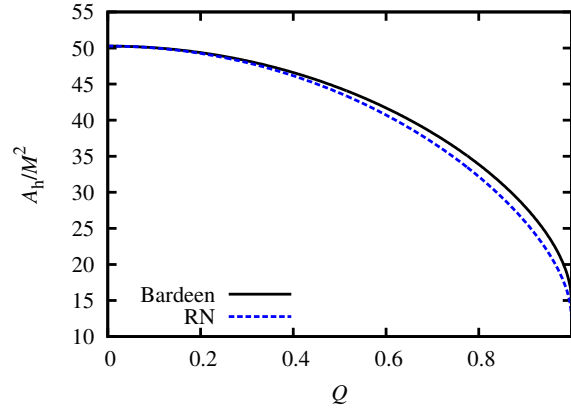


Figure 10.2: Event horizon area of Bardeen and RN BHs as a function of the normalized charge.

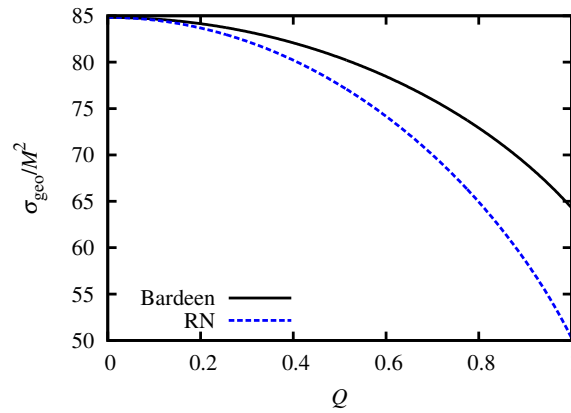


Figure 10.3: Capture cross section of null geodesics ( $\sigma_{\text{geo}}$ ) by Bardeen and RN BHs. The results for Bardeen BHs have qualitatively the same behavior of the RN BHs, with the former presenting a bigger capture cross section for the same value of the normalized charge.

$|\mathcal{T}_{\omega l}^{\text{in}}|^2$  are the reflection and transmission coefficients, respectively, and are related through

$$|\mathcal{R}_{\omega l}^{\text{in}}|^2 + |\mathcal{T}_{\omega l}^{\text{in}}|^2 = 1. \quad (10.13)$$

Using the solution (10.10), the absorption cross section of planar massless scalar waves can be written as

$$\sigma_{\text{abs}} = \sum_{l=0}^{\infty} \sigma_l, \quad (10.14)$$

with  $\sigma_l$  being the partial absorption cross sections, given by

$$\sigma_l = \frac{\pi}{\omega^2} (2l+1) |\mathcal{T}_{\omega l}^{\text{in}}|^2. \quad (10.15)$$

### 10.2.2 Low- and high-frequency limits

In the low-frequency regime, it has been proven that the absorption cross section of massless scalar fields by static BHs [370], as well as stationary BHs [317, 318], tends to the area of the BH horizon. Our numerical results agree remarkably well with this low-frequency limit. In Fig. 10.2 we plot the area of the event horizon for the Bardeen and RN BHs, as a function of the normalized charge. We can see that the event horizon area of a Bardeen BH is bigger than the corresponding one of the RN BH with the same normalized charge.

In the high-frequency limit, a massless scalar wave can be described by the propagation of a null vector, which follows a null geodesic. Therefore, in this limit we can consider the classical capture cross section of null geodesics to describe the absorption cross section of massless fields.

Geodesics around Bardeen BHs were also studied in Ref. [371]. Here we consider null geodesics in spherically symmetric BHs. Their motion is described by the Lagrangian  $L_{\text{geo}}$ , that satisfies

$$2L_{\text{geo}} = -f(r)\dot{t}^2 + f(r)r^2 + r^2\dot{\phi}^2 = 0, \quad (10.16)$$

in which we consider, without loss of generality, the motion in the plane  $\theta = \pi/2$ . The overdot indicates derivative with respect to the affine parameter of the curve. Considering the conserved quantities, namely the energy  $E$  and angular momentum  $L$  (see, e.g., Ref. [190]), the equation of motion becomes

$$\dot{r}^2 + L^2 \frac{f(r)}{r^2} = E^2, \quad (10.17)$$

which can be regarded as an energy balance equation with the effective potential

$$V_{\text{eff}} = L^2 f(r)/r^2. \quad (10.18)$$

The high-frequency limit of the absorption cross section, also called geometric cross section,  $\sigma_{\text{geo}}$ , is then found by computing the classical capture radius of light rays in the spacetime under investigation. For spherically symmetric spacetimes, the null geodesic radius  $r_l$  is obtained through  $V'(r_l) = 0$ , with the prime denoting derivative with respect to  $r$ . The critical impact parameter is given by  $b_c = L_c/E_c$ , with  $(L_c, E_c)$  being characteristic of the null circular geodesic. Therefore, we have

$$r_l f'(r_l) - 2f(r_l) = 0, \quad (10.19)$$

and

$$\sigma_{\text{geo}} = \pi b_c^2 = \pi \frac{r_l^2}{f(r_l)}. \quad (10.20)$$

With Eq. (10.19) one finds the value of  $r_l$ , and by substituting this value in Eq. (10.20) one finds the capture (or geometric) cross section  $\sigma_{\text{geo}}$ .

In Fig. 10.3 we compare the capture cross section of the Bardeen BH with the RN BH case, as a function of the normalized charge. In general, a Bardeen BH has a bigger capture cross section, compared with the RN BH with the same value of  $Q(> 0)$ .

An improvement of the high-frequency approximation to compute the absorption cross section for spherically symmetric BHs was proposed in Ref. [349]. It was shown that the oscillatory

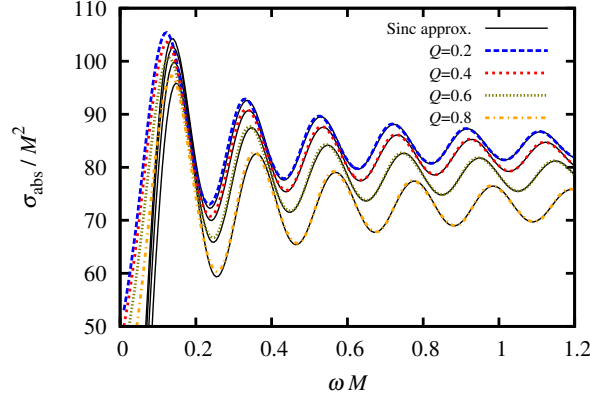


Figure 10.4: Comparison between the full numerical computation of the total absorption cross section of Bardeen regular BHs, given by Eq. (10.14), with the high-frequency (sinc) approximation, given by Eq. (10.22). We can see that the numerical and the approximate analytical results agree remarkably well even for intermediate values of the frequency.

part of the absorption cross section in the eikonal limit can be written as

$$\sigma_{\text{osc}}(\omega) = -\frac{4\Lambda_l}{\omega\Omega_l^2} e^{-\frac{\Lambda_l}{\Omega_l}} \sin\left(\frac{2\pi\omega}{\Omega_l}\right), \quad (10.21)$$

where  $\Lambda_l = \pi\lambda_l$ , with  $\lambda_l$  being the Lyapunov exponent of the null geodesic [190, 349], and  $\Omega_l = d\varphi/dt = \sqrt{f(r_l)}/r_l$  being the angular velocity of the null geodesic. Therefore, we can write the high-frequency absorption cross section as

$$\sigma_{\text{abs}}^{\text{hf}} \sim \sigma_{\text{geo}} + \sigma_{\text{osc}}. \quad (10.22)$$

Equation (10.22) is usually referred to in the literature as the sinc approximation. In Fig. 10.4 we compare the results obtained through Eq. (10.22) with the full numerical computation of the absorption cross section, given by Eq. (10.14). It is interesting to note that, although Eq. (10.22) is obtained within the assumption of high frequencies, it is still a very good approximation for intermediate frequency values.

## 10.3 Results

We have computed numerically the absorption cross section of planar massless scalar waves impinging on Bardeen BHs. In this section we show a selection of our results.

In Fig. 10.5 we present the partial absorption cross sections [given by Eq. (10.15)] for  $Q = 0.4, 0.6, 0.8$  and  $0.9999$  and for different values of  $l$ . We see that for  $l = 0$  the limit  $\omega \rightarrow 0$  results in  $\sigma_{\text{abs}} \rightarrow A_h$ , in agreement with the result mentioned in Sec. 10.2.2.

In Fig. 10.6 we present the total absorption cross section [given by Eq. (10.14)] in the Bardeen BH case, for  $Q = 0.6, 0.8$  and  $0.9999$ , as well as in the Schwarzschild BH case. The horizontal lines are the high-frequency limits in each case. We see that the increasing of the

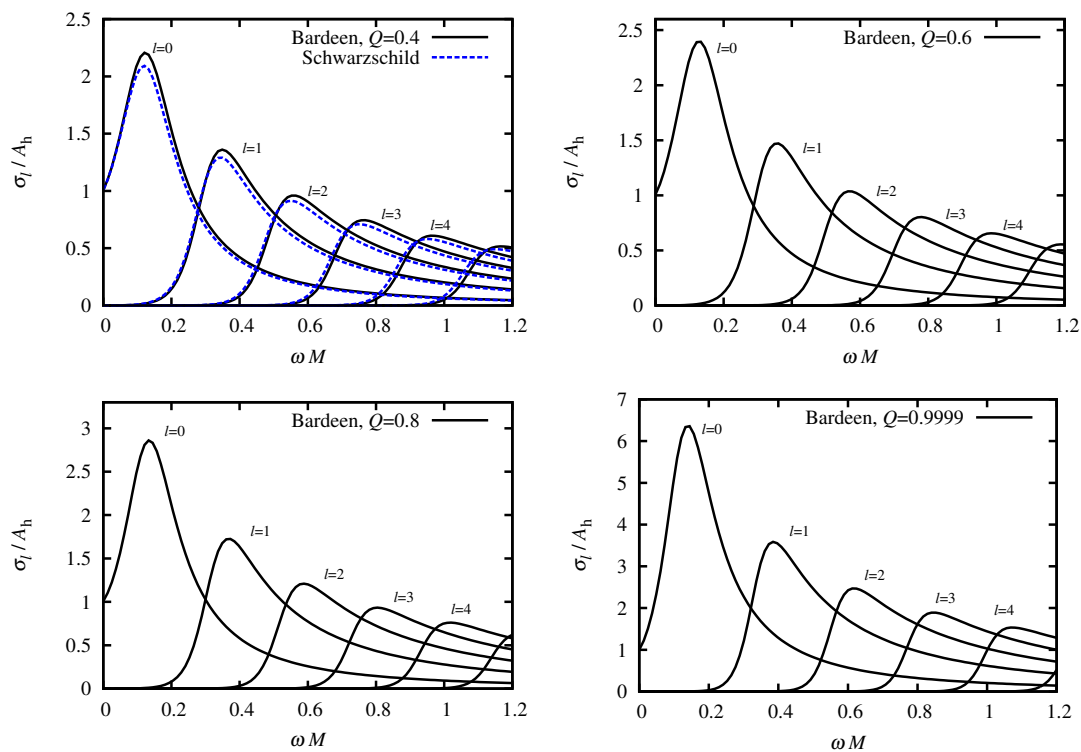


Figure 10.5: Partial absorption cross sections of massless scalar waves by Bardeen BHs. Different frames correspond to different values of the normalized monopole charge  $Q$ . For comparison, in the top-left frame we also plot the partial absorption cross sections of the Schwarzschild BH (dotted lines).

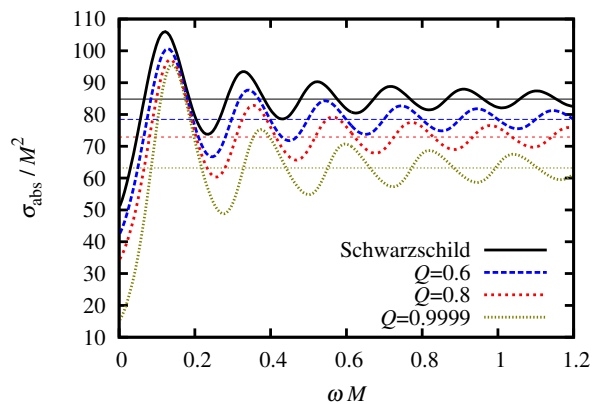


Figure 10.6: Absorption cross section of massless scalar waves by Bardeen BHs, compared with the capture cross section in each case (horizontal lines). The Schwarzschild BH case is also exhibited, for comparison.

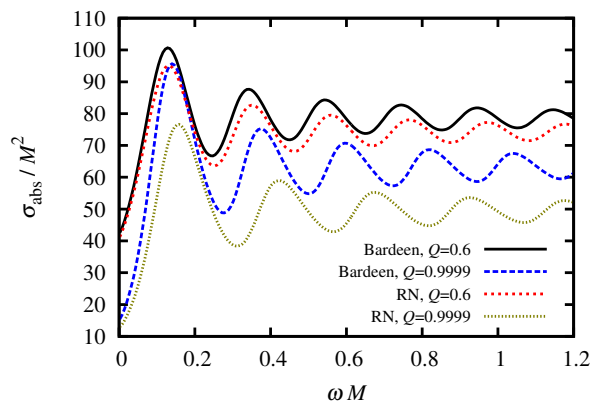


Figure 10.7: Comparison between the Bardeen and the RN BH cases with the same values of  $Q$ . The plots show  $Q = 0.6$  and  $0.9999$ .

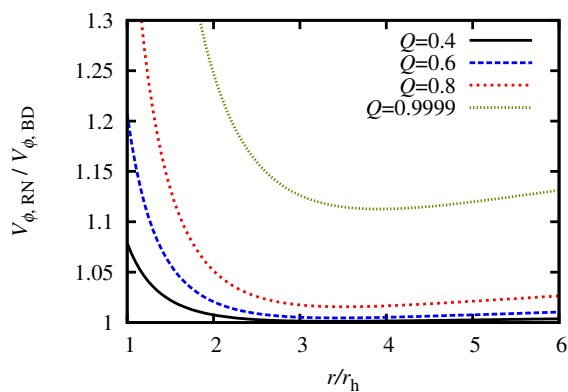


Figure 10.8: Ratio between the scalar field potential of the RN ( $V_{\phi,RN}$ ) and Bardeen BHs ( $V_{\phi,BD}$ ), for  $l = 0$  and  $Q = 0.4, 0.6, 0.8,$  and  $0.9999$ . Similar results hold for higher values of  $l$ .

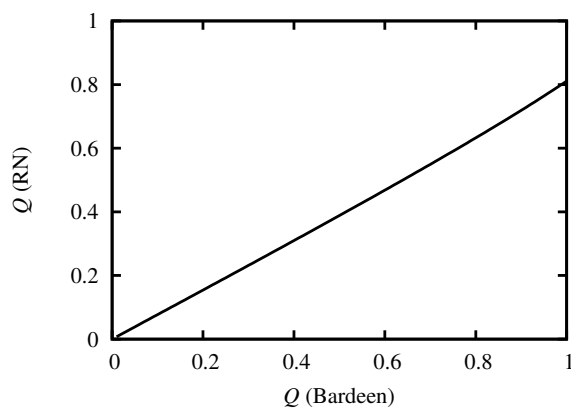


Figure 10.9: Values of the normalized charge for which the capture cross section of Bardeen and RN BHs are the same.

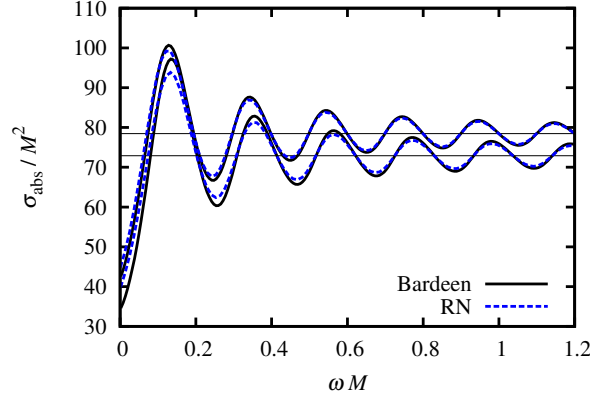


Figure 10.10: Total absorption cross section for Bardeen and RN BHs with the same high-frequency limit (horizontal lines). We have chosen  $(Q_{\text{RN}}, Q_{\text{BD}})$  to be  $(0.6, 0.46809)$  and  $(0.8, 0.63252)$ . We see that their oscillation profiles are similar, but their low-frequency limits are different.

monopole charge implies in a decreasing of the absorption cross section, in agreement with the increasing of the scattering potential (cf. Fig. 10.1), as well as with the decreasing of the horizon area (cf. Fig. 10.2). The sum of the partial absorption cross sections generates the oscillatory profile shown in the plots of Fig. 10.6.

In Fig. 10.7 we compare the absorption cross section of Bardeen and RN BHs, for the same values of  $Q$ . As already mentioned in Sec. 10.2.2 (cf. Fig. 10.3), the high-frequency limit of the absorption cross section of the Bardeen BH is bigger than the correspondent RN BH case with the same value of  $Q$ . We verified that this behavior (bigger absorption for the Bardeen BH) also applies to the total absorption cross section as a whole, for any fixed value of the frequency  $\omega$ , for the same normalized charge  $Q(> 0)$ . This is in accordance with the fact that the scalar field potential for the RN BH is always bigger than the corresponding one for the Bardeen BH, as it is shown in Fig. 10.8, where we plot the case in which  $l = 0$ . Larger values of  $l$  present a similar behavior.

Although for the same values of  $Q$  the Bardeen BH has a bigger absorption cross section than the corresponding RN BH, for different values of the normalized charge  $Q$  they can have the same capture cross section, i.e. the same high-frequency limit of the absorption cross section. In Fig. 10.9 we plot the values of the normalized charge for which the capture (or high-frequency absorption) cross section is the same for Bardeen and RN BHs. We can see from Fig. 10.9 that the RN BH must have a lower value of the normalized charge in order to have the same capture cross section of a Bardeen BH.

The equality between the high-frequency values of the absorption cross section of RN and Bardeen BHs with different normalized charges raises the following question: Can a Bardeen BH produce the same absorption spectrum of a RN BH? To answer this, we have computed the absorption cross section for configurations which have the same high-frequency limits. Some results are shown in Fig. 10.10, where we plot the configurations for which  $(Q_{\text{RN}}, Q_{\text{BD}})$  are chosen to be  $(0.6, 0.46809)$  and  $(0.8, 0.63252)$ . We can see that the low-frequency absorption cross section is different, although not only the high-frequency limits are the same, but also the oscillation profiles are similar.

The similarity of the oscillation profile of Bardeen and RN BHs with the same  $\sigma_{\text{geo}}$  can be understood as follows. From Eq. (10.21), we see that the oscillation pattern depends on  $2\pi/\Omega_l$ .

Since we use configurations with the same capture cross section, the angular velocity ( $\Omega_l$ ) of the null geodesics are also the same, once  $b_c = 1/\Omega_l$ . Therefore, the frequency of oscillation of the two configurations will be similar.

The above scenario suggests that a regular black hole can, in principle, mimic a black hole with singularities, as far as mid-to-high-frequency absorption cross section is concerned. However, we should note that, as Fig. 10.9 shows, there is no complete correspondence between Bardeen and RN BHs absorption spectra with the same capture cross section, as it can be seen in Fig. 10.10. Moreover, as it can be verified in Fig. 10.9, for a Bardeen BH with  $Q = 1$ , the corresponding RN BH with the same value of the capture cross section has a normalized charge  $Q = 0.8109$ . Therefore, for a RN BH with a charge  $Q > 0.8109$  there is no correspondent Bardeen BH with the same capture cross section.

## 10.4 Final remarks

In this chapter we presented a study of the absorption properties of regular black holes: objects which have event horizons but not singularities. For that purpose, we analyzed the case of an asymptotic planar massless scalar wave impinging upon a Bardeen regular black hole<sup>1</sup>.

We computed numerically the massless scalar absorption cross section of Bardeen regular black holes showing that the generic oscillation behavior of spherical black holes with singularities, like the Schwarzschild and Reissner–Nordström ones, is also present in the case of Bardeen regular black holes. The increasing of the monopole charge, starting from the Schwarzschild black hole case (for which  $Q = 0$ ), implies a decreasing of the absorption cross section. Our numerical results are in full agreement with the low- and high-frequency limits of the absorption cross section, which can be obtained analytically.

We compared the massless absorption cross section of a Bardeen black hole with the one of a Reissner–Nordström black hole with the same value of the normalized charge  $Q$ . We obtained that the behavior of the absorption cross section is qualitatively similar in both cases, but the Bardeen case always presents a bigger absorption cross section than the Reissner–Nordström case, for any fixed values of  $(\omega, Q)$ .

Based on the behavior of null geodesics, we have shown that the capture cross section of a Bardeen black hole is always bigger than the corresponding one of a Reissner–Nordström black hole with the same value of  $Q$ . We have also shown that a Bardeen black hole can have the same capture cross section of a Reissner–Nordström black hole with a different value of  $Q$ .

We computed numerically the massless scalar absorption cross section for arbitrary frequencies by Bardeen and Reissner–Nordström black holes with the same high-frequency limit. We concluded that, more than having the same capture cross section, the oscillation of the absorption cross section is similar for both cases. This comes from the fact that the oscillation depends

---

<sup>1</sup>After this work has been basically concluded, we became aware of an attempt to compute the scalar absorption cross section of regular black holes in Ref. [372]. The authors of Ref. [372] used the WKB method with the Pöschl–Teller potential to solve the differential Eq. (10.8). However, their results do not seem correct, and they differ considerably from ours. In particular, the authors of Ref. [372] do not obtain the well known results for low-frequency (given by the horizon area) and high-frequency (given by the capture cross section) absorption cross section limits. Moreover, their results for small black hole charge do not agree with the Schwarzschild limit, as it should also be the case.

---

on the angular velocity of the null circular geodesic, which is the same for the two cases. Our results suggest that some regular black holes could be mimicked by black holes with singularities, as far as mid-to-high-frequency absorption properties are concerned. The differences between the two cases manifest mainly in the low-frequency regime.

# Chapter 11

## Scattering by regular black holes: Planar massless scalar waves impinging upon a Bardeen black hole

Black holes (BHs) are among the most interesting objects of general relativity (GR). Although GR is a highly nonlinear theory, BHs come out of it with a very simple structure. Standard GR BH solutions are parameterized by their mass, charge and angular momentum [354] (see, e.g., Refs. [136, 139] for interesting counterexamples of the previous statement). Although related to the earliest predictions of GR, the strong field regime of BHs is still an experimental challenge [1, 9, 59]. Notwithstanding, the observational data presently available suggest that BHs populate basically all the galaxies in the Universe [291].

Although very successful in explaining the available data, standard GR BHs suffer from one of the main problems of GR: the presence of singularities. Hawking and Penrose indeed showed that, for some hypotheses on the gravitational collapse, the formation of singularities in BHs would be unavoidable [4, 357]. These singularities were conjectured by Penrose to be hidden by a horizon [355, 356], and were claimed to be possibly avoided within an improved theory of gravity (extension or modification of GR) [8].

The study of BHs without singularities can help us to understand the role played by singularities in astrophysics. Still within GR, one can obtain BHs without singularities — dubbed regular BHs — by relaxing one of the energy conditions on the stress-energy tensor. Bardeen proposed the first regular BH solution [358], which was later identified as a solution for a nonlinear magnetic monopole [359]. Since then, other regular BHs appeared in the literature, in different scenarios (see, e.g., Refs. [360–362], and references therein). Moreover, regular BHs can be relevant in the context of quantum gravity [373, 374], and some of them reproduce the quantum weak field regime of GR [375].

Studies of scattering by BHs have been extensively made [347]. Reference [298] presented the results of the scattering of all basic massless (spin 0, 1/2, 1 and 2) fields by Schwarzschild BHs. Moreover, the shadows of BHs [341, 376] may become visible with future telescopes, like

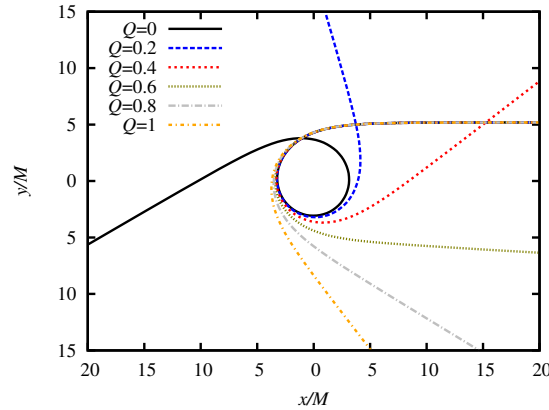


Figure 11.1: Geodesics approaching a Bardeen BH from infinity with an impact parameter of  $b = 5.2M$ , for different values of the BH charge. The Schwarzschild case ( $Q = 0$ ) is also exhibited (solid line).

the Event Horizon Telescope [377], and the scattering of light, considering wave and semiclassical approximations, may be important in anticipating subtle characteristics of the shadows. However, a careful study of the scattering of fields by regular BHs is still lacking in the literature<sup>1</sup>.

The line element of the Bardeen BH can be written as

$$ds^2 = -f(r)dt^2 + f(r)^{-1}dr^2 + r^2(d\theta^2 + \sin^2\theta d\varphi^2), \quad (11.1)$$

where the lapse function  $f(r)$  is given by

$$f(r) = 1 - \frac{2Mr^2}{(r^2 + q^2)^{3/2}}. \quad (11.2)$$

The Bardeen BH has a structure similar to the Reissner-Nordström (RN) BH (see, e.g., Ref. [360]). For  $q < q_{\text{ext}} = 4M/(3\sqrt{3})$  (henceforth, without loss of generality, we shall assume  $q \geq 0$ ) the spacetime has two horizons and for  $q = q_{\text{ext}}$  the horizons degenerate, characterizing the extremal case. Following Ref. [378], we shall display our results in terms of the normalized charge  $Q = q/q_{\text{ext}}$ <sup>2</sup>.

It is interesting to note that the variation of the charge of the regular BH changes considerably the deflection angle of light rays [371]. In Fig. 11.1 we plot null geodesics coming from infinity with an impact parameter of  $b = 5.2M$ , for different values of the BH charge. The behavior is qualitatively similar to the case of RN BHs [379]. We see that, adjusting the BH charge, we can have scattering in basically any direction.

The remainder of this chapter is organized as follows: In Sec. 11.1 we review the main aspects of the classical geodesic scattering and semiclassical glory approximation to compute

<sup>1</sup>An approximation scheme to compute the scattering cross section of regular BHs was performed in Ref. [372]. The scheme relies on the Wentzel-Kramers-Brillouin (WKB) approximation, using a modification of the effective potential (11.13), leading to inaccurate results (see, e.g., Ref. [378]).

<sup>2</sup>The parameter presented here as  $Q$  can also be interpreted as a natural length when one considers that the Bardeen BH comes from a quantum generalization of GR. See, for instance, Ref. [374] for more details.

the differential scattering cross section. In Sec. 11.2 we present the partial-wave method used to compute the scattering cross section of planar massless scalar waves. In Sec. 11.3 we present the results for the scattering of planar massless scalar waves impinging upon a Bardeen regular BH, comparing the three different approaches used to compute the scattering cross section. In Sec. 11.4 we end up with our final remarks. Throughout this work we use  $G = c = \hbar = 1$  and metric signature  $(-, +, +, +)$ .

## 11.1 Classical scattering and semiclassical glory

In this section we investigate the scattering by BHs by using two approaches: classical geodesic scattering and the semiclassical glory approximation. These approaches allow us to foresee some of the aspects of the scattering cross section obtained within the full partial-wave analysis.

### 11.1.1 Geodesic scattering

The analysis of null geodesics in the Bardeen spacetime can be seen in Ref. [378]. For the classical approximation of the scattering we may consider a stream of parallel null geodesics coming from infinity. In this case, the analysis of Ref. [380] suits the problem of classical scattering by Bardeen BHs. The classical scattering cross section is given by

$$\frac{d\sigma}{d\Omega} = \frac{1}{\sin \chi} \sum b(\chi) \left| \frac{db(\chi)}{d\chi} \right|, \quad (11.3)$$

where  $b(\chi)$  is the impact parameter associated with a scattering angle  $\chi$ . The summation in Eq. (11.3) is such that we also consider the case in which the null geodesic rotates (one or many times) around the BH before going to infinity (for instance, see the solid curve of Fig. 11.1). It is interesting to note that the classical scattering formula given by Eq. (11.3) describes very well the planar-wave case for small scattering angles, although it gives discrepant results for moderate-to-high scattering angles, as we shall see in Sec. 11.3.

Let us now obtain  $b(\chi)$  through a geodesic analysis. Without loss of generality, we shall restrict the geodesic motion to the plane  $\theta = \pi/2$ . From the line element (11.1), we can write, for null geodesics

$$\left( \frac{du}{d\varphi} \right)^2 = \frac{1}{b^2} - f(1/u)u^2, \quad (11.4)$$

where we have defined  $u \equiv 1/r$ ,  $b \equiv L/E$  is the impact parameter given in terms of the constants of motion

$$E = f\dot{t} \quad \text{and} \quad L = r^2\dot{\varphi}, \quad (11.5)$$

and the overdot denotes differentiation with respect to an affine parameter of the curve.

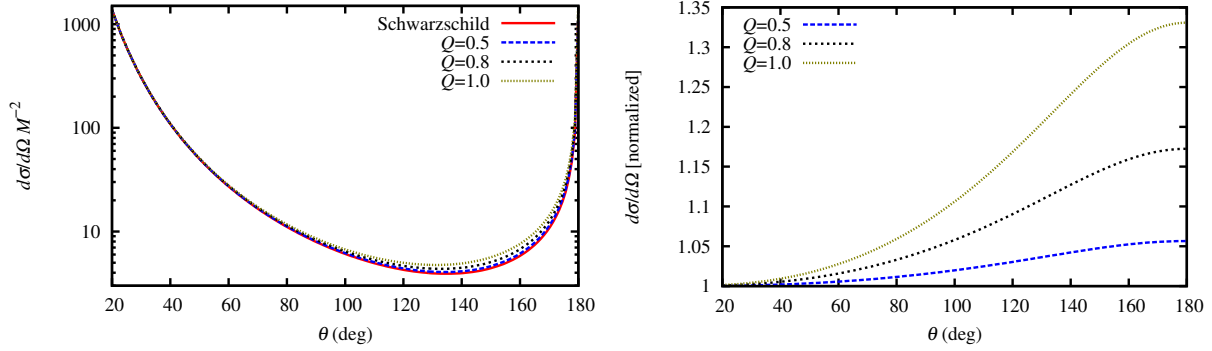


Figure 11.2: *Left panel:* Classical scattering cross section of Bardeen BHs, with  $Q = 0.5, 0.8$  and  $1$ , and for the Schwarzschild BH ( $Q = 0$ ). *Right panel:* Classical scattering cross section of Bardeen BHs, normalized by the Schwarzschild case.

Differentiating Eq. (11.4) with respect to  $\varphi$ , we obtain

$$\frac{d^2 u}{d\varphi^2} = -\frac{u^2}{2} \frac{df(1/u)}{du} - uf(1/u). \quad (11.6)$$

Solving Eq. (11.6) with the appropriate boundary conditions, one can obtain the geodesics followed by massless particles, such as the ones shown in Fig. 11.1. The smallest positive root of the right-hand side of Eq. (11.6) corresponds to the radius of the critical orbit for null geodesics,  $u_c = 1/r_c$ . Substituting its value in the right-hand side of Eq. (11.4) and setting it to zero, we obtain the impact parameter associated with the critical orbits,  $b_c$ . Going in the other way around, i.e., choosing a value  $b > b_c$ , the smallest root of the right-hand side of Eq. (11.4) is  $u_0 = 1/r_0$ , where  $r_0$  is the turning point — or the radius of maximum approximation — of the geodesic.

Finally, by integrating Eq. (11.4) in the case of scattered geodesics, we obtain

$$\alpha = \int_0^{u_0} \left[ \frac{1}{b^2} - f(1/u)u^2 \right]^{-1/2} du. \quad (11.7)$$

The deflection angle following directly from Eq. (11.7) is given by

$$\Theta(b) = 2\alpha(b) - \pi. \quad (11.8)$$

By inverting Eq. (11.8), one obtains  $b(\Theta)$ , and substituting it in Eq. (11.3), one obtains the classical scattering cross section. Plots of the classical scattering cross section obtained by Eq. (11.3) are exhibited in Fig. 11.2, where we compare the Bardeen cases with the Schwarzschild one. We see from Fig. 11.2 that the increase of the BH charge contributes to an increase of the BH classical scattering cross section.

### 11.1.2 Glory scattering

The interference that occurs between scattered partial waves with different angular momenta is not taken into account by the classical formula (11.3). In order to obtain a scattering cross section that takes into account the interference processes, we need to perform a wave analysis of the problem. Before going into the full wave analysis, however, it is interesting to apply an approximate method that works remarkably well for high scattering angles ( $\theta \sim \pi$ ) and that captures some key features of the scattering cross section in this regime, including the interference process: the semiclassical glory approximation [381]. Indeed, one of the main advantages of this semiclassical approximation is that one can find an analytical formula that gives some physical insight for the width of interference fringes in the scattering cross section as well as the intensity of the scattered flux for  $\theta \sim \pi$ . As a semiclassical approximation, it is valid for  $\omega M \gg 1$ , although it can still reproduce remarkably well some results for  $\omega M \sim 1$ .

The semiclassical formula for the glory scattering by spherically symmetric BHs is given by [381]

$$\frac{d\sigma_{\text{sc}}}{d\Omega} = 2\pi\omega b_g^2 \left| \frac{db}{d\theta} \right|_{\theta=\pi} J_{2s}^2(\omega b_g \sin \theta), \quad (11.9)$$

where  $b_g$  is the impact parameter of backscattered rays ( $\theta = \pi$ ),  $J_{2s}(x)$  is the Bessel function of the first kind (of order  $2s$ ), and  $s$  is the wave spin. In our case, since we are considering a scalar wave,  $s = 0$ . We note that there are multiple values of  $b_g$  corresponding to the multiple values of the deflection angle, namely  $\Theta = \pi + 2n\pi$ , with  $n = 0, 1, 2, \dots$ , that result on backscattered rays. All the rays scattered close to the backward direction ( $\theta \sim \pi$ ) contribute to the glory scattering, but the most important contribution comes from the  $n = 0$  case. The next contribution,  $n = 1$ , has an intensity that is about 0.2 % of the  $n = 0$  one in the Schwarzschild case, and about 0.8 % in the case of the extreme Bardeen BH. This is a consequence of the derivative  $|db/d\theta|_{\theta=\pi}$  in Eq. (11.9) getting rapidly suppressed as  $n$  increases. In fact, the values of  $b_g$  for rays that pass multiple times around the BH are very close to each other and also to  $b_c$ . Here, we consider only the most important contribution to the glory scattering.

Once we have the knowledge of the glory scattering formula, Eq. (11.9), we only need to determine  $b_g$  and  $|db/d\theta|_{\theta=\pi}$  in order to obtain the glory scattering cross section. Therefore, we apply Newton's method and numerical integration to obtain the parameters  $b_g$  and  $|db/d\theta|_{\theta=\pi}$ . Numerical results for  $r_c$ ,  $b_c$ ,  $b_g$  and  $b_g^2|db/d\theta|_{\theta=\pi}$  are presented in Fig. 11.3. From these results and Eq. (11.9), we may expect that (i) interference fringes get wider and (ii) backscattered flux intensity is enhanced for higher values of the BH charge. Expectation (i) comes from the fact that the interference fringe width is inversely proportional to  $b_g$ , as indicated by the argument of the Bessel function in Eq. (11.9). Moreover, Fig. 11.3 shows that  $b_g$  decreases monotonically as  $Q$  increases. We also note from Eq. (11.9) that the scattering intensity is proportional to  $b_g^2|db/d\theta|_{\theta=\pi}$ , and to the wave frequency. As shown in Fig. 11.3, although  $b_g$  decreases monotonically with the increase of  $Q$ ,  $b_g^2|db/d\theta|_{\theta=\pi}$  increases monotonically with  $Q$ , justifying expectation (ii).

The above analysis may be compared with the results for the glory scattering from RN BHs [379]. In the latter case,  $b_g$  decreases monotonically with the increase of the BH charge, while  $|db/d\theta|_{\theta=\pi}$  increases monotonically (*cf.* Fig. 9 of Ref. [379]). Therefore, considering the change of the BH charge, the behavior of the parameters  $b_g$  and  $|db/d\theta|_{\theta=\pi}$  are qualitatively the same for Bardeen and RN BHs. In the case of RN BHs, however, the combination  $b_g^2|db/d\theta|_{\theta=\pi}$

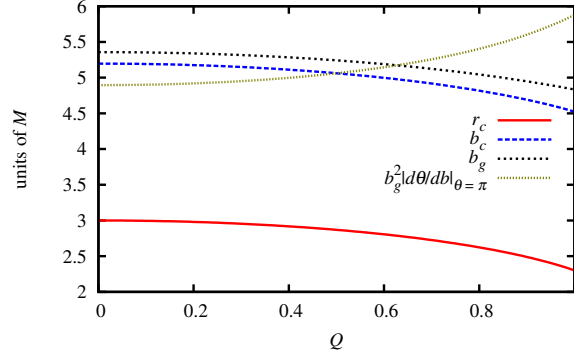


Figure 11.3: Glory scattering parameters for Bardeen BHs with varying charge, considering only the dominant contribution ( $\Theta = \pi$ ). We note that, with the exception of  $|db/d\theta|_{\theta=\pi}$ , all the important parameters related to the glory scattering decrease monotonically with the increase of  $Q$ .

does not increase monotonically with the charge — as it happens for Bardeen BHs. Instead, the glory scattering amplitude as a function of  $Q$  presents a local minimum in the RN case (cf. Fig. 10 of Ref. [379]).

In Sec. 11.3, we compare results obtained from Eq. (11.9) with partial-wave results, exhibiting excellent agreement in the regime  $\theta \lesssim \pi$ .

## 11.2 Planar wave scattering

Planar massless scalar waves, represented by the wave function  $\Phi$ , are described by the Klein-Gordon equation

$$\frac{1}{\sqrt{-g}} \partial_a (\sqrt{-g} g^{ab} \partial_b \Phi) = 0. \quad (11.10)$$

Here we shall be interested in monochromatic plane waves. We have

$$\Phi_\omega = \sum_{lm} \frac{\phi(r)}{r} Y_l^m(\theta, \varphi) e^{-i\omega t}, \quad (11.11)$$

where  $Y_l^m(\theta, \varphi)$  are the scalar spherical harmonics. Substituting Eq. (11.11) into Eq. (11.10), we obtain the following radial equation:

$$\left( -\frac{d}{dr_*^2} + V_\phi(r) - \omega^2 \right) \phi(r) = 0, \quad (11.12)$$

in which  $r_*$  is the tortoise coordinate, defined through  $dr_* = f(r)^{-1} dr$ , and

$$V_\phi(r) = f \left( \frac{l(l+1)}{r^2} + \frac{f'}{r} \right) \quad (11.13)$$

is the scalar field effective potential. The scalar field potential is localized, going to zero at both asymptotic limits of  $r_*$  (infinity and horizon) [378].

Plane waves coming from infinity can be described in terms of the so-called *in* modes. These modes are purely incoming from the past null infinity, obeying the following boundary conditions:

$$\phi(r) \sim \begin{cases} R_I + \mathcal{R}_{\omega l} R_I^*, & \text{as } r_* \rightarrow +\infty \ (r \rightarrow +\infty), \\ \mathcal{T}_{\omega l} R_{II}, & \text{as } r_* \rightarrow -\infty \ (r \rightarrow r_h), \end{cases} \quad (11.14)$$

with

$$R_I = e^{-i\omega r_*} \sum_{j=0}^N \frac{A_{\infty}^{(j)}}{r^j}, \quad (11.15)$$

$$R_{II} = e^{-i\omega r_*} \sum_{j=0}^N (r - r_h)^j A_{r_h}^{(j)}, \quad (11.16)$$

where  $|\mathcal{R}_{\omega l}|^2$  and  $|\mathcal{T}_{\omega l}|^2$  are the reflection and transmission coefficients, respectively. Flux conservation implies that  $|\mathcal{R}_{\omega l}|^2 + |\mathcal{T}_{\omega l}|^2 = 1$ . Note that the summations in Eqs. (11.15) and (11.16) are required to keep track of the convergence of the solutions. The numerical infinity and horizon are chosen such that  $V_{\phi}(r) \ll \omega^2$  at the boundaries.

The scalar differential scattering cross section for Bardeen BHs can be written in terms of partial waves as [347]

$$\frac{d\sigma}{d\Omega} = |g(\theta)|^2, \quad (11.17)$$

where

$$g(\theta) = \frac{1}{2i\omega} \sum_{l=0}^{\infty} (2l+1) [e^{2i\delta_l(\omega)} - 1] P_l(\cos \theta) \quad (11.18)$$

is the scattering amplitude, with the phase shifts ( $\delta_l$ ) given by

$$e^{2i\delta_l(\omega)} \equiv (-1)^{l+1} \mathcal{R}_{\omega l}. \quad (11.19)$$

## 11.3 Results

In order to obtain the phase shifts to compute the scattering cross section via the partial-wave method, we have applied a fourth-fifth Runge-Kutta method to solve the radial equation (11.12). We have typically started with the near-horizon condition at  $r_s = 1.0001r_h$ , and the outer boundary (numerical infinity) chosen depends on the value of  $l$ . Results were obtained with boundary conditions (11.14), as well as with alternative conditions in terms of spherical Hankel functions (see, e.g., Eq. (18) of Ref. [379]). Both conditions lead basically to the same results. Since the sum in Eq. (11.18) does not converge very quickly, because of the Coulomb characteristic of the problem, we have applied the convergence method first introduced by Yennie *et al.* [382], and first applied to the BH scattering problem by Dolan *et al.* in Ref. [383].

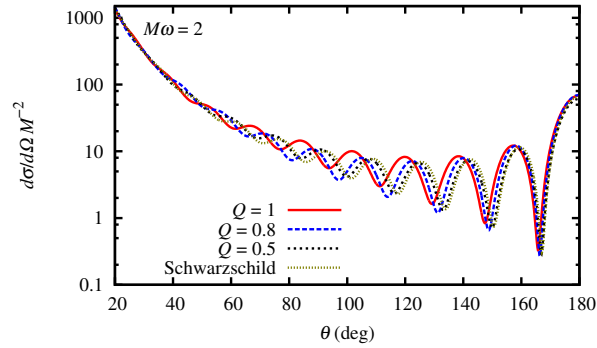


Figure 11.4: Scattering cross sections for Bardeen BHs considering different BH charges. We also plot the Schwarzschild case, for comparison. We see that the value of the charge affects the fringe widths, while the (average) amount of scattered flux remains basically the same.

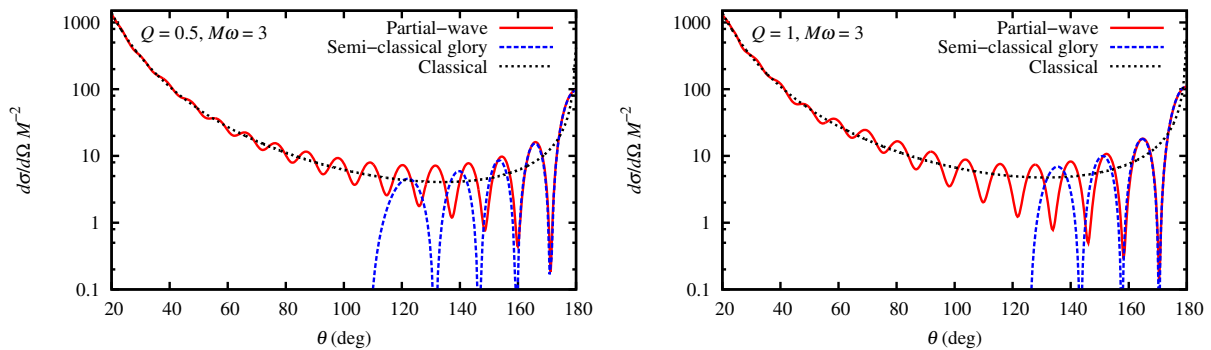


Figure 11.5: Comparison of partial-wave, semiclassical glory and classical geodesic approaches for the differential scattering cross section, for  $M\omega = 3$  (in the first two cases), and different values of the Bardeen BH charge [ $Q = 0.5$  (left) and  $Q = 1$  (right)]. The semiclassical glory approximation reproduces very well the results for backscattered waves ( $\theta \sim \pi$ ), while the classical approach works well for small scattering angles.

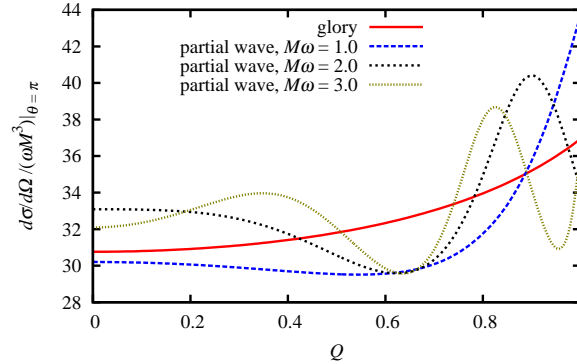


Figure 11.6: Glory intensity in the backward direction (normalized by the wave frequency) ( $\theta = \pi$ ) as a function of the Bardeen BH charge. We see that the amplitude computed through the partial-wave method oscillates around the one computed through the glory approximation.

In Fig. 11.4 we show the scattering cross section for Bardeen BHs with different charges ( $Q = 0.5, 0.8, 1$ ), as well as for the Schwarzschild BH, and  $M\omega = 2$ . We see that the fringe widths increase with the increase of the BH charge. This, as anticipated by the semiclassical analysis of Sec. 11.1.2, is in accordance with the fact that  $b_g$  decreases monotonically with the increase of  $Q$ , as previously seen in Fig. 11.3. The amount of scattered flux (on average) remains basically the same. These general behaviors are similar to the ones presented by the RN BHs [379].

Figure 11.5 presents comparisons of the numerical scalar scattering cross sections for Bardeen BHs with the approximated geodesic and glory results. We see that the glory results fit remarkably well the numerical results for large angles ( $\theta \lesssim \pi$ ), while the geodesic results fit well the small-angle region. This very good agreement can also be considered as a consistency check of our results.

The glory approximation can be used to capture most of the features of the back-scattered wave. Some caution, however, should be taken when one considers the glory intensity in the backward direction (normalized by the wave frequency). To illustrate this, in Fig. 11.6 we plot the amplitudes of the back-scattered wave, for  $M\omega = 1, 2$  and  $3$ , computed through the partial-wave method and through the glory approximation, as a function of the Bardeen BH charge. We see that the results obtained via the partial-wave method oscillate around the one obtained using the glory approximation. This agrees with the analysis presented in Ref. [379] for RN BHs.

In Fig. 11.7 we compare the differential scattering cross sections of Bardeen and RN BHs. While RN and Bardeen BHs with the correspondent charge produce different scattering patterns — illustrated by the top-left panel of Fig. 11.7 — we can have configurations with different charges that produce almost the same scattering pattern. A similarity of the patterns also happens in the case of absorption cross sections, when the critical impact parameter ( $b_c$ ) of the RN and Bardeen cases are the same [378]. Here, however, the similarity of the scattering cross sections intensifies when  $b_g$  for the RN and Bardeen cases match. The similarities are illustrated in the top-right and bottom panels of Fig. 11.7, where we show the scattering cross section for a RN BH with  $Q = 0.753$  and for a Bardeen BH with  $Q = 1$ , for different values of the frequency. The scattering flux intensities are different for intermediate-to-high scattering angles, while the

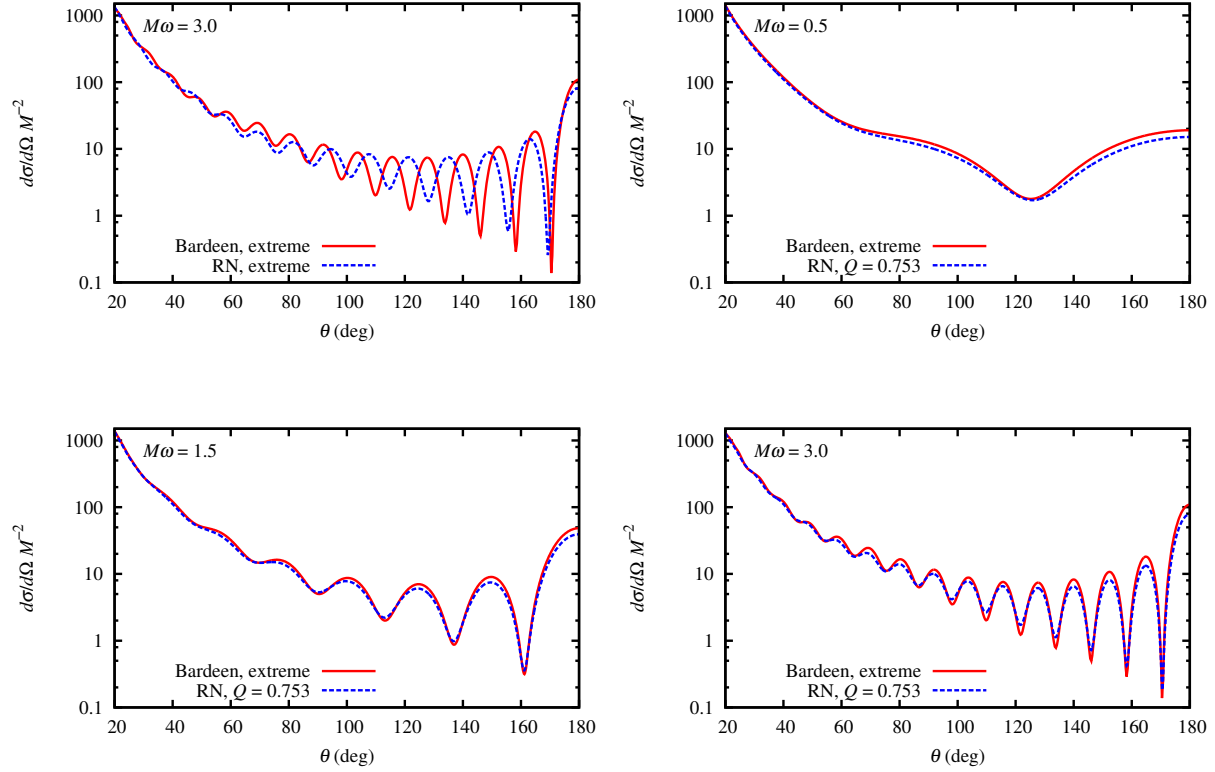


Figure 11.7: Comparison between Bardeen and RN BH scalar scattering. *Top-left panel:* The case of extremal Bardeen and RN BHs for  $M\omega = 3.0$ . *Top-right panel:* Bardeen extreme BH scattering compared with the scattering from a RN BH with  $Q = 0.753$ , for  $M\omega = 0.5$ . *Bottom panels:* The same as the top-right panel, but with  $M\omega = 1.5$  (left) and  $M\omega = 3.0$  (right).

interference widths are essentially the same for all scattering angles.

## 11.4 Final remarks

We have computed the scalar scattering cross section of regular Bardeen BHs. Numerical results were compared with both geodesic and glory approximations, and we have found excellent agreement within the validity limits of each approximation.

From the glory approximation, it is known that the interference fringe widths depend inversely on the impact parameter of backscattered waves,  $b_g$ . The classical analysis from geodesics shows that  $b_g$  decreases monotonically with the increase of  $Q$ . Therefore, we expect that the interference fringes get wider as  $Q$  increases. This was confirmed from our numerical results obtained via partial-wave method.

Comparison of Bardeen BHs with RN BHs reveals that the scattering of these two kinds of BHs can be similar but not identical. By similar we mean that in both cases the scattering cross section presents (i) intense oscillations in the near-backward scattering, (ii) rapidly growing flux amount and smoother oscillations for smaller angles, and (iii) similar results for very small scattering angles. (i) is a consequence of the strong interference between rays passing by

the opposite sides of the BH, as it is well described by the glory approximation in both cases. (ii) is a consequence of the fact that for small scattering angles both  $b$  and  $|db/d\theta|$  increase as  $\theta$  diminishes, and the difference between paths followed by neighboring rays becomes smaller, weakening interference effects. We can conclude that the main contribution to the scattering cross section for very small angles comes from rays with high impact parameters<sup>3</sup>. We may treat such cases in the weak-field regime, where the main contribution to the gravitational interaction comes from the BH mass, i.e.,  $f(r) \sim 1 - 2M/r + \mathcal{O}(r^{-n})$ , where  $n = 2$  in the case of RN BHs, and  $n = 3$  in the case of Bardeen BHs. This explains (iii), i.e., why, for BHs with the same mass, in the regime of small angles, all results tend to be the same, regardless of the nature and value of their charge.

The results presented in this chapter reinforce in a way the results presented in Ref. [378], implying the conclusion that some properties of Bardeen BHs can be very similar to those of RN BHs (with different charge). In this sense, we conclude that it may be difficult to discriminate regular BHs from the standard ones, as far as absorption and scattering of scalar plane waves are concerned. It should be interesting to extend the analyses presented here and in Ref. [378] to the scattering and absorption of waves with higher spins and compare with recently obtained results for RN BHs [307, 384–387].

---

<sup>3</sup>There are also contribution from rays with  $b \sim b_c$  that pass multiple times around the BH, but since  $|db/d\theta|$  is very small in these cases, their contribution to the scattering cross section can be neglected.

# Appendices

# Appendix A

## Slowly rotating approximation

The modified field equations are obtained by varying the action (1.1) with respect to the metric and to the scalar field. Varying the action (1.1) with respect to the metric, neglecting the  $S_{mat}$  term and the potential  $V(\phi)$ , we find

$$G_{ab} + \alpha_1 \mathcal{H}_{ab} + \alpha_2 \mathcal{I}_{ab} + \alpha_3 \mathcal{J}_{ab} + \alpha_4 \mathcal{K}_{ab} = T_{ab}^\phi, \quad (\text{A.1})$$

where  $T_{ab}^\phi = \nabla_a \phi \nabla_b \phi - \frac{1}{2} g_{ab} \nabla_c \phi \nabla^c \phi$  and  $\mathcal{H}_{ab}$ ,  $\mathcal{I}_{ab}$ ,  $\mathcal{J}_{ab}$ ,  $\mathcal{K}_{ab}$  are explicitly given in Ref. [13]. Varying the action (1.1) with respect to the scalar field  $\phi$ , we get

$$-2\Box\phi = \alpha_1 R^2 + \alpha_2 R_{ab} R^{ab} + \alpha_3 R_{abcd} R^{abcd} + \alpha_4 R_{abcd} {}^* R^{abcd}.$$

We shall neglect terms of order  $\alpha_i^2$  in the equation above. Since the Ricci scalar and the Ricci tensor are both zero in the background spacetime, the scalar field equation reduces to

$$\Box\phi = -\frac{1}{2}(\alpha_3 \tilde{R}_{abcd} \tilde{R}^{abcd} + \alpha_4 {}^* \tilde{R}_{abcd} \tilde{R}^{abcd}), \quad (\text{A.2})$$

where the tilde stands for background quantities. We note here that, when  $a = 0$ , we recover the scalar field for spherically symmetric Gauss-Bonnet BHs [22], since at this order the Gauss-Bonnet term is just the Kretschmann invariant and there is no correction from the Chern-Simons term [28]. On the other hand, for  $\alpha_3 = 0$  we recover the scalar field for slowly rotating Chern-Simons BHs. Also, there is no correction of order  $\alpha_3 a$ , since the Kretschmann invariant has only corrections in even powers of  $a$ . Therefore, we can write

$$\phi = \phi^{GB,CS} + \alpha_3 a^2 \phi^c(t, \theta), \quad (\text{A.3})$$

where  $\phi^{GB,CS}$  is the scalar field for spherically symmetric Gauss-Bonnet BHs plus the correction of slowly rotating Chern-Simons BHs, both assuming small coupling constants. Substitut-

ing Eq. (A.3) in Eq. (A.2), we find that the only solution for  $\phi^c$  which is regular at the horizon and goes to zero in the limit  $\frac{r}{\mathcal{M}} \gg 1$ , is given by the corresponding term in Eq. (3.2).

Considering corrections up to  $\alpha_i^2$ , the modified Einstein's equations read

$$\begin{aligned} G_{ab} + 8\alpha_3 \tilde{R}_{abcd} \tilde{\nabla}^c \tilde{\nabla}^d \phi + 8\alpha_4 {}^* \tilde{R}_{(a}{}^c{}_{b)}{}^d \tilde{\nabla}_d \tilde{\nabla}_c \phi \\ = \frac{1}{2} \left( 2\tilde{\nabla}_a \phi \tilde{\nabla}_b \phi - \tilde{g}_{ab} \tilde{\nabla}_c \phi \tilde{\nabla}^c \phi \right), \end{aligned} \quad (\text{A.4})$$

in which the scalar field  $\phi$  is given by Eq. (1.7). We note here that the lowest dynamical corrections to the metric are given by second order terms in  $\alpha_3$  and  $\alpha_4$ . Therefore, we can write

$$g_{ab} = g_{ab}^{GB,CS} + \alpha_3^2 a g_{ab}^c, \quad (\text{A.5})$$

where  $g_{ab}^{GB,CS}$  is the metrics for the spherically symmetric Gauss-Bonnet BH plus the correction for slowly rotating Chern-Simons BH, both assuming small coupling constants. In the slowly rotating regime, the only non-vanishing term in  $g_{ab}^c$  is  $g_{t\varphi}^c$  [25]. With the ansatz  $g_{t\varphi}^c = -\omega(r) \sin^2 \theta$ , we find that the only solution for  $\omega(r)$  that goes to zero in the regime  $\frac{r}{\mathcal{M}} \gg 1$ , is given by the corresponding term in Eq. (1.5).

# Appendix B

## Derivation of equation (2.32)

In this Appendix we present a derivation of the integral (2.32), used to compute the moment of inertia  $I$  of slowly rotating stars in scalar-tensor theory. We begin by noting that

$$\frac{d\Lambda}{dr} = \frac{r}{r - 2\mu} \left( \frac{1}{r} \frac{d\mu}{dr} - \frac{\mu}{r^2} \right), \quad (\text{B.1})$$

where Eq. (2.15) implies that  $\Lambda = -(1/2) \log(1 - 2\mu/r)$  and where  $d\mu/dr$  is given by Eq. (2.20). Introducing the auxiliary variable  $j \equiv e^{-\Phi - \Lambda}$  we find, using Eqs. (2.21) and (B.1), that

$$\frac{dj}{dr} = -j \left[ 4\pi A^4(\varphi) \frac{r^2}{r - 2\mu} (\tilde{\epsilon} + \tilde{p}) + r\psi^2 \right]. \quad (\text{B.2})$$

Multiplying the frame dragging equation (2.24) by  $j$  and rearranging, we obtain

$$\frac{1}{r^4} \frac{d}{dr} \left( r^4 j \frac{d\bar{\omega}}{dr} \right) = 16\pi A^4(\varphi) \frac{j r^2}{r - 2\mu} (\tilde{\epsilon} + \tilde{p}) \left( 1 - \frac{\tilde{\sigma}}{\tilde{\epsilon} + \tilde{p}} \right) \frac{\bar{\omega}}{r}. \quad (\text{B.3})$$

If we multiply by  $r^4$ , integrate from  $r = 0$  to infinity and use the fact that

$$j = 1 + \mathcal{O}(r^{-1}), \quad \text{and} \quad \frac{d\bar{\omega}}{dr} = \frac{6 I \Omega}{r^4} + \mathcal{O}(r^{-5}). \quad (\text{B.4})$$

as  $r \rightarrow \infty$ , we finally get Eq. (2.32).

# Appendix C

## Massive scalar modes of a constant density star

In this appendix we compute the massive scalar modes of a constant density star and show that they share many features with those obtained for the BS models presented in the main text. The background metric of a spherically symmetric star reads

$$ds_0^2 = -e^{v(r)} dt^2 + e^{u(r)} dr^2 + r^2(d\theta^2 + \sin^2\theta d\varphi^2), \quad (\text{C.1})$$

where  $e^{-u(r)} = 1 - 2m(r)/r$ . In the case of an isotropic, perfect-fluid star, the Einstein's equations are given by [69]:

$$m'(r) = 4\pi r^2 \rho(r), \quad (\text{C.2})$$

$$v'(r) = 2 \frac{m(r) + 4\pi r^3 P(r)}{r^2 - 2rm(r)}, \quad (\text{C.3})$$

$$P'(r) = - \frac{(m(r) + 4\pi r^3 P(r)) (P(r) + \rho(r))}{r(r - 2m(r))}, \quad (\text{C.4})$$

together with an equation of state, relating  $\rho$  with  $P$ .

We consider a probe scalar field which satisfies the massive Klein-Gordon equation  $\square\psi - \mu^2\psi = 0$ . In order to facilitate a comparison with the BS cases, we assume an ansatz  $\psi = \Psi(r)r^{-1}Y_{lm}e^{i(\sigma\pm\omega)t}$ . The scalar perturbation equation then reads

$$\frac{d^2}{dx^2}\Psi + [(\sigma \pm \omega)^2 - V_0]\Psi = 0, \quad (\text{C.5})$$

with

$$V_0 = e^v \left( \mu^2 + \frac{l(l+1)}{r^2} + \frac{2m}{r^3} + 4\pi(P - \rho) \right), \quad (\text{C.6})$$

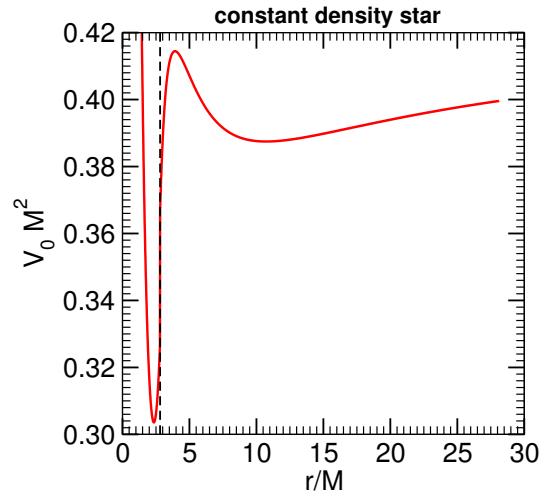


Figure C.1: Example of Schroedinger-like potential for massive scalar perturbation of a constant density star with  $l = 2$ ,  $R/M \approx 2.81$  and  $M\mu = 0.65$ . For this choice of parameters, the potential has two minima. The location of the star radius is marked by the vertical dashed line.

where we have used Eqs. (C.2) and (C.3) in order to eliminate of  $v'$  and  $m'$ .

For constant density stars we have that  $\rho(r) = \rho_c$ , and the equations (C.2)–(C.4) can be solved analytically, resulting in

$$m = \frac{4}{3}\pi r^3 \rho_c, \quad (\text{C.7})$$

$$e^v = \left[ \frac{3}{2} \left( 1 - \frac{2M}{R} \right)^{1/2} - \frac{1}{2} \left( 1 - \frac{2Mr^2}{R^3} \right)^{1/2} \right]^2, \quad (\text{C.8})$$

$$P = \rho_c \left[ \frac{R(R - 2M)^{1/2} - (R^3 - 2Mr^2)^{1/2}}{(R^3 - 2Mr^2)^{1/2} - 3R(R - 2M)^{1/2}} \right]. \quad (\text{C.9})$$

In the equations above,  $R$  is the star radius and  $M = m(R)$  is the total mass. The solution above is valid for  $r < R$ , whereas for  $r > R$  the spacetime coincides with the Schwarzschild one due to Birkhoff's theorem.

For constant density stars, the potential (C.6) can support bound states in a certain region of the  $\mu$ – $M$  parameter space. An example is shown in Fig. C.1.

The potential may develop up to two minima: (i) one is located in the outer region for a certain range of nonvanishing  $\mu$  and exists for sufficiently compact stars; (ii) the other is located inside the star and it exists also at small density if the scalar mass  $\mu$  is sufficiently large. Furthermore, the inner minimum exists also when  $\mu = 0$  in a small range of compactness. In both cases, the system allows for *normal*, bound modes, i.e. modes characterized by a purely real frequency, which can be straightforwardly computed. In Table C.1 we show some modes computed using a direct integration method for  $l = 2$ ,  $R/M \approx 6.93$ ,  $M\mu \approx 2.257$  and  $M\omega = 1.865$  and  $l = 2$ ,  $R/M \approx 3.10$ ,  $M\mu \approx 7.37$  and  $M\omega = 0.899$ . These parameters were chosen to reproduce the massive and solitonic BS configuration I, analyzed in the main text (cf. Table 5.1). In those cases, the potential only has one minimum, located in the interior of

Table C.1: A selection of massive scalar modes  $\omega_n$  of a constant density star for  $l = 2$ . The parameters chosen in the left table are  $R/M \approx 6.93$ ,  $M\mu \approx 2.257$  and  $M\omega = 1.865$ . For the right table we have chosen  $R/M \approx 3.10$ ,  $M\mu \approx 7.37$  and  $M\omega = 0.899$ . We adopted this choice of parameters to represent the massive BS I and solitonic BS I.

$n$	$M\sigma_n$	$M\Omega_p$	$M\sigma_n$	$M\Omega_p$
1	0.030	0.015	2.632	1.316
2	0.119	0.059	2.850	1.425
3	0.188	0.094	3.065	1.532
4	0.236	0.118	3.277	1.638
5	0.271	0.135	3.486	1.743
6	0.296	0.148	3.692	1.846
7	0.314	0.157	3.891	1.945

the star. In Table C.1 we also exhibit the orbital frequency of a particle that excites the modes when  $m = 2$ , i.e. when the condition  $\sigma_n = 2\Omega_p$  is met. This configuration is qualitatively similar to the case of a point-particle orbiting a BS, due to the coupling between scalar and gravitational perturbations. Indeed, the resonance frequencies are qualitatively similar to those obtained for the massive BS configuration I in the main text. An important difference to the BS case is that even localized scalar modes acquire a small imaginary part. This is due to the fact that scalar perturbations are coupled to the gravitational ones and, although the former are localized in a region of width  $\sim 1/\mu$  close to the BS, the latter dissipate energy at infinity through gravitational-wave emission. Thus, part of the scalar field energy is converted and emitted as gravitational waves. We refer the reader to the discussion in the main text for the interpretation of these results and for more details.

# Appendix D

## Radiation-driven inspiral in the exterior

Within a Newtonian approximation the inspiral in the exterior of the central object is simple and we follow [246]. In absence of dissipation, the motion is elliptical with the mass  $M$  located at the focus and the eccentricity  $e$  and the semi-major axis  $b$  are conserved quantities. At lowest order, the secular evolution of  $e(t)$  and  $b(t)$  driven by the GW emission can be modelled by the simple quadrupole formula. Clearly, this approach neglects any truly relativistic effect like the resonances discussed in the main text. On the other hand, the quadrupole formula provides a good approximation at large distances, when the orbital velocity is nonrelativistic. At first order in the mass ratio  $\mu_p/M \ll 1$ , the equations for the orbital evolution are

$$\dot{e} = -\frac{304}{15} e \frac{\mu_p M^2}{b^4 (1-e^2)^{5/2}} \left( 1 + \frac{121}{304} e^2 \right), \quad (\text{D.1})$$

$$\dot{b} = -\frac{64}{5} \frac{\mu_p M^2}{b^3 (1-e^2)^{7/2}} \left( 1 + \frac{73}{24} e^2 + \frac{37}{96} e^4 \right), \quad (\text{D.2})$$

$$\dot{\varphi} = \frac{(1 + e \cos \varphi)^2}{1 - e^2} \sqrt{\frac{M}{b^3}}, \quad (\text{D.3})$$

where  $\varphi$  is the angle in polar coordinates  $(r, \varphi)$  and the motion occurs in the  $\theta = \pi/2$  plane. The evolution is obtained solving the system above with some initial condition for  $e$ ,  $b$  and  $\varphi$ . The radius and angular momentum of the orbit read

$$r(t) = \frac{b(1-e^2)}{1+e \cos \varphi}, \quad L^2 = \mu_p^2 M b (1-e^2). \quad (\text{D.4})$$

Finally, the GW signal produced during the evolution is governed by the functions  $h_+$  and  $h_\times$ , which can be written in terms of  $r(t)$ ,  $\varphi(t)$  and of the relative position of the distant observer (see, Eqs. (6.30) and (6.31) in the main text). Note that the adiabatical evolution is valid provided radiation-reaction effects are small and the orbits evolve on timescales much longer than a typical orbital period. This is indeed the case in the EMRI limit, at least when the orbital

separation is large. Relativistic corrections to the quadrupolar formula are indeed important in the final stages of the exterior inspiral, close to the radius of compact stars.

# Appendix E

## Motion of particles in a spring-like potential

In this section we discuss the motion of a small particle inside a Newtonian, constant density star assuming the particle interacts only gravitationally with the star. This configuration should be a good approximation during the latest stages of the inspiral inside compact scalar configurations, where the density profile is nearly constant. The motion of a body inside a constant density medium is described by a gravitational potential of the form

$$V(r) = -\beta\mu_p + \gamma\mu_p r^2. \quad (\text{E.1})$$

Here  $\gamma = M/(2R^3)$ ,  $\beta = 3M/(2R)$ , where  $M, R$  are the mass and the radius of the constant density object and  $\mu_p$  is the test particle's mass. In polar coordinates, the motion of the body is described by

$$\mu_p r^2 \dot{\varphi} = L, \quad (\text{E.2})$$

$$\frac{1}{2}\mu_p \dot{r}^2 + \frac{L^2}{2\mu_p r^2} + V(r) = E, \quad (\text{E.3})$$

where  $L, E$  are the conserved angular momentum and energy parameter, respectively. We can re-express the above as

$$\left( \frac{1}{r^2} \frac{dr}{d\varphi} \right)^2 = \frac{2\mu_p E}{L^2} - \frac{1}{r^2} - \frac{2\mu_p V(r)}{L^2} = \frac{2}{k} - \frac{1}{r^2} - \frac{2\mu_p^2 \gamma r^2}{L^2}, \quad (\text{E.4})$$

where  $k^{-1} = \mu_p(E + \beta\mu_p)/L^2$ . Changing to  $z = 1/r^2 - 1/k$ , we get

$$\left(\frac{dz}{d\varphi}\right)^2 = -4z^2 + 4B^2, \quad (\text{E.5})$$

where

$$B = \sqrt{\frac{1}{k^2} - \frac{2\mu_p^2\gamma}{L^2}}. \quad (\text{E.6})$$

The solution to this equation is  $z = B \cos 2\varphi$ . Thus, we get

$$\frac{1}{r^2} = \frac{1}{k} (1 + kB \cos 2\varphi). \quad (\text{E.7})$$

In cartesian coordinates, this can be expressed as the standard equation for an ellipse:

$$\frac{x^2}{a^2} + \frac{y^2}{b^2} = 1, \quad (\text{E.8})$$

where  $a$  and  $b$  are the semi-minor and semi-major axis and

$$a^2 = \frac{k}{1 + kB}, \quad b^2 = \frac{k}{1 - kB}. \quad (\text{E.9})$$

Thus, we get the interesting result that test masses follow ellipses which are centered at the origin and whose eccentricity reads

$$e \equiv \sqrt{1 - a^2/b^2} = \sqrt{2kB/(1 + kB)}. \quad (\text{E.10})$$

Recalling that  $a^2 = b^2(1 - e^2)$ , we can re-express the energy and angular momentum in terms of the eccentricity and semi-major axis  $b$  as

$$E = -\beta\mu_p + \gamma\mu_p b^2(2 - e^2), \quad (\text{E.11})$$

$$L^2 = 2\mu_p^2\gamma(1 - e^2)b^4. \quad (\text{E.12})$$

Finally, using  $\dot{A} = r^2\dot{\varphi}/2 = L/(2\mu_p)$  and integrating over one orbit we get  $A = LT/(2\mu_p)$ , with  $T$  the orbital period and  $A$  the area of an ellipse. Using  $A = \pi ab$ , we find the analog of Kepler's third law:

$$T^2 = \frac{2\pi^2}{\gamma(1 - e^2)}, \quad (\text{E.13})$$

and we obtain the interesting result that the orbital period is completely independent from semi-major axis, as could be anticipated from the circular orbit case. Note that  $T \propto \rho^{-1/2}$ , where  $\rho$  is the density of the medium.

# Appendix F

## Energy conditions

Using the line element (9.1), it can be shown that the non-zero components of the Einstein tensor  $G_a^b$  [124] are

$$G_t^t = -\frac{B'}{r} - \frac{B}{r^2} + \frac{1}{r^2}, \quad (\text{F.1})$$

$$G_r^r = -\frac{A'B}{Ar} - \frac{B}{r^2} + \frac{1}{r^2}, \quad (\text{F.2})$$

$$G_\theta^\theta = -\frac{A''B}{2A} - \frac{A'B'}{4A} + \frac{A'^2B}{4A^2} - \frac{B'}{2r} - \frac{A'B}{2Ar}, \quad (\text{F.3})$$

$$G_\phi^\phi = G_\theta^\theta, \quad (\text{F.4})$$

where  $'$  stands for derivatives with respect to the radial coordinate  $r$ . From the Einstein equations  $G_a^b = 8\pi T_a^b$ , we note that the energy-momentum tensor  $T_a^b$  has only diagonal non-zero components, then the energy density is directly given by  $\rho = -T_t^t$ , and the pressures or tensions along a direction  $j = 1, 2, 3$  are given by  $p_j = T_j^j$ .

### Dominant energy condition (DEC)

The shell has to be carefully placed for the dominant energy condition to be obeyed. Then using <sup>1</sup>

$$U_a^b = \lim_{\epsilon \rightarrow 0^+} \int_{R_s - \epsilon}^{R_s + \epsilon} T_a^b \frac{dr}{\sqrt{B}}. \quad (\text{F.5})$$

The following relation must hold

$$|U_t^t| \geq |U_q^q|, \quad (\text{F.6})$$

with no implicit sum on  $q$ .

At the shell position the energy-momentum tensor have non-null components  $T_a^b$  and the

---

<sup>1</sup>We should point out that the derivations present along this Appendix follow the same steps done in Ref. [332].

components of the Einstein tensor  $G_a^b$  are non-zero only if they contain terms involving the second derivative of  $A$  or first derivative of  $B$ . Thus,

$$U_t^t = \frac{1}{8\pi} \lim_{\epsilon \rightarrow 0^+} \int_{R_S - \epsilon}^{R_S + \epsilon} \left( -\frac{B'}{r} \right) \frac{dr}{\sqrt{B}}, \quad (\text{F.7})$$

using the Einstein equations  $G_a^b = 8\pi T_a^b$  and inserting (F.1) in (F.5), we obtain

$$U_t^t = -\frac{1}{4\pi R_S} \left( \sqrt{1 - \frac{2M}{R_S}} - \sqrt{1 - \frac{2M_H}{R_S}} \right), \quad (\text{F.8})$$

Analogously, we find that

$$U_\theta^\theta = -\frac{1}{8\pi R_S} \left( \frac{1 - \frac{M}{R_S}}{\sqrt{1 - \frac{2M}{R_S}}} - \frac{1 - \frac{M_H}{R_S}}{\sqrt{1 - \frac{2M_H}{R_S}}} \right). \quad (\text{F.9})$$

Using (F.6) together with (F.8) and (F.9), it is possible to show that the lower bound for  $R_S$ , according to DEC, is given by

$$r_{\min}^{DEC} = \frac{5}{24} \left( 5M + 5M_H + \sqrt{25M^2 + M_H(-46M + 25M_H)} \right).$$

### Strong energy condition (SEC)

We may carry out a similar analysis considering the strong energy condition, obtaining

$$|U_t^t| + |U_q^q| \geq 0, \quad (\text{F.10})$$

and

$$|U_t^t| + 2|U_q^q| \geq 0. \quad (\text{F.11})$$

Now, using (F.10), with the aid of (F.8) and (F.9), we arrive at

$$r_{\min}^{SEC} = \frac{3}{8} \left( \sqrt{9M^2 - 14MM_H + 9M_H^2} + 3M + 3M_H \right).$$

We note that for this value of  $r_{\min}$ , both (F.10) and (F.11) hold, so that the strong energy condition is fully satisfied.

# Bibliography

- [1] C. M. Will, *Living Rev. Relativity* **9** (2006).
- [2] C. W. F. Everitt *et al.*, *Phys. Rev. Lett.* **106**, 221101 (2011), arXiv:1105.3456.
- [3] The collected papers of albert einstein, <http://einsteinpapers.press.princeton.edu/>, Accessed in 9 June 2015.
- [4] R. Penrose, *Phys. Rev. Lett.* **14**, 57 (1965).
- [5] S. Hawking, *Mon. Not. Roy. Astron. Soc.* **152**, 75 (1971).
- [6] K. Schwarzschild, *Sitzungsber. Preuss. Akad. Wiss. Berlin (Math. Phys.)* **1916**, 189 (1916), arXiv:physics/9905030.
- [7] L. Parker and D. Toms, *Quantum field theory in curved spacetime: quantized fields and gravity* (Cambridge University Press, Cambridge, 2009).
- [8] T. Clifton, P. G. Ferreira, A. Padilla, and C. Skordis, *Phys. Rept.* **513**, 1 (2012), arXiv:1106.2476.
- [9] D. Psaltis, *Living Rev. Relativity* **11** (2008).
- [10] E. Berti and V. Cardoso, *Int. J. Mod. Phys. D* **15**, 2209 (2006), arXiv:gr-qc/0605101.
- [11] P. Pani, E. Berti, V. Cardoso, and J. Read, *Phys. Rev. D* **84**, 104035 (2011), arXiv:1109.0928.
- [12] C. Bambi and D. Malafarina, *Phys. Rev. D* **88**, 064022 (2013), arXiv:1307.2106.
- [13] N. Yunes and L. C. Stein, *Phys. Rev. D* **83**, 104002 (2011), arXiv:1101.2921.
- [14] D. Psaltis, *Living Rev. Relativity* **11** (2008).
- [15] E. Berti, A. Buonanno, and C. M. Will, *Phys. Rev. D* **71**, 084025 (2005), arXiv:gr-qc/0411129.
- [16] S. S. Doeleman, V. L. Fish, A. E. Broderick, A. Loeb, and A. E. E. Rogers, *Astrophys. J.* **695**, 59 (2009), 0809.3424.
- [17] J. D. Bekenstein, *Phys. Rev. D* **51**, 6608 (1995).

- [18] P. Kanti, N. Mavromatos, J. Rizos, K. Tamvakis, and E. Winstanley, *Phys. Rev. D* **54**, 5049 (1996), arXiv:hep-th/9511071.
- [19] N. A. Collins and S. A. Hughes, *Phys. Rev. D* **69**, 124022 (2004), arXiv:gr-qc/0402063.
- [20] S. Vigeland, N. Yunes, and L. Stein, *Phys. Rev. D* **83**, 104027 (2011), arXiv:1102.3706.
- [21] T. Johannsen and D. Psaltis, *Phys. Rev. D* **83**, 124015 (2011), arXiv:1105.3191.
- [22] B. A. Campbell, N. Kaloper, and K. A. Olive, *Phys. Lett. B* **285**, 199 (1992).
- [23] S. Mignemi and N. Stewart, *Phys. Lett. B* **298**, 299 (1993), arXiv:hep-th/9206018.
- [24] T. Torii, H. Yajima, and K.-i. Maeda, *Phys. Rev. D* **55**, 739 (1997), arXiv:gr-qc/9606034.
- [25] P. Pani and V. Cardoso, *Phys. Rev. D* **79**, 084031 (2009).
- [26] B. Kleihaus, J. Kunz, and E. Radu, *Phys. Rev. Lett.* **106**, 151104 (2011), arXiv:1101.2868.
- [27] S. Alexander and N. Yunes, *Phys. Rept.* **480**, 1 (2009), arXiv:0907.2562.
- [28] N. Yunes and F. Pretorius, *Phys. Rev. D* **79**, 084043 (2009), arXiv:0902.4669.
- [29] N. Yunes and C. F. Sopuerta, *Phys. Rev. D* **77**, 064007 (2008), arXiv:0712.1028.
- [30] C. Molina, P. Pani, V. Cardoso, and L. Gualtieri, *Phys. Rev. D* **81**, 124021 (2010), arXiv:1004.4007.
- [31] L. Amarilla, E. F. Eiroa, and G. Giribet, *Phys. Rev. D* **81**, 124045 (2010), arXiv:1005.0607.
- [32] N. Yunes and F. Pretorius, *Phys. Rev. D* **80**, 122003 (2009), arXiv:0909.3328.
- [33] L. Herrera and N. O. Santos, *Phys. Rep.* **286**, 53 (1997).
- [34] R. Kippenhahn and A. Weigert, *Stellar Structure and Evolution* (Springer-Verlag, Berlin, 2012).
- [35] S. S. Yazadjiev, *Phys. Rev. D* **85**, 044030 (2012).
- [36] V. Folomeev and V. Dzhunushaliev, *Phys. Rev. D* **91**, 044040 (2015), arXiv:1501.06275.
- [37] F. Kamiab, A. E. Broderick, and N. Afshordi, (2015), arXiv:1503.03898.
- [38] H. Heiselberg and M. Hjorth-Jensen, *Phys. Rept.* **328**, 237 (2000), arXiv:nucl-th/9902033.
- [39] M. Ruderman, *Ann. Rev. Astron. Astrophys.* **10**, 427 (1972).
- [40] V. Canuto and S. Chitre, *Phys. Rev. D* **9**, 1587 (1974).

- [41] R. Sawyer, Phys. Rev. Lett. **29**, 382 (1972).
- [42] B. Carter and D. Langlois, Nucl. Phys. B **531**, 478 (1998), arXiv:gr-qc/9806024.
- [43] S. Nelmes and B. Piette, Phys. Rev. D **85**, 123004 (2012), arXiv:1204.0910.
- [44] C. Adam, C. Naya, J. Sanchez-Guillen, R. Vazquez, and A. Wereszczynski, Phys. Lett. B **742**, 136 (2015), arXiv:1407.3799.
- [45] C. Adam, C. Naya, J. Sanchez-Guillen, R. Vazquez, and A. Wereszczynski, (2015), arXiv:1503.03095.
- [46] P. S. Letelier, Phys. Rev. D **22**, 807 (1980).
- [47] R. L. Bowers and E. P. T. Liang, Astrophysical J. **188**, 657 (1974).
- [48] D. Horvat, S. Ilijic, and A. Marunovic, Classical Quantum Gravity **28**, 025009 (2011), arXiv:1010.0878.
- [49] K. Dev and M. Gleiser, Gen. Rel. Grav. **35**, 1435 (2003), arXiv:gr-qc/0303077.
- [50] C. Cattoen, T. Faber, and M. Visser, Classical Quantum Gravity **22**, 4189 (2005), arXiv:gr-qc/0505137.
- [51] F. Schunck and E. Mielke, Classical Quantum Gravity **20**, R301 (2003), arXiv:0801.0307.
- [52] S. S. Bayin, Phys. Rev. D **26**, 1262 (1982).
- [53] Y. Fujii and K.-I. Maeda, *The Scalar-Tensor Theory of Gravitation* (Cambridge University Press, Cambridge, 2003).
- [54] T. P. Sotiriou and V. Faraoni, Rev. Mod. Phys. **82**, 451 (2010), arXiv:0805.1726 [gr-qc].
- [55] A. De Felice and S. Tsujikawa, Living Rev. Relativity **13**, 3 (2010), arXiv:1002.4928.
- [56] C. M. Will, Living Rev. Relativity **9** (2006).
- [57] T. Damour and G. Esposito-Farèse, Classical Quantum Gravity **9**, 2093 (1992).
- [58] T. Damour and G. Esposito-Farèse, Phys. Rev. Lett. **70**, 2220 (1993).
- [59] E. Berti *et al.*, (2015), arXiv:1501.07274.
- [60] T. P. Sotiriou and V. Faraoni, Phys. Rev. Lett. **108**, 081103 (2012), arXiv:1109.6324.
- [61] I. Z. Stefanov, S. S. Yazadjiev, and M. D. Todorov, Mod. Phys. Lett. **A23**, 2915 (2008), arXiv:0708.4141.
- [62] D. D. Doneva, S. S. Yazadjiev, K. D. Kokkotas, and I. Z. Stefanov, Phys. Rev. **D82**, 064030 (2010), arXiv:1007.1767.

- [63] V. Cardoso, I. P. Carucci, P. Pani, and T. P. Sotiriou, *Phys. Rev. D* **88**, 044056 (2013), arXiv:1305.6936.
- [64] V. Cardoso, I. P. Carucci, P. Pani, and T. P. Sotiriou, *Phys. Rev. Lett.* **111**, 111101 (2013), arXiv:1308.6587.
- [65] M. Horbatsch and C. Burgess, *JCAP* **1205**, 010 (2012), arXiv:1111.4009.
- [66] E. Berti, V. Cardoso, L. Gualtieri, M. Horbatsch, and U. Sperhake, *Phys. Rev. D* **87**, 124020 (2013), arXiv:1304.2836.
- [67] B. K. Harrison, K. S. Thorne, M. Wakano, and J. A. Wheeler, *Gravitation Theory and Gravitational Collapse* (University of Chicago Press, Chicago, 1965).
- [68] C. W. Misner, K. S. Thorne, and J. A. Wheeler, *Gravitation* (W. H. Freeman, San Francisco, 1973).
- [69] S. L. Shapiro and S. A. Teukolsky, *Black Holes, White Dwarfs and Neutron Stars: The Physics of Compact Objects*, 1st ed. (Wiley-Interscience, Weinheim, 1983).
- [70] J. L. Friedman and N. Stergioulas, *Rotating Relativistic Stars* (Cambridge University Press, Cambridge, 2013).
- [71] M. Horbatsch and C. Burgess, *JCAP* **1108**, 027 (2011), arXiv:1006.4411.
- [72] T. Damour and G. Esposito-Farèse, *Phys. Rev. D* **54**, 1474 (1996), arXiv:gr-qc/9602056.
- [73] T. Harada, *Phys. Rev. D* **57**, 4802 (1998), arXiv:gr-qc/9801049.
- [74] P. C. Freire *et al.*, *Mon. Not. Roy. Astron. Soc.* **423**, 3328 (2012), arXiv:1205.1450.
- [75] N. Wex, (2014), arXiv:1402.5594.
- [76] D. D. Doneva and S. S. Yazadjiev, *Phys. Rev. D* **85**, 124023 (2012), arXiv:1203.3963.
- [77] A. Akmal, V. Pandharipande, and D. Ravenhall, *Phys. Rev. C* **58**, 1804 (1998), arXiv:nucl-th/9804027.
- [78] P. B. Demorest, T. Pennucci, S. M. Ransom, M. S. E. Roberts, and J. W. T. Hessels, *Nature* **467**, 1081 (2010), 1010.5788.
- [79] J. Antoniadis *et al.*, *Science* **340**, 6131 (2013), arXiv:1304.6875.
- [80] K. Glampedakis, S. J. Kapadia, and D. Kennefick, *Phys. Rev. D* **89**, 024007 (2014), arXiv:1312.1912.
- [81] J. B. Hartle, *Astrophys. J.* **150**, 1005 (1967).
- [82] J. B. Hartle and K. S. Thorne, *Astrophys. J.* **153**, 807 (1968).
- [83] P. Pani and E. Berti, *Phys. Rev. D* **90**, 024025 (2014), arXiv:1405.4547.

- [84] K. V. Staykov, D. D. Doneva, S. S. Yazadjiev, and K. D. Kokkotas, *JCAP* **10**, 6 (2014), 1407.2180.
- [85] A. Lyne *et al.*, *Science* **303**, 1153 (2004), arXiv:astro-ph/0401086.
- [86] J. M. Lattimer and B. F. Schutz, *Astrophys. J.* **629**, 979 (2005), arXiv:astro-ph/0411470.
- [87] M. Kramer and N. Wex, *Classical Quantum Gravity* **26**, 073001 (2009).
- [88] D. D. Doneva, S. S. Yazadjiev, N. Stergioulas, and K. D. Kokkotas, *Phys. Rev. D* **88**, 084060 (2013), arXiv:1309.0605.
- [89] E. Berti, F. White, A. Maniopoulou, and M. Bruni, *Mon. Not. Roy. Astron. Soc.* **358**, 923 (2005), arXiv:gr-qc/0405146.
- [90] K. Kokkotas and J. Ruoff, *Astron. Astrophys.* **366**, 565 (2001), arXiv:gr-qc/0011093.
- [91] F. Douchin and P. Haensel, *Astron. Astrophys.* **380**, 151 (2001), arXiv:astro-ph/0111092.
- [92] J. Arponen, *Nucl. Phys. A* **191**, 257 (1972).
- [93] J. Novak, *Phys. Rev. D* **58**, 064019 (1998), arXiv:gr-qc/9806022.
- [94] P. Pani, V. Cardoso, E. Berti, J. Read, and M. Salgado, *Phys. Rev. D* **83**, 081501 (2011), arXiv:1012.1343.
- [95] K. Yagi and N. Yunes, *Science* **341**, 365 (2013), arXiv:1302.4499.
- [96] K. Yagi and N. Yunes, *Phys. Rev. D* **88**, 023009 (2013), arXiv:1303.1528.
- [97] G. Pappas and T. A. Apostolatos, *Phys. Rev. Lett.* **112**, 121101 (2014), arXiv:1311.5508.
- [98] K. Yagi, K. Kyutoku, G. Pappas, N. Yunes, and T. A. Apostolatos, *Phys. Rev. D* **89**, 124013 (2014), arXiv:1403.6243.
- [99] D. D. Doneva, S. S. Yazadjiev, K. V. Staykov, and K. D. Kokkotas, (2014), arXiv:1408.1641.
- [100] D. D. Doneva, S. S. Yazadjiev, N. Stergioulas, K. D. Kokkotas, and T. M. Athanasiadis, *Phys. Rev. D* **90**, 044004 (2014), arXiv:1405.6976.
- [101] H. Sotani and K. D. Kokkotas, *Phys. Rev. D* **70**, 084026 (2004), arXiv:gr-qc/0409066.
- [102] H. Sotani and K. D. Kokkotas, *Phys. Rev. D* **71**, 124038 (2005), arXiv:gr-qc/0506060.
- [103] H. O. Silva, H. Sotani, E. Berti, and M. Horbatsch, *Phys. Rev. D* **90**, 124044 (2014), arXiv:1410.2511.
- [104] C. M. Will and H. W. Zaglauer, *Astrophys. J.* **346**, 366 (1989).
- [105] H. Zaglauer, *Astrophys. J.* **393**, 685 (1992).

- [106] J. Alsing, E. Berti, C. M. Will, and H. Zaglauer, *Phys. Rev. D* **85**, 064041 (2012), arXiv:1112.4903.
- [107] R. P. Kerr, *Phys. Rev. Lett.* **11**, 237 (1963).
- [108] P. T. Chruściel, J. L. Costa, and M. Heusler, *Living Rev. Relativity* **15** (2012).
- [109] E. Berti, V. Cardoso, and A. O. Starinets, *Classical Quantum Gravity* **26**, 163001 (2009), arXiv:0905.2975.
- [110] J. Frank, A. King, and D. Raine, *Accretion power in astrophysics* (Cambridge University Press, Cambridge, 2002).
- [111] D. L. Wiltshire, M. Visser, and S. Scott, *The Kerr spacetime: Rotating black holes in general relativity* (Cambridge University Press, Cambridge, 2009).
- [112] R. A. Breuer, *Gravitational perturbation theory and synchrotron radiation* (Springer Verlag, Heidelberg, 1975).
- [113] L. C. B. Crispino, G. E. A. Matsas, and A. Higuchi, *Classical Quantum Gravity* **17**, 19 (2000).
- [114] L. C. B. Crispino, *Phys. Rev. D* **77**, 047503 (2008).
- [115] J. Castiņeiras, L. C. B. Crispino, and D. P. M. Filho, *Phys. Rev. D* **75**, 024012 (2007).
- [116] J. Castiņeiras, L. C. B. Crispino, R. Murta, and G. E. Matsas, *Phys. Rev. D* **71**, 104013 (2005), arXiv:gr-qc/0503050.
- [117] L. C. B. Crispino, A. R. R. da Silva, and G. E. A. Matsas, *Phys. Rev. D* **79**, 024004 (2009).
- [118] M. Walker and R. Penrose, *Communications in Mathematical Physics* **18**, 265 (1970).
- [119] D. R. Brill, P. L. Chrzanowski, C. M. Pereira, E. D. Fackerell, and J. R. Ipser, *Phys. Rev. D* **5**, 1913 (1972).
- [120] B. Carter, *Commun. Math. Phys.* **10**, 280 (1968).
- [121] C. Flammer, *Spheroidal wave functions* (Dover Publications, New York, 2014).
- [122] G. Duffy, *Scalar quantum field theory on the Kerr black hole background*, PhD thesis, University College Dublin, Ireland, 2001.
- [123] A. C. Ottewill and E. Winstanley, *Phys. Rev. D* **62**, 084018 (2000).
- [124] R. Wald, *General Relativity* (The University of Chicago Press, Chicago, 1984).
- [125] W. G. Unruh, *Phys. Rev. D* **10**, 3194 (1974).
- [126] L. H. Ford, *Phys. Rev. D* **12**, 2963 (1975).

- [127] S. Chandrasekhar, *The mathematical theory of black holes* (Oxford University Press, Oxford, 1985).
- [128] R. F. P. Mendes and G. E. A. Matsas, *Phys. Rev. D* **84**, 124035 (2011).
- [129] P. L. Chrzanowski and C. W. Misner, *Phys. Rev. D* **10**, 1701 (1974).
- [130] Y. B. Zeldovich, *Zh. Eksp. Teor. Fiz* **62**, 2076 (1972).
- [131] A. A. Starobinski, *JETP* **37**, 28 (1973).
- [132] K. D. Kokkotas and B. G. Schmidt, *Living Rev. Relativity* **2**, 2 (1999), arXiv:gr-qc/9909058.
- [133] Y. Kojima, *Prog.Theor.Phys.* **77**, 297 (1987).
- [134] J. A. Pons, E. Berti, L. Gualtieri, G. Miniutti, and V. Ferrari, *Phys. Rev. D* **65**, 104021 (2002), arXiv:gr-qc/0111104.
- [135] E. Barausse, V. Cardoso, and P. Pani, *Phys. Rev. D* **89**, 104059 (2014), arXiv:1404.7149.
- [136] C. A. R. Herdeiro and E. Radu, *Phys. Rev. Lett.* **112**, 221101 (2014), arXiv:1403.2757.
- [137] C. A. R. Herdeiro and E. Radu, (2015), arXiv:1504.08209.
- [138] S. Hod, *Phys. Rev. D* **86**, 104026 (2012), arXiv:1211.3202.
- [139] C. L. Benone, L. C. B. Crispino, C. Herdeiro, and E. Radu, *Phys. Rev. D* **90**, 104024 (2014), arXiv:1409.1593.
- [140] R. C. Duncan and C. Thompson, *Astrophys. J.* **392**, L9 (1992).
- [141] S. Yazadjiev, *Phys. Rev. D* **85**, 044030 (2012), arXiv:1111.3536.
- [142] G. Bertone and M. Fairbairn, *Phys. Rev. D* **77**, 043515 (2008), arXiv:0709.1485.
- [143] D. J. Kaup, *Phys. Rev.* **172**, 1331 (1968).
- [144] S. L. Liebling and C. Palenzuela, *Living Rev. Relativity* **15**, 6 (2012), arXiv:1202.5809.
- [145] J. C. Degollado and C. A. R. Herdeiro, *Phys. Rev. D* **90**, 065019 (2014), arXiv:1408.2589.
- [146] P. Pani, *Int. J. Mod. Phys. A* **28**, 1340018 (2013), arXiv:1305.6759.
- [147] O. Benhar, E. Berti, and V. Ferrari, *Mon. Not. Roy. Astron. Soc.* **310**, 797 (1999), arXiv:gr-qc/9901037.
- [148] H.-P. Nollert, *Classical Quantum Gravity* **16**, R159 (1999).
- [149] C. F. B. Macedo, P. Pani, V. Cardoso, and L. C. B. Crispino, *Phys. Rev. D* **88**, 064046 (2013), arXiv:1307.4812.

- [150] D. Brizuela, *Classical Quantum Gravity* **32**, 135005 (2015), arXiv:1505.05278.
- [151] S. Chandrasekhar and S. L. Detweiler, *Proc. Roy. Soc. Lond. A* **344**, 441 (1975).
- [152] S. Chandrasekhar and V. Ferrari, *Proceedings: Mathematical and Physical Sciences* **434**, 449 (1991).
- [153] E. Leaver, *Proc. Roy. Soc. Lond. A* **402**, 285 (1985).
- [154] P. Pani, E. Berti, V. Cardoso, Y. Chen, and R. Norte, *Phys. Rev. D* **80**, 124047 (2009), arXiv:0909.0287.
- [155] R. A. Konoplya and A. Zhidenko, *Rev. Mod. Phys.* **83**, 793 (2011).
- [156] C. F. B. Macedo, P. Pani, V. Cardoso, and L. C. B. Crispino, *Astrophys. J.* **774**, 48 (2013), arXiv:1302.2646.
- [157] M. Gleiser, *Phys. Rev. D* **38**, 2376 (1988).
- [158] R. Konoplya and A. Zhidenko, *Phys. Lett. B* **609**, 377 (2005), arXiv:gr-qc/0411059.
- [159] Y. Kojima, S. Yoshida, and T. Futamase, *Prog. Theor. Phys.* **86**, 401 (1991).
- [160] S. Yoshida, Y. Eriguchi, and T. Futamase, *Phys. Rev. D* **50**, 6235 (1994).
- [161] T. Lee and Y. Pang, *Nucl. Phys. B* **315**, 477 (1989).
- [162] F. V. Kusmartsev, E. W. Mielke, and F. E. Schunck, *Phys. Rev. D* **43**, 3895 (1991), arXiv:0810.0696.
- [163] P. Jetzer, *Phys. Rept.* **220**, 163 (1992).
- [164] R. Ruffini and S. Bonazzola, *Phys. Rev.* **187**, 1767 (1969).
- [165] A. Arvanitaki, S. Dimopoulos, S. Dubovsky, N. Kaloper, and J. March-Russell, *Phys. Rev. D* **81**, 123530 (2010), arXiv:0905.4720.
- [166] M. Colpi, S. Shapiro, and I. Wasserman, *Phys. Rev. Lett.* **57**, 2485 (1986).
- [167] R. Friedberg, T. D. Lee, and Y. Pang, *Phys. Rev. D* **35**, 3658 (1987).
- [168] D. F. Torres, *Nucl. Phys. B* **626**, 377 (2002), arXiv:hep-ph/0201154.
- [169] F. S. Guzman, *Phys. Rev. D* **73**, 021501 (2006), arXiv:gr-qc/0512081.
- [170] Y. Lu and D. F. Torres, *Int. J. Mod. Phys. D* **12**, 63 (2003), arXiv:astro-ph/0205418.
- [171] A. Y. Bin-Nun, (2013), arXiv:1301.1396.
- [172] F. D. Lora-Clavijo, A. Cruz-Osorio, and F. S. Guzman, *Phys. Rev. D* **82**, 023005 (2010), arXiv:1007.1162.

- [173] M. Kesden, J. Gair, and M. Kamionkowski, *Phys. Rev. D* **71**, 044015 (2005), arXiv:astro-ph/0411478.
- [174] N. Yunes, P. Pani, and V. Cardoso, *Phys. Rev. D* **85**, 102003 (2012), arXiv:1112.3351.
- [175] P. Pani, V. Cardoso, and L. Gualtieri, *Phys. Rev. D* **83**, 104048 (2011), arXiv:1104.1183.
- [176] M. Gleiser and R. Watkins, *Nucl. Phys. B* **319**, 733 (1989).
- [177] T. Regge and J. A. Wheeler, *Phys. Rev.* **108**, 1063 (1957).
- [178] F. Zerilli, *Phys. Rev. D* **2**, 2141 (1970).
- [179] N. Sago, H. Nakano, and M. Sasaki, *Phys. Rev. D* **67**, 104017 (2003), arXiv:gr-qc/0208060.
- [180] K. Thorne and A. Campolattaro, *Astrophysical Journal* **149**, 591 (1988).
- [181] G. Allen, N. Andersson, K. D. Kokkotas, and B. F. Schutz, *Phys. Rev. D* **58**, 124012 (1998), arXiv:gr-qc/9704023.
- [182] J. R. Ipser and R. H. Price, *Phys. Rev. D* **43**, 1768 (1991).
- [183] Y. Kojima, *Phys. Rev. D* **46**, 4289 (1992).
- [184] W. H. Press, S. A. Teukolsky, W. T. Vetterling, and B. P. Flannery, *Numerical recipes in FORTRAN: the art of scientific computing* (Cambridge University Press, Cambridge, 1992).
- [185] R. Ferrell and M. Gleiser, *Phys. Rev. D* **40**, 2524 (1989).
- [186] P. Amaro-Seoane, J. Barranco, A. Bernal, and L. Rezzolla, *JCAP* **1011**, 002 (2010), arXiv:1009.0019.
- [187] T. Lee and Y. Pang, *Phys. Rept.* **221**, 251 (1992).
- [188] B. Kleihaus, J. Kunz, and M. List, *Phys. Rev. D* **72**, 064002 (2005), arXiv:gr-qc/0505143.
- [189] P. Peters, *Phys. Rev.* **136**, B1224 (1964).
- [190] V. Cardoso, A. S. Miranda, E. Berti, H. Witek, and V. T. Zanchin, *Phys. Rev. D* **79**, 064016 (2009), arXiv:0812.1806.
- [191] V. Diemer, K. Eilers, B. Hartmann, I. Schaffer, and C. Toma, *Phys. Rev. D* **88**, 044025 (2013), arXiv:1304.5646.
- [192] K. Kokkotas, *Mon. Not. Roy. Astron. Soc.* **268**, 1015 (1994).
- [193] M. Leins, H. P. Nollert, and M. H. Soffel, *Phys. Rev. D* **48**, 3467 (1993).
- [194] E. W. Leaver, *Phys. Rev. D* **41**, 2986 (1990).

- [195] S. R. Dolan, Phys. Rev. D **76**, 084001 (2007), arXiv:0705.2880.
- [196] J. G. Rosa and S. R. Dolan, Phys. Rev. D **85**, 044043 (2012), arXiv:1110.4494.
- [197] P. Pani, V. Cardoso, L. Gualtieri, E. Berti, and A. Ishibashi, Phys. Rev. D **86**, 104017 (2012), arXiv:1209.0773.
- [198] P. Pani, E. Berti, V. Cardoso, Y. Chen, and R. Norte, Phys. Rev. D **81**, 084011 (2010), arXiv:1001.3031.
- [199] K. Martel, Phys. Rev. D **69**, 044025 (2004), arXiv:gr-qc/0311017.
- [200] K. Martel and E. Poisson, Phys. Rev. D **71**, 104003 (2005), arXiv:gr-qc/0502028.
- [201] R. Breuer, P. Chrzanowski, H. Hughes, and C. W. Misner, Phys. Rev. D **8**, 4309 (1973).
- [202] S. L. Detweiler, Phys. Rev. D **22**, 2323 (1980).
- [203] V. Cardoso, S. Chakrabarti, P. Pani, E. Berti, and L. Gualtieri, Phys. Rev. Lett. **107**, 241101 (2011), arXiv:1109.6021.
- [204] S. Yoshida and Y. Eriguchi, Phys. Rev. D **56**, 762 (1997).
- [205] P. Pani, E. Berti, and L. Gualtieri, Phys. Rev. Lett. **110**, 241103 (2013), arXiv:1304.1160.
- [206] G. Bertone, D. Hooper, and J. Silk, Phys. Rept. **405**, 279 (2005), arXiv:hep-ph/0404175.
- [207] R. Genzel, N. Thatte, A. Krabbe, H. Kroker, and L. Tacconi-Garman, Astrophys. J. **472**, 153 (1996).
- [208] M. A. Abramowicz, W. Kluzniak, and J.-P. Lasota, Astron. Astrophys. **396**, L31 (2002), arXiv:astro-ph/0207270.
- [209] S. Doeleman *et al.*, Nature **455**, 78 (2008), arXiv:0809.2442.
- [210] V. L. Fish *et al.*, Astrophys. J. **727**, L36 (2011), arXiv:1011.2472.
- [211] F. Eisenhauer *et al.*, (2008), arXiv:0808.0063.
- [212] K. Eda, Y. Itoh, S. Kuroyanagi, and J. Silk, Phys. Rev. Lett. **110**, 221101 (2013), arXiv:1301.5971.
- [213] F. D. Ryan, Phys. Rev. D **52**, 5707 (1995).
- [214] F. D. Ryan, Phys. Rev. D **56**, 1845 (1997).
- [215] P. Pani, Eur. Phys. J. PlusD **127**, 67 (2012).
- [216] P. Amaro-Seoane *et al.*, GW Notes **6**, 4 (2013), arXiv:1201.3621.
- [217] P. Amaro-Seoane *et al.*, Class. Quant. Grav. **29**, 124016 (2012), arXiv:1202.0839.

- [218] J. R. Gair, M. Vallisneri, S. L. Larson, and J. G. Baker, *Living Rev. Relativity* **16**, 7 (2013), arXiv:1212.5575.
- [219] K. Yagi, N. Yunes, and T. Tanaka, *Phys. Rev. Lett.* **109**, 251105 (2012), arXiv:1208.5102.
- [220] E. Poisson, *Living Rev. Relativity* **7**, 6 (2004), arXiv:gr-qc/0306052.
- [221] L. Barack, *Classical Quantum Gravity* **26**, 213001 (2009), arXiv:0908.1664.
- [222] E. W. Kolb and I. I. Tkachev, *Phys. Rev. Lett.* **71**, 3051 (1993), arXiv:hep-ph/9303313.
- [223] A. Henriques, A. R. Liddle, and R. Moorhouse, *Nucl. Phys. B* **337**, 737 (1990).
- [224] J. Wheeler, *Phys. Rev.* **97**, 511 (1955).
- [225] D. F. Torres, S. Capozziello, and G. Lambiase, *Phys. Rev. D* **62**, 104012 (2000), arXiv:astro-ph/0004064.
- [226] J. A. Frieman, G. Gelmini, M. Gleiser, and E. W. Kolb, *Phys. Rev. Lett.* **60**, 2101 (1988).
- [227] J. A. Frieman, A. V. Olinto, M. Gleiser, and C. Alcock, *Phys. Rev. D* **40**, 3241 (1989).
- [228] D. Grasso, *Phys. Rev. D* **41**, 2998 (1990).
- [229] M. S. Madsen and A. R. Liddle, *Phys. Lett. B* **251**, 507 (1990).
- [230] I. Tkachev, *Phys. Lett. B* **261**, 289 (1991).
- [231] A. R. Liddle and M. S. Madsen, *Int. J. Mod. Phys. D* **1**, 101 (1992).
- [232] ATLAS Collaboration, G. Aad *et al.*, *Phys. Lett. B* **716**, 1 (2012), arXiv:1207.7214.
- [233] S. Chandrasekhar, *Astrophys. J.* **97**, 255 (1943).
- [234] E. C. Ostriker, *Astrophys. J.* **513**, 252 (1999), arXiv:astro-ph/9810324.
- [235] A. Arvanitaki and S. Dubovsky, *Phys. Rev. D* **83**, 044026 (2011), arXiv:1004.3558.
- [236] H. Yoshino and H. Kodama, *Prog. Theor. Phys.* **128**, 153 (2012), arXiv:1203.5070.
- [237] P. Pani, V. Cardoso, L. Gualtieri, E. Berti, and A. Ishibashi, *Phys. Rev. Lett.* **109**, 131102 (2012), arXiv:1209.0465.
- [238] H. Witek, V. Cardoso, A. Ishibashi, and U. Sperhake, *Phys. Rev. D* **87**, 043513 (2013), arXiv:1212.0551.
- [239] K. Dev and M. Gleiser, *Gen. Rel. Grav.* **34**, 1793 (2002), arXiv:astro-ph/0012265.
- [240] E. Barausse and L. Rezzolla, *Phys. Rev. D* **77**, 104027 (2008), arXiv:0711.4558.
- [241] S. B. Giddings and M. L. Mangano, *Phys. Rev. D* **78**, 035009 (2008), arXiv:0806.3381.
- [242] A. Gould, B. T. Draine, R. W. Romani, and S. Nussinov, *Phys. Lett. B* **238**, 337 (1990).

- [243] H. Bondi, *Mon. Not. Roy. Astron. Soc.* **112**, 195 (1952).
- [244] H. Bondi and F. Hoyle, *Mon. Not. Roy. Astron. Soc.* **104**, 273 (1944).
- [245] H. Kim and W.-T. Kim, *Astrophys. J.* **665**, 432 (2007), arXiv:0705.0084.
- [246] M. Maggiore, *Gravitational Waves. Vol. 1: Theory and Experiments* (Oxford University Press, Oxford, 2008).
- [247] L. Gualtieri, E. Berti, J. Pons, G. Miniutti, and V. Ferrari, *Phys. Rev. D* **64**, 104007 (2001), arXiv:gr-qc/0107046.
- [248] T. Zouros and D. Eardley, *Annals Phys.* **118**, 139 (1979).
- [249] P. A. Sundararajan, G. Khanna, and S. A. Hughes, *Phys. Rev. D* **76**, 104005 (2007), arXiv:gr-qc/0703028.
- [250] S. A. Hughes, *Phys. Rev. D* **61**, 084004 (2000).
- [251] E. Barausse, *Mon. Not. Roy. Astron. Soc.* **382**, 826 (2007), arXiv:0709.0211.
- [252] V. Cardoso, P. Pani, M. Cadoni, and M. Cavaglia, *Phys. Rev. D* **77**, 124044 (2008), arXiv:0709.0532.
- [253] P. O. Mazur and E. Mottola, (2001), arXiv:gr-qc/0109035.
- [254] V. Cardoso, P. Pani, M. Cadoni, and M. Cavaglia, *Classical Quantum Gravity* **25**, 195010 (2008), arXiv:0808.1615.
- [255] E. Berti, V. Cardoso, and C. M. Will, *Phys. Rev. D* **73**, 064030 (2006), arXiv:gr-qc/0512160.
- [256] J. L. Friedman, *Communications in Mathematical Physics* **63**, 243 (1978).
- [257] C. B. Chirenti and L. Rezzolla, *Phys. Rev. D* **78**, 084011 (2008), arXiv:0808.4080.
- [258] J. Keir, (2014), arXiv:1404.7036.
- [259] N. Comins and B. F. Schutz, *Royal Society of London Proceedings Series A* **364**, 211 (1978).
- [260] E. Barausse, V. Cardoso, and P. Pani, *J. Phys. Conf. Ser.* **610**, 012044 (2015), arXiv:1404.7140.
- [261] H. Okawa, H. Witek, and V. Cardoso, *Phys. Rev. D* **89**, 104032 (2014), arXiv:1401.1548.
- [262] P. O. Mazur and E. Mottola, *Proc. Nat. Acad. Sci.* **101**, 9545 (2004), arXiv:gr-qc/0407075.
- [263] M. Visser and D. L. Wiltshire, *Classical Quantum Gravity* **21**, 1135 (2004), arXiv:gr-qc/0310107.

- [264] C. B. Chirenti and L. Rezzolla, *Classical Quantum Gravity* **24**, 4191 (2007), arXiv:0706.1513.
- [265] W. Israel, *Il Nuovo Cimento B Series 10* **44**, 1 (1966).
- [266] G. Festuccia and H. Liu, *Adv. Sci. Lett.* **2**, 221 (2009), arXiv:0811.1033.
- [267] E. Berti, V. Cardoso, and P. Pani, *Phys. Rev. D* **79**, 101501 (2009), arXiv:0903.5311.
- [268] S. Gurvitz, *Phys. Rev. A* **38**, 1747 (1988).
- [269] S. Chandrasekhar and V. Ferrari, *Royal Society of London Proceedings Series A* **434**, 449 (1991).
- [270] N. Andersson, Y. Kojima, and K. D. Kokkotas, *Astrophys. J.* **462**, 855 (1996), arXiv:gr-qc/9512048.
- [271] Y. Kojima, N. Andersson, and K. D. Kokkotas, *Proc. Roy. Soc. Lond.* **451**, 341 (1995), arXiv:gr-qc/9503012.
- [272] LIGO Scientific Collaboration, B. Abbott *et al.*, *Phys. Rev. D* **80**, 062001 (2009), arXiv:0905.1654.
- [273] LIGO Scientific Collaboration, VIRGO Collaboration, J. Aasi *et al.*, *Phys. Rev. D* **89**, 102006 (2014), arXiv:1403.5306.
- [274] S. Yoshida and Y. Eriguchi, *Mon. Not. Roy. Astron. Soc.* **282**, 580 (1996).
- [275] K. D. Kokkotas, J. Ruoff, and N. Andersson, *Phys. Rev. D* **70**, 043003 (2004), arXiv:astro-ph/0212429.
- [276] P. Pani, E. Barausse, E. Berti, and V. Cardoso, *Phys. Rev. D* **82**, 044009 (2010), arXiv:1006.1863.
- [277] L. A. Oliveira, V. Cardoso, and L. C. B. Crispino, *Phys. Rev. D* **89**, 124008 (2014), arXiv:1405.4038.
- [278] S. Hod, *Phys. Rev. D* **90**, 027501 (2014), arXiv:1405.7702.
- [279] C. Cutler and L. Lindblom, *Astrophys. J.* **314**, 234 (1987).
- [280] P. Bizon and A. Rostworowski, *Phys. Rev. Lett.* **107**, 031102 (2011), arXiv:1104.3702.
- [281] M. Maliborski, *Phys. Rev. Lett.* **109**, 221101 (2012), arXiv:1208.2934.
- [282] O. J. Dias, G. T. Horowitz, D. Marolf, and J. E. Santos, *Classical Quantum Gravity* **29**, 235019 (2012), arXiv:1208.5772.
- [283] V. Balasubramanian, A. Buchel, S. R. Green, L. Lehner, and S. L. Liebling, *Phys. Rev. Lett.* **113**, 071601 (2014), arXiv:1403.6471.

- [284] A. Buchel, S. L. Liebling, and L. Lehner, Phys. Rev. D **87**, 123006 (2013), arXiv:1304.4166.
- [285] F. W. Dyson, Phil. Trans. Roy. Soc. **184**, 43 (1893).
- [286] F. W. Dyson, Phil. Trans. Roy. Soc. **184A**, 1041 (1893).
- [287] S. Chandrasekhar and E. Fermi, The Astrophysical Journal **118**, 116 (1953).
- [288] V. Cardoso and L. Gualtieri, Classical Quantum Gravity **23**, 7151 (2006), arXiv:hep-th/0610004.
- [289] L. Lehner and F. Pretorius, Phys. Rev. Lett. **105**, 101102 (2010), arXiv:1006.5960.
- [290] R.-S. Lu *et al.*, The Astrophysical Journal **788**, 120 (2014).
- [291] R. Narayan, New J. Phys. **7**, 199 (2005), arXiv:gr-qc/0506078.
- [292] L. Ferrarese and H. Ford, Space Sci. Rev. **116**, 523 (2005), arXiv:astro-ph/0411247.
- [293] E. Berti, V. Cardoso, and O. Starinets, Classical Quantum Gravity **26**, 163001 (2009).
- [294] G. Risaliti *et al.*, Nature **494**, 449 (2013), arXiv:1302.7002.
- [295] P. Pani, C. F. B. Macedo, L. C. B. Crispino, and V. Cardoso, Phys. Rev. D **84**, 087501 (2011), arXiv:1109.3996.
- [296] K. Yagi, N. Yunes, and T. Tanaka, Phys. Rev. D **86**, 044037 (2012), arXiv:1206.6130.
- [297] C. Boehm and P. Fayet, Nucl. Phys. B **683**, 219 (2004), arXiv:hep-ph/0305261.
- [298] L. C. B. Crispino, S. R. Dolan, and E. S. Oliveira, Phys. Rev. Lett. **102**, 231103 (2009), arXiv:0905.3339.
- [299] R. Fabbri, Phys. Rev. D **12**, 933 (1975).
- [300] N. G. Sanchez, Phys. Rev. D **18**, 1030 (1978).
- [301] S. S. Gubser, Phys. Rev. D **56**, 7854 (1997), arXiv:hep-th/9706100.
- [302] C. Doran, A. Lasenby, S. Dolan, and I. Hinder, Phys. Rev. D **71**, 124020 (2005), arXiv:gr-qc/0503019.
- [303] L. C. B. Crispino, E. S. Oliveira, A. Higuchi, and G. E. Matsas, Phys. Rev. D **75**, 104012 (2007).
- [304] E. Jung and D. Park, Nucl. Phys. B **717**, 272 (2005), arXiv:hep-th/0502002.
- [305] L. C. B. Crispino, S. R. Dolan, and E. S. Oliveira, Phys. Rev. D **79**, 064022 (2009).
- [306] L. C. B. Crispino and E. S. Oliveira, Phys. Rev. D **78**, 024011 (2008).

- [307] E. S. Oliveira, L. C. B. Crispino, and A. Higuchi, *Phys. Rev. D* **84**, 084048 (2011).
- [308] K. Glampedakis and N. Andersson, *Classical Quantum Gravity* **18**, 1939 (2001), arXiv:gr-qc/0102100.
- [309] S. Dolan, *Scattering, absorption and emission by black holes*, PhD thesis, Trinity Hall and Astrophysics Group, Cavendish Laboratory, University of Cambridge, Cambridge, England, 2006.
- [310] S. R. Dolan, *Classical Quantum Gravity* **25**, 235002 (2008), arXiv:0801.3805.
- [311] L. C. B. Crispino, E. S. Oliveira, and G. E. Matsas, *Phys. Rev. D* **76**, 107502 (2007).
- [312] S. R. Dolan, E. S. Oliveira, and L. C. B. Crispino, *Phys. Rev. D* **79**, 064014 (2009), arXiv:0904.0010.
- [313] S. R. Dolan, L. A. Oliveira, and L. C. B. Crispino, *Phys. Rev. D* **85**, 044031 (2012), arXiv:1105.1795.
- [314] E. S. Oliveira, S. R. Dolan, and L. C. B. Crispino, *Phys. Rev. D* **81**, 124013 (2010).
- [315] C. F. B. Macedo, L. C. B. Crispino, and V. Cardoso, *Phys. Rev. D* **86**, 024002 (2012).
- [316] W. H. Press and S. A. Teukolsky, *Nature* **238**, 211 (1972).
- [317] A. Higuchi, *Classical Quantum Gravity* **18**, L139 (2001), arXiv:hep-th/0108144.
- [318] A. Higuchi, *Classical and Quantum Gravity* **19**, 599 (2002).
- [319] A. Zakharov, A. Nucita, F. DePaolis, and G. Ingrosso, (2005), arXiv:gr-qc/0507118.
- [320] Y. Décanini, G. Esposito-Farèse, and A. Folacci, *Phys. Rev. D* **83**, 044032 (2011).
- [321] Y. Décanini, A. Folacci, and B. Raffaelli, *Classical Quantum Gravity* **28**, 175021 (2011), arXiv:1104.3285.
- [322] H. Yang *et al.*, *Phys. Rev. D* **86**, 104006 (2012).
- [323] S. R. Dolan, *Phys. Rev. D* **82**, 104003 (2010).
- [324] C. S. Reynolds and M. A. Nowak, *Phys. Rept.* **377**, 389 (2003), arXiv:astro-ph/0212065.
- [325] G. L. Granato, G. De Zotti, L. Silva, A. Bressan, and L. Danese, *Astrophys. J.* **600**, 580 (2004), arXiv:astro-ph/0307202.
- [326] A. Marconi *et al.*, *Mon. Not. Roy. Astron. Soc.* **351**, 169 (2004), arXiv:astro-ph/0311619.
- [327] S. K. Chakrabarti, *Phys. Rept.* **266**, 229 (1996), arXiv:astro-ph/9605015.
- [328] M. Visser, *Phys. Rev. D* **46**, 2445 (1992), arXiv:hep-th/9203057.
- [329] M. Visser, *Phys. Rev. D* **48**, 583 (1993), arXiv:hep-th/9303029.

- [330] A. Medved, D. Martin, and M. Visser, *Classical Quantum Gravity* **21**, 1393 (2004), arXiv:gr-qc/0310009.
- [331] P. Leung, Y. Liu, W. Suen, C. Tam, and K. Young, *Phys. Rev. Lett.* **78**, 2894 (1997), arXiv:gr-qc/9903031.
- [332] P. Leung, Y. Liu, W. Suen, C. Tam, and K. Young, *Phys. Rev. D* **59**, 044034 (1999).
- [333] N. Gürlebeck, *Phys. Rev. Lett.* **114**, 151102 (2015), arXiv:1503.03240.
- [334] J. H. Davis and J. Silk, *Phys. Rev. Lett.* **114**, 051303 (2015), arXiv:1410.5423.
- [335] L. C. B. Crispino, S. R. Dolan, and E. S. Oliveira, *Phys. Rev. D* **79**, 064022 (2009), arXiv:0904.0999.
- [336] L. C. B. Crispino, A. Higuchi, and E. S. Oliveira, *Phys. Rev. D* **80**, 104026 (2009).
- [337] C. F. B. Macedo, L. C. S. Leite, E. S. Oliveira, S. R. Dolan, and L. C. B. Crispino, *Phys. Rev. D* **88**, 064033 (2013).
- [338] C. L. Benone, E. S. de Oliveira, S. R. Dolan, and L. C. B. Crispino, *Phys. Rev. D* **89**, 104053 (2014), arXiv:1404.0687.
- [339] C. F. B. Macedo and L. C. B. Crispino, *Phys. Rev. D* **90**, 064001 (2014).
- [340] L. I. Petrich, S. L. Shapiro, and S. A. Teukolsky, *Phys. Rev. Lett.* **60**, 1781 (1988).
- [341] L. Huang, M. Cai, Z.-Q. Shen, and F. Yuan, *Mon. Not. Roy. Astron. Soc.* **379**, 833 (2007), arXiv:astro-ph/0703254.
- [342] T. Johannsen and D. Psaltis, *Astrophys. J.* **718**, 446 (2010), arXiv:1005.1931.
- [343] Z. Li and C. Bambi, *JCAP* **1401**, 041 (2014), arXiv:1309.1606.
- [344] K. Thorne, <http://elmer.tapir.caltech.edu/ph237/week6/KipNewWindow5.pdf>, Unpublished .
- [345] W. Israel, *Nuovo Cimento B Serie* **48**, 463 (1967).
- [346] J. Frauendiener, C. Hoenselaers, and W. Konrad, *Classical and Quantum Gravity* **7**, 585 (1990).
- [347] J. Futterman, F. Handler, and R. Matzner, *Scattering from black holes* (Cambridge University Press, Cambridge, 1988).
- [348] S. R. Das, G. Gibbons, and S. D. Mathur, *Phys. Rev. Lett.* **78**, 417 (1997).
- [349] Y. Decanini, G. Esposito-Farese, and A. Folacci, *Phys. Rev. D* **83**, 044032 (2011), arXiv:1101.0781.
- [350] W. Lewin *et al.*, *Compact Stellar X-ray Sources* (Cambridge University Press, Cambridge, 2006).

- [351] A. W. McConnachie, *Astron. J.* **144**, 4 (2012), arXiv:1204.1562.
- [352] V. Cardoso, L. C. B. Crispino, C. F. B. Macedo, H. Okawa, and P. Pani, *Phys. Rev. D* **90**, 044069 (2014), arXiv:1406.5510.
- [353] H. Okawa, V. Cardoso, and P. Pani, *Phys. Rev. D* **90**, 104032 (2014), arXiv:1409.0533.
- [354] M. Heusler, *Living Rev. Relativity* **1** (1998).
- [355] R. Penrose, *Riv.Nuovo Cim.* **1**, 252 (1969).
- [356] R. M. Wald, (1997), arXiv:gr-qc/9710068.
- [357] S. W. Hawking and G. F. R. Ellis, *The Large Scale Structure of Space-Time* (Cambridge University Press, Cambridge, 1973).
- [358] J. Bardeen, Proceedings of gr 5, USSR, 1968, Tbilisi.
- [359] E. Ayon-Beato and A. Garcia, *Phys. Lett. B* **493**, 149 (2000), arXiv:gr-qc/0009077.
- [360] S. Ansoldi, (2008), arXiv:0802.0330.
- [361] J. P. Lemos and V. T. Zanchin, *Phys. Rev. D* **83**, 124005 (2011), arXiv:1104.4790.
- [362] A. Flachi and J. P. Lemos, *Phys. Rev. D* **87**, 024034 (2013), arXiv:1211.6212.
- [363] J. Li, M. Hong, and K. Lin, *Phys. Rev. D* **88**, 064001 (2013), arXiv:1308.6499.
- [364] K. Lin, J. Li, and S. Yang, *Int.J.Theor.Phys.* **52**, 3771 (2013).
- [365] C. Vishveshwara, *Nature* **227**, 936 (1970).
- [366] N. Andersson, *Phys. Rev. D* **55**, 468 (1997), arXiv:gr-qc/9607064.
- [367] R. A. Matzner, *Journal of Mathematical Physics* **9**, 163 (1968).
- [368] C. F. B. Macedo, L. C. Leite, E. S. Oliveira, S. R. Dolan, and L. C. B. Crispino, *Phys. Rev. D* **88**, 064033 (2013), arXiv:1308.0018.
- [369] S. Fernando and J. Correa, *Phys. Rev. D* **86**, 064039 (2012), arXiv:1208.5442.
- [370] S. R. Das, G. W. Gibbons, and S. D. Mathur, *Phys. Rev. Lett.* **78**, 417 (1997), arXiv:hep-th/9609052.
- [371] S. Zhou, J. Chen, and Y. Wang, *Int. J. Mod. Phys. D* **21**, 1250077 (2012), arXiv:1112.5909.
- [372] H. Huang, P. Liao, J. Chen, and Y. Wang, *J. Gravity* **2014**, 231727 (2014).
- [373] S. A. Hayward, *Phys. Rev. Lett.* **96**, 031103 (2006), arXiv:gr-qc/0506126.
- [374] T. De Lorenzo, C. Pacilio, C. Rovelli, and S. Speziale, (2014), arXiv:1412.6015.

- [375] N. E. J. Bjerrum-Bohr, J. F. Donoghue, and B. R. Holstein, *Phys. Rev. D* **67**, 084033 (2003), arXiv:hep-th/0211072.
- [376] H. Falcke, F. Melia, and E. Agol, (1999), arXiv:astro-ph/9912263.
- [377] Event horizon telescope, <http://www.eventhorizontelescope.org/>, Accessed in 4 May 2015.
- [378] C. F. B. Macedo and L. C. B. Crispino, *Phys. Rev. D* **90**, 064001 (2014), arXiv:1408.1779.
- [379] L. C. B. Crispino, S. R. Dolan, and E. S. Oliveira, *Phys. Rev. D* **79**, 064022 (2009).
- [380] P. Collins, R. Delbourgo, and R. Williams, *J. Phys. A* **6**, 161 (1973).
- [381] R. A. Matzner, C. DeWitt-Morette, B. Nelson, and T.-R. Zhang, *Phys. Rev. D* **31**, 1869 (1985).
- [382] D. R. Yennie, D. G. Ravenhall, and R. N. Wilson, *Phys. Rev.* **95**, 500 (1954).
- [383] S. Dolan, C. Doran, and A. Lasenby, *Phys. Rev. D* **74**, 064005 (2006), arXiv:gr-qc/0605031.
- [384] L. C. B. Crispino and E. S. Oliveira, *Phys. Rev. D* **78**, 024011 (2008).
- [385] L. C. B. Crispino, A. Higuchi, and E. S. Oliveira, *Phys. Rev. D* **80**, 104026 (2009).
- [386] L. C. B. Crispino, A. Higuchi, and G. E. A. Matsas, *Phys. Rev. D* **82**, 124038 (2010).
- [387] L. C. B. Crispino, S. R. Dolan, A. Higuchi, and E. S. de Oliveira, *Phys. Rev. D* **90**, 064027 (2014).